MATHEMATICAL MODELS FOR WOUND HEALING LYMPHANGIOGENESIS AND OTHER BIOMEDICAL PHENOMENA

by

Arianna Bianchi

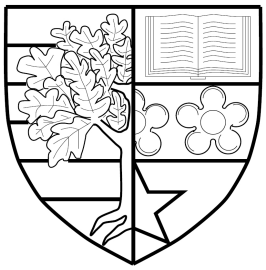

Submitted for the degree of
Doctor of Philosophy

Department of Mathematics
School of Mathematical and Computer Sciences
Heriot-Watt University

January 2016

Abstract

In this thesis we explore the mathematical modelling of wound healing lymphangiogenesis, tumour neoneurogenesis and *Drosophila* courtship behaviour.

We begin by focussing on the mathematical modelling of lymphatic regeneration in wound healing. Indeed, several studies suggest that one possible cause of impaired wound healing is failed or insufficient lymphangiogenesis, that is the formation of new lymphatic capillaries. Although many mathematical models have been developed to describe the formation of blood capillaries (angiogenesis), very few have been proposed for the regeneration of the lymphatic network. In Chapter 2 a model of five ordinary differential equations is presented to describe lymphangiogenesis in a skin wound. The variables represent different cell densities and growth factor concentrations, and where possible the parameters are estimated from experimental and clinical data. The system output is compared with the available biological literature and, based on parameter sensitivity analysis, new therapeutic approaches are suggested to enhance lymphangiogenesis in diabetic wounds.

Chapter 3 extends the aforementioned work to two PDE systems aimed at describing two possible hypotheses for the lymphangiogenesis process: 1) lymphatic capillaries sprout from existing and interrupted capillaries at the edge of the wound, in analogy to the blood angiogenesis case; 2) lymphatic endothelial cells first collect together in the wound region through following the lymph flow and then begin to form a network. Furthermore, we include the effect of advection from both background interstitial flow and additional lymph flow from the open capillaries, and address the question of their relative importance in the lymphangiogenesis process.

Malignant tumours induce not only the formation of a lymphatic and a blood vascular network, but also innervation around themselves. However, the relationship between tumour progression and the nervous system is still poorly understood. In Chapter 4 we study the interactions between the nervous system and tumour cells through an 8-dimensional ODE model. The model confirms experimental observations that a tumour promotes nerve formation around itself, and that high levels of nerve growth factor (NGF) and axon guidance molecules (AGMs) are recorded in the presence of a tumour. Our results also reflect the observation that high stress levels (represented by higher norepinephrine release by sympathetic nerves) contribute to tumour development and spread, indicating a mutually beneficial relationship between tumour cells and neurons.

In Chapter 5 a preliminary model for courtship behavioural patterns of *Drosophila melanogaster* is suggested. *Drosophila* courtship behaviour is considered a good model to investigate neurodegenerative diseases (such as Parkinson's) in humans. The present chapter illustrates the biological and health-care related background to this topic, and then presents a possible modelling approach based on Pasemann's work on neural networks.

We conclude with a brief discussion that summarises the main results and outlines directions for future work.

Acknowledgements

I would like to acknowledge and thank my supervisors Prof. Jonathan Sherratt and Dr. Kevin Painter for their excellent supervision during my three years as a PhD student: their careful attention, insightful suggestions and patience helped me to make the very most of my postgraduate education. I would also like to thank Dr. Georgios Lolas for proposing an interesting project for collaboration and for the enthusiasm he put in the work and our meetings in general. I must also mention the varied community of students and staff in the School of Mathematical and Computer Sciences who have contributed to the fantastic time I have had in Edinburgh over the years. Finally, I wish to acknowledge the generous financial support from the Maxwell Institute, without which my work here would not have been possible.

Declaration Statement

The Research Thesis Submission form is attached.

Contents

1 Introduction **1**

1.1 Wound healing lymphangiogenesis 1

1.2 Tumour-nerve interactions 4

1.3 *Drosophila* courtship behaviour 6

2 A model for lymphangiogenesis in normal and diabetic wounds **8**

2.1 Introduction 9

2.1.1 Motivation 9

2.1.2 Biology 10

2.2 Modelling 13

2.2.1 Brief review of existing models 13

2.2.2 Model development 14

2.2.3 Parameters and initial conditions 22

2.3 Results and analysis 24

2.3.1 Modelling the diabetic case 25

2.3.2 Comparison of results in the normal and diabetic cases 28

2.3.3 Analysis of the model 30

2.4 Therapies 33

2.4.1 Existing experimental treatments 33

2.4.2 Novel therapeutic approaches 38

2.5 Conclusions 39

3 Spatio-temporal models for wound healing lymphangiogenesis **41**

3.1 Introduction 42

3.2 Biological background 43
3.2.1 Wound healing 43
3.2.2 Sprouting versus self-organising lymphangiogenesis 44
3.2.3 Interstitial versus lymph flow 44
3.3 Mathematical Modelling 46
3.3.1 Review of lymphatic-related models 46
3.3.2 Model targets 47
3.3.3 Model variables and domain 47
3.3.4 Advection velocity and open capillaries 48
3.3.5 Self-organising hypothesis 50
3.3.6 Sprouting hypothesis 56
3.3.7 Parameters and initial and boundary conditions 58
3.4 Numerical solutions 62
3.4.1 Self-organising hypothesis 63
3.4.2 Sprouting hypothesis 65
3.4.3 Comparison between the two models 65
3.5 Conclusions 69

4 Modelling (direct) tumour-nerve interactions 71

4.1 Introduction 72
4.2 Biological background 73
4.2.1 Neurons, neurotransmitters and the Autonomic Nervous System (ANS) 73
4.2.2 Tumour-induced neoneurogenesis 74
4.2.3 ANS effects on tumour progression 75
4.3 Mathematical model 76
4.3.1 Model equations 77
4.3.2 Parameters and initial conditions 80
4.4 Results 81
4.4.1 Parameter sensitivity analysis 85
4.4.2 Stress and tumour progression 86

4.4.3 Blocking tumour acetylcholine receptors . . . 87
4.5 Discussion . . . 87

5 Modelling *Drosophila*'s courtship behaviour 90
5.1 Introduction . . . 92
5.1.1 Ethology of *Drosophila* courtship . . . 93
5.1.2 A "courtship tracker" . . . 95
5.1.3 Relevance for the 3Rs and human health . . . 95
5.2 Mathematical Modelling . . . 96
5.2.1 Pasemann's model . . . 97
5.2.2 A "Pasemann-like" model . . . 99
5.2.3 Simulations . . . 103
5.2.4 Rejective and receptive females . . . 105
5.3 Future work . . . 108

6 Conclusions 110
6.1 Results . . . 110
6.1.1 Wound healing lymphangiogenesis . . . 110
6.1.2 Tumour neoneurogenesis and (direct) tumour-nerve interactions 111
6.1.3 *Drosophila* courtship behaviour . . . 112
6.1.4 Remark – parameter estimation . . . 112
6.2 Future work . . . 112
6.2.1 Angio- and lymphangio-genesis in wound healing . . . 112
6.2.2 Tumour-nerve interactions . . . 113
6.2.3 Ecological models for cancer . . . 113
6.2.4 Wound healing peripheral nerve regeneration . . . 113
6.2.5 Nerve-mediated cell migration . . . 114
6.2.6 *Drosophila* courtship model . . . 115

A Lymphangiogenesis ODE model – Appendix 116
A.1 ODE Parameter estimation . . . 116
A.1.1 Equilibrium values and standard sizes . . . 116

A.1.2 TGF-β equation . . . 117
A.1.3 Macrophage equation . . . 118
A.1.4 VEGF equation . . . 122
A.1.5 LECs equation . . . 124
A.2 Calculation of the steady states . . . 128

B Lymphangiogenesis PDE model – Parameter estimation 133

B.1 Sizes, weights, equilibria and velocities . . . 133
B.1.1 Domain size . . . 133
B.1.2 Macrophage volume . . . 133
B.1.3 Molecular weights . . . 133
B.1.4 TGF-β equilibrium T^{eq} . . . 133
B.1.5 Macrophage equilibrium M^{eq} . . . 134
B.1.6 VEGF equilibrium V^{eq} . . . 134
B.1.7 Normal capillary density C^{eq} . . . 134
B.1.8 Maximum capillary density C_{max} . . . 134
B.1.9 Lymph velocity . . . 135
B.1.10 Interstitial flow velocity . . . 136
B.2 Re-calculation of s_M and k_1 . . . 136
B.3 Diffusion coefficients . . . 136
B.3.1 VEGF diffusion coefficient D_V . . . 136
B.3.2 TGF-β diffusion coefficient D_T . . . 137
B.3.3 Macrophage random motility μ_M . . . 137
B.4 Advection parameters λ_1 and λ_2 . . . 137
B.5 Rate at which TGF-β is internalised by macrophages γ_1 . . . 138
B.6 Chemotaxis parameters . . . 138
B.6.1 Macrophage chemotactic sensitivity towards TGF-β χ_1 . . . 138
B.6.2 LEC chemotactic sensitivity towards VEGF χ_2 . . . 139
B.6.3 Density-dependence of the macrophage chemotactic sensitivity ω . . . 139
B.7 Macrophage inflow ϕ_1 . . . 140

C Tumour-nerve interactions – Parameter estimation **141**

C.1 Standard sizes and weights 141

C.2 Initial and equilibrium values 142

C.3 Primary tumour cells equation 145

C.4 NGF equation 151

C.5 AGM equation 154

C.6 SNC equation 155

C.7 PNC equation 159

C.8 Norepinephrine (noradrenaline) equation 161

C.9 Acetylcholine equation 163

Bibliography **165**

Chapter 1

Introduction

1.1 Wound healing lymphangiogenesis

The main focus of this thesis concerns the modelling of wound-healing related processes. In particular, we examine the phenomenon of *lymphangiogenesis* (that is, lymphatic vasculature regeneration) as the main topic of study due to the presence of exciting recent biological literature and the scarcity of mathematical models in this area. Recent reviews of lymphangiogenesis can be found in [129, 187, 247]; among experimental research papers, [20, 26, 223] are of particular significance for my work. On the mathematical modelling side, there is a significant gap between the amount of models developed for blood angiogenesis (for a comprehensive review, see [229]) and those describing its sibling process lymphangiogenesis; of these, most focus on tumour-induced lymphangiogenesis (see for instance [89]). To the writer's knowledge, only one modelling paper has been produced that deals with wound healing lymphangiogenesis: this work, presented in [218], uses elasticity theory to explain the lymphatic network pattern in collagen gels.

The lymphatic system first came to the anatomists' attention with Hippocrates' mention of lymph nodes in his 5^{th} century BC work *On Joints* [276]. Later, the Roman physician Rufus of Ephesus identified the axillary, inguinal and mesenteric nodes and the thymus in the 1^{st}-2^{nd} century [169]. The earliest reference to lymphatic vessels is instead attributed to the anatomist Herophilus, who lived in Alexandria in the 3^{rd} century BC; he described the lymphatics as "absorptive

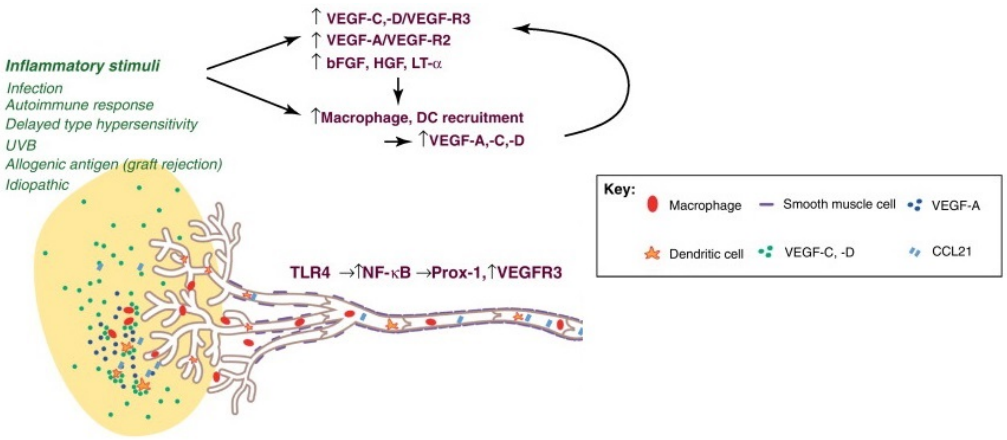

Figure 1.1: Inflammatory stimuli (such as those observed during wound healing) stimulate (extranodal) lymphangiogensis; from [129, adapted from Figure 1].

veins" [58, 264]. This rudimentary knowledge of the lymphatic system was lost during the Middle Ages, until Gabriele Falloppio re-discovered lymphatic capillaries in the mid-16$^{\text{th}}$ century [32]. Since then, there has been a steady but slow increase in our awareness of the "second" circulatory system of our body. Major impetus to study the lymphatic system came only in the 1990s, after the discovery of a suitable lymphatic marker that allowed quantifiable observation of lymphatic dynamics [40]. Lymphatic research is still a current trend in biomedicine and a source of sensational new discoveries, such as the 2015 finding of lymphatic vessels in the central nervous system [150].

An impetus for studying lymphatic regeneration is provided by recent biological studies that propose lymphangiogenesis as a major target for the treatment of non-healing wounds: functional lymphangiogenesis is nowadays regarded as a crucial factor in wound healing [39, 117, 191, 277] and delayed or failed lymphatic regeneration (such as the one observed in diabetic patients) constitutes a major cause of impairment to wound healing [5, 167, 224] (see Figure 1.1).

Our work conducted on wound healing lymphangiogenesis is reported in Chapters 2 and 3.

The first model developed to describe lymphangiogenesis is discussed in Chapter 2. It is a five-dimensional ODE model which has many strong points: the predictions of the model are in good agreement with experimental data and the majority of the parameters have been estimated from biological sources. The model

is then used to compare lymphangiogenesis dynamics between healthy and diabetic patients through changing the values of a specific set of parameters. These parameter changes, informed by biological observations, induce a model output which is characteristic of the diabetic scenario, thus supporting our assumptions for the disturbances of normal healing via altering the "diabetic" parameters. Finally, parameter sensitivity analysis is performed in order to identify the parameters to which the system is most sensitive; these indeed constitute promising targets for therapy, and different possible (effective) treatments are proposed.

The second work on lymphangiogenesis modelling is discussed in Chapter 3. Here, two systems of PDEs are proposed to model two different possible mechanisms of lymphatic regeneration after a skin wound. In fact, this process is not very well understood by experimentalists and different theories have been suggested to describe the exact way a lymphatic network is restored. Specifically, two main hypotheses have been advanced:

a. free lymphatic endothelial cells resulting from the interrupted capillaries pool into the wound space and spontaneously cluster into a network structure once they have reached a critical density (the *"self-organising" hypothesis*);

b. lymphatic capillaries regenerate "continuously" by sprouting from the interrupted network at the wound edge, in analogy to blood angiogenesis (the *"sprouting" hypothesis*).

These two hypotheses are translated into two distinct systems of PDEs and their solutions are compared. Simulations suggest that both cases can give rise to lymphatic regeneration occurring in the direction of the lymph flow; a discriminating factor could be the exact determination of relative contribution of different fluid flows in the tissue. Indeed, the concept of interstitial flow as a morphoregulator has recently emerged from the biological community [222]; however, it is not clear from the biological literature whether this is a major factor in shaping chemical concentrations in tissue regeneration, or if the main contribution to flow comes from the interrupted capillaries. Our model investigates such issue and suggests that lymph

flux into the wound from open capillaries is the main advection force in wound healing lymphangiogenesis.

1.2 Tumour-nerve interactions

Chapter 4 contains research work conducted in collaboration with Dr. Georgios Lolas from Technische Universität Dresden on tumour-nerve interactions.

Although a connection between a tumour and the patient's mood has been empirically known by physicians since antiquity, it is only in recent decades that a biochemical explanation of this phenomenon has been speculated [154, 263]. Yet even still, the bilateral interactions between a tumour and the nervous system are not fully understood and little is known about the *direct* connections between the two (indirect connections are, for instance, those involving the immune system). Inspiring experiments conducted recently which provide a better understanding of the "cross-talk" between a tumour and the host nervous system are reported in [6, 160]. While there is still a substantial amount of information that needs to be uncovered, what appears for certain is that interactions between nerves and tumour cells are bilateral: on the one hand, nerve-released substances affect tumour cell behaviour [64, 74, 137] (see Figure 1.2), and on the other a tumour mass can induce nerve proliferation around itself through a process named *neoneurogenesis* (in analogy with lymphangiogenesis and (blood) angiogenesis [72], which also both occur in the peritumoural area).

Our model is the first attempt (to the best of our knowledge) to mathematically study this phenomenon. The model's assumptions are based on topical biological papers and the parameters are carefully estimated from the experimental literature. A system of eight ODEs is developed in order to describe how tumour cells and nerves interact through various chemicals, such as neurotransmitters. Then, the model is simulated for both normal and stress conditions, the latter being characterised by high norepinephrine release. The simulations in the stress-free case confirm and explain the following experimental observations:

- nerve density is increased after tumour cell implantation;

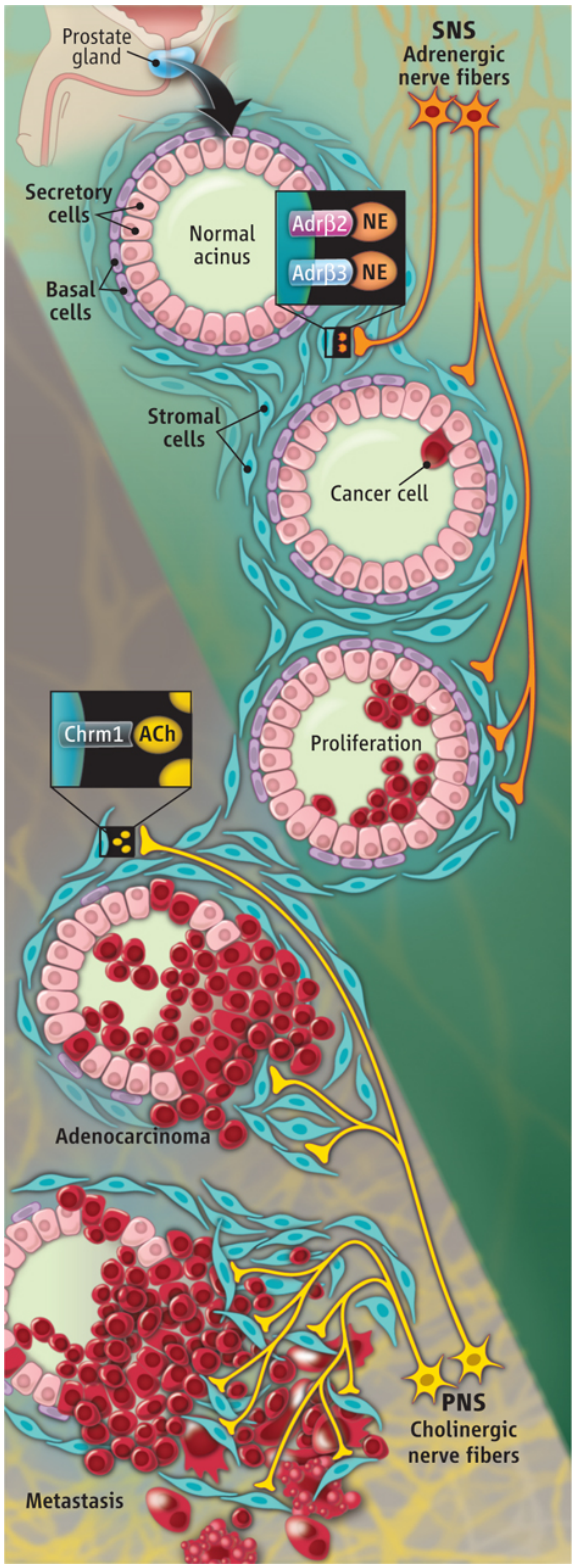

Figure 1.2: This picture from [112] illustrates how prostate cancer is initiated by sympathetic nerves that release norepinephrine (NE), which also induces tumour growth through adrenergic receptors (Adrβ2, Adrβ3); on the other hand, parasympathetic nerves release acetylcholine (ACh), which promotes cancer cell proliferation and metastasis by binding with (muscarinic) cholinergic receptors (Chrm1).

- the initial condition for primary tumour cells determines whether the tumour mass develops and has the potential to form metastases;
- factors such as nerve growth factor and axon guidance molecules are found at higher levels around tumours.

In addition, by simulating a stress condition we found that stress generally enhances tumour proliferation and the potential to form metastases. Even more noticeably, an initial condition for tumour cells that would normally evolve to a zero steady state (that is, a tumour free scenario) can tend to a non-zero equilibrium (i.e. persistent tumour) in a stress situation. Finally, we simulated a possible metastasis-reducing treatment by blocking acetylcholine receptors on tumour cells, with positive results.

Although at first glance a very different subject from wound healing lymphangiogenesis, studying tumour neoneurogenesis can help one to understand wound healing-related phenomena. Indeed, insufficient or impaired nerve regeneration is increasingly seen as a major obstacle for healing in diabetic patients.

1.3 *Drosophila* courtship behaviour

An entirely different modelling approach can be found in Chapter 5, where work is presented from a multidisciplinary team assembled during the *NC3Rs/POEMS Network Maths Study Group: Applying mathematics to 3Rs problems* (8-12 September 2014 in Cambridge). The aim of the working group was to develop models capable of describing courtship behaviour in the male fruit fly, *Drosophila melanogaster* (see Figure 1.3). These behavioural patterns provide, in fact, a good model for studying human neurodegenerative diseases shared with *Drosophila*, including Alzheimer's and Parkinson's [116, 231]. A mathematical model correctly describing these patterns would therefore help our understanding of the physiological and pathological connections between neural stimulation, innate reactions, memory and behaviour in general. As a result of the workshop and a subsequent meeting in Oxford, our team proposed three preliminary models. In Chapter 5 the one designed and simulated by the thesis' author is outlined. It consists of a set of four difference equations, each

of which describes the neural activity of a specific neural cluster associated with a certain behavioural pattern. The underlying assumption is that high neuronal activity in a certain cluster causes the male fly to display the behaviour corresponding to that cluster. To the author's knowledge, there is only one model similar to that presented here: a neural model developed in [127], where the authors propose a network model for cricket courtship. While further work is required to improve the model and compare it with available behavioural data, the ideas presented in this chapter are promising and offer a different perspective on the connection between behaviour and neural activity.

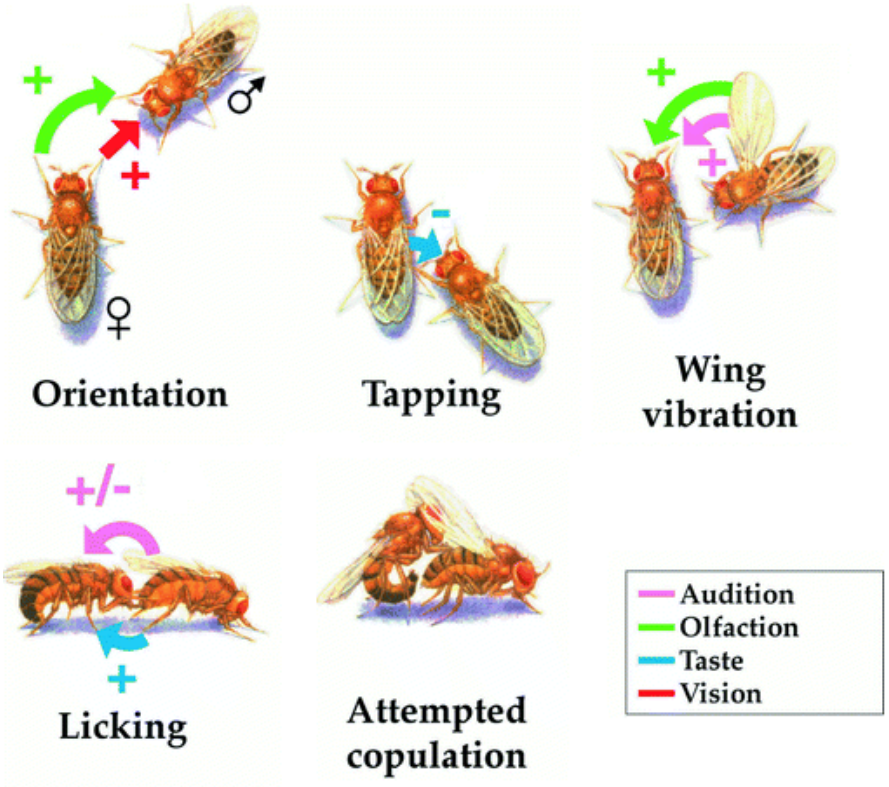

Figure 1.3: This picture from [99, Figure 1] illustrates the sequence of behaviours during the courtship of *Drosophila*. The coloured arrows represent sensory signals by which flies communicate: (+) for stimulatory and (–) for inhibitory inputs.

Chapter 2

A model for lymphangiogenesis in normal and diabetic wounds

The work presented in this chapter has been published in [17].

Abstract: *Several studies suggest that one possible cause of impaired wound healing is failed or insufficient lymphangiogenesis, that is the formation of new lymphatic capillaries. Although many mathematical models have been developed to describe the formation of blood capillaries (angiogenesis) very few have been proposed for the regeneration of the lymphatic network. Moreover, lymphangiogenesis is markedly distinct from angiogenesis, occurring at different times and in a different manner. Here a model of five ordinary differential equations is presented to describe the formation of lymphatic capillaries following a skin wound. The variables represent different cell densities and growth factor concentrations, and where possible the parameters are estimated from experimental and clinical data. The system is then solved numerically and the results are compared with the available biological literature. Finally, a parameter sensitivity analysis of the model is taken as a starting point for suggesting new therapeutic approaches targeting the enhancement of lymphangiogenesis in diabetic wounds. The work provides a deeper understanding of the phenomenon in question, clarifying the main factors involved. In*

particular, the balance between TGF-β and VEGF levels, rather than their absolute values, is identified as crucial to effective lymphangiogenesis. In addition, the results indicate lowering the macrophage-mediated activation of TGF-β and increasing the basal lymphatic endothelial cell growth rate, inter alia, as potential treatments. It is hoped the findings of this paper may be considered in the development of future experiments investigating novel lymphangiogenic therapies.

2.1 Introduction

2.1.1 Motivation

Much effort has been spent in order to better understand and potentially treat the impaired wound healing of diabetic patients. In this regard, one phenomenon that has recently gained attention from biologists is *lymphangiogenesis*; that is, the formation or reformation of lymphatic vasculature [108, 109, 129, 247]. Insufficient lyphangiogenesis, as observed in diabetic subjects, appears to correlate with failed or delayed wound healing.

Impaired wound healing is a major health problem worldwide and in recent decades has attracted the attention of both biologists and mathematicians. In many cases unresolved wound healing correlates with prolonged infection, which negatively affects the patient's quality of life, causing pain and impairing their physical abilities. A particularly serious infection may even require the amputation of the affected limb [139]. Furthermore, impaired wound healing also constitutes a major problem for health care systems, accounting for approximately 3% of all health service expenses in the UK and 20 billion dollars annually in the USA [55, 63, 65, 211]. Several systemic factors contribute to the delay or complete failure of the wound healing process [5, 77, 115, 141, 245]. In particular, diabetic patients exhibit a slower and sometimes insufficient response to infection after injury. Such a delay often results in a chronic wound; that is, the wound fails to progress through the normal stages of healing and usually remains at the inflammation stage [24, 207].

Interest in lymphangiogenesis in reference to wound healing is very recent: for example in the Singer & Clark 1999 review [238] the process is not mentioned. Nevertheless, lymphatic vessels have recently become regarded as a crucial factor in wound healing [39, 117]. They mediate the immune response and maintain the right pressure in the tissues [243], thus playing a very important role in inflammation and contributing to the healing of a wound [191, 277]. Moreover, failed restoration of a lymphatic network (observed, for example, in diabetic patients) is now thought to be a major cause of impairment to wound healing [5, 167, 224].

Mathematical modelling has proven a useful tool in understanding the mechanisms behind numerous biological processes. It is therefore of interest, and potentially great utility, to build a model describing lymphangiogenesis in wound healing, considering both the normal and pathological (diabetic) cases.

2.1.2 Biology

Wound healing is a very complex process involving a number of entwined events, which partially overlap in time and influence one another. For simplicity and educational purposes, it is often divided into four different phases: hemostasis, inflammation, proliferation and remodelling. Here the key events in each of the phases are summarised; for further details, see for instance [55, 91, 197, 238, 240]. A few minutes after injury, the contact between blood and the extracellular matrix (ECM) causes a biochemical reaction that leads to the formation of a blood clot. This "crust" has the double function of stopping the bleeding (*hemostasis*) and providing a "scaffold" for other cells involved in the process to be described below. Concurrently, chemical regulators (such as Transforming Growth Factor β, or TGF-β) are released, which attract cells such as neutrophils and monocytes to the wound site. These cells clean the wound of debris and neutralise any infectious agents that have invaded the tissue. This stage is called *inflammation*; in a normal wound inflammation begins a couple of hours after wounding and lasts a few weeks. Monocytes differentiate into macrophages, which complete the removal of the pathogens and also secrete some proteins (like Vascular Endothelial Growth Factor, or VEGF). This leads to the next

stage: the *proliferation* or *reepithelialisation* phase. At this point VEGF and other substances stimulate the growth and aggregation of the surrounding cells, restoring the different tissue functions. The clot is slowly substituted by a "temporary skin" called *granulation tissue* and the interrupted blood and lymphatic capillary networks are restored in processes named *(blood) angiogenesis* and *lymphangiogenesis*, respectively. After a lengthy period the granulation tissue is replaced by normal skin; this happens during the final, long phase of *remodelling*, which can take up to one or two years.

Although wound healing has been studied extensively and the main underlying mechanisms are well understood, little is known about how lymphangiogenesis takes place. Far more biological (and mathematical) literature has been produced about its sibling process, blood angiogenesis; it was not until the 1990s that lymphangiogenesis received significant attention from researchers [2, 15, 40]. This discrepancy was mainly due to the previous lack of markers and information on the growth factors involved in the lymphangiogenesis process; such a dearth of biochemical tools impeded a detailed and quantifiable study of lymphatic dynamics [40, 191]. For biological reviews about lymphangiogenesis see [129, 187, 247] and for particularly significant biological research papers see [20, 26, 223].

Naively, lymphatic vessels may appear "interchangeable" with their blood equivalents from a modelling perspective. However, it is stressed that the two vasculatures are quite different; for biological papers comparing lymphangiogenesis with (blood) angiogenesis see [2, 149, 244]. First of all, the capillary structure is completely distinct: while blood vessel walls are relatively thick, surrounded by smooth muscles which pump the blood around the body, lymphatic capillaries are made of a single layer of endothelial cells known as *lymphatic endothelial cells* (LECs) [187] (see Figure 2.1).

Moreover, the formation of new lymphatic capillaries, or the restoration of pre-existing ones, is very different from blood angiogenesis. While growing blood capillaries are known to sprout from existing interrupted ones, several studies suggest that lymphangiogenesis occurs in a different way [15, 182]. For instance, in [223] it

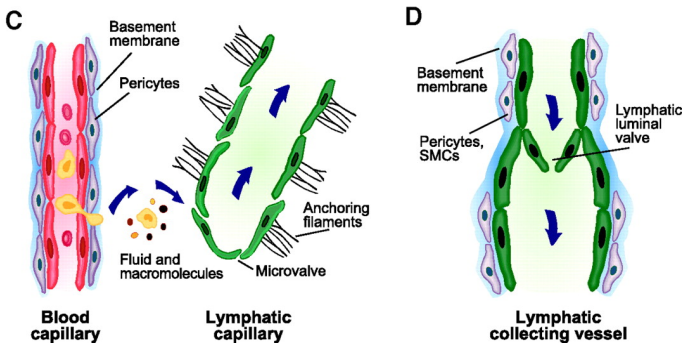

Figure 2.1: This figure, from [187, Figure 2], shows the structural differences between blood and lymphatic vessels.

is observed that LECs migrate as single cells in the direction of interstitial flow and after sufficient numbers have congregated in the wound region, they organise into vessels (see Figure 2.2).

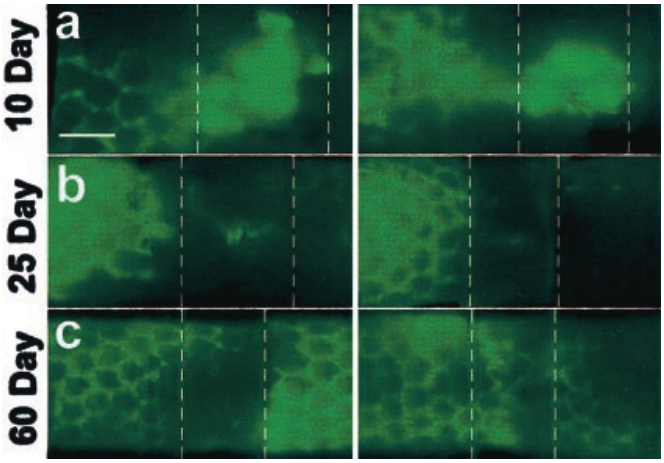

Figure 2.2: The photo is taken from [20, Figure 2] and shows lymphatic channels formation in the mouse tail. Note that at day 10 (a) fluid channelling is not observed, but at day 25 (b) discrete channels are present and at day 60 (c) a hexagonal lymphatic network is nearly complete. Notice also that lymph and interstitial fluid flows from left (tail tip) to right (tail base): this is in contrast to what happens during blood angiogenesis, which occurs equally from both sides of the implanted tissue equivalent. In [20] the authors use a new model of skin regeneration consisting of a collagen implant in a mouse tail (whose location is indicated by the dashed lines in the picture). The aim of the experiment is mainly to characterise the process of lymphatic regeneration. Lymph fluid is detected (green in the photograph) and in [20] it is shown that LECs follow this fluid. Therefore, this photo can be seen as the migration of LECs into the wound. (Bar=1mm)

We are therefore facing a new process whose mathematical description cannot be directly drawn from any previous model for blood angiogenesis. In the following section more details are given about the lymphangiogenesis process and a mathematical model is proposed.

2.2 Modelling

2.2.1 Brief review of existing models

Being of such a complicated nature and evident medical interest, wound healing has been the subject of mathematical modelling for decades; see for instance [235, 254] for the first models in the 1990s, [234] for a 2002 review and [94] for a 2010 review. A variety of mathematical formalisms have been involved in wound models: from classical PDEs [50, 192, 235], often derived from bio-mechanical considerations [90, 179], to stochastic models [23], to discrete models [52]. Some authors have used moving boundary methods to study the movement of the wound edge during healing [114], and attempts have been made to understand more specific aspects of the healing process, for example macrophage dynamics in diabetic wounds [271] and the resolution of the inflammatory phase [66]. One aspect of wound healing that has received considerable attention from mathematicians is (blood) angiogenesis (see, for instance, [27, 34, 85, 92, 158, 204, 226, 286]). A comprehensive review of mathematical models for vascular network formation can be found in Scianna et al.'s 2013 review [229]. Little work has been done with regards to modelling lymphangiogenesis and, indeed, [229] cites only a limited number of mathematical works concerning this topic. Of these a representative sample is given by [89, 203], which deal with tumour lymphangiogenesis, and [218], which describes the collagen pre-patterning caused by interstitial fluid flow. More specifically, [218] uses the physical theory of rubber materials to develop a model explaining the morphology of the lymphatic network in collagen gels, following the experimental observations of [20]. This is the only existent model for lymphangiogenesis in wound healing known to the authors. A further brief review of lymphatic modelling can be found in [164], where the phenomenon is approached from an engineering perspective.

In summary, a small number of papers have considered modelling the lymphangiogenesis process in the context of tumours; the modelling of lymphangiogenesis in wound healing is confined to [218], where two fourth order PDEs are used to describe the evolution of the collagen volume fraction and of the proton concentration

in a collagen implant. That work does not address the healing process as a whole which is the aim of the present chapter. Here a simple model (comprised of a system of ODEs) is presented that provides an effective description of the main dynamics observed in wound healing lymphangiogenesis.

2.2.2 Model development

In the present model five time-dependent variables are considered: two chemical concentrations (TGF-β and VEGF) and three cell densities (macrophages, LECs and lymphatic capillaries). Their interactions are described in Figure 2.3 and the formulation of the ODE model is based on the following set of processes (the full system is given by the set of equations (2.10)). The initial (or pre-wounding) state is altered when latent TGF-β is activated (thus becoming active TGF-β, denoted in the sequel by T) by macrophages and enzymes released immediately after wounding. This active form of TGF-β attracts more macrophages (M) to the wound site, through chemotaxis. Macrophages in turn produce VEGF (V), a growth factor that chemoattracts and stimulates the proliferation of LECs (L). Note that LEC growth is also inhibited by TGF-β. In the final stage of the process, LECs cluster in a network structure, transdifferentiating into lymphatic capillaries (C). This latter process happens spontaneously, although it is enhanced by VEGF.

In the following the time-dependent variables introduced above are discussed in detail. In particular, the derivation of the corresponding evolution equation is individually presented for each variable.

TGF-β This chemical is normally stored in an inactive or latent form in the body; however, only *active* TGF-β plays an important role in wound healing lymphangiogenesis, and therefore we will only consider the dynamics of the active chemical. Effectively, the active TGF-β protein is bound to a molecule called Latency Associated Peptide, forming the so-called Small Latent TGF-β Complex; this in turn is linked to another protein called Latent TGF-β Binding Protein, overall forming the Large Latent TGF-β Complex [250]. Hence, the two "peptide shells" must be removed before the organism can use the TGF-β.

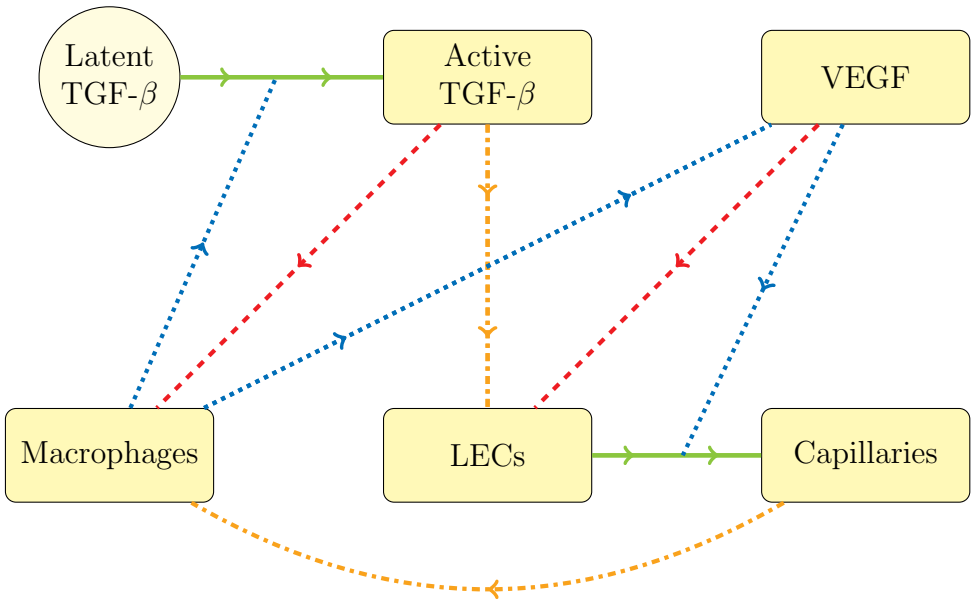

Figure 2.3: A schematic representation of the model dynamics. The five time-dependent variables correspond to the levels of the factors in each of the rectangular boxes; the quantity in the circle (latent TGF-β) is assumed constant. Concerning the arrows, **dashed red** denotes chemotactic attraction, **solid green** denotes activation/transdifferentiation, **dotted blue** denotes production/enhancement and **dash-dotted orange** denotes inhibition.

Another feature of this growth factor is that it exists in at least three isoforms (TGF-β1, 2 and 3) which play different roles at different stages of wound healing [36]. The isoform of primary interest in our application is TGF-β1.

The differential equation describing (active) TGF-β concentration has the following form:

$$\begin{array}{ccccccc} \text{change in} & & \text{activation by} & & & & \\ \text{TGF-}\beta & = & \text{enzymes and} & \times & \text{latent TGF-}\beta & - & \text{decay.} \\ \text{concentration} & & \text{macrophages} & & & & \end{array}$$

A review of the activation process is presented in [250] where it is reported that TGF-β can be activated in two ways. The first is *enzyme-mediated activation* whereby enzymes, mainly plasmin, release the Large Latent TGF-β Complex from the ECM and then the Latency Associated Peptide binds to surface receptors. The second form of activation is *receptor-mediated activation*. Here cells bind the Latency Associated Peptide and later deliver active TGF-β to their own TGF-β-Receptors or to the receptors of another cell. This behaviour is often observed in activated macrophages [97, 188].

Thus both enzyme concentration and macrophage density M are influential in the activation process and thereby appear in the activation term, $a_p p_0 e^{-a_p T_L t} + a_M M$. Here a_p and a_M denote the activation rates by enzymes and by macrophages, respectively. T_L denotes the (constant) amount of available latent TGF-β (more details in the next paragraph). In addition, the enzyme/plasmin concentration is assumed to decrease exponentially from the initial value p_0, as in [51]; this reproduces quite well the enzyme dynamics in real wounds [237].

It is widely accepted that a variety of cells have the potential to secrete latent TGF-β, including platelets, keratinocytes, macrophages, lymphocytes and fibroblasts [11, 124, 250]. Moreover, this latent complex is stored in the ECM in order to be constantly available to the surrounding cells [236]. This fact is manifested in a constant production rate T_L in our model equation. Furthermore, it is well known that macrophages secrete latent TGF-β [124], we assume that this occurs at a constant rate r_1. Together these considerations imply that the amount of available latent TGF-β in the wound will be modelled by $T_L + r_1 M$. Finally, TGF-β naturally decays at rate d_1, so the term $-d_1 T$ will be included in the differential equation. Therefore, the full equation for active TGF-β is

$$\frac{dT}{dt} = [a_p p_0 \exp(-a_p T_L t) + a_M M] \cdot [T_L + r_1 M] - d_1 T \, . \tag{2.1}$$

Macrophages These are a type of white blood cell that removes debris, pathogenic microorganisms and cancer cells through a process known as phagocytosis (as in Figure 2.4). They are produced by the differentiation of monocytes and are found in most of the tissues, patrolling for potential pathogens.

Perversely, in addition to enhancing inflammation and stimulating the immune system, macrophages can also contribute to decreased immune reactions. For this reason they are classified either as *M1* (or *inflammatory*) macrophages if they encourage inflammation, or as *M2* (or *repair*) macrophages if they decrease inflammation and encourage tissue repair [166]. Henceforth we restrict attention to inflammatory macrophages, since they are the most involved in lymphangiogenesis-related processes. A useful review of the multifaceted and versatile role of macrophages in

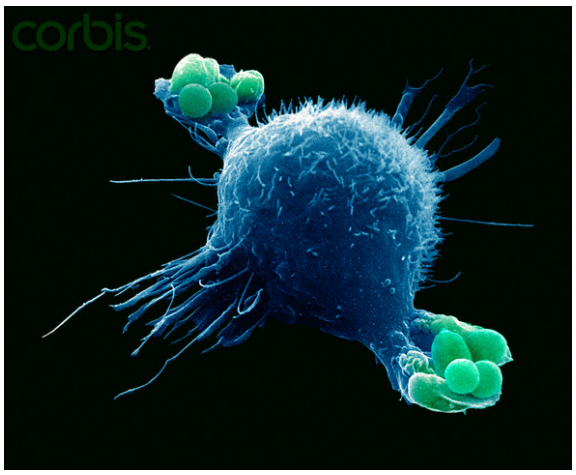

Figure 2.4: Macrophage engulfing bacteria as part of the immune system's response to infection. Credit: Dr. David Phillips/Visuals Unlimited/Corbis.

wound healing can be found in [217].

The following scheme will be considered for macrophage dynamics:

$$\begin{array}{c}\text{change in}\\ \text{macrophage}\\ \text{density}\end{array} = \begin{array}{c}\text{constant}\\ \text{source}\end{array} + \begin{array}{c}\text{chemotaxis}\\ \text{by TGF-}\beta\end{array} + \begin{array}{c}\text{logistic}\\ \text{growth}\end{array} - \begin{array}{c}\text{removal}\\ \text{and differ-}\\ \text{entiation.}\end{array}$$

The various terms appearing in the right-hand side of this equation are discussed below.

The number of inflammatory macrophages increases due to their migration into the wound, in part due to movement of existing inflammatory macrophages from the surrounding tissue, as well as by chemotaxis of monocytes up gradients of TGF-β [265], a fraction α of which differentiate into inflammatory macrophages [163]. The former is modelled by assuming a constant source s_M dictated by the non-zero level of inflammatory macrophages [272], and the latter by the term $\alpha h_1(T) = \alpha b_1 T^2/(b_2 + T^4)$. Here $h_1(T)$ is the "chemotactic function", whose form is discussed in detail in Appendix A.1. Only a (small) percentage β of macrophages undergo mitosis [100]; we thus assume the logistic growth term $\beta r_2 M\,(1 - M/k_1)$ where r_2 denotes the macrophage growth rate and k_1 the carrying capacity of the wound. Notice that here only M appears over the carrying capacity and the other cell types L and C are omitted. However, since the logistic term is small overall, adding L and C here would just increase the numerical complexity of the system without adding any significant contribution to the dynamics of the problem. This is reflected

in the parameter sensitivity analysis provided later in the paper, and simulations (not shown) including all populations showed no appreciable difference. Finally, inflammatory macrophages can die, differentiate into repair macrophages or be washed away by the lymph flow. This is embodied in the removal term $-(d_2+\rho C)M$, where d_2 denotes the constant death rate. Here polarisation and removal are considered to be linearly proportional to the capillary density C through the coefficient ρ: in particular, capillary formation is an index of progression through the healing process and, to reflect the decreased requirement for inflammatory macrophages as wounding proceeds, we assume the polarisation/removal rate increases with the size of C. Combining these observations one derives the macrophage equation

$$\frac{dM}{dt} = s_M + \alpha\frac{b_1T^2}{b_2+T^4} + \beta r_2 M\left(1-\frac{M}{k_1}\right) - (d_2+\rho C)M\ . \tag{2.2}$$

VEGF This is a signal protein whose main function is to induce the formation of vascular networks by stimulating proliferation, migration and self-organisation of cells after binding to specific receptors on their surface. There are many kinds of VEGF: while VEGF-A and VEGF-B are involved mainly in blood angiogenesis, VEGF-C and VEGF-D are the most important biochemical mediators of lymphangiogenesis via the receptor VEGFR3 (although VEGF-C can also stimulate angiogenesis via VEGFR2 – see Figure 2.5). For a comprehensive description of the growth factors involved in lymphangiogenesis see [118, 148]. Henceforth "VEGF" refers to VEGF-C (and, to a lesser extent, VEGF-D), unless otherwise stated.

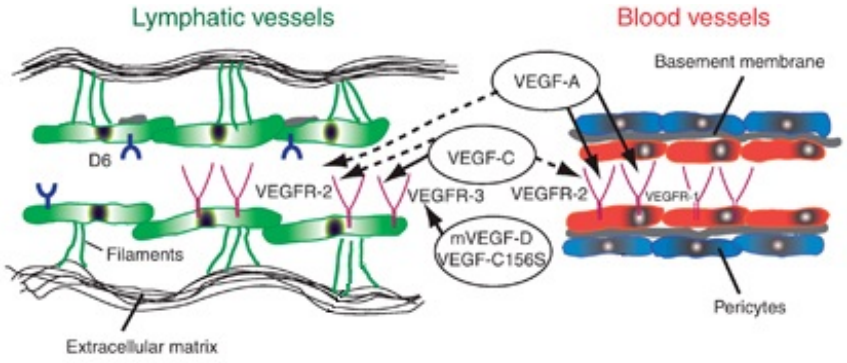

Figure 2.5: This picture, from [109, adapted from Figure 1], summarises the effects of different VEGF types on lymphatic and blood endothelial cells.

For VEGF we assume the following dynamics:

$$\begin{array}{c}\text{change in}\\ \text{VEGF}\\ \text{concentration}\end{array} = \begin{array}{c}\text{constant}\\ \text{source}\end{array} + \begin{array}{c}\text{production by}\\ \text{macrophages}\end{array} - \text{decay} - \begin{array}{c}\text{use by}\\ \text{LECs.}\end{array}$$

Since the normal VEGF level in the skin is nonzero [107, 196], it is assumed there is a constant source s_V of this growth factor from the surrounding tissues. VEGF is produced by several cells, but macrophages are considered to be one of its main sources in the context of wound healing [130, 279]. It is therefore natural to add the production term $+r_3M$ to the VEGF equation, where r_3 is the production rate of the chemical by macrophages. On the other hand, the VEGF level is reduced by natural decay at constant rate d_3, taken into account by the term $-d_3V$. In addition VEGF is internalised by cells: effectively, LECs use VEGF to divide and form capillaries [168, 284]; it is assumed this process occurs at a constant rate γ, leading to the term $-\gamma VL$. Thus, in this model the equation for VEGF dynamics is

$$\frac{dV}{dt} = s_V + r_3M - d_3V - \gamma VL\ . \tag{2.3}$$

LECs As discussed above, lymphatic vessel walls are made of (lymphatic) endothelial cells. The equation describing the presence of LECs in the wound consists of the following terms:

$$\begin{array}{c}\text{change in}\\ \text{LEC}\\ \text{density}\end{array} = \begin{array}{c}\text{growth,}\\ \text{upregulated by}\\ \text{VEGF and}\\ \text{downregulated}\\ \text{by TGF-}\beta\end{array} + \begin{array}{c}\text{inflow and}\\ \text{chemotaxis}\\ \text{by VEGF}\end{array} - \begin{array}{c}\text{crowding}\\ \text{effect and}\\ \text{apoptosis}\end{array} - \begin{array}{c}\text{transdiffer-}\\ \text{entiation}\\ \text{into}\\ \text{capillaries.}\end{array}$$

LEC growth is upregulated by VEGF [16, 275, 284] and downregulated by TGF-β [178, 242]. The former observation is described mathematically by augmenting the normal/basal constant growth rate c_1 with V in an increasing saturating manner through the parameters c_2 and c_3. To account for the latter, the growth term is multiplied by a decreasing function of T. Explicitly, the whole proliferation term is

$$\left(c_1 + \frac{V}{c_2 + c_3V}\right)\left(\frac{1}{1 + c_4T}\right)L \tag{2.4}$$

where c_4 takes into account the "intensity" of the TGF-β inhibition on LEC growth. It is assumed that LECs are brought into the wound by lymph flow at a constant rate s_L and are chemoattracted by VEGF [16, 247]. Considering a chemotactic function $h_2(V)$ of the same form as that used for TGF-β-mediated chemotaxis (see Appendix A.1), these phenomena are captured by the terms

$$s_L + h_2(V) = s_L + \frac{b_3 V^2}{b_4 + V^4} \, .$$

Since both of these movements originate from the interrupted lymphatic vasculature at the edges of the wound, this flow will tend to decrease as the lymphatic network is restored. Hence, supposing a linear correlation between the term above and the lymphatic regeneration, the former is multiplied by the piecewise linear function $f(C)$ defined by

$$f(C) = \begin{cases} 1 - \frac{C}{C^*} & \text{if } C < C^* \\ 0 & \text{if } C \geq C^* \end{cases} \, . \tag{2.5}$$

Here C^* is a capillary density threshold value above which the lymphatic network is functional and uninterrupted and LEC flow stops. Hence the final term for LEC inflow and chemotaxis is

$$\left(s_L + \frac{b_3 V^2}{b_4 + V^4} \right) f(C) \, . \tag{2.6}$$

LEC growth is limited by over-crowding of the wound space, a fact that is taken into account by the negative term $-L(M + L + C)/k_2$ where k_2 relates to the carrying capacity. Finally, individual or small clusters of LECs migrate into the wound and later form multicellular groups that slowly connect to one another, organising into vessel structures [20, 223]. Here it is assumed that when LECs are sufficiently populous (that is, their density becomes larger than a threshold value L^*) they self-organise into capillaries at a rate which depends linearly on VEGF concentration via the term $\delta_2 V$. In particular, endothelial cells tend to form network structures spontaneously (at a constant rate δ_1, say) but the rate is increased by the presence of VEGF [209]. These observations result in the transdifferentiation term

$-\sigma(L,C)\cdot(\delta_1+\delta_2 V)L$ where $\sigma(L,C)$ is the step function

$$\sigma(L,C)=\begin{cases}1 & \text{if } L+C\geq L^*\\ 0 & \text{if } L+C<L^*\end{cases}\ . \tag{2.7}$$

Note that σ depends both on L and C: this is justified by the observation that the self-organisation process begins when L reaches the threshold L^* and then continues as LECs start forming the first capillaries. Therefore the complete LEC equation is

$$\begin{aligned}\frac{dL}{dt} &= \left(c_1+\frac{V}{c_2+c_3V}\right)\left(\frac{1}{1+c_4T}\right)L+\left(s_L+\frac{b_3V^2}{b_4+V^4}\right)f(C)\\ &\quad -\frac{M+L+C}{k_2}L-\sigma(L,C)\cdot(\delta_1+\delta_2V)L.\end{aligned} \tag{2.8}$$

Lymphatic capillaries We assume that the lymphatic capillaries form simply from the self-organisation of LECs into a network structure. Thus the capillary formation term is just the transdifferentiation term from the LEC equation above and the dynamics of C are modelled by

$$\frac{dC}{dt}=\sigma(L,C)\cdot(\delta_1+\delta_2V)L\ . \tag{2.9}$$

The full system of equations is therefore given by

$$
\begin{aligned}
\frac{dT}{dt} &= \underbrace{[a_p p_0 \exp(-a_p T_L t) + a_M M]}_{\substack{\text{activation by}\\ \text{enzymes \& M}\Phi\text{s}}} \cdot \underbrace{[T_L + r_1 M]}_{\text{latent TGF-}\beta} - \underbrace{d_1 T}_{\text{decay}} \\
\frac{dM}{dt} &= \underbrace{s_M}_{\substack{\text{constant}\\ \text{source}}} + \underbrace{\alpha \frac{b_1 T^2}{b_2 + T^4}}_{\substack{\text{chemotaxis}\\ \text{by TGF-}\beta}} + \underbrace{\beta r_2 M \left(1 - \frac{M}{k_1}\right)}_{\text{logistic growth}} - \underbrace{(d_2 + \rho C) M}_{\substack{\text{removal and}\\ \text{differentiation}}} \\
\frac{dV}{dt} &= \underbrace{s_V}_{\substack{\text{constant}\\ \text{source}}} + \underbrace{r_3 M}_{\substack{\text{production}\\ \text{by M}\Phi\text{s}}} - \underbrace{d_3 V}_{\text{decay}} - \underbrace{\gamma V L}_{\text{use by LECs}} \\
\frac{dL}{dt} &= \underbrace{\left(c_1 + \frac{V}{c_2 + c_3 V}\right)\left(\frac{1}{1 + c_4 T}\right) L}_{\substack{\text{growth upregulated by VEGF}\\ \text{and downregulated by TGF-}\beta}} + \underbrace{\left(s_L + \frac{b_3 V^2}{b_4 + V^4}\right) f(C)}_{\substack{\text{inflow and}\\ \text{chemotaxis by VEGF}}} \\
&\quad - \underbrace{\frac{M + L + C}{k_2} L}_{\substack{\text{crowding effect}\\ \text{and apoptosis}}} - \underbrace{\sigma(L, C) \cdot (\delta_1 + \delta_2 V) L}_{\substack{\text{transdifferentiation}\\ \text{into capillaries}}} \\
\frac{dC}{dt} &= \underbrace{\sigma(L, C) \cdot (\delta_1 + \delta_2 V) L}_{\text{transdifferentiation of LECs}}
\end{aligned}
\tag{2.10}
$$

where $f(C)$ and $\sigma(L, C)$ are defined in (2.5) and (2.7), respectively.

2.2.3 Parameters and initial conditions

Parameters Table 2.1 gives a full list of parameter values, their units and the sources used for their estimation in the normal (non-diabetic) case. It is remarked that great care was put into assessing the parameter values, and of the 31 parameters listed in the table, 25 have been estimated from biological data. A detailed description of the estimation of each parameter can be found in Appendix A.1.

Initial conditions In the present model, the initial time-point $t = 0$ corresponds to the release of enzymes by platelets within the first hour after wounding [237, 238]. The initial amounts of active TGF-β, macrophages and VEGF are taken to be their equilibrium values, estimated from experimental data as shown in Table 2.2. It is assumed that there are no endothelial cells or capillaries at $t = 0$.

PARAMETER	VALUE	UNITS	SOURCE
a_p	2.9×10^{-2}	$\text{mm}^3\text{pg}^{-1}\text{day}^{-1}$	[54]
p_0	2.5×10^5	pg mm^{-3}	no data found
a_M	0.45	$\text{mm}^3\text{cells}^{-1}\text{day}^{-1}$	[97, 188]
T_L	18	pg mm^{-3}	([189])
r_1	3×10^{-5}	$\text{pg cells}^{-1}\text{day}^{-1}$	[124]
d_1	5×10^2	day^{-1}	[120]
s_M	5.42×10^2	$\text{cells mm}^{-3}\text{day}^{-1}$	([272])
α	0.5	1	[271]
b_1	8×10^8	$\text{cells pg}^2(\text{mm}^3)^{-3}\text{day}^{-1}$	([186])
b_2	8.1×10^9	$(\text{pg mm}^{-3})^4$	[265, 283]
β	5×10^{-3}	1	[100]
r_2	1.22	day^{-1}	[289]
k_1	6×10^5	$\text{mm}^3\text{cells}^{-1}$	[289]
d_2	0.2	day^{-1}	[44]
ρ	10^{-5}	$\text{day}^{-1}\text{cells}^{-1}$	[223]
s_V	1.9	cells day^{-1}	([107, 196])
r_3	1.9×10^{-3}	$\text{pg cells}^{-1}\text{day}^{-1}$	([130, 233])
d_3	11	day^{-1}	[131]
γ	1.4×10^{-3}	$\text{mm}^3\text{cells}^{-1}\text{day}^{-1}$	[155]
c_1	0.42	day^{-1}	[183]
c_2	42	day	[275]
c_3	4.1	pg day mm^{-3}	[275]
c_4	0.24	$\text{mm}^3\text{pg}^{-1}$	[178]
s_L	5×10^2	cells day^{-1}	no data found
b_3	10^7	$\text{cells pg}^2(\text{mm}^3)^{-3}\text{day}^{-1}$	no data found
b_4	8.1×10^9	$(\text{pg mm}^{-3})^4$	estimated $\approx b_2$
C^*	10^4	cells mm^{-3}	[223]
k_2	4.71×10^5	cells day mm^{-3}	[183]
L^*	10^4	cells mm^{-3}	[223]
δ_1	5×10^{-2}	day^{-1}	no data found
δ_2	10^{-3}	$\text{mm}^3\text{pg}^{-1}\text{day}^{-1}$	no data found

Table 2.1: A list of all the parameters appearing in the model equations (details of the estimation are provided in Appendix A.1). Each one is supplied with its estimated value, units and source used (when possible) to assess it. References in brackets mean that although the parameter was not *directly* estimated from a dataset, its calculated value was compared with the biological literature; the caption "no data found" signifies that no suitable data were found to estimate the parameter. Concerning the VEGF value corresponding to maximum LEC chemotaxis b_4, it was assumed that its value is similar to its TGF-β correspondent b_2; this choice was dictated by the lack of relevant/applicable biological data, to the authors' knowledge.

INIT.VALUE	VALUE	UNITS	SOURCE
$T(0)$	30	pg/mm^3	[283]
$M(0)$	1875	cells/mm^3	[272]
$V(0)$	0.5	pg/mm^3	[107, 196]
$L(0)$	0	cells/mm^3	assumption
$C(0)$	0	cells/mm^3	assumption

Table 2.2: Values of the model variables at $t = 0$.

2.3 Results and analysis

We now present a typical solution of the system (2.10) and compare it with biological data. The system is solved numerically with the MatLab standard ODE solver `ode45` with relative tolerance 10^{-6} and absolute tolerance 10^{-9} over a time interval of 100 days. It is remarked that the present model chiefly addresses inflammation and the early proliferation stage of the wound healing process. In healthy subjects the inflammatory phase starts a few hours after injury and lasts approximately 1 or 2 weeks, but it is prolonged in diabetic patients. Moreover, lymphangiogenesis occurs between 25 and 60 days after wounding, much later than blood angiogenesis which is observed between day 7 and day 17 [15, 223]. Thus, the equations are expected to realistically describe the phenomenon for about the first 100 days post-wounding.

The TGF-β level is expected to display a rapid spike in the first day post injury before returning to its equilibrium value [283]. In Figure 2.6 the simulation output is compared with a biological dataset. Both demonstrate the expected initial spike, but in the data a second peak is visible around day 5, reported also in [186]. We recall that TGF-β exists in at least three known isoforms: TGF-β1, TGF-β2 and TGF-β3; the biological data set concerns all kinds of TGF-β involved in other wound healing processes, such as collagen deposition, which are not modelled here (the time dynamics of the different TGF-β isoforms can be found in [281]). Nevertheless, the overall predicted trend of TGF-β concentration in the wound matches the biological reality fairly well.

Macrophage levels are observed to reach a peak approximately 5 days after injury before returning to their equilibrium level [186]. Again the model prediction is consistent with the biological literature, as in Figure 2.7.

VEGF is also reported to reach its maximum concentration 5 days after wounding

[233]. This is unsurprising given the above macrophage dynamics and the fact that macrophages are understood to be primarily responsible for the production of the protein. Once again there is a strong correlation between the results of the theoretical model and experimental observations, as shown in Figure 2.8.

LEC levels are expected to increase immediately after wounding but only later do the LECs self-organise into capillaries, around day 25 [223]. This is reflected in the simulation shown in Figure 2.9. Here LECs proliferate in the wound space until reaching the threshold level $L^* = 10^4$ around day 20. They then start agglomerating into capillary structures, commencing the lymphangiogenesis process proper.

2.3.1 Modelling the diabetic case

In order to simulate the diabetic case, some parameter values are changed as described in the following. Unfortunately, it is difficult to obtain precise quantitative assessment of the appropriate changes, and therefore the values chosen here only have a qualitative significance.

Several studies report that the TGF-β level is significantly lower in diabetic wounds compared with controls. This seems to be caused by impaired TGF-β activation both by platelets and macrophages and by reduced production of TGF-β by macrophages [3, 173, 281]. These features of the diabetic case are modelled by applying the following modifications to the parameters:

$$a_p^{diab} = \frac{1}{2} a_p^{norm} < a_p^{norm} \quad , \quad a_M^{diab} = \frac{1}{2} a_M^{norm} < a_M^{norm} \quad .$$

Furthermore, in diabetic wounds the macrophage density is higher than normal. In particular, the inflammatory macrophage phenotype persists through several days after injury, showing an impaired transition to the repair phenotype [173]. In addition, macrophage functions (such as phagocytosis and migration) are impaired in the diabetic case [126, 280]. These differences from the normal case are reflected in

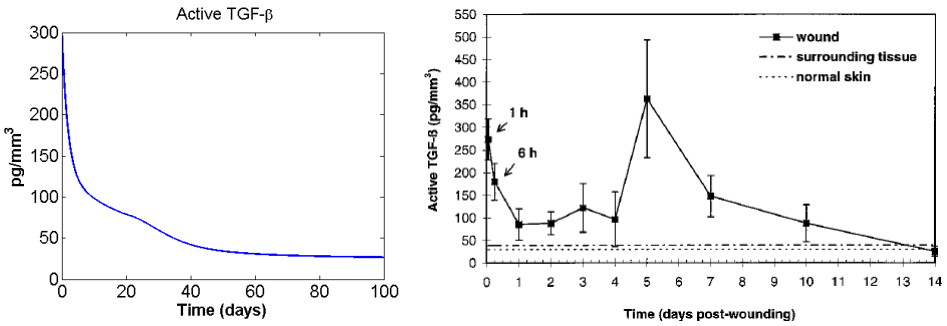

Figure 2.6: A comparison of the simulation output for the time course of TGF-β concentration with data from [283, Figure 2], showing the time course of active TGF-β generation during wound repair in rats.

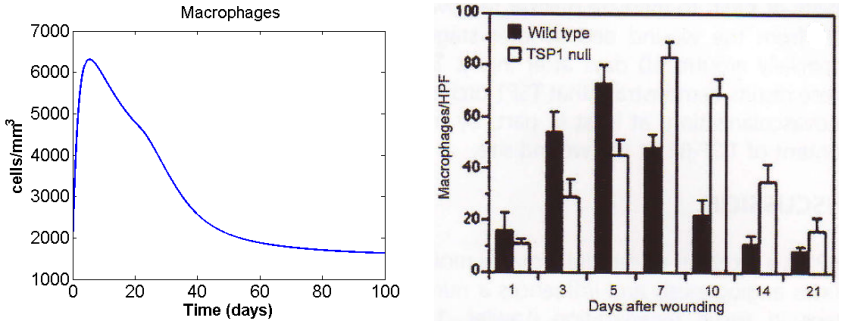

Figure 2.7: A comparison between model and experimental data for the time course of macrophage density. Experimental data taken from [186, Figure 3c]: note that the time-course comparison here is against the black bars, representing macrophage numbers in normal (wild-type) mice.

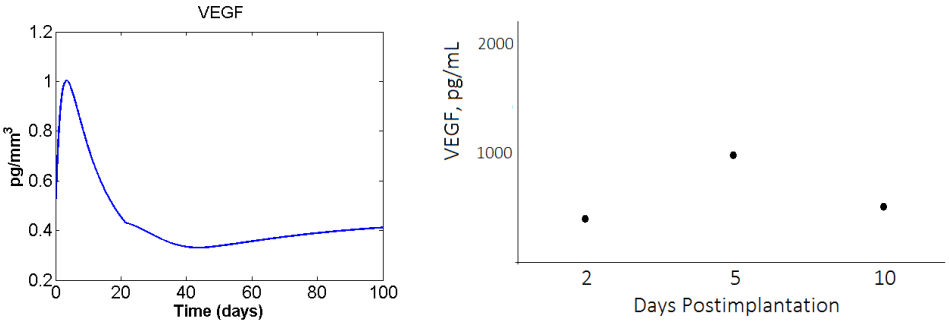

Figure 2.8: A comparison of the simulation output for the time course of VEGF concentration with data from [233, adapted from Figure 2], where VEGF was measured in rat wound fluid (note that the units on the vertical axis are pg/mL, where 1000 pg/mL = 1 pg/mm^3, and that here we reported only the median values).

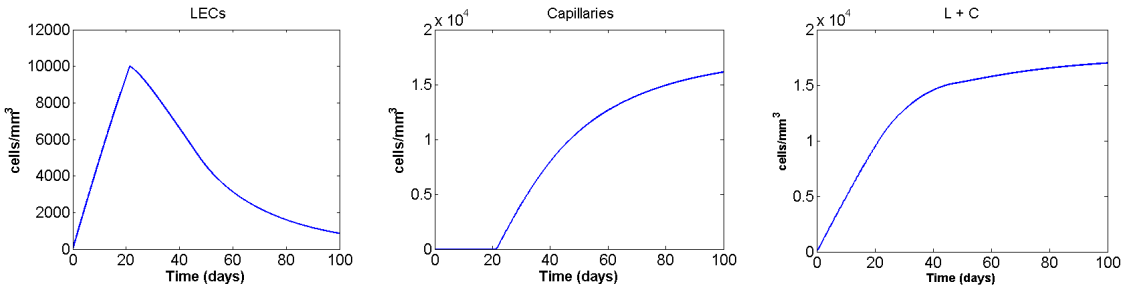

Figure 2.9: Simulation output for the time course of LEC density, lymphatic capillary density and their sum. Note that the sum density has also been plotted the sum, since LEC and capillary cells are difficult to differentiate and any cell counts are likely to reflect the total density of these two cell types.

the following choice of parameter changes:

$$\alpha^{diab} = 0.8 > \alpha^{norm}, \qquad b_1^{diab} = \tfrac{3}{4} b_1^{norm} < b_1^{norm},$$

$$d_2^{diab} = \tfrac{1}{2} d_2^{norm} < d_2^{norm}, \qquad r_3^{diab} = \tfrac{1}{2} r_3^{norm} < r_3^{norm}.$$

Finally, it is reported that endothelial cell proliferation is markedly reduced in diabetic wounds when compared with the normal case [48, 53, 132] (a detailed discussion of endothelial dysfunction in diabetes can be found in [28]). This phenomenon is reflected in the model by reducing the basal proliferation rate of endothelial cells:

$$c_1^{diab} = \frac{1}{2} c_1^{norm} < c_1^{norm} \ .$$

A summary of some of the differences between normal and diabetic wounds can be found in Figure 2.10.

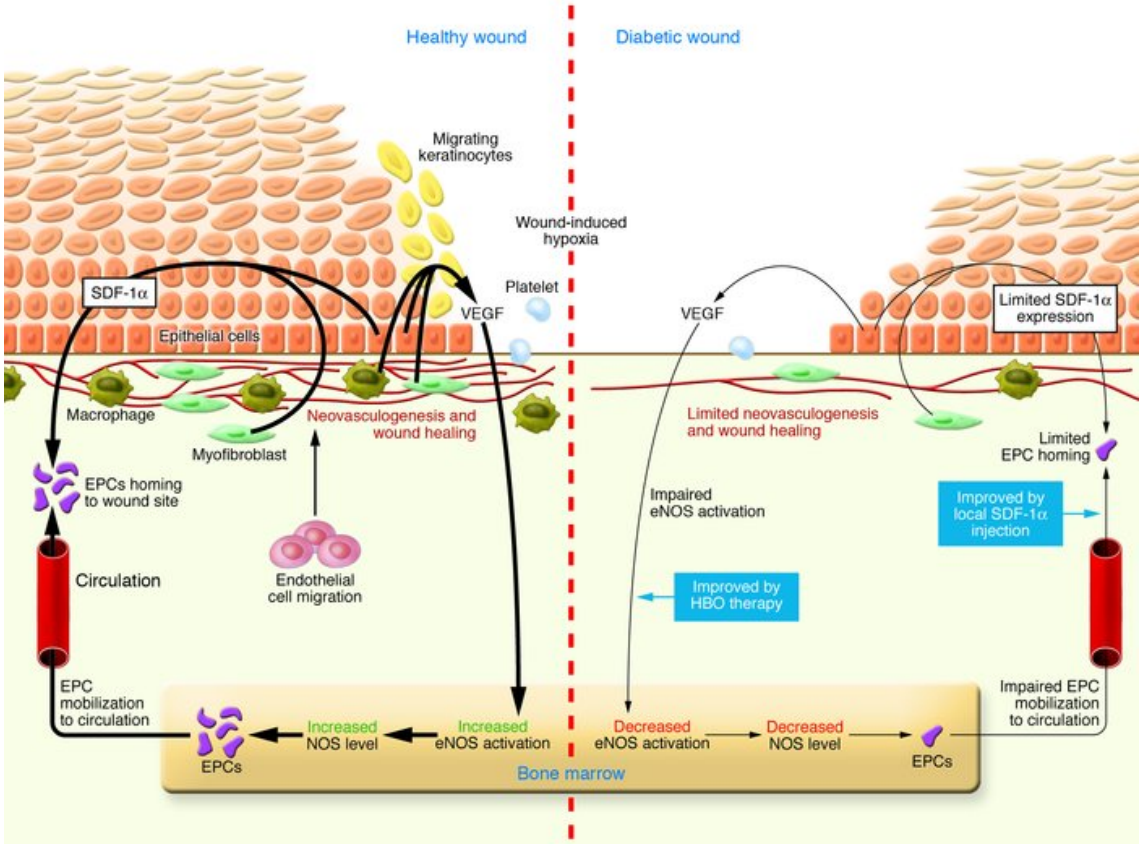

Figure 2.10: A summary of the differences between normal and diabetic wound healing, from [24, Figure 1].

2.3.2 Comparison of results in the normal and diabetic cases

Figures 2.11-2.14 show numerical simulations of the model comparing the time-course of the five model variables in the normal (blue solid line) and diabetic (red dashed line) case.

TGF-β The level of TGF-β recorded in diabetic wounds is lower than in the normal case, at least in the first 20 days after injury [3, 173, 281]. Model simulations are consistent with this observation (Figure 2.11).

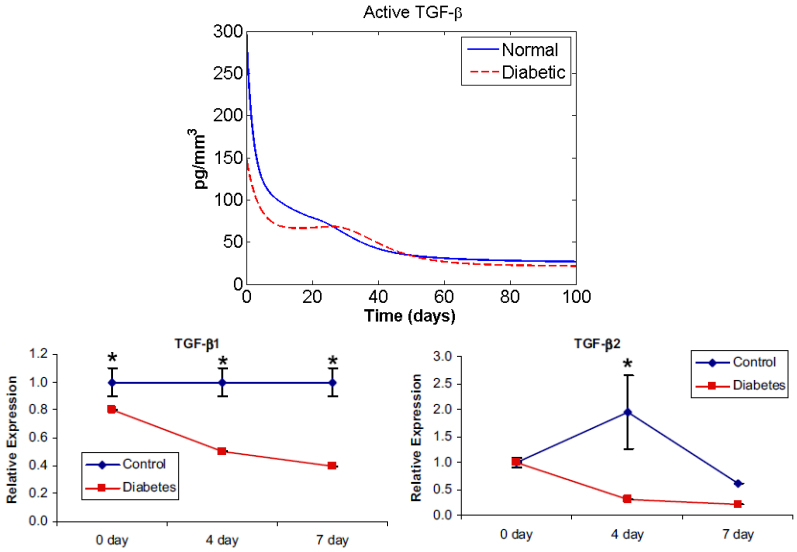

Figure 2.11: Time course of TGF-β concentration in normal and diabetic wounds as predicted by the model and as found empirically in [281, Figures 3G and 3H], where the authors study molecular dynamics during oral wound healing in normal (blue lines) and diabetic (red lines) mice.

Macrophages Experiments show that the density of macrophages in diabetic wounds is higher than in the normal case and they persist for longer in the wound site [173, 217, 280]. Model simulations match these observations (Figure 2.12).

VEGF The VEGF level during wound healing is lower in diabetic patients [3, 173]. In fact, as described below, a key target for the design of new therapies has been increasing VEGF levels. The simulation output and a biological dataset are compared in Figure 2.13.

LECs & Capillaries In diabetic patients, lymphatic capillary formation is delayed and insufficient [5, 167, 224]. The model simulations are consistent with this fact (Figure 2.14).

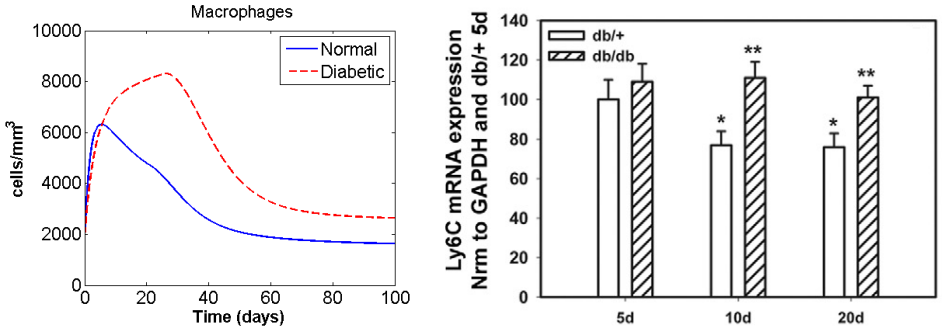

Figure 2.12: Time course of macrophage density in the normal and diabetic cases. We compare the model prediction with [173, Figure 1B]. In the experimental results, the relative height of shaded to solid white bars indicates the relative macrophage density in diabetic/non-diabetic wounds in mice (assessed via Ly6C expression, a marker for the macrophage lineage).

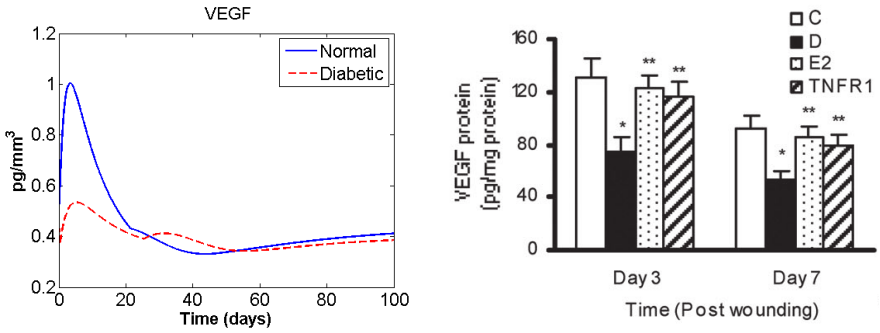

Figure 2.13: Time course of VEGF in normal and diabetic case wounds. Compare the simulation with the data reported in [3, Figure 2G], representing VEGF presence in control (white bars) and diabetic (black bars) rats. In fact, [3] investigates the connection between a defect in resolution of inflammation and the impairment of TGF-β signaling, resulting in delayed wound healing in diabetic female rats. The abbreviations in the legend stand for: C, control; D, diabetic; E2, diabetic-treated with estrogen; TNFR1, diabetic treated with the TNF receptor antagonist PEG-sTNF-RI; VEGF, vascular endothelial growth factor.

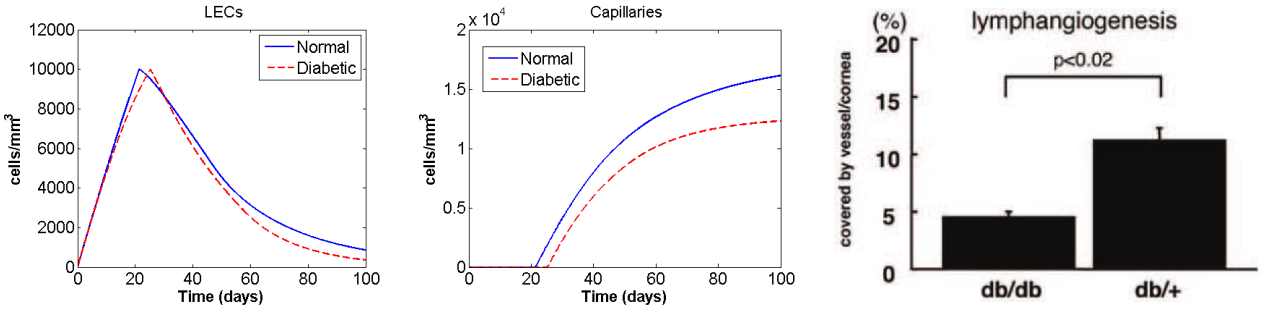

Figure 2.14: Time course of LEC and capillary density in normal and diabetic cases, compared with [167, Figure 2b]. The study presented in [167] investigates the role of wound-associated lymphatic vessels in corneal inflammation and in a skin wound model of wild-type and diabetic mice. The figure shows a quantification of lymphangiogenesis in the corneal suture model assay in the wild-type (db/+) and diabetic (db/db) cases. No suitable data were found in the skin wound model.

2.3.3 Analysis of the model

In this section the steady states of the system are identified and a sensitivity analysis of the model parameters is performed.

Steady States

For the parameter set studied, at $t = 0$ there are no LECs in the wound, but subsequently they increase towards a positive value of approximately 2×10^5 cells/mm^3. However, when they reach the "threshold" density $L^* = 10^4$ cells/mm^3, the system steady states change and L starts to decrease towards zero. In the meantime, lymphatic capillaries start forming; their final value will depend on the dynamics of the system, but in any case it will be bigger than $C^* = 10^4$ cells/mm^3. This "switch" in the steady state values is due to the presence of two piecewise defined functions (σ and f) in the system. On the other hand, there is always one stable steady state for M which also defines one for T:

$$M^{eq} \approx 1875 \text{ cells/mm}^3 \quad \text{and} \quad T^{eq} = \frac{a_M}{d_1}(T_L + r_1 M^{eq})M^{eq} \approx 30 \text{ pg/mm}^3 .$$

Note that the M-steady state (and thus also that for T) is unique for parameters with biologically relevant values. For the V-equilibrium, the following expression is found:

$$V^{eq} = \frac{s_V + r_3 M^{eq}}{d_3 + \gamma L^{eq}} .$$

Note that V^{eq} depends on L; therefore V will tend to different values according to the current L-steady state; for $L^{eq} = 0$ it is $V^{eq} = 0.5$ pg/mm^3. Details about how these steady states were determined can be found in Appendix A.2.

The stability of the steady states is determined numerically. The stability of M^{eq} is deduced from the shape of the numerically-plotted M-nullcline, and the stability of the other steady states can be inferred from the simulations of the full system. See for instance the simulation shown in Figure 2.15, where the model is run over a time interval of 250 days: here it is evident that all the variables tend to stay at a stable value after about 100 days post-wounding. Since some of the parameters were modified to simulate diabetes-related conditions, the steady states for the diabetic

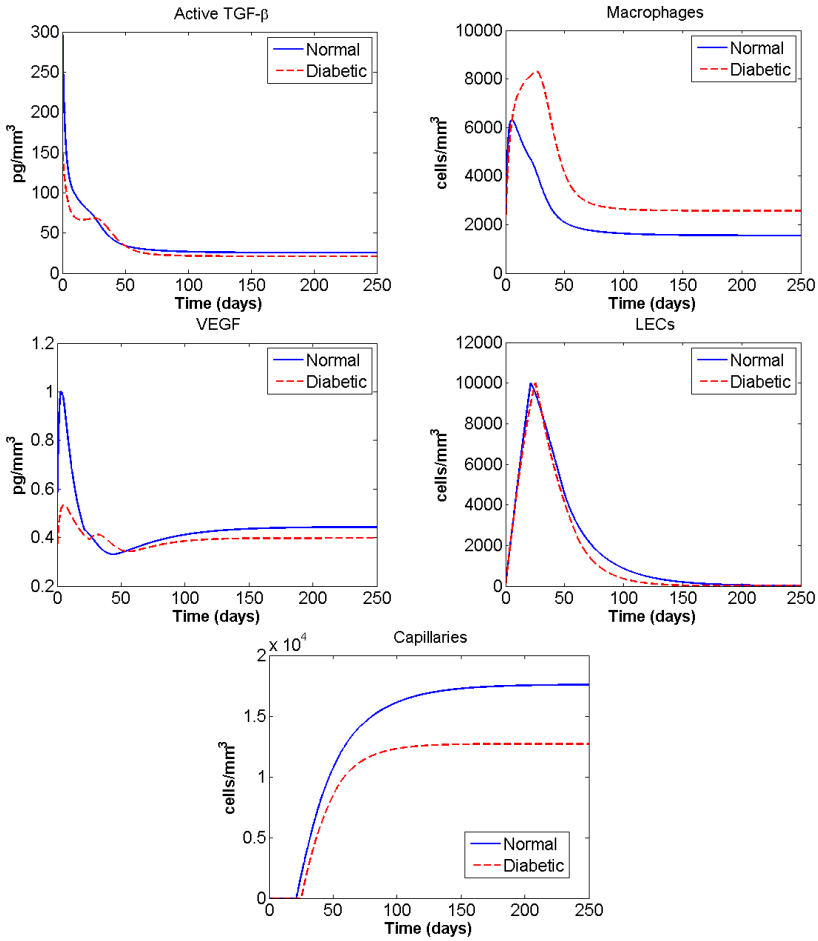

Figure 2.15: Simulation of the model in both normal (solid blue) and diabetic (dashed red) cases over a time period of 250 days.

case are different than the corresponding "normal" ones. In particular, TGF-β, VEGF and capillary equilibrium values are lower in the diabetic case, while the macrophage level is higher than in the normal case. LECs go to zero in both cases.

Although this analysis does not give very profound insights into the understanding of lymphangiogenesis, it provides some extra information about the dynamics of the system. More specifically, it shows that for realistic parameter values the system has only one steady state, which is in agreement with experimental observations.

Parameter Sensitivity Analysis

Here a numerical parameter sensitivity analysis of the model is presented which plays two important roles. On the one hand, it demonstrates which parameters are most significant in the model, and thereby provides a deeper understanding of the dynamics of the system. On the other hand, it constitutes the first step towards the design of new therapeutic approaches.

To estimate the dependence of the model on a given parameter p, a quantification of the affect of a change in p on the (final) capillary density C at day 100 is calculated. To begin, p is increased by 10% and thereafter the system is solved over the time interval $[0, 100]$. The final value of the capillary density thus obtained, denoted $C^{+10\%}$, is then compared with the reference value C^{ref} of the corresponding density in the original system. The percentage change in C is defined by

$$100 \times \frac{C^{+10\%} - C^{ref}}{C^{ref}} \quad . \tag{2.11}$$

The same procedure is then repeated, this time substituting the parameter p with its value *decreased* by 10% and the corresponding change $C^{-10\%}$ is calculated. The results are summarised in Figure 2.16.

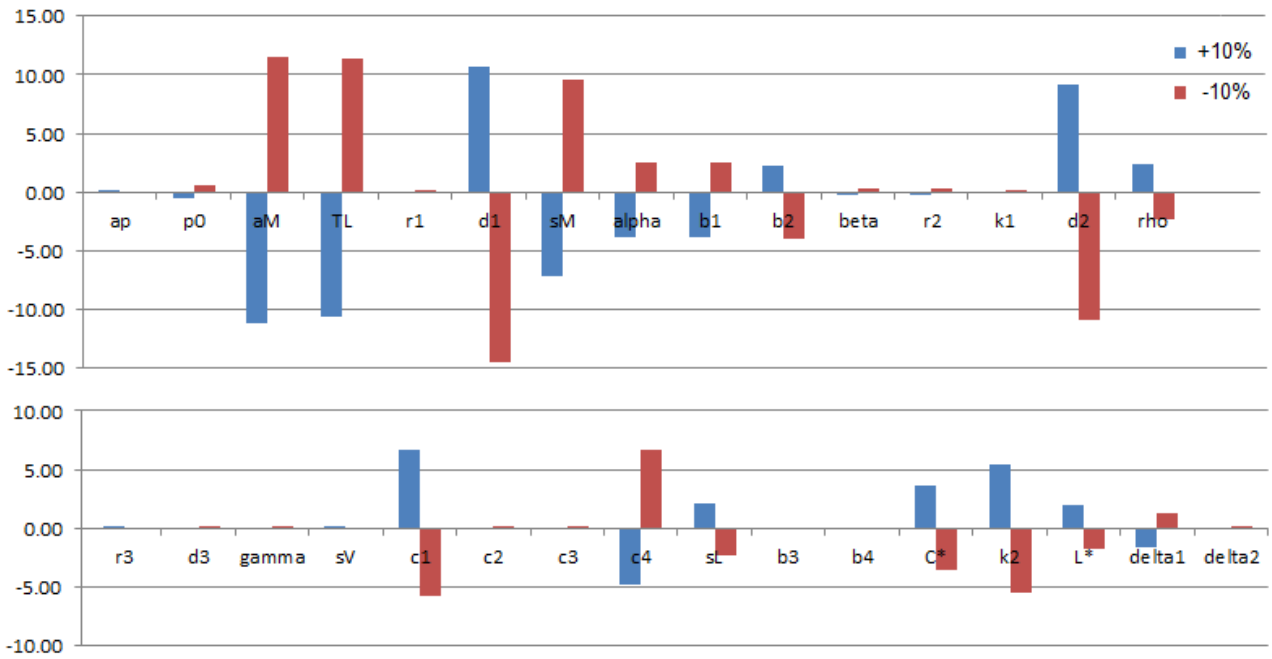

Figure 2.16: Percentage change in the final capillary density $C(100)$ when every parameter is increased/decreased by 10%.

It is notable that perturbing any parameter does not result in a percentage change in final capillary density of more than 15%. Thus, the model is quite robust in terms of dependence on the parameters. Percentage changes over 5% are observed only for eight parameters. Of these, one needs to *decrease* a_M, T_L, s_M or c_4 to observe an increase in the final capillary density; while a similar enhancement is obtained by *increasing* d_1, d_2, c_1 or k_2.

2.4 Therapies

2.4.1 Existing experimental treatments

Although there is at present no approved therapy for enhancement of lymphangiogenesis (in wound healing or in any other context), many studies and experiments have been published exploring potential treatments. In the following three such experiments are reported and then simulated.

Administration of TGF-β Receptor-Inhibitor This substance binds to the TGF-β receptors on the surface of surrounding cells, thus making them "insensitive" to TGF-β molecules and their effect. [190] reports a study of the effect of TGF-β on lymphangiogenesis in which human LECs are cultured and quantified after treatments with TGF-β1 or TβR-I inhibitor to assess cell growth, cord formation and cell migration. It is observed that TGF-β1 treatment decreases cord formation, while TβR-I inhibitor treatment increases it. These results are consistent with those found in [42], where it is reported that a higher level of TGF-β1 is associated with delayed recruitment and decreased proliferation of LECs during wound repair.

To simulate the treatment with TβR-I inhibitor, the cell migration assay is considered. Here, the inhibitor was added at 3 μM = 817 pg/mm^3 (the molecular weight is 272). Since this is significantly bigger than the concentration of TGF-β in our model and in normal skin (in both cases the maximum level is 300 pg/mm^3), this treatment is simulated by setting the parameters α and c_4 equal to zero (that is, TGF-β molecules have no effect on cells because their receptors are "occupied" by the inhibitor). The effect of this "virtual treatment" are shown in Figure 2.17, and match well with the described TGF-β inhibitor experiment: LEC and capillary densities are markedly increased by the treatment.

Macrophage-based treatments Another therapeutic approach is to add macrophages to the wound, so that they secrete VEGF and other substances that are known to induce lymphangiogenesis. In [121] an "opposite" experiment is implemented: here a systemic depletion of macrophages is reported to markedly reduce lymphangiogenesis. This is in accordance with [270], in which it is observed that

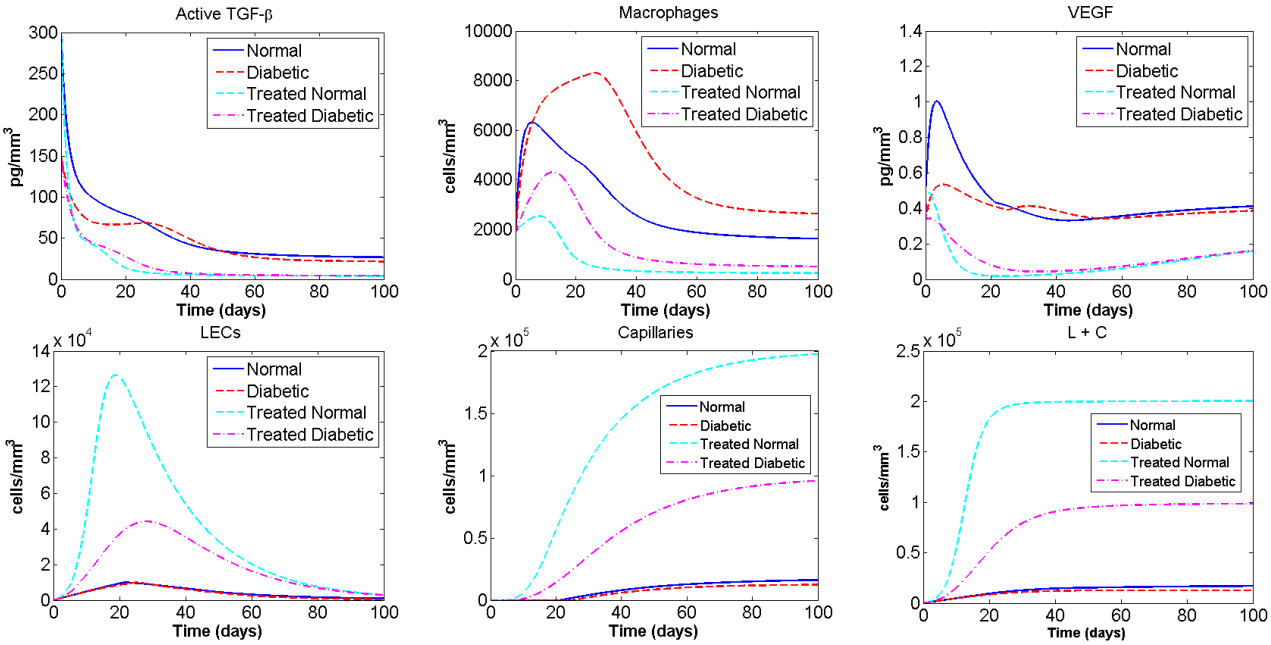

Figure 2.17: Time courses of T, M, V, L, C and $L+C$ in a simulation of the TβR-I inhibitor experiment described in [190].

the induction of macrophage apoptosis inhibits IL-1β-induced lymphangiogenesis. One hypothesis suggested to explain such results is that because of the reduced level of macrophages, less VEGF is produced and this impairs LEC proliferation and capillary formation.

We simulated the increase in macrophage apoptosis by taking a bigger (for instance, the double) value of d_2 in the system. The output of the model in which d_2 is doubled (both in normal and diabetic cases) is reported in Figure 2.18. In this case, the output is in contrast with what is described in the biological studies: although fewer macrophages and consequently less VEGF are present, more LECs and capillaries form after the simulated treatment.

This result could be explained by the fact that, in the model, a reduction in macrophage density implies a reduction in TGF-β level, so that the inhibition of LEC proliferation is smaller and hence there are more endothelial cells to form the capillaries. In fact, in the previous section it was found that the system is much more sensitive to c_4 than to c_2, c_3 or δ_2. It is then natural to consider the effect of fixing $T = 30$ pg/mm^3 in the LEC growth term (2.4); this level of T corresponds to the TGF-β equilibrium. The simulation output in this case is shown in Figure 2.19.

With T fixed, the difference between the treated and untreated cases is very

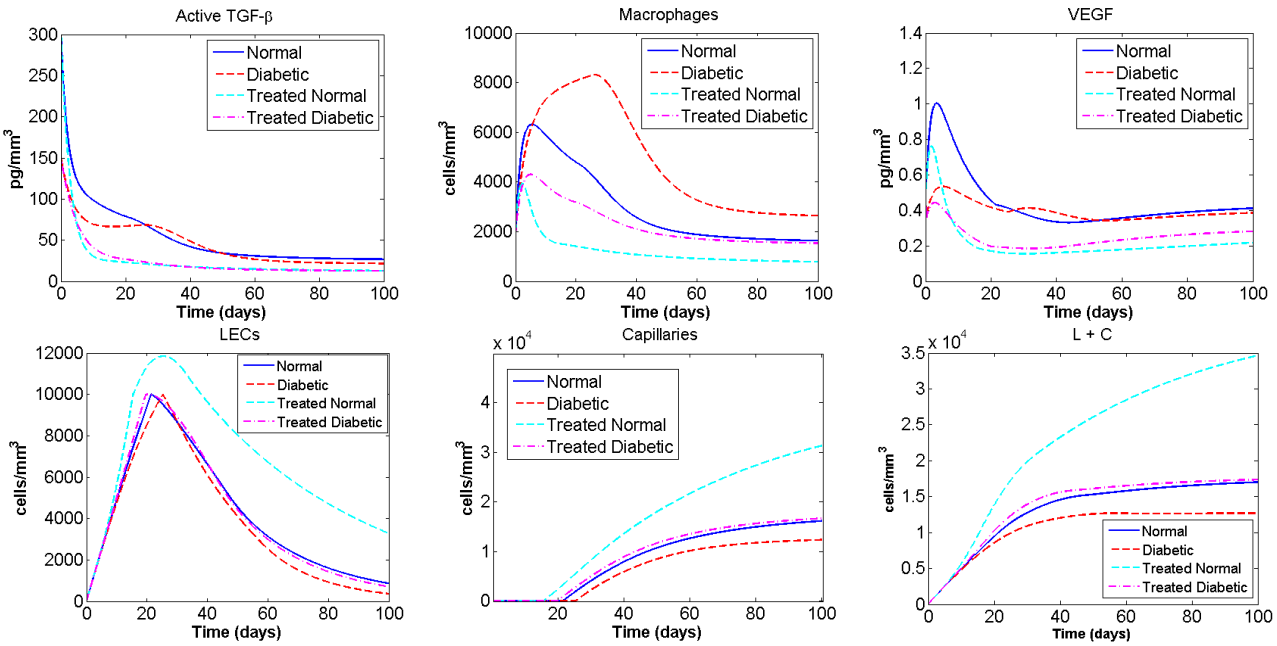

Figure 2.18: Time courses of T, M, V, L, C and $L + C$ in a simulation of the macrophage-depletion experiment described in [121].

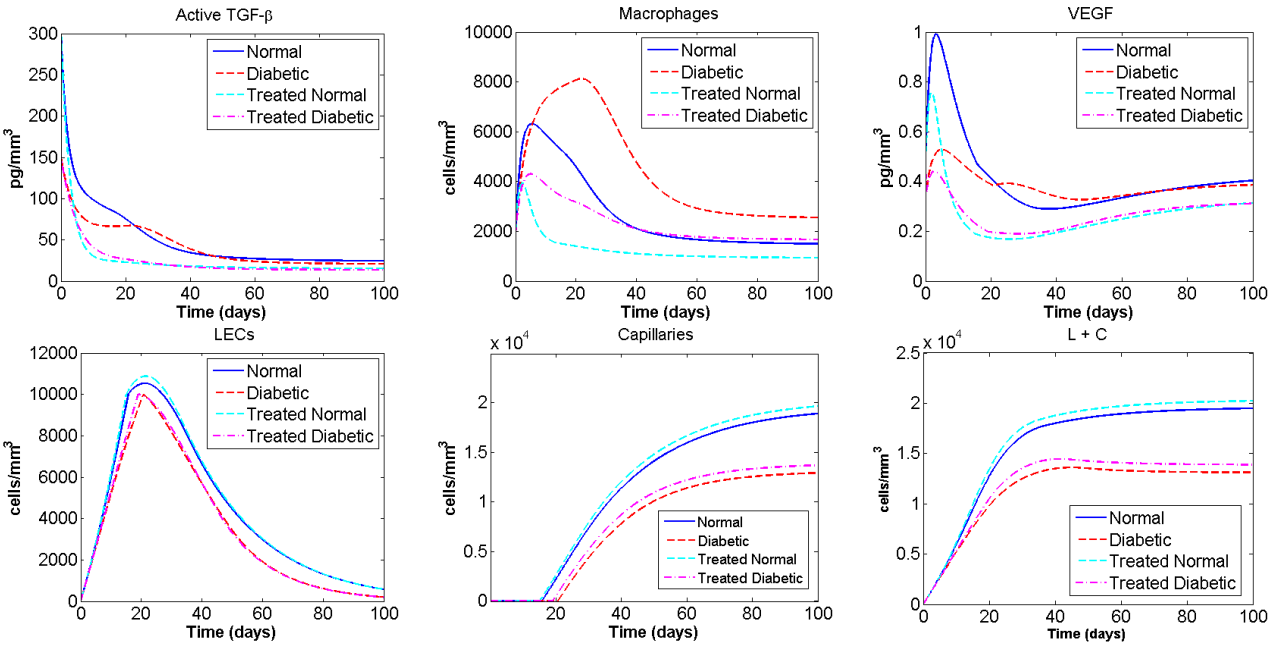

Figure 2.19: Time courses of T, M, V, L, C and $L + C$ in a simulation of the macrophage-depletion experiment described in [121], where the T in the LEC growth inhibition term is substituted by $T^{eq} = 30$ pg/mm^3.

small, but still an increase in capillary formation is observed in spite of the lower VEGF level. This may be due to the fact that, with fewer macrophages, the crowding term in the LEC equation is smaller, which facilitates the growth and accumulation of endothelial cells. In fact, if the M in the crowding term is fixed at its equilibrium value of 1,875 cells/mm^3, there is no difference at all between treated and untreated cases. Note that this result could have been foreseen from the parameter sensitivity analysis (Figure 2.16) which predicted that a 10% increase in d_2 induces a 5 to 10% *increase* in final capillary density.

VEGF supply A third documented approach to enhance lymphangiogenesis consists of supplying VEGF to the wound, since this protein promotes both LEC growth and the ability of LECs to form a network-like structure. For instance, in [287] a wound healing assessment is done in normal and diabetic mice after a VEGF-treatment. More precisely, two different types of VEGF were studied: VEGF-A_{164} and VEGF-E_{NZ7}. The authors observed that the treatment with VEGF-A_{164} increased macrophage numbers and the extent of lymphangiogenesis in both wild-type and diabetic cases, while VEGF-E_{NZ7} did not induce any significant change.

In order to reproduce the experiment *in silico*, the amount of supplied VEGF is estimated in Appendix A.1.4. Then, a 10 days constant VEGF supply of 1.8×10^2 pg/mm^3 is introduced in the model system. The output is reported in Figure 2.20. There is apparently no difference between capillary formation of treated and untreated cases. Moreover this result is relatively insensitive to the amount of VEGF supplied. What if the same treatment is applied for 30 days instead of 10? A simulation of this is shown in Figure 2.21.

There is now a clear difference in the treated cases (especially the diabetic one) showing a lower level of macrophages and an earlier onset of capillary formation, even if the final capillary density is similar to that in the untreated case.

Observation There is an important feature common to all three modelled therapies: in order to stimulate lymphatic capillary formation one cannot consider TGF-β or VEGF levels individually. A precise balance of TGF-β and VEGF is necessary for successful lymphangiogenesis. This mutual equilibrium may be reached *in vivo* by

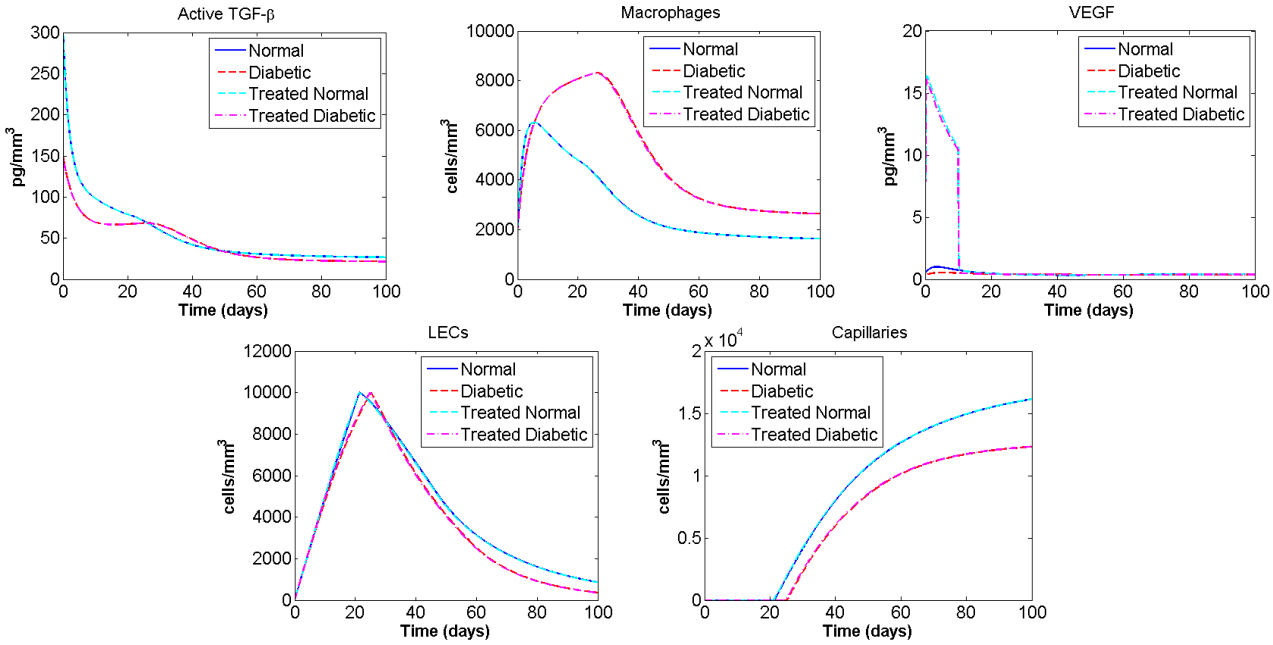

Figure 2.20: Time courses of TGF-β, macrophage, VEGF, LEC and capillary densities in a simulation of the 10-days VEGF-supply experiment described in [287]. Here the original model is altered by adding a constant VEGF supply of 1.8×10^2 pg/mm^3 for $0 \leq t \leq 10$.

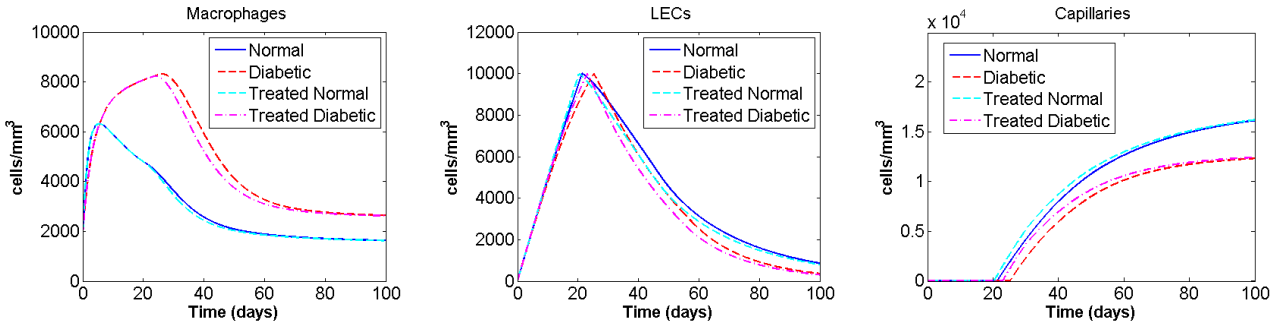

Figure 2.21: Time courses of M, L, C and $L + C$ in a simulation of the 30-days VEGF-supply experiment.

the production of either of these growth factors by other cell types not considered in the present work. In particular, this suggests the model does not take into account certain elements of the process. Nevertheless, the model does effectively describe both normal and diabetic lymphangiogenesis in wound healing which suggests that the variables considered here are the most relevant. This indicates that potential therapies should focus on these aspects of the regeneration process.

2.4.2 Novel therapeutic approaches

As mentioned above, parameter sensitivity analysis proves useful in designing novel therapeutic approaches. Among the "sensitive" parameters only a_M, d_2 and c_1 vary between the normal and diabetic cases (note that the *increasing* d_2-case was discussed above in the macrophage-based treatment). Thus, at least theoretically, a_M, d_2 and c_1 are the natural targets for a therapeutic strategy aiming to increase the final lymphatic capillary density. The feasibility of each suggested parameter change is now explored.

Decreasing a_M Decreasing a_M means lowering the macrophage-mediated activation of TGF-β. First of all, note that the increase in final capillary density due to a decrease in a_M is explained by the fact that less active TGF-β implies less TGF-β-inhibition of LEC growth and hence a larger LEC growth term. For the practical implementation of this change, it is recalled that receptor-mediated TGF-β activation consists of the binding of Latency Associated Peptide to the cell surface through receptors such as TSP-1/CD36, M6PR and multiple αV-containing integrins [250]. Hence, a decrease of a_M might be obtainable by blocking these receptors.

Increasing c_1 Increasing c_1 would be achieved by increasing the LEC growth rate. Several possible implementations of this are found in the literature. *Recombinant human IL-8* induces (human umbilical vein and dermal microvascular) endothelial cell proliferation and capillary tube organisation [142]. *DNA dependent protein kinase* (DNA-PK) is well known for its importance in repairing DNA double strand breaks; in [162] it is observed that DNA-PKcs suppression induces basal endothelial cell proliferation. In [153] it is reported that *polydopamine*-modified surfaces were beneficial to the proliferation of endothelial cells. Finally, *non-thermal dielectric barrier discharge plasma* is being developed for a wide range of medical applications, including wound healing; in particular, [119] reports that endothelial cells treated with plasma for 30 seconds demonstrated twice as much proliferation as untreated cells, five days after plasma treatment.

Other parameters To increase the final capillary density, one could also think

about targeting other parameters to which the system is sensitive. In particular:

- *Decreasing* T_L means reducing available (latent) TGF-β and hence reducing the TGF-β-inhibition over LECs. Suppression of TGF-β by antibodies has been proposed as a possible therapy to reduce scar formation [75, 81, 230]. Thus many studies of TGF-β antibodies are available.

- *Decreasing* c_4 involves reducing the (inhibitory) effect of TGF-β on LECs, which can be achieved by blocking specific TGF-β-receptors on the endothelial cell surface. Now, TGF-β signalling is very well studied [177]; in particular, it is known that TGF-β family proteins act through two type II and two type I receptors and that ALK-1 antagonises the activities of the canonical TGF-β type I receptor, TβRI/ALK-5, in the control of endothelial function [56]. Moreover, a few studies have been published which deal with blocking of TGF-β receptors in the specific case of endothelial cells [144, 259, 268].

- Changes in the other "sensitive" parameters do not appear feasible. Increasing d_1 would mean increasing the TGF-β decay rate; decreasing s_M would mean reducing the constant source of macrophages; increasing k_2 requires an increased "carrying capacity" for the wound. We are not aware of practical approaches that could cause these changes.

- Finally, among the parameters that, when changed by 10% of their value, induce a change in final capillary density between 2 and 5% (that is, a bit less than those analysed above), only b_1 merits discussion. *Reducing* b_1 corresponds to reducing macrophage chemotaxis towards TGF-β, which might be achievable by blocking specific receptors on the macrophage surface.

2.5 Conclusions

Our model procures new insights into the mechanisms behind lymphangiogenesis in wound healing. The major contributors to the process have been identified (TGF-β, macrophages, VEGF and LECs); the self-organisation hypothesis for the lymphatic

network formation described in [20, 223] has been confirmed and the importance of the *balance* between different factors has been highlighted. Moreover, the present work suggests novel therapeutic approaches to enhance the lymphangiogenic process in impaired wound healing. In addition, nearly all of the relevant parameters have been estimated from biological data and therefore this work provides fairly reliable numerical values for the parameters encountered. However, any parameter estimation is limited by, for example, the specific experimental method used or discrepancies between the system considered here and that studied in a given reference. The results should therefore be viewed with care. In particular, the numerical values pertaining to the aforementioned balance between the TGF-β and VEGF may be shifted under an alteration of the parameter set.

The ODE model presented in this chapter is intended as a first step in studying wound healing lymphangiogenesis through mathematical modelling. In the next chapter we will develop a PDE model describing the same phenomenon: the inclusion of a spatial variable will allow to take into account the important role of lymph and interstitial flow in lymphatic capillary network formation. Introducing a spatial variable also enables a fuller description of chemotaxis. The PDE model will also be able to reflect further differences between angiogenesis and lymphangiogenesis. In particular, contrary to blood angiogenesis, lymphangiogenesis is unidirectional: as opposed to sprouting from both sides of the wound, LECs appear to predominantly migrate downstream to the wound space in the direction of the interstitial flow [20].

Chapter 3

Spatio-temporal models for wound healing lymphangiogenesis

This chapter is currently in preparation for publication.

Abstract: *Several studies suggest that one possible cause of impaired wound healing is failed or insufficient lymphangiogenesis, that is the formation of new lymphatic capillaries. Although many mathematical models have been developed to describe the formation of blood capillaries (angiogenesis), very few have been proposed for the regeneration of the lymphatic network. Lymphangiogenesis is a markedly different process from angiogenesis, occurring at different times and in response to different chemical stimuli. Two main hypotheses have been proposed: 1) lymphatic capillaries sprout from existing interrupted ones at the edge of the wound in analogy to the blood angiogenesis case; 2) lymphatic endothelial cells first pool into the wound region following the lymph flow and then, once sufficiently populated, start to form a network. Here we present two PDE models describing lymphangiogenesis according to these two different hypotheses. Further, we include the effect of advection due to interstitial flow and lymph flow coming from open capillaries. The variables represent different cell densities and growth factor concentrations, and where possible the parameters are estimated from real biological*

data. The system is then solved numerically and the results are compared with the available biological literature.

3.1 Introduction

Interest in lymphatics is not just a mere scientific curiosity: their importance as pressure regulators in tissues and, moreover, as vectors of the immune response has been emphasised in recent decades, particularly in the context of wound healing [109]. The healing of a skin wound is a complex process made of different overlapping phases that, if well orchestrated by the organism, lead to the restoration of the skin and vasculature to a healthy, functional condition. Unfortunately, this delicate sequence of events can fail to proceed to full healing in diabetic or aged patients [5, 115, 245]; indeed, if the organism response to infection is insufficient, wound healing does not proceed through all normal stages, halting at the inflammation stage and resulting in a chronic wound [24, 207].

Non-healing wounds constitute a major health problem, seriously affecting the patient's quality of life and accounting for approximately 3% of all health care expenses in the UK [65, 211]. *Lymphangiogenesis*, or the regeneration of the lymphatic vasculature, is now regarded as a crucial factor for functional wound healing [39, 117]. Being the main mediators of the immune response, lymphatics seem to significantly contribute to healing [191, 277] and it has been observed that failed lymphangiogenesis correlates with impaired wound healing [5, 167, 224]. However, little is known about the actual mechanisms involved in the lymphangiogenic process, in contrast with the (blood) angiogenic case [15, 40].

Mathematical modelling potentially provides an alternative, powerful tool to back up experimental observations, generate a better understanding of wound healing lymphangiogenesis and identify potential clinical targets. Here we build upon our ODE model presented in the previous chapter to address the spatial elements of lymphangiogenesis, specifically focussing on modelling two different hypotheses proposed to describe the exact lymphangiogenesis mechanism.

3.2 Biological background

3.2.1 Wound healing

For educational purposes, wound healing is usually presented as a sequence of four different (overlapping) phases, namely:

1. *Hemostasis*: Shortly after injury, a blood clot is formed as a result of the interaction between blood and the extracellular matrix; the clot stops the bleeding and provides a scaffold for cells and chemicals that will consequently contribute to the healing process.

2. *Inflammation*: Substances activated during hemostasis attract the inflammatory cells *leukocytes* (Figure 3.1): these clean the wound from debris and pathogens and secrete chemicals which promote the evolution of the system to the next phase.

3. *Proliferation (or reepithelialisation)*: The chemicals released during inflammation enhance the growth and aggregation of the surrounding cells, restoring different tissue functions and elements such as the blood and lymphatic networks; the regeneration of blood and lymphatic vessels is named *(blood) angiogenesis* and *lymphangiogenesis*, respectively. In this phase, the blood clot is slowly substituted by a "temporary skin" called *granulation tissue*.

4. *Remodelling*: Finally, the granulation tissue is slowly replaced by normal skin tissue; this stage can take up to two years to be completed.

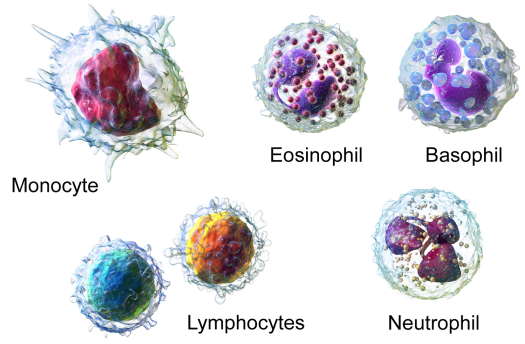

Figure 3.1: 3-D rendering of various types of leukocytes. Credit: Blausen.com staff.

For further details about wound healing we refer to [238] for normal cutaneous wound healing, and to [240] for an account of chronic wounds dynamics.

3.2.2 Sprouting versus self-organising lymphangiogenesis

The lymphatic system is a circulatory system responsible for mediating the immune response of the body and maintaining the physiological pressure in tissues by draining excess liquid. It is mainly constituted of vessels and lymph nodes. Lymphatic vessel walls are made of so-called lymphatic endothelial cells (LECs); contrary to the blood case, lymphatic capillaries are very thin and are formed from a single layer of LECs.

To date, little is known about the biological events taking place during lymphangiogenesis and different hypotheses have been proposed by biologists. Although important reviews on the subject such as [187, 247] state that lymphangiogenesis "occurs primarily by sprouting from pre-existing vessels", in a fashion which resembles the (blood) angiogenic case, recent experiments suggest that this may not be the case, at least not in some specific experimental settings [15, 223]. In [15] it is stated that lymphangiogenesis "can occur both by recruitment of isolated lymphatic islands to a connected network and by filopodial sprouting". Similarly, in [223] it is reported that in an adult mouse tail wound model LECs migrate as single cells in the wound space and later connect to each other forming vessel structures (see Figure 3.2). According to the authors of [223], single LEC migration following the lymph/interstitial flow would explain why lymphatic vessel regeneration appears to happen in this direction (from left to right in the figure).

Comparative reviews of lymphangiogenesis and (blood) angiogenesis can be found in [2, 149, 244].

3.2.3 Interstitial versus lymph flow

Interstitial flow is a fluid flow induced by dynamic stresses and pressure gradients through the extracellular matrix. It is generally slower than fluid flow inside vessels, because of the resistance of the extracellular matrix components; nonetheless, inter-

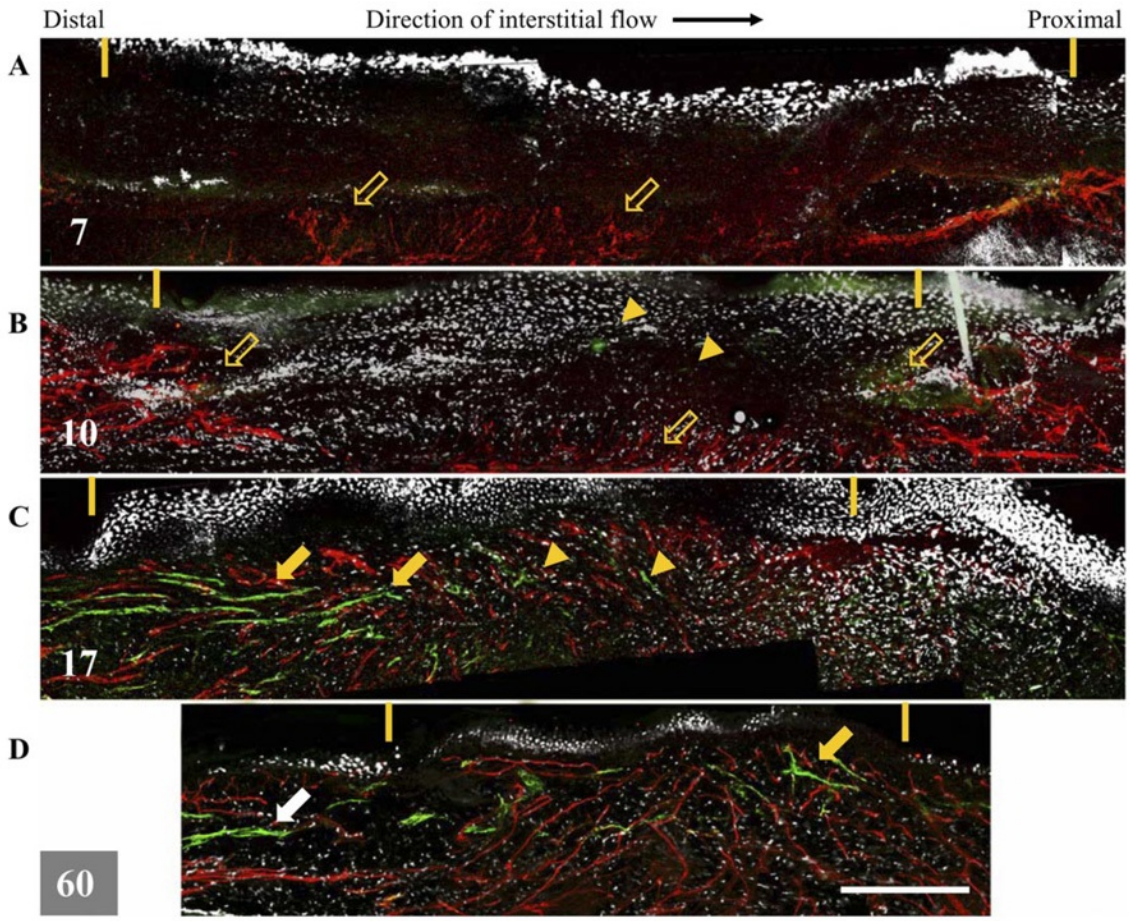

Figure 3.2: In the photo, taken from [223, Figure 2], one observes blood and lymphatic vessel regeneration; the latter appears to occur in the direction of the interstitial flow. The different photos refer to different times after wounding: A was taken at day 7, B at day 10, C at day 17 and D at day 60. The yellow dashes mark the regenerating region (note its overall contraction over time); the red colour indicates blood vessels, while LEC presence is highlighted by green colour. The open arrows signal how blood vessels seem to sprout from deeper vessels, while other arrows point out LEC organisation at day 17 after a higher LEC density is reached; arrowheads indicate single LECs migrating towards the proximal side of the wound. Scale bar in D = 300 μm.

stitial flow has recently been shown to play an important role in many processes, including cell migration. Such effects can be purely mechanical, for example by "pushing" on the cell, or can act indirectly by shifting the distribution of chemicals in the surroundings of the cell (see Figure 3.3). A nice review of the effects of interstitial flow on cell biology can be found in [222].

In recent years, a number of studies have investigated the role of interstitial flow on lymphangiogenesis, mainly through the formation of concentration gradients of pro-lymphangiogenic factors. In particular, in [20] the authors propose that interstitial flow, enhanced by the lymph flow resulting from interrupted lymphatic vessels,

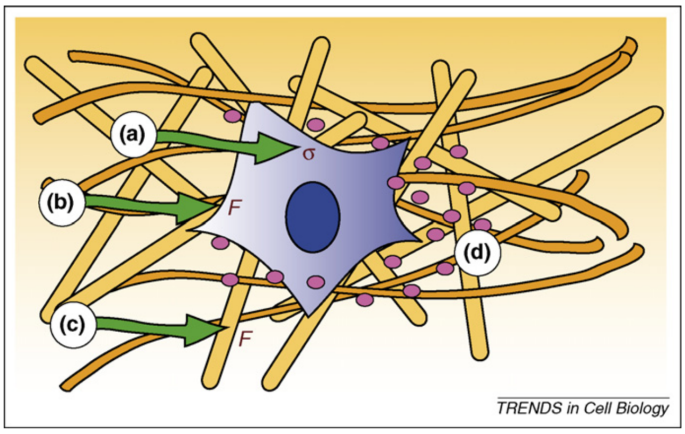

Figure 3.3: Direct effects of interstitial flow on cells, from [222, Figure 3]: (a) shear stress on cell surface; (b) forces normal to the cell surface; (c) shear and normal forces to the pericellular matrix; (d) redistribution of pericellular proteins.

can direct wound healing lymphangiogenesis by transporting LECs into the wound space and creating a gradient in chemicals (such as vascular endothelial growth factor – VEGF) which stimulate LEC growth and chemotaxis.

However, the relative role of interstitial and lymph flow on capillary regeneration has yet to be investigated in depth; therefore, it is not clear which of the two takes on the greatest importance. In fact, although interstitial flow is slower than the flux of the lymph coming from interrupted capillaries, the former persists after wound closure, while the latter is more localised to open capillaries and stops once the lymphatic network has been restored.

3.3 Mathematical Modelling

3.3.1 Review of lymphatic-related models

Contrary to the blood angiogenesis case, modelling literature about lymphangiogenesis is relatively immature and sparse, and mostly refers to tumour-induced lymphangiogenesis (see for instance [89]). To the authors' knowledge, the only models addressing lymphangiogenesis in wound healing are [218], which focuses on the mechanical elements that lend the lymphatic network its characteristic shape (at least in the mouse tail), and our previous work [17], which we are going to extend here. A good review of mathematical models of vascular network formation is [229], where

indeed the imbalance between blood angio- and lympangio-genesis modelling is manifest.

A number of models have been produced by the bioengineering community, describing specific mechanical features of lymphatic physiology; in particular, mechanics of contracting lymph valves have been presented in [93, 105, 157, 171, 213]. A brief review of engineering models proposed in the lymphatic context can be found in [164].

Very few attempts have been made to specifically model the effect of flow on capillary regeneration, although one interesting example is [86], where the authors use a convection-diffusion model to analyse the effects of flow on matrix-binding protein gradients.

3.3.2 Model targets

The model hereby presented aims to investigate the following questions about wound healing lymphangiogenesis:

- which hypothesis (self-organising or sprouting) offers a better explanation for the lymphangiogenesis mechanics?
- what are the relative contributions of interstitial and lymph flow on the lymphangiogenic process?
- how does the initial wounded state impact on lymphatic regeneration?

3.3.3 Model variables and domain

In the following, we propose two distinct PDE models to describe the two different theories advanced by biologists to describe lymphangiogenesis in wound healing (see Section 3.2.2). We will refer to them as the "self-organising" (O) hypothesis and the "sprouting" (S) hypothesis.

For both cases, we consider the following basic dynamics: immediately after healing, transforming growth factor-β (TGF-β) is activated and chemotactically attracts

macrophages, which in turn secrete VEGF which induces capillary regeneration acting on either LECs (in the self-organising case) or capillary tips (in the sprouting case). The variables included in the models are summarised in Table 3.1, where they are reported together with their names and units.

VARIABLE	MODEL	QUANTITY	UNITS
$T(t,x)$	O,S	active TGF-β concentration	$\text{pg} \cdot \text{mm}^{-3}$
$M(t,x)$	O,S	macrophage density	$\text{cells} \cdot \text{mm}^{-3}$
$V(t,x)$	O,S	VEGF concentration	$\text{pg} \cdot \text{mm}^{-3}$
$L(t,x)$	O	lymphatic endothelial cell density	$\text{cells} \cdot \text{mm}^{-3}$
$E(t,x)$	S	lymphatic capillary end (tip) density	$\text{cells} \cdot \text{mm}^{-3}$
$C(t,x)$	O,S	lymphatic capillary density	$\text{cells} \cdot \text{mm}^{-3}$

Table 3.1: A summary of the model variables.

We consider a 1D space variable x that varies between 0 and ℓ; this interval includes the wound space and a portion ε of healthy tissue on its edges, so that the wound is enclosed (at least initially) between ε and $\ell - \varepsilon$. This kind of domain describes a narrow cut, where at every point we average chemical and cell densities over the depth of the wound. We take the increasing-x direction to be the lymph flow (and interstitial flow) direction. A schematic of the model domain is shown in Figure 3.4.

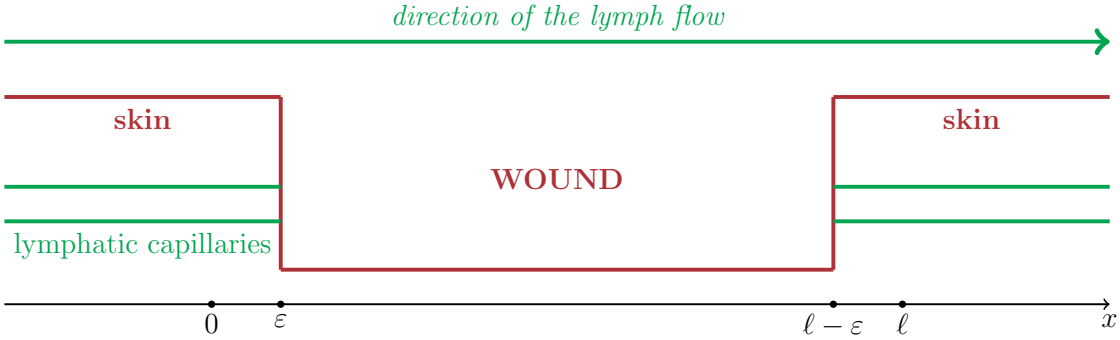

Figure 3.4: The model 1D domain.

3.3.4 Advection velocity and open capillaries

The models incorporate an advection term for the majority of variables that accounts for the effect of flow on the lymphatic regeneration process. In biological references (such as [20]) it is not clear whether flow is mainly a result of lymph fluid exiting

the interrupted capillaries, or the "normal" interstitial flow. We hence investigate the relative contribution from these two components by considering an advection term motivated as follows.

In general, interstitial flow does not have a constant direction; however, in the wound healing experimental setting of [20], both lymph and interstitial flow occur in the increasing direction of x (from left to right in Figure 3.4). We assume the interstitial flow to be constant and present across the full tissue, reflecting its persistent nature in healthy tissues. On the other hand, the contribution due to leaking lymphatic capillaries is assumed to specifically depend on the density of open capillaries C_{op} and we assume a linear dependence for simplicity. However, since we do not know the precise contribution of each element to the total advection, we introduce a single "weight" parameter ξ, $0 \leq \xi \leq 1$, which can be varied. Specifically, the advection velocities for chemicals and cells, λ^{chem} and λ^{cells} respectively, will be taken to be of the forms

$$\lambda^{chem}(C_{op}) = \xi \cdot (\lambda_1^{chem} \cdot C_{op}) + (1-\xi) \cdot \lambda_2^{chem} \quad \text{and} \tag{3.1}$$

$$\lambda^{cell}(C_{op}) = \xi \cdot (\lambda_1^{cell} \cdot C_{op}) + (1-\xi) \cdot \lambda_2^{cell} \,, \tag{3.2}$$

where $0 \leq \xi \leq 1$ and λ_1^{chem},λ_2^{chem},λ_1^{cell},λ_2^{cell} are four parameters to be determined. In Appendix B.4 we estimate the values of λ_1^{chem} and λ_2^{chem}, while corresponding parameters for cells are assumed to be significantly smaller, since advective cell velocity is likely to be smaller due to the higher environmental friction. A value of $\xi = 0$ corresponds to purely interstitial flow advection, while $\xi = 1$ represents pure lymphatic flow induced advection.

To quantify the open capillary density, we assume that as the "cut" in capillary density C becomes steeper (and thus $|^{\partial C}/_{\partial x}| \to +\infty$), more capillaries are open and the open capillary density will tend to equalise C. The open capillary density C_{op} is then defined as

$$C_{op}\left(C, \frac{\partial C}{\partial x}\right) = \frac{|^{\partial C}/_{\partial x}|}{\eta_0 + |^{\partial C}/_{\partial x}|} \cdot C \tag{3.3}$$

where η_0 is a parameter for whose estimation no relevant experimental data were

found. See Figure 3.5 for a plot of (3.3).

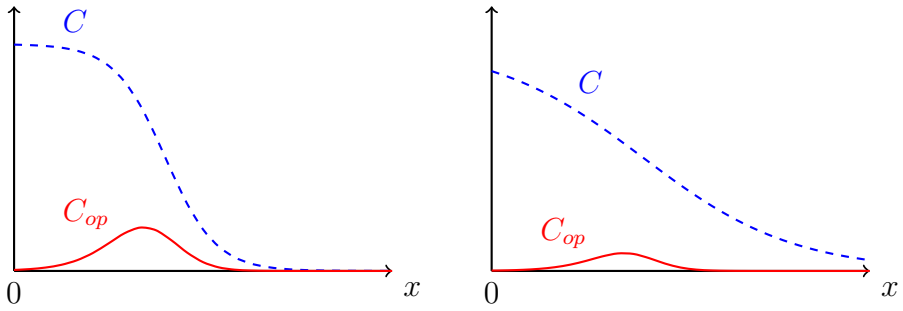

Figure 3.5: Plots of C_{op} (solid red) for different steepness of C (dashed blue).

3.3.5 Self-organising hypothesis

In this case, single LECs migrate into the wound and start to self-organise into capillary structures only after reaching a certain threshold density L^*. This case represents the direct extension of the ODE model developed in Chapter 2 and the variable and parameter names have been kept as consistent as possible.

(Active) TGF-β equation

The differential equation describing active TGF-β concentration has the following form:

$$\begin{array}{c}\text{change in}\\ \text{TGF-}\beta\\ \text{concentration}\end{array} = \begin{array}{c}\text{diffusion and}\\ \text{advection}\end{array} + \text{activation} - \text{decay} - \begin{array}{c}\text{internalisation}\\ \text{by macrophages.}\end{array}$$

Of these terms, the following three are assumed to have standard forms:

$$\text{Diffusion: } D_T\frac{\partial^2 T}{\partial x^2} \quad , \quad \text{Decay: } d_1 T \quad , \quad \text{Internalisation: } \gamma_1 T M \quad ,$$

and advection will be taken to be $-\partial/\partial x(\lambda^{chem}(C_{op})\cdot T)$, with velocity $\lambda^{chem}(C_{op})$ as defined in (3.1).

Concerning the activation, we consider a constant amount of latent TGF-β in the skin T_L [236, 250], which is increased by macrophage production at rate r_1 [124]. This latent form of TGF-β is activated by macrophages [54, 97, 188, 250] and by

the enzymes (mainly plasmin) present in the blood clot, which is mainly made of platelets [98, 110, 125] (for a review of TGF-β activation see [250]). Therefore, we take the following activation term:

$$\underbrace{[a_M M + a_p p(C)]}_{\substack{\text{activation by macro-}\\\text{-phages \& plasmin}}} \cdot \underbrace{[T_L + r_1 M]}_{\text{latent TGF-}\beta} .$$

The C-dependent quantity p is an estimate of plasmin presence in the wound, which is proportional to the platelet mass. In fact, although activation of platelet-released TGF-β is still poorly understood, it seems that plasmin, while degrading the blood clot, activates the latent TGF-β contained in the platelets [98]. We assume that plasmin level is proportional to the wound space which is not occupied by capillaries; this is motivated by the fact that capillary presence can be considered as a measure of the healing stage of the wound.[1] When capillary density gets close to its equilibrium (healthy state) value C^{eq} (say 90% of it), the plasmin-induced TGF-β activation switches to zero. We will thus take

$$p(C) = \begin{cases} -\frac{\psi}{C^{eq}} C + \psi & \text{if } C \leq 9/10 \cdot C^{eq} \\ 0 & \text{if } C \geq 9/10 \cdot C^{eq} . \end{cases} \tag{3.4}$$

A plot of $p(C)$ is shown in Figure 3.6.

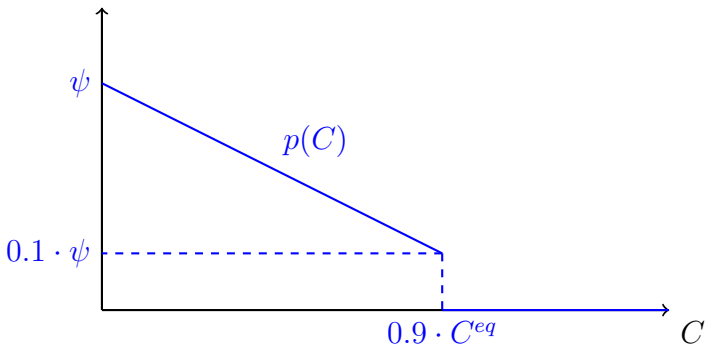

Figure 3.6: Plot of $p(C)$.

[1] However, it would maybe be more appropriate to consider fibroblasts instead of capillaries here, but the introduction of a new variable and consequently a new equation does not seem to be worthwhile, since capillary presence is a good indication of the healing state of the wound.

Macrophage equation

The following scheme will be considered for macrophage dynamics:

$$\begin{array}{ccccccc} \text{change in} & & \text{random movement} & & \text{chemotaxis by} & & \\ \text{macrophage} & = & \text{and advection} & + & \text{TGF-}\beta & + & \text{constant source} \\ \text{density} & & & & & & \\ & + & \text{influx from open} & - & \text{removal and} & - & \text{crowding effect.} \\ & & \text{capillaries} & & \text{differentiation} & & \end{array}$$

Macrophages are assumed to move randomly with diffusion coefficient μ_M, while their advection will be modelled by the term $-\frac{\partial}{\partial x}\left(\lambda^{cell}(C_{op})\cdot M\right)$, with $\lambda^{cell}(C_{op})$ as discussed above in Section 3.3.4.

For the chemotaxis term, we first point out that only a fraction α of the monocytes that are chemoattracted by TGF-β differentiate into (inflammatory) macrophages [163, 265]. Therefore, the term describing macrophage chemotaxis up to TGF-β gradients will have the form

$$-\alpha\chi_1\frac{\partial}{\partial x}\left(\frac{M}{1+\omega M}\cdot\frac{{}^{\partial T}/_{\partial x}}{1+\eta_1\left|{}^{\partial T}/_{\partial x}\right|}\right)$$

where the macrophage velocity $\frac{1}{1+\omega M}\cdot\frac{{}^{\partial T}/_{\partial x}}{1+\eta_1|{}^{\partial T}/_{\partial x}|}$ decreases as cell density increases (as in [260, 261]) and is bounded as $|{}^{\partial T}/_{\partial x}|\to\infty$.

The presence of a constant source s_M (from the bottom of the wound) is justified by the observation that macrophage equilibrium in the skin is nonzero [272].

The introduction of an influx term is motivated by the fact that macrophages are "pumped out" from interrupted capillaries [20, 223] and into the wound. We consider the following form for the influx term:

$$\varphi_1\left(C_{op},\frac{\partial C}{\partial x}\right)=C_{op}\cdot\zeta_1\left(\frac{\partial C}{\partial x}\right)\ , \tag{3.5}$$

where C_{op} was introduced in (3.3) and ζ_1 is defined as

$$\zeta_1\left(\frac{\partial C}{\partial x}\right) = \begin{cases} \phi_1 & \text{if } {}^{\partial C}/_{\partial x} < 0 \\ 0 & \text{otherwise} \quad . \end{cases} \tag{3.6}$$

In (3.6) ϕ_1 is a parameter estimated in Appendix B.7. The presence of the Heaviside function ζ_1 is due to the influx only occurring from the open lymphatic capillaries on the side of the wound from which lymph fluid flows (see Figure 3.4).

The removal term includes (inflammatory) macrophage death, differentiation into repair macrophages and reintroduction into the vascular system, the latter being proportional to the capillary density. Thus, we take the removal term to be $(d_2 + \rho C)M$.

We also include a crowding effect through the term $-\frac{M+L+C}{k_1} \cdot M$.

VEGF equation

For VEGF we assume the following dynamics:

$$\begin{aligned} \text{change in VEGF concentration} &= \text{diffusion and advection} + \text{constant source} + \text{production by macrophages} \\ &\quad - \text{decay} - \text{internalisation by LECs.} \end{aligned}$$

VEGF diffusion is modelled via the standard term $D_V \frac{\partial^2 V}{\partial x^2}$ and advection by $-\frac{\partial}{\partial x}\left(\lambda^{chem}(C_{op}) \cdot V\right)$ where $\lambda^{chem}(C_{op})$ is the expression defined in (3.1). The constant source is called s_V, while the production term will be $r_3 M$ and the decay $d_3 V$. Internalisation is assumed to be linearly dependent on LEC density and the corresponding term will consequently be $\gamma_2 VL$.

LEC equation

The equation describing the presence of LECs in the wound consists of the following terms:

change in LEC density	=	random movement and advection	+	chemotaxis by VEGF	+	growth, upregulated by VEGF and downregulated by TGF-β
	+	influx from open capillaries	−	crowding effect	−	transdifferentiation into capillaries.

Again, random cell movement is modelled via a diffusion term $\mu_L {}^{\partial^2 L}/_{\partial x^2}$ and the advection is taken to be $-\frac{\partial}{\partial x}\left(\lambda^{cell}(C)\cdot L\right)$.

LECs are chemoattracted by VEGF [16, 247], and their chemotaxis term is assumed to be of a similar form to the one used to describe the macrophage counterpart:

$$-\chi_2 \frac{\partial}{\partial x}\left(\frac{L}{1+\omega L}\cdot\frac{{}^{\partial V}/_{\partial x}}{1+\eta_2\left|{}^{\partial V}/_{\partial x}\right|}\right) .$$

LEC growth is upregulated by VEGF [16, 275, 284] and downregulated by TGF-β [178, 242]:

$$\left(c_1+\frac{V}{c_2+c_3V}\right)\left(\frac{1}{1+c_4T}\right)L .$$

LECs are "pumped out" from the interrupted capillaries in a similar manner to macrophages, but also result (with less intensity) from interrupted capillaries downstream of the lymph flow. The influx term this time takes the form:

$$\varphi_2\left(C_{op},\frac{\partial C}{\partial x}\right)=C_{op}\cdot\zeta_2\left(\frac{\partial C}{\partial x}\right) \tag{3.7}$$

where C_{op} is the same as in (3.3) and ζ_2 is defined as

$$\zeta_2\left(\frac{\partial C}{\partial x}\right)=\begin{cases}\phi_2^+ & \text{if } {}^{\partial C}/_{\partial x}<0\\ \phi_2^- & \text{if } {}^{\partial C}/_{\partial x}>0\ ,\end{cases} \tag{3.8}$$

where $\phi_2^+ > \phi_2^-$.

LECs cannot grow excessively due to crowding, taken into account via the term $-\frac{(M+L+C)}{k_2}\cdot L$.

When LECs have *locally* sufficiently populated the wound (i.e. when their density

exceeds a threshold L^* [20, 223]) they are assumed to self-organise into capillaries at a rate which is increased by the presence of VEGF [209]:

$$\sigma(L, C) \cdot (\delta_1 + \delta_2 V)L$$

where

$$\sigma(L, C) = \begin{cases} 1 & \text{if } L + C \geq L^* \\ 0 & \text{if } L + C < L^* \, . \end{cases} \tag{3.9}$$

Lymphatic capillary equation

After LECs have occupied enough of the wound space, they "stick" together and form a capillary network; also, they undergo remodelling, which we model via a logistic term. Thus, the C-equation will be

$$\frac{\partial C}{\partial t} = \underbrace{\sigma(L, C) \cdot (\delta_1 + \delta_2 V)L}_{\text{source}} + \underbrace{c_5 \left(1 - \frac{C}{k_3}\right) C}_{\text{remodelling}} \, .$$

Full system – "self-organising" hypothesis

The full system of equations in the "self-organising" hypothesis is therefore given by

$$\begin{aligned}
\frac{\partial T}{\partial t} &= D_T \frac{\partial^2 T}{\partial x^2} - \frac{\partial}{\partial x}\left(\lambda^{chem}(C_{op}) \cdot T\right) + \left[a_M M + a_p p(C)\right] \cdot \left[T_L + r_1 M\right] \\
&\quad - d_1 T - \gamma_1 T M \qquad (3.10) \\
\frac{\partial M}{\partial t} &= \mu_M \frac{\partial^2 M}{\partial x^2} - \frac{\partial}{\partial x}\left(\lambda^{cell}(C_{op}) \cdot M + \alpha \chi_1 \frac{M}{1+\omega M} \cdot \frac{{}^{\partial T}/_{\partial x}}{1+\eta_1 \left|{}^{\partial T}/_{\partial x}\right|}\right) \\
&\quad + s_M + \varphi_1\left(C_{op}, \frac{\partial C}{\partial x}\right) - (d_2 + \rho C) M - \frac{M+L+C}{k_1} M \qquad (3.11) \\
\frac{\partial V}{\partial t} &= D_V \frac{\partial^2 V}{\partial x^2} - \frac{\partial}{\partial x}\left(\lambda^{chem}(C_{op}) \cdot V\right) + s_V + r_3 M - d_3 V - \gamma_2 V L \qquad (3.12) \\
\frac{\partial L}{\partial t} &= \mu_L \frac{\partial^2 L}{\partial x^2} - \frac{\partial}{\partial x}\left(\lambda^{cell}(C_{op}) \cdot L + \chi_2 \frac{L}{1+\omega L} \cdot \frac{{}^{\partial V}/_{\partial x}}{1+\eta_2 \left|{}^{\partial V}/_{\partial x}\right|}\right) \\
&\quad + \left(c_1 + \frac{V}{c_2 + c_3 V}\right)\left(\frac{1}{1+c_4 T}\right) L + \varphi_2\left(C_{op}, \frac{\partial C}{\partial x}\right) \\
&\quad - \frac{M+L+C}{k_2} L - \sigma(L,C) \cdot (\delta_1 + \delta_2 V) L \qquad (3.13) \\
\frac{\partial C}{\partial t} &= \sigma(L,C) \cdot (\delta_1 + \delta_2 V) L + c_5 \left(1 - \frac{C}{k_3}\right) C \qquad (3.14)
\end{aligned}$$

where λ^{chem} is defined in (3.1), λ^{cell} in (3.2), p in (3.4), φ_1 in (3.5), φ_2 in (3.7) and σ in (3.9). Parameters, initial and boundary conditions are discussed in Section 3.3.7. See Figure 3.7 for a summary of the fluxes included in the model.

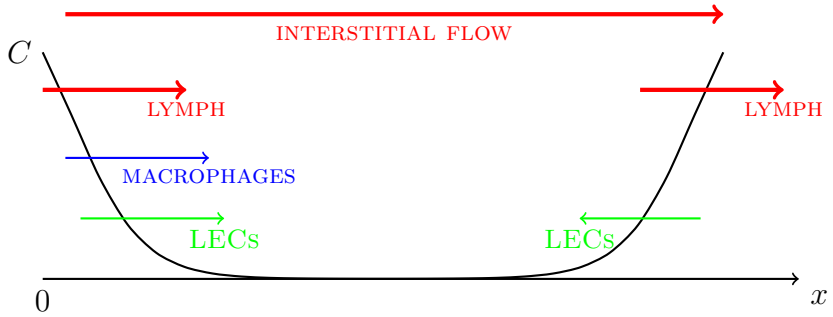

Figure 3.7: A summary of the fluxes included in the model: capillaries; **fluid fluxes**; **macrophage influx**; **LEC influx** (only in O).

3.3.6 Sprouting hypothesis

Here, instead of LECs we consider capillary tip density E. Capillary tips are attached to the vessel ends and therefore, contrary to LECs, are not subject to advection. As we will see, the introduction of this variable is necessary in order to model directed capillary growth in response to a gradient.

TGF-β, macrophage and VEGF equations are the same as in the self-organising case, except for the fact that in the crowding term for M there is E instead of L and that in the V internalisation term there is E instead of L.

Lymphatic capillary ends (tips) equation

Capillary ends (or tips) are assumed to sprout from interrupted lymphatic capillaries, the density of which (C_{op}) was defined in (3.3). Tip growth is enhanced by VEGF and inhibited by TGF-β and this is reflected by the following term, similar to the one used for LECs in the self-organising case:

$$\left(c_1 + \frac{V}{c_2 + c_3 V}\right)\left(\frac{1}{1 + c_4 T}\right) C_{op} \, .$$

Importantly, capillary ends move in the direction of the (positive) gradient of VEGF with an upper-bounded velocity, modelled by the term

$$-\chi_2 \frac{\partial}{\partial x}\left(E \cdot \frac{\partial V/\partial x}{1 + \eta_2 \left|\partial V/\partial x\right|}\right) \, .$$

Finally, we assume that capillary tip death is due predominantly to overcrowding, and thus we include the removal term $-\frac{(M+E+C)}{k_2} \cdot E$.

Lymphatic capillary equation

New capillaries are formed continuously from the interrupted ones in the direction defined by their tips. This is modelled here according to the "snail trail" concept introduced in [67] for fungal colonies: newly formed capillaries are laid after the sprouting tips, which therefore leave a sort of "track" behind.

Capillaries also undergo remodelling. Therefore, their dynamics are captured by the terms:

$$\underbrace{\chi_2 \left| E \cdot \frac{\partial V/\partial x}{1 + \eta_2 \left|\partial V/\partial x\right|} \right|}_{\text{sprouting}} + \underbrace{c_5 \left(1 - \frac{C}{k_3}\right) C}_{\text{remodelling}} \, .$$

Full system – "sprouting" hypothesis

Thus, the full system for the "sprouting" hypothesis is

$$\begin{aligned}
\frac{\partial T}{\partial t} &= D_T \frac{\partial^2 T}{\partial x^2} - \frac{\partial}{\partial x}\left(\lambda^{chem}(C_{op}) \cdot T\right) + [a_M M + a_p p(C)] \cdot [T_L + r_1 M] \\
&\quad -d_1 T - \gamma_1 T M \qquad (3.15)\\
\frac{\partial M}{\partial t} &= \mu_M \frac{\partial^2 M}{\partial x^2} - \frac{\partial}{\partial x}\left(\lambda^{cell}(C_{op}) \cdot M + \alpha\chi_1 \frac{M}{1+\omega M} \cdot \frac{\partial T/\partial x}{1+\eta_1 \left|\partial T/\partial x\right|}\right) \\
&\quad +s_M + \varphi_1\left(C_{op}, \frac{\partial C}{\partial x}\right) - (d_2 + \rho C)M - \frac{M+E+C}{k_1} M \qquad (3.16)\\
\frac{\partial V}{\partial t} &= D_V \frac{\partial^2 V}{\partial x^2} - \frac{\partial}{\partial x}\left(\lambda^{chem}(C_{op}) \cdot V\right) + s_V + r_3 M - d_3 V - \gamma_2 V E \qquad (3.17)\\
\frac{\partial E}{\partial t} &= \left(c_1 + \frac{V}{c_2 + c_3 V}\right)\left(\frac{1}{1+c_4 T}\right) C_{op} - \chi_2 \frac{\partial}{\partial x}\left(E \cdot \frac{\partial V/\partial x}{1+\eta_2 \left|\partial V/\partial x\right|}\right) \\
&\quad -\frac{M+E+C}{k_2} E \qquad (3.18)\\
\frac{\partial C}{\partial t} &= \chi_2 \left| E \cdot \frac{\partial V/\partial x}{1+\eta_2 \left|\partial V/\partial x\right|} \right| + c_5 \left(1 - \frac{C}{k_3}\right) C \qquad (3.19)
\end{aligned}$$

where λ^{chem} is defined in (3.1), λ^{cell} in (3.2), p in (3.4), φ_1 in (3.5) and C_{op} in (3.3). See Figure 3.7 for a summary of the fluxes of the model.

3.3.7 Parameters and initial and boundary conditions

Parameters

Most of the parameters were already considered in Chapter 2; these are reported here in Table 3.2 and we refer to Appendix A.1 for the details of their estimation.

The other parameters are listed in Table 3.3 and the details of their estimation can be found in Appendix B.

Initial Conditions

As initial time $t = 0$ we take the moment of wounding, at which time little chemical or cell populations are assumed to have entered in the wound space.

We assume that at the beginning there are no LECs (for model O) or capillary tips (for S), while other variables can be present near the edges (recall our domain

PARAMETER	VALUE	UNITS	SOURCE
a_p	2.9×10^{-2}	$\text{mm}^3\text{pg}^{-1}\text{day}^{-1}$	[54]
a_M	0.45	$\text{mm}^3\text{cells}^{-1}\text{day}^{-1}$	[97, 188]
T_L	18	pg mm^{-3}	([189])
r_1	3×10^{-5}	$\text{pg cells}^{-1}\text{day}^{-1}$	[124]
d_1	5×10^2	day^{-1}	[120]
α	0.5	1	[271]
β	5×10^{-3}	1	[100]
r_2	1.22	day^{-1}	[289]
d_2	0.2	day^{-1}	[44]
ρ	10^{-5}	$\text{day}^{-1}\text{cells}^{-1}$	[223]
s_V	1.94	cells day^{-1}	([107, 196])
r_3	1.9×10^{-3}	$\text{pg cells}^{-1}\text{day}^{-1}$	([130, 233])
d_3	11	day^{-1}	[131]
γ_2	1.4×10^{-3}	$\text{mm}^3\text{cells}^{-1}\text{day}^{-1}$	[155]
c_1	0.42	day^{-1}	[183]
c_2	42	day	[275]
c_3	4.1	pg day mm^{-3}	[275]
c_4	0.24	$\text{mm}^3\text{pg}^{-1}$	[178]
k_2	4.71×10^5	cells day mm^{-3}	[183]
L^*	10^4	cells mm^{-3}	[223]
δ_1	5×10^{-2}	day^{-1}	no data found
δ_2	10^{-3}	$\text{mm}^3\text{pg}^{-1}\text{day}^{-1}$	no data found

Table 3.2: A list of parameters appearing in the model equations with values precisely the same as in Chapter 2 – see Appendix A.1. Each one is supplied with its estimated value, units and source used (when possible) to assess it. References in brackets mean that although the parameter was not *directly* estimated from a dataset, its calculated value was compared with the biological literature; the caption "no data found" signifies that no suitable data were found to estimate the parameter. Note that γ_2 here corresponds to γ in Chapter 2.

includes portions of healthy skin surrounding the wound). We will then take the following initial conditions:

$$\nu(0,x) = a_\nu \cdot \left[1 - \frac{\tanh(b(x-\varepsilon)) + \tanh(b(-x+\ell-\varepsilon))}{2}\right], \tag{3.20}$$

$$L(0,x) = E(0,x) = 0\,, \tag{3.21}$$

where $\nu \in \{T, M, V, C\}$. For each variable ν the value of a_ν is chosen to be such that $\nu(0,0) = \nu(0,\ell)$ is equal to the boundary conditions discussed in the following. Concerning b, we will vary its value to see how the "sharpness" of the initial condition will affect lymphangiogenesis. For higher values of b, the initial conditions become more step-like and we can interpret this as a deep wound with sharp edges: in this case, there would be (almost) no capillaries in the centre of the wound. On the other

PARAMETER	VALUE	UNITS	SOURCE
η_0	10^4		no data found
D_T	2.76	$\text{mm}^2\text{day}^{-1}$	[140, 179]
ψ	10^5	pg mm^{-3}	no data found
γ_1	4.2×10^{-3}	$\text{mm}^3\text{cells}^{-1}\text{day}^{-1}$	([283])
λ_1^{chem}	1.35×10^{-2}	mmday^{-1}	[82, 83]
λ_2^{chem}	8.64×10^2	mmday^{-1}	[222]
λ_1^{cell}	1.35×10^{-3}	mmday^{-1}	estimated $\approx 0.1 \times \lambda_1^{chem}$
λ_2^{cell}	86.4	mmday^{-1}	estimated $\approx 0.1 \times \lambda_2^{chem}$
ξ	$0 \leq \xi \leq 1$	1	*variable*
μ_M	0.12	$\text{mm}^2\text{day}^{-1}$	[78]
s_M	8.6×10^2	$\text{cells mm}^{-3}\text{day}^{-1}$	([272])
χ_1	4×10^{-2}	$\text{mm}^5\text{pg}^{-1}\text{day}^{-1}$	[143]
ω	1.67×10^{-6}	$\text{mm}^3\text{cells}^{-1}$	estimated $\approx 1/k_1^{old}$
η_1	100	$\text{mm}^9\text{pg}^{-1}$	no data found
ϕ_1	2.05×10^3	day^{-1}	[29, 82]
k_1	10^5	$\text{mm}^3\text{cells}^{-1}$	[289]
D_V	2.4	$\text{mm}^2\text{day}^{-1}$	[174]
μ_L	0.1	$\text{mm}^2\text{day}^{-1}$	estimated $\approx \mu_M$
χ_2	0.173	$\text{mm}^5\text{pg}^{-1}\text{day}^{-1}$	[10]
η_2	1	$\text{mm}^9\text{pg}^{-1}$	no data found
ϕ_2^+	10^2	day^{-1}	no data found
ϕ_2^-	1	day^{-1}	estimated to be 1% of ϕ_2^+
d_4	0.1	day^{-1}	estimated $\approx d_2$
c_5	0.42	day^{-1}	estimated $= c_1$
k_3	1.2×10^4	$\text{mm}^3\text{cells}^{-1}$	estimated $\approx C^{eq}$

Table 3.3: The remaining parameters. See Appendix B for details on the estimation of each of these parameters. k_1^{old} denotes the parameter k_1 in Chapter 2, where it is the macrophage carrying capacity. d_4 appears in the boundary conditions for L. The parameter ξ will be taken o assume different values between 0 and 1 in order to investigate the relative importance of lymph and interstitial flow.

hand, assigning smaller values of b would correspond to a shallower initial wound, such that when averaging over the wound depth a certain number of capillaries still remain.

As an example, the plot of (3.20) for $\nu = T$ is shown in Figure 3.8 for different values of b.

Boundary Conditions

We consider Dirichlet boundary conditions for all variables except L, for which we assume Robin boundary conditions. The choice of Dirichlet boundary conditions is dictated by the fact that at the boundary the tissue is in a non-wounded state, and we expect variables to remain close to their normal, equilibrium value there. For L,

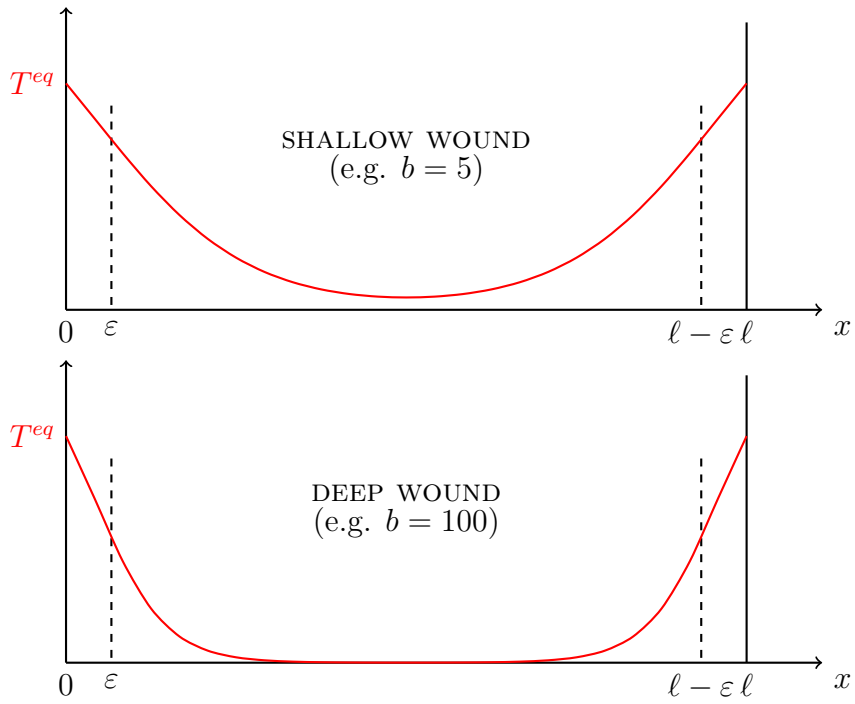

Figure 3.8: Initial condition $T(0,x) = a_T \cdot \{1 - [\tanh(b(x-\varepsilon)) + \tanh(b(-x+\ell-\varepsilon))]/2\}$ for different values of b. T^{eq} denotes the T-equilibrium level in non-wounded skin.

instead, we apply the following reasoning.

For LECs, we assume that once they pass the domain edge they will move randomly and will die at a constant rate d_4; in fact, it seems unrealistic to assume that they will just vanish once reaching the domain edge. Therefore we will follow what is suggested in [152] for the spruce budworm: we set a different evolution equation for L inside and outside the domain. In the interior (i.e. for $0 < x < \ell$), the dynamics of L will be described by the equation (3.13); in the exterior (i.e. for $x < 0$ and $x > \ell$) instead we assume that LECs move randomly and die (or transdifferentiate) with (high) constant rate d_4, thus following the equation

$$\frac{\partial L}{\partial t} = \mu_L \frac{\partial^2 L}{\partial x^2} - d_4 L \,, \tag{3.22}$$

whose solution at equilibrium is given by

$$L_o(x) = A_o \exp\left(\sqrt{\frac{d_4}{\mu_L}}x\right) + B_o \exp\left(-\sqrt{\frac{d_4}{\mu_L}}x\right) \tag{3.23}$$

where A_o and B_o are constants. Note that, since we want solutions to be bounded in order to be biologically meaningful, we will take $B_o = 0$ for $x < 0$ and $A_o = 0$ for

$x > \ell$. Since at the boundaries the outer and the inner solutions should have the same value and the same flux, we have that

$$\text{at } x = 0: \quad L = A_o \text{ and } \frac{\partial L}{\partial x} = A_o\sqrt{\frac{d_4}{\mu_L}} \quad \Rightarrow \frac{\partial L}{\partial x}(t,0) = \sqrt{\frac{d_4}{\mu_L}}L(t,0)$$

$$\text{at } x = \ell: \quad L = B_o \exp\left(-\sqrt{\frac{d_4}{\mu_L}}\ell\right) \text{ and } \frac{\partial L}{\partial x} = -B_o\sqrt{\frac{d_4}{\mu_L}}\exp\left(-\sqrt{\frac{d_4}{\mu_L}}\ell\right)$$

$$\Rightarrow \frac{\partial L}{\partial x}(t,\ell) = -\sqrt{\frac{d_4}{\mu_L}}L(t,\ell)$$

which give the boundary conditions for L.

Summarising, the boundary conditions are

$$\nu(t,0) = \nu(t,\ell) = \nu^{eq} \quad , \quad E(t,0) = E(t,\ell) = 0\,, \tag{3.24}$$

$$\frac{\partial L}{\partial x} - \sqrt{\frac{d_4}{\mu_L}}L = 0 \quad \text{at } x = 0 \quad , \quad \frac{\partial L}{\partial x} + \sqrt{\frac{d_4}{\mu_L}}L = 0 \quad \text{at } x = \ell \tag{3.25}$$

with $\nu \in \{T, M, V, C\}$ and where ν^{eq} denotes the equilibrium value in the unwounded skin for each variable.

3.4 Numerical solutions

To simulate the two systems (3.10)-(3.14) and (3.15)-(3.19), a specific code was written in MatLab which applies the Crank-Nicolson method for the diffusion terms and a first-order upwind scheme for the chemotactic terms.

As a datum for comparison of the time-scale of the process, we take the observation that in the experimental setting lymphatic vasculature is complete at day 60 post-wounding [20, 223].

In the figures that follow, numerical solutions are plotted at different times. In particular, **dotted green** refers to $t = 5$ days, **solid blue** to $t = 15$ days, **dashed red** to $t = 30$ days, **solid green** to $t = 60$ days, **dashed blue** to $t = 80$ days and **dotted red** to $t = 100$ days. Where appropriate, a waterfall plot of the solutions is also supplied.

3.4.1 Self-organising hypothesis

We start by taking $\xi = 0.5$ (representing that both interstitial and lymph flow contribute equally to overall advection) and a very smooth initial condition, with $b = 5$ – see (3.20). In this case, actual lymphatic regeneration appears to be almost symmetric and a nearly-complete network is restored by around day 60 (see Figure 3.9). Biologically, this represents the situation in which a less deep wound leaves more capillaries in the domain after wounding, so that regeneration occurs mainly from remodelling of the pre-existing network. We note, however, that the distribution of chemicals is highly asymmetric in form.

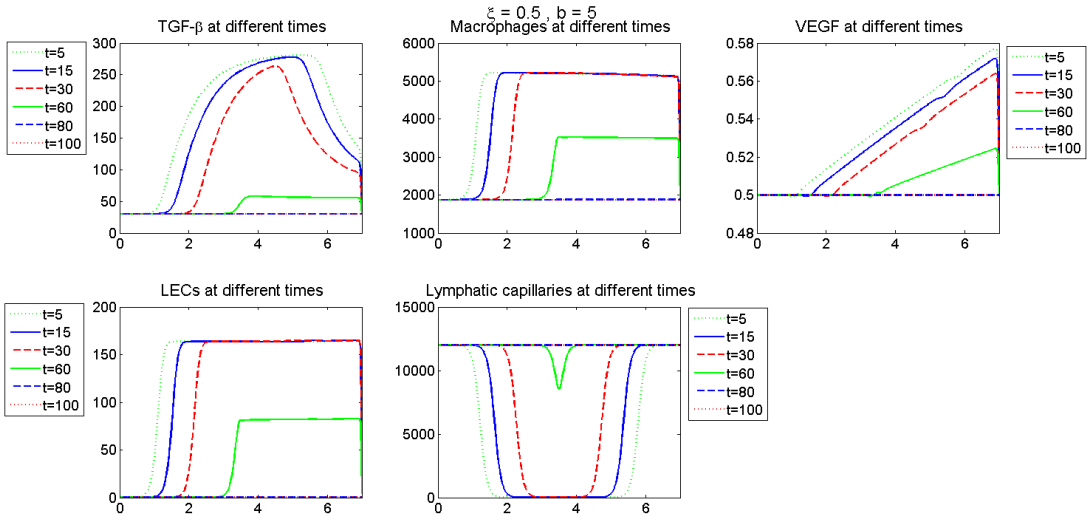

Figure 3.9: Simulation of equations (3.10)-(3.14) with parameters from Tables 3.2 and 3.3 and initial condition as defined in 3.3.7, with $b = 5$. $\xi = 0.5$.

A steeper initial condition ($b = 100$) appears to significantly slow down the process, such that almost no regeneration occurs in the first 100 days (see Figure 3.10). A similar scenario is observed if one takes $\xi = 0$ instead.

However, when $\xi = 1$ (i.e. the advection is due only to the lymph coming from the interrupted capillaries), the same initial condition gives rise to much faster healing, with complete vasculature at day 60; even more interestingly, in this case lymphatic regeneration occurs only from left to right, that is in the direction of the lymph flow (see Figure 3.11). Notice that in this case TGF-β, macrophages and VEGF have not returned to their equilibrium levels by day 100 (as we would expect): instead, they remain present at a higher level on the down-lymph flow side

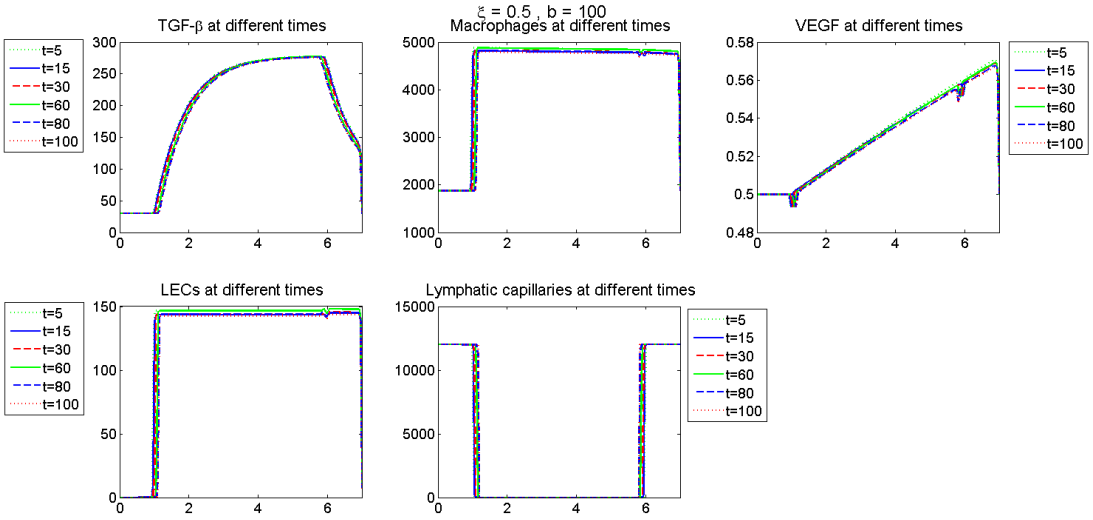

Figure 3.10: Simulation of equations (3.10)-(3.14) with parameters from Tables 3.2 and 3.3 and initial condition as defined in 3.3.7, with $b = 100$. $\xi = 0.5$.

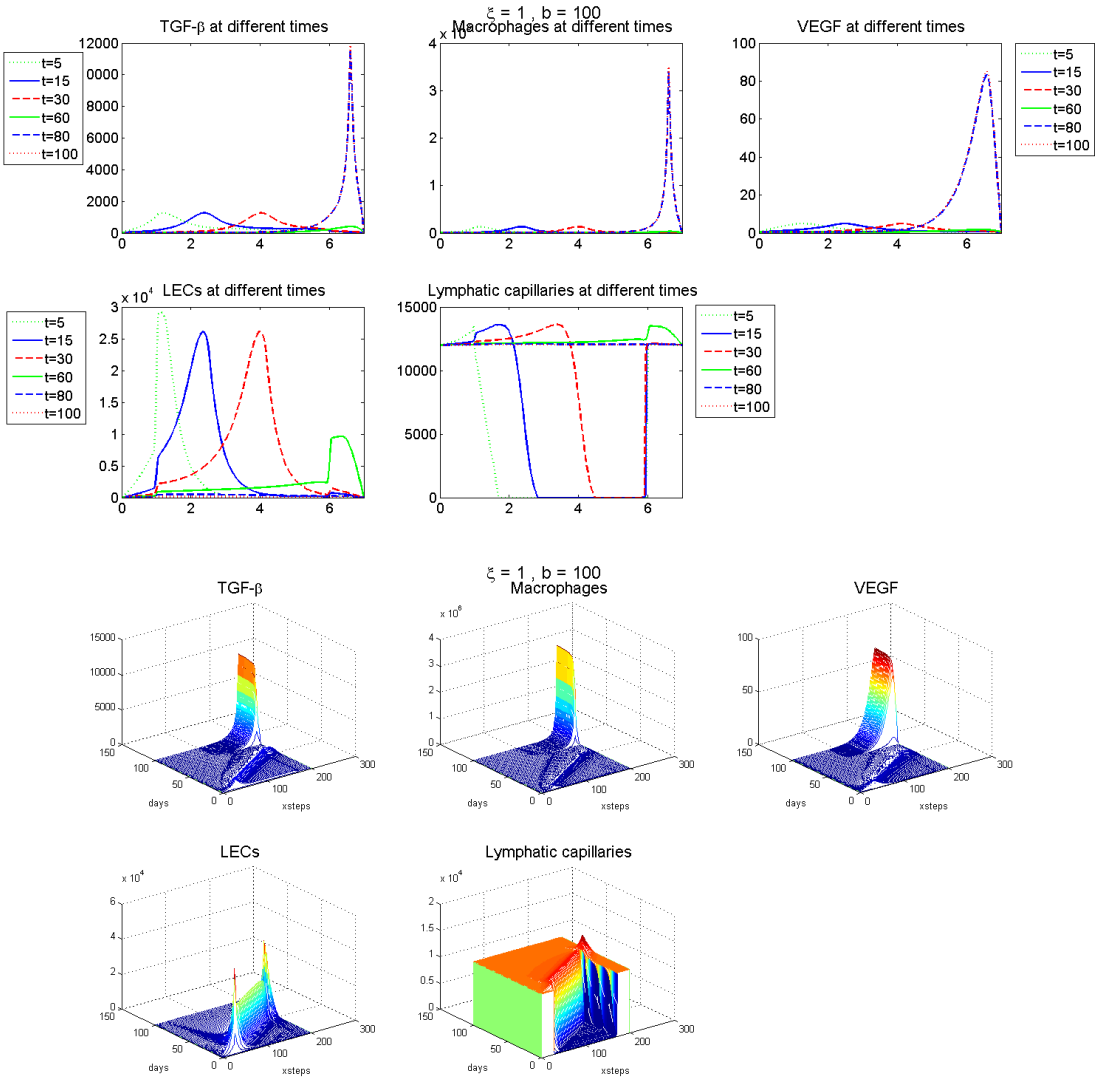

Figure 3.11: Simulation of equations (3.10)-(3.14) with parameters from Tables 3.2 and 3.3 and initial condition as defined in 3.3.7, with $b = 100$. $\xi = 1$.

of the domain. Also, as the front of regenerating capillaries move from left to right, a "bump" of excessive capillary is generated, before remodelling returns it to the equilibrium level.

Simulations over longer periods indicate that T, M and V persist at elevated levels. However, as our model is only expected to simulate post wounding dynamics, we can exclude effects after 100 days or so.

3.4.2 Sprouting hypothesis

For $\xi = 0.5$ and initial conditions (3.20) with $b = 5$, the model prediction for the sprouting case is very similar to its self-organising counterpart (see Figure 3.12).

A steeper function for the initial conditions ($b = 100$) will again slow down the process, but contrary to the self-organising case we observe a clear left-to-right regeneration pattern in this case (see Figure 3.13). A very similar, just slightly slower process is observed when $\xi = 0$ (simulation not shown).

Interestingly, when $\xi = 1$, lymphangiogenesis is only slightly enhanced, but occurs from right to left (Figure 3.14).

However, for $\xi = 0.9$, we observe again a left-to-right occurring lymphangiogenesis (Figure 3.15).

Contrary to the self-organising case, here a simulation over 300 days shows that all the variables will tend towards values which are close to their estimated equilibrium levels in the normal skin; with the exception of capillary tips, which instead of going to zero stay at a high level around the original edges of the wound, causing a slightly higher capillary density in these areas.

3.4.3 Comparison between the two models

Summarising, for shallower wounds (Figures 3.9 and 3.12), lymphangiogenesis appears to be dominated by logistic growth/remodelling and occurs symmetrically from both sides of the wound. In this case, there is little difference between the O and S hypothesis in terms of the rate and form of wound healing lymphangiogenesis.

Steeper initial conditions lead to slower capillary regeneration. This may be ex-

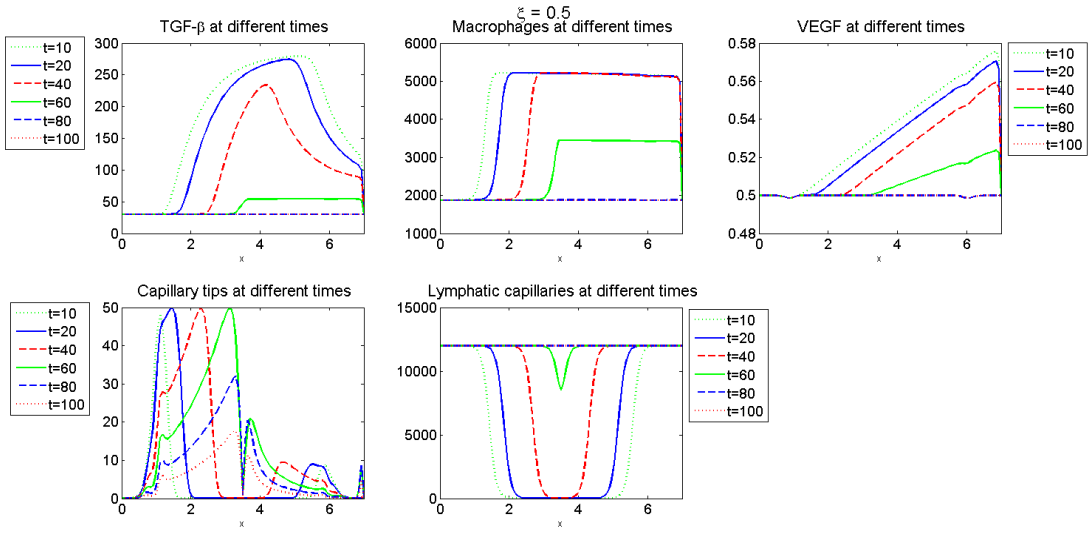

Figure 3.12: Simulation of equations (3.15)-(3.19) with parameters from Tables 3.2 and 3.3 and initial condition as defined in 3.3.7, with $b = 5$. $\xi = 0.5$.

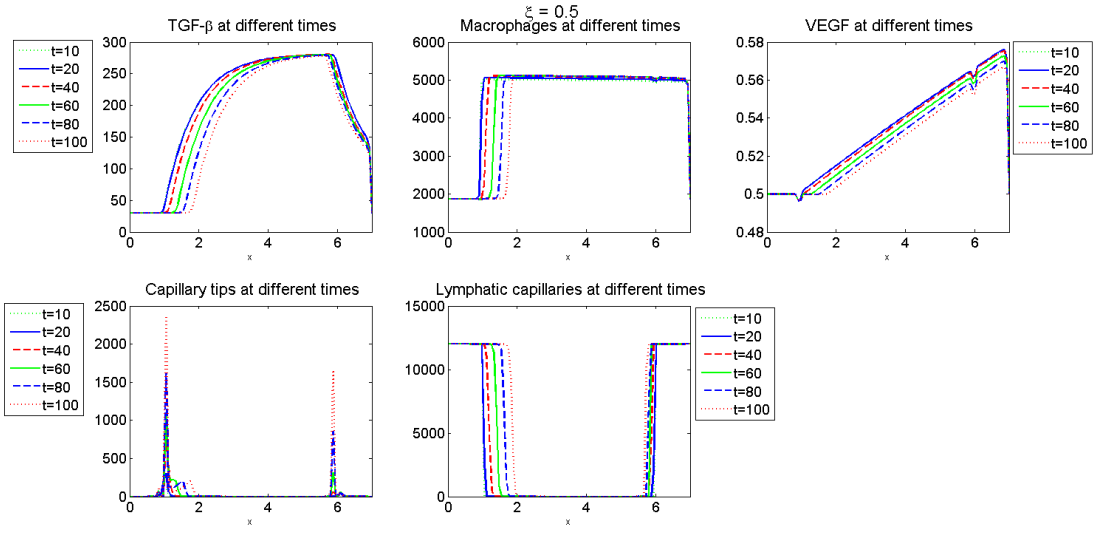

Figure 3.13: Simulation of equations (3.15)-(3.19) with parameters from Tables 3.2 and 3.3 and initial condition as defined in 3.3.7, with $b = 100$. $\xi = 0.5$.

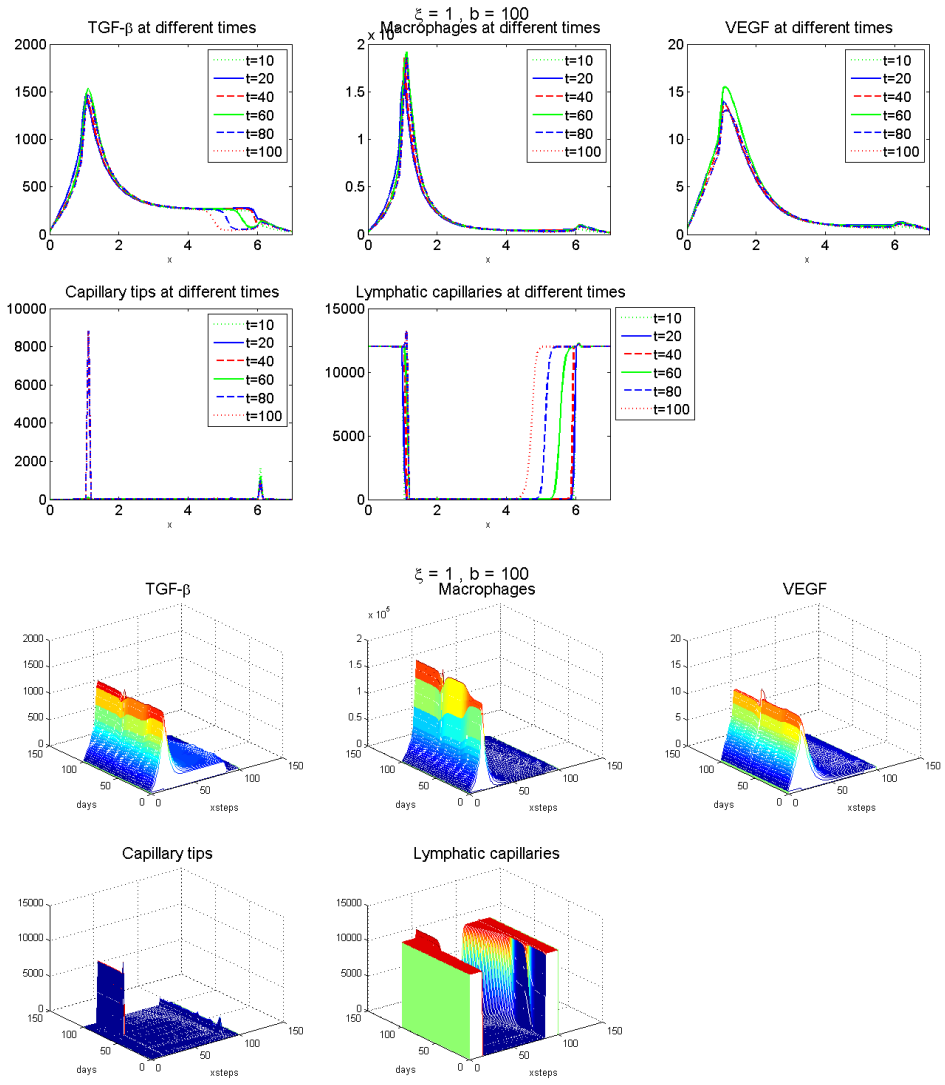

Figure 3.14: Simulation of equations (3.15)-(3.19) with parameters from Tables 3.2 and 3.3 and initial condition as defined in 3.3.7, with $b = 100$. $\xi = 1$.

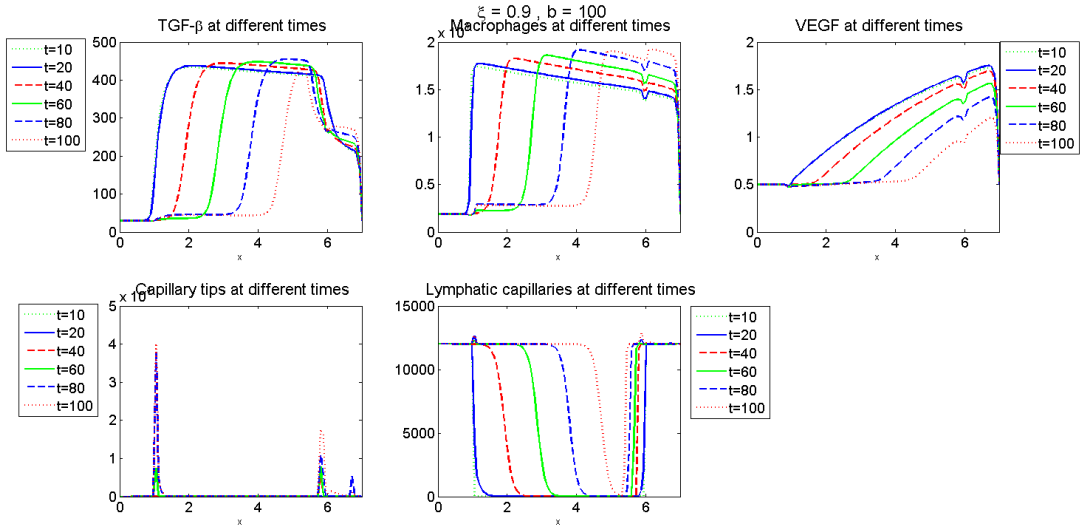

Figure 3.15: Simulation of equations (3.15)-(3.19) with parameters from Tables 3.2 and 3.3 and initial condition as defined in 3.3.7, with $b = 100$. $\xi = 0.9$.

plained with the observation that travelling wave solutions of Fisher-type equations exhibit minimum speed in the case of a step-like function initial condition. However, to confirm this more calculations are required.

For deeper wounds we observe markedly distinct behaviour between the two hypotheses according to the "advection balance" between interstitial and lymph flow. Observations are summarised in Table 3.4.

$\xi = 0$	self-organising:	extremely slow dynamics (seems symmetric)
	sprouting:	slow but visible lymphangiogenesis, from left to right
$\xi = 0.5$	self-organising:	extremely slow dynamics (seems symmetric)
	sprouting:	slow but visible lymphangiogenesis, from left to right
$\xi = 0.9$	self-organising:	extremely slow dynamics (seems symmetric)
	sprouting:	lymphangiogenesis from left to right, complete just after $t = 100$
$\xi = 1$	self-organising:	lymphangiogenesis from left to right, complete at $t = 60$
	sprouting:	lymphangiogenesis visible but not fast, from right to left

Table 3.4: Self-organising and sprouting model predictions for different ξ.

We compare these predictions with experimental data reported in Figure 3.16. These experimental observations show that the overall LECs (both free and in a capillary structure) increase steadily after wounding, and that while at day 10 the vast majority are in the distal half (i.e. upstream the lymph flow) by 60 days they are almost evenly distributed over the two sides.

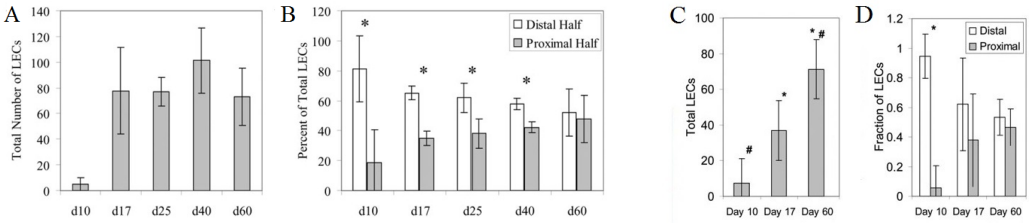

Figure 3.16: Left: Quantification of total LECs (A) and relative distribution of LEcs (B) in regenerating region in a mouse tail wound – from [223, Figure 2]. Right: Same data for a similar experimental setting described in [95, adapted from Figure 1]: LEC numbers (C) and distribution of LECs (D) in mouse tail regenerating region.

Hence, from experimental data:

- lymphatics should have reached a density close to C^{eq} at day 60;
- LEC migration and/or lymphatic capillary formation should happen predominantly in the direction of the lymph/interstitial flow.

Since these data refer to full-thickness wounds with almost no capillaries left in the region, we can limit our comparisons to the steep initial condition case (high b). The first fact suggests that ξ should be bigger than 0.5 and in general close to 1, since lymphatic regeneration appears to be faster in this case. This suggests that flow due to lymph coming from interrupted capillaries, rather than interstitial flow, is the major factor during lymphangiogenesis. The second experimental observation is consistent with simulations of both the self-organising and the sprouting model; however, a very high ξ is required in this context for both self-organising and sprouting case, and in the latter an inverted lymphangiogenesis direction (from right to left) occurs for $\xi = 1$.

Therefore, we can infer that there exists a threshold value for ξ, namely ξ^*, such that:

- $0.9 < \xi^* < 1$;
- if $\xi > \xi^*$, then the sprouting model predicts the lymphangiogenesis will occur from right to left and thus we can assume the self-organising hypothesis better describes the phenomenon in question (although chemical and macrophage values do not go back to their equilibrium level);
- if $\xi < \xi^*$, then both models predict a left to right development of the lymphatic vasculature, but this process is faster (and thus closer to aforementioned data) in the sprouting case.

Therefore, once the real value of ξ is assessed, one of the two models can be selected as the most suitable for describing the mechanisms of wound healing lymphangiogenesis.

3.5 Conclusions

The preliminary results presented in this chapter provide new insights in the understanding of lymphangiogenesis mechanisms. First of all, both models show the importance of advection in order to form a concentration gradient of the chemoattractants and thus promote cell migration and capillary regeneration. Furthermore,

the models presented here constitute a first attempt at exploring the relative importance of interstitial flow and lymph flow in lymphatic vessel regeneration; our results seem to be in favour of a predominant role of lymph flow in lymphangiogenesis dynamics. Further biological investigation is required to confirm this result.

A reliable value of ξ is also needed in order to choose between the two hypotheses modelled in this chapter. Interestingly, a sprouting assumption also has the potential to explain lymphatic restoration in the direction of the lymph flow; this is a notable result, since this experimental observation has been brought as support of the self-organising hypothesis. However, the sprouting scenario also includes an opposite tendency of lymphangiogenesis development for a value of ξ close to 1. Thus, one way to further select one of these theories is to inform the value of ξ from biological data. Other discriminating factors are that:

- capillary density in the sprouting case never significantly exceeds its normal value C^{eq}, while passing of this value is predicted in the self-organising case along with the capillary front;
- in the self-organising case there is an excess of TGF-β, VEGF and macrophages persisting downstream of the lymph flow.

Finally, our simulations suggest that initial conditions (that is, the type of wound) strongly affect the speed and the shape of the regeneration process: deeper wounds will require more time to heal, and lymphangiogenesis will occur more markedly in the direction of the lymph flow.

Chapter 4

Modelling (direct) tumour-nerve interactions

The content of this chapter has been accepted for publication in Scientific Reports.

Abstract: *Tumours induce the formation of a lymphatic and a blood vasculature around themselves. A similar but far less studied process occurs in relation to the nervous system and is referred to as* neoneurogenesis. *The relationship between tumour progression and the nervous system is still poorly understood and is likely to involve a multitude of factors. The present work is a first attempt to model the neurobiological aspect of cancer development through a system of differential equations. The model confirms the experimental observations that a tumour is able to promote nerve formation/elongation around itself, and that high levels of nerve growth factor and axon guidance molecules are recorded in the presence of a tumour. Our results also reflect the observation that high stress levels (represented by higher norepinephrine release by sympathetic nerves) contribute to tumour development and spread, indicating a mutually beneficial relationship between tumour cells and neurons. The model predictions suggest novel therapeutic strategies, aimed at blocking the stress effects on tumour growth and dissemination.*

4.1 Introduction

A relationship between tumours and the nervous system has been suspected since the second century AD with the work of the Greek physician Galen [251]. Traditionally, the nervous system has not been considered to be actively involved in the process of metastasis. However, recent studies have demonstrated the presence of neurons in peritoneum regions of several human tumours, and the number of tumour-associated neurons has been correlated with metastases [6, 151]. The relative importance of pre-existing versus newly-formed neurons to metastasis is not understood. Although pre-existing peritumoural neurons are likely to be sufficient for tumour spread, recruitment of neurons into the close proximity of a tumour may increase the propensity of tumours to metastasise. Increased nerve density and/or presence of intratumoural neurons should be regarded as an additional pathway for metastasis.

Significant progress has also been made in understanding the effects of stress- and depression-mediated release of chemicals by the nervous system on tumour cell dissemination [154, 263]. On the one hand tumour cells produce factors that induce the formation of a neural network, and on the other the newly formed nerves release neurotransmitters that affect tumour growth and migration [137, 160]. Following the terminology suggested by Entschladen and co-workers [72], the formation of new nerve branches is herein called *neoneurogenesis*, in analogy to lymphangiogenesis and (blood) angiogenesis. The (direct) interaction between peripheral nerve cells and tumour cells is usually called the *neuro-neoplastic synapse* (see Figure 4.1).

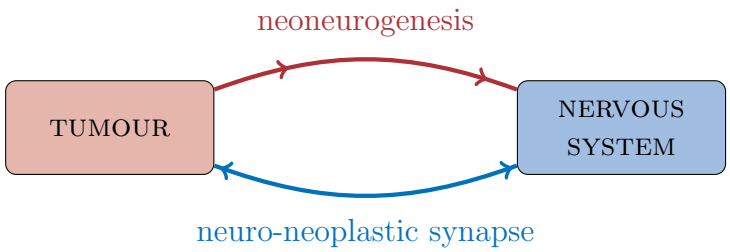

Figure 4.1: Tumour-nerve interaction is bilateral.

The present model aims to investigate how solid tumours induce peripheral nerve proliferation and how different types of nerves affect tumour growth and metastasis

by releasing substances such as neurotransmitters (see Figure 4.2); in particular, we see how an increase in norepinephrine production by sympathetic nerves (usually associated with stress) affects cancer progression. This model was mainly inspired by recent works that focus predominantly on prostate cancer [6, 160, 246]. The study in Ayala et al. [6] combines *in vitro* experiments with autopsy analysis of prostate cancer patients; Magnon and collaborators [160] explore the effects of the nervous system on tumour progression by altering nerve structure and receptor activity in mice, after implanting human tumour cells in the animals. Since the scope of our work does not include tumorigenesis, our model simulations start with a non-zero initial condition for primary tumour cells, reflecting the tumour cells implantation described in the study by Magnon et al. [160]. Our aim is to investigate the further evolution of these cells and their interactions with the pre-existing prostate-surrounding nerves. The model takes major inspiration from the work by Ayala et al. [6], supporting the hypothesis of a symbiosis between nerves and tumour cells.

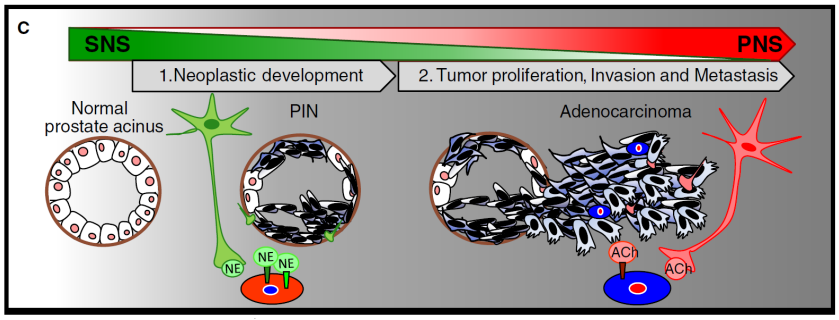

Figure 4.2: Scheme of tumour-nerve interaction proposed in [160, Figure 8].

4.2 Biological background

4.2.1 Neurons, neurotransmitters and the Autonomic Nervous System (ANS)

Neurons (or *nerve cells*) are the core components of the nervous system. The electrical signals travelling inside a neuron are converted into signals transmitted by certain chemicals (*neurotransmitters*); these are then passed to another neuron across a *synapse*. A neurotransmitter released by a nerve binds to a receptor on another

cell and, according to the receptor type, induces a certain action (see Figure 4.3).

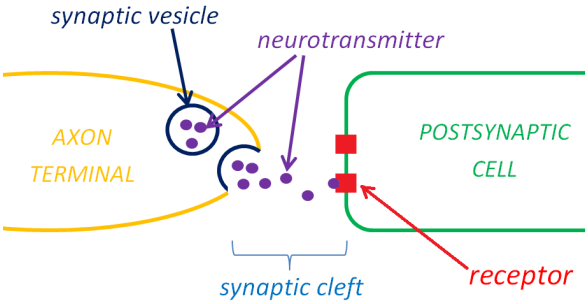

Figure 4.3: Neurotransmitters in a synapse.

The collection of all the neuronal structures that together control body functions below the level of consciousness (for instance, heart and respiratory rate, digestion and pupillary dilation) constitute the Autonomic Nervous System (ANS). The ANS is in turn made of three sub-systems; here we will focus only on two of them: the Sympathetic Nervous System (SNS, also called the "fight or flight" system), which is responsible for quick response processes, and the Parasympathetic Nervous System (PNS, also known as the "rest and digest" system), which governs slower responses such as gastrointestinal functions.

4.2.2 Tumour-induced neoneurogenesis

Tumours induce innervation around themselves [151, 194] and, in general, high levels of innervation in tumours correlate with a poor disease outcome [6, 160]. Tumour cells have the ability to produce substances, such as Nerve Growth Factor (NGF), that stimulate the growth and improve the survival of nerve cells [60, 215]. NGF also promotes tumour growth [60] and inhibits aggregation of cancer cells and thus enhances tumour invasion, although this process is currently poorly understood [61].

Tumours also release Axon Guidance Molecules (AGMs). These molecules were originally considered only for their role in the nervous system as guidance cues for axons. The term *axon guidance* denotes the process by which neurons send out axons along a precise path in order to reach the correct targets. The tip of an axon (or *growth cone*) is equipped with receptors that can sense (gradients of) chemicals, called *guidance cues*, which "tell" them where to expand [57]. In recent years,

however, it was shown that many AGMs can also influence neuronal survival and migration and likely play an important role in cancer progression [170]. There are at least three different families of AGMs (semaphorins, slits and netrins), which seem to have different roles in nervous system development and cancer progression. They are found in many different body tissues and can regulate cell migration and apoptosis (for a review of the role of AGMs in cancers, see Chédotal et al.[35]).

4.2.3 ANS effects on tumour progression

It was originally believed that the nervous system only indirectly affected cancer development, through perineural invasion (that is, the spread of tumours along nerve fibres [73, 262]) and modulation of the immune function [263]. Indeed, neurotransmitters regulate the cytotoxicity of T lymphocytes and natural killer cells [138] and induce leukocyte migration [70, 137]; the consequent immunosuppression can favour tumour growth and progression, impairing the anti-tumour response [8, 263]. However, it is the migratory effect of neurotransmitters that first suggested a *direct* link between nerves and tumour progression. One theory for the spread of metastases from a primary tumour to a certain organ claims that circulating cancer cells are attracted and settle in a specific region of the body due to the presence of factors such as chemokines or AGMs [35, 147]. This assumption is in agreement with the well-known "seed and soil" hypothesis [80]. In particular, several studies have shown that neurotransmitters influence the migratory activity of cancer cells, perhaps by inducing a phenotypic change towards a more motile phenotype via intracellular signalling [74], or simply by chemotaxis [64]. In addition, some neurotransmitters also induce tumour growth [137]. Indeed, tumour cells express many receptors, including serpentine receptors [71] to which neurotransmitters are ligands. Neurotransmitters can induce several behavioural changes in tumour cells, mostly increasing their proliferation and/or migration (a summary of such effects can be found in Lang & Bastian [137]).

4.3 Mathematical model

We define the *main domain* of our study as a portion of the body containing the prostate and its near surroundings, thus including both the tumour and the neighbouring nerves. All the variables, with the exception of the migrating tumour cells (see below), are average concentrations/densities over this domain, which vary in time. We develop a compartmental model in which an *extra domain* is considered for the tumour cells which leave the main domain. A schematic of the model, showing the variables and their interactions, can be found in Figure 4.4.

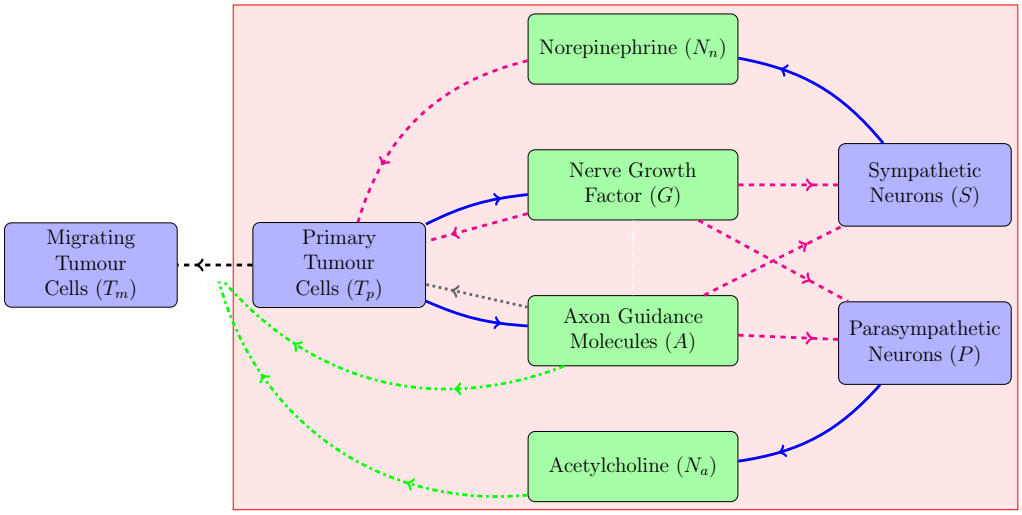

Figure 4.4: A schematic representation of the interactions among the model variables. Each variable corresponds to a rounded-corners rectangular box; note that cells are in BLUE while chemicals are in GREEN. The light red-shaded rectangular area represents the main domain, that is the prostate and its immediate surroundings. Concerning the arrows, **solid blue** denotes production, **dashed magenta** denotes enhancement of growth and/or survival (and axon extension in the case of neurons), **dash-dotted green** denotes migration enhancement, **dash-dotted black** actual migration and **dotted grey** denotes apoptosis induction.

We distinguish between *primary* tumour cells (T_p) and *migrating* tumour cells (T_m). The former are those that constitute the original tumour mass; when they detach and leave the orthotopic site of the tumour they are then designated migrating. The migrating cells are particularly dangerous because they have the potential to form metastases. Herein we do not explicitly account for the further development of the migrated tumour cells: our variable T_m represents an indication of *potential* metastasis formation.

NGF (G) is a neurotrophin (a kind of protein) which stimulates the growth and enhances the survival of both Sympathetic Nerve Cells (SNCs) and Parasympathetic Nerve Cells (PNCs). It has been found to be secreted by tumour cells. AGMs (A) also affect the survival and moreover the growth of both SNCs and PNCs. In reality, there are many kinds of AGMs, which can have completely different effects on nerve and tumour development. Here, for simplicity, we consider them as a single variable; taking into account the different types of AGMs would be one step towards improving the model in future.

The growth of both SNCs (S) and PNCs (P) is enhanced by NGF and AGMs. In addition, both types of nerve cell respond to a neurotransmitter called *acetylcholine* (N_a), but only PNCs produce it; SNCs instead secrete *epinephrine* (also known as *adrenaline*) and *norepinephrine* (N_n, also called *noradrenaline*) – see Figure 4.5. Norepinephrine is understood to be the main tumour-related sympathetic neurotransmitter; there are less documented effects of epinephrine on tumour cell growth and dissemination [137]. We are mainly interested in these neurotransmitters in relation to their effects on tumour cells: while norepinephrine enhances tumour cell survival, growth and chemotaxis, acetylcholine seems to stimulate tumour cell invasion and migration [160].

Figure 4.5: Neuro-signalling in a sympathetic (left) and parasympathetic (right) innervation. Neurotransmitters are in blue, nerves are in yellow and receptors in red.

4.3.1 Model equations

It is well documented that tumour cells naturally undergo mitosis (see for instance Friberg & Mattson [87]). The model accounts for this by taking constant growth rates r_{T_p} and r_{T_m} for primary and migrating tumour cells, respectively. Only a fraction of primary tumour cells exhibit proliferation; this is due to the presence

of a necrotic core, that we assume to be defined by the half inner radius of the (spherical) tumour mass [9]. This assumption leads to the conclusion that only 7/8 of the tumour volume (and thus primary tumour cells) proliferate. Primary tumour cells are also exposed to the chemicals present in the domain which influence the tumour development. Since tumour growth is enhanced by NGF, we assume that the growth rate of T_p is increased in a saturating manner by this factor. It has been shown that a classic logistic equation is often not suitable for modelling tumour growth [133]. Here we include an *Allee effect* in the growth term to take into account the fact that tumour cell populations tend to die out at low densities. The Allee effect is an ecological term describing a correlation between the size and the per capita growth rate of a population; its inclusion in cancer modelling was already suggested by Korolev et al. [133]. Here we take the *Allee threshold* (in the sense of Korolev et al. [133]) to be a function $\vartheta = \vartheta(N_n)$ that decreases as the norepinephrine level increases. This choice reflects the observation that norepinephrine enhances tumour cell survival [69].

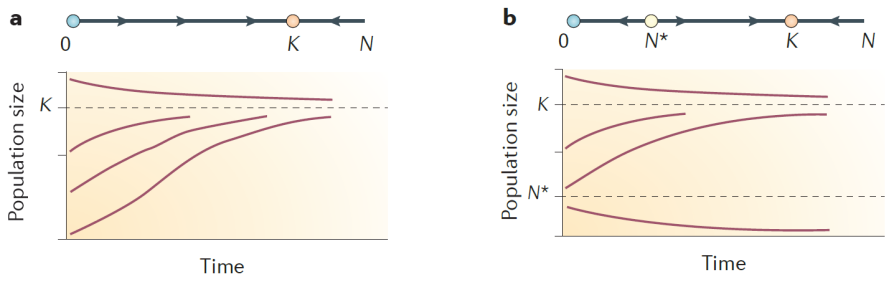

Figure 4.6: Graphical comparison between solutions of a standard logistic model (**a**) and of a logistic model with an Allee threshold (**b**), from [133]. Here, K denotes the carrying capacity and N^* the Allee threshold.

Tumour cells also die at a constant rate d_T. Interestingly, some AGMs (such as netrin-1) are also thought to control tumour cell apoptosis [252]; we model this phenomenon by adding a linear dependence on A to the death term. Finally, another relevant aspect of tumour cell dynamics is migration. Tumour cells can spontaneously disaggregate and move away from their original site. This process is enhanced by substances produced by nerve cells and distant organs, including AGMs [30] and acetylcholine [70, 137]. Hence, the densities of primary and migrated tumour cells

are described by the following equations:

$$\frac{dT_p}{dt} = \frac{7}{8}T_p \cdot \underbrace{\left(r_{T_p} + \frac{G}{\tau_1 + \tau_2 G}\right)}_{\text{growth up-regulated by NGF}} \cdot \underbrace{\left(1 - \frac{T_p}{k_T}\right) \cdot \left(\frac{T_p}{\vartheta(N_n)} - 1\right)}_{\text{logistic growth with Allee effect}} \tag{4.1}$$

$$- \underbrace{d_T\,(1 + \delta A) \cdot T_p}_{\substack{\text{cell death} \\ \text{increased by AGM}}} - \underbrace{(\mu_0 + \mu_1 A + \mu_2 N_a) \cdot T_p}_{\substack{\text{migration induced by} \\ \text{AGM and acetylcholine}}}, \tag{4.2}$$

$$\frac{dT_m}{dt} = \underbrace{(r_{T_m} - d_T) \cdot T_m}_{\substack{\text{natural cell} \\ \text{growth/death}}} + \underbrace{(\mu_0 + \mu_1 A + \mu_2 N_a) \cdot T_p}_{\substack{\text{tumour cell migration} \\ \text{from the primary tumour}}}, \tag{4.3}$$

where

$$\vartheta(N_n) = \frac{\theta_1}{1 + \theta_2 N_n}$$

(see Appendix C for the motivation of the definition of $\vartheta(N_n)$).

We are interested in the effects that tumour-secreted NGF and AGMs have on the system; here the tumour secretion rate of these two growth factors is assumed to be constant [72, 74]. We do not include other sources of NGF and AGMs in the main domain since these have a negligible effect on the dynamics that we want to study here (their effect on nerve growth in the absence of tumour is implicitly included in the logistic growth of nerve cells – see below). As chemicals, both NGF and AGMs decay at constant rate d_G and d_A, respectively. They are also internalised by both tumour and nerve cells, which bind them to their surface receptors. Here we assume that SNCs and PNCs bind the proteins at the same rate (namely, γ_2 for NGF and γ_4 for AGM). The evolution equations describing NGF and AGM dynamics in the domain are therefore given by

$$\frac{dG}{dt} = \underbrace{s_G T_p}_{\substack{\text{production by} \\ \text{tumour cells}}} - \underbrace{d_G G}_{\text{decay}} - \underbrace{[\gamma_1 T_p + \gamma_2 (S + P)]\, G}_{\substack{\text{internalisation by tumour} \\ \text{and nerve cells}}}, \tag{4.4}$$

$$\frac{dA}{dt} = \underbrace{s_A T_p}_{\substack{\text{production by} \\ \text{tumour cells}}} - \underbrace{d_A A}_{\text{decay}} - \underbrace{[\gamma_3 T_p + \gamma_4 (S + P)]\, A}_{\substack{\text{internalisation by tumour} \\ \text{and nerve cells}}}. \tag{4.5}$$

We assume that in a normal (i.e. tumour-free) setting both SNCs and PNCs grow in a logistic manner and tend to their carrying capacities k_S and k_P, which are

equal to their normal equilibrium values. However, when tumour cells are present nerve growth is enhanced by the secreted NGF [146] and AGMs [267]. This additional growth is modelled by two saturating functions and is not subject to logistic limitation. This is due to the fact that, given the complex shape of neurons, it is difficult to estimate an actual maximum density. Nerve growth can also occur as axon elongation, which does not take a significant portion of space. Thus, the equations characterizing SNC and PNC rate of change are

$$\frac{dS}{dt} = \underbrace{r_S\left(1-\frac{S}{k_S}\right)\cdot S}_{\substack{\text{logistic growth}\\ \text{and remodelling}}} + \underbrace{\left(\frac{G}{\sigma_1+\sigma_2 G}+\frac{A}{\sigma_3+\sigma_4 A}\right)\cdot S}_{\substack{\text{extra growth up-regulated}\\ \text{by NGF and AGM}}}, \tag{4.6}$$

$$\frac{dP}{dt} = \underbrace{r_P\left(1-\frac{P}{k_P}\right)\cdot P}_{\substack{\text{logistic growth}\\ \text{and remodelling}}} + \underbrace{\left(\frac{G}{\pi_1+\pi_2 G}+\frac{A}{\pi_3+\pi_4 A}\right)\cdot P}_{\substack{\text{extra growth up-regulated}\\ \text{by NGF and AGM}}}. \tag{4.7}$$

Norepinephrine and acetylcholine are produced by SNCs and PNCs, respectively, [101] at respective net rates s_n and s_a that we assume to be constant. However, these two neurotransmitters are also released by other cell types [172, 273] and we include constant sources c_n, c_a in their equations. As chemicals, they decay at constant rates d_n and d_a, respectively. Finally, they are absorbed by tumour cells [137, 160] at constant rates γ_5 and γ_6, respectively. The evolution equations for the neurotransmitters are then expressed by

$$\frac{dN_n}{dt} = \underbrace{c_n}_{\substack{\text{const.}\\ \text{source}}} + \underbrace{s_n S}_{\substack{\text{production}\\ \text{by SNCs}}} - \underbrace{d_n N_n}_{\text{decay}} - \underbrace{\gamma_5 T_p N_n}_{\substack{\text{uptake by}\\ \text{tumour cells}}}, \tag{4.8}$$

$$\frac{dN_a}{dt} = \underbrace{c_a}_{\substack{\text{const.}\\ \text{source}}} + \underbrace{s_a P}_{\substack{\text{production}\\ \text{by PNCs}}} - \underbrace{d_a N_a}_{\text{decay}} - \underbrace{\gamma_6 T_p N_a}_{\substack{\text{uptake by}\\ \text{tumour cells}}}. \tag{4.9}$$

4.3.2 Parameters and initial conditions

Parameters

Table 4.1 reports a list of all the parameters appearing in the model equations. Each parameter is supplied with its estimated value and units. A detailed description of

the estimation of each parameter (together with used sources) can be found in Appendix C. The parameter values were informed from the most relevant available datasets. Although these data are not "uniform" (in the sense that some are taken from experiments *in vivo* and others *in vitro*; some refer to human cell lines, others to rodents), we stress that, to the authors' knowledge, no entirely homogeneous and complete experiment related to neoneurogenesis has been performed to date; thus a consistent estimation of the parameters is not possible. To test the robustness of the model to parameter alterations, we performed a parameter sensitivity analysis (see below).

Initial conditions

In order to explore model predictions in different scenarios we will run simulations under different initial conditions on the primary tumour cells. In particular, $T_0^{10\%}$ and $T_0^{5\%}$ denote an initial density of primary tumour cells corresponding to 10% and 5% of the prostate volume, respectively (see Appendix C for details). A relatively high percentage is used due to the fact that data concerning the tumour-nerve system evolution are only available for advanced stages of tumour progression (as in Ayala et al. [6]). We assume that a certain amount of tumour cells, corresponding to our initial data, has been implanted in previously tumour-free individuals (as done by Magnon et al. [160], although there human tumour cells were implanted in mice). We also assume zero initial conditions for T_m, NGF and AGMs, because we are interested in the growth factors produced by the tumour (see above section). All the other values are assumed to be at their normal (tumour-free) level when the model simulation starts. A list of the initial values for all the model variables can be found in Table 4.2.

4.4 Results

A simulation of the system of equations (4.1)–(4.9) with initial primary tumour cell density $T_0^{10\%}$ (see above) is shown in Figure 4.7, where the MatLab function `ode45` was used to obtain the approximate solutions. The output of the model

PARAMETER	VALUE	UNITS	SOURCE
r_{T_p}	4.81×10^{-4}	day^{-1}	Schmid et al.[225]
r_{T_m}	1×10^{-4}	day^{-1}	estimated $\approx r_{T_p}$
τ_1	134.27	pg day $(\text{mm}^3)^{-1}$	Zhu et al.[288], Sortino et al.[239]
τ_2	2.39	day	Zhu et al.[288], Sortino et al.[239]
k_T	10^6	cells $(\text{mm}^3)^{-1}$	(Park et al.[198])
θ_1	10^4	$\text{cells}(\text{mm}^3)^{-1}$	estimated $\approx 1\%$ of k_T
θ_2	1	$\text{mm}^3\text{pg}^{-1}$	(Chiang et al.[37])
d_T	1.27×10^{-2}	day^{-1}	Dachille et al.[49]
δ	1.29×10^{-2}	$\text{mm}^3\text{pg}^{-1}$	Castro-Rivera et al.[33]
μ_0	0.22	day^{-1}	Pienta et al.[205]
μ_1	9.8×10^{-6}	$\text{mm}^3\text{pg}^{-1}\text{day}^{-1}$	Herman & Meadows[106]
μ_2	2×10^{-3}	$\text{mm}^3\text{pg}^{-1}\text{day}^{-1}$	Magnon et al.[160]
s_G	2.22×10^{-3}	$\text{pg cell}^{-1}\text{day}^{-1}$	Dolle et al.[60]
d_G	22.18	day^{-1}	Tang et al.[248]
γ_1	5.57×10^{-5}	$\text{mm}^3\text{cell}^{-1}\text{day}^{-1}$	Rakowicz-Szulczynska et al.[212]
γ_2	5×10^{-2}	$\text{mm}^3\text{cell}^{-1}\text{day}^{-1}$	Claude et al.[41]
s_A	5.42×10^{-3}	$\text{pg cell}^{-1}\text{day}^{-1}$	Kigel et al.[128]
d_A	2.4	day^{-1}	Sharova et al.[232]
γ_3	10^{-5}	$\text{mm}^3\text{cell}^{-1}\text{day}^{-1}$	estimated $\approx \gamma_4$
γ_4	1.47×10^{-5}	$\text{mm}^3\text{cell}^{-1}\text{day}^{-1}$	Keino-Masu et al.[123]
r_S	6×10^{-2}	day^{-1}	Dolle et al.[60]
k_S	0.26	cells $(\text{mm}^3)^{-1}$	Magnon et al.[160]
σ_1	1.29×10^2	pg day $(\text{mm}^3)^{-1}$	Collins & Dawson[47], Ruit et al.[220]
σ_2	50	day	Collins & Dawson[47], Ruit et al.[220]
σ_3	7.79	pg day $(\text{mm}^3)^{-1}$	Kuzirian et al.[135]
σ_4	0.01	day	(Kuzirian et al.[135])
r_P	7	day^{-1}	Collins & Dawson[46, 47]
k_P	0.03	cells $(\text{mm}^3)^{-1}$	Magnon et al.[160]
π_1	0.33	$\text{pg cell}^{-1}\text{day}^{-1}$	Collins & Dawson[47]
π_2	0.1	day	(Collins & Dawson[47])
π_3	1	pg day $(\text{mm}^3)^{-1}$	estimated $\approx \sigma_3$
π_4	0.01	day	estimated $\approx \sigma_4$
c_n	0.41	pg $(\text{mm}^3)^{-1}\text{day}^{-1}$	(Dodt et al.[59])
s_n	1.6	$\text{pg cells}^{-1}\text{day}^{-1}$	Esler et al.[76]
d_n	1.66	day^{-1}	Taubin et al.[249]
γ_5	2×10^{-3}	$\text{mm}^3\text{cell}^{-1}\text{day}^{-1}$	Jaques et al.[113]
c_a	3.99×10^3	pg $(\text{mm}^3)^{-1}\text{day}^{-1}$	(Wessler et al.[274], Watanabe et al.[269])
s_a	0.73	day^{-1}	Paton et al.[201]
d_a	49.91	day^{-1}	Bechem et al.[14]
γ_6	10^{-3}	$\text{mm}^3\text{cell}^{-1}\text{day}^{-1}$	estimated $\approx \gamma_5$

Table 4.1: A list of all the parameters appearing in the model equations, together with the sources used for their estimation.

INIT.VALUE	VALUE	UNITS	SOURCE
$T_p(0)$	$T_0^{10\%}$,$T_0^{5\%}$	cells/mm^3	calculated
$T_m(0)$	0	cells/mm^3	assumption
$G(0)$	0	pg/mm^3	assumption
$A(0)$	0	pg/mm^3	assumption
$S(0)$	0.26	cells/mm^3	Magnon et al.[160]
$P(0)$	0.03	cells/mm^3	Magnon et al.[160]
$N_n(0)$	0.5	pg/mm^3	Dodt et al.[59]
$N_a(0)$	80	pg/mm^3	Wessler et al.[274], Watanabe et al.[269]:

Table 4.2: Values of the model variables at $t = 0$.

will be compared with the experimental observations reported in Ayala et al.[6] and Magnon et al.[160]. Note that, to the authors' knowledge, these are the only published experiments that specifically address tumour-nerve interaction dynamics; yet, these results are not completely consistent and therefore we will not carry out a quantitative comparison. Indeed, Ayala and collaborators [6] use three different cell lines for *in vitro* experiments (human prostate cancer, mouse neuroblastoma and rat pheochromocytoma) and data from human patients for the nerve density analysis; Magnon and co-workers implanted human prostate cancer cells into mice to collect most of their data (only the assessment of nerve density in normal tissues surrounding tumour was done on human patients). Therefore, the only possible comparison between the model results and the experimental observations is of a qualitative, rather than a quantitative, nature.

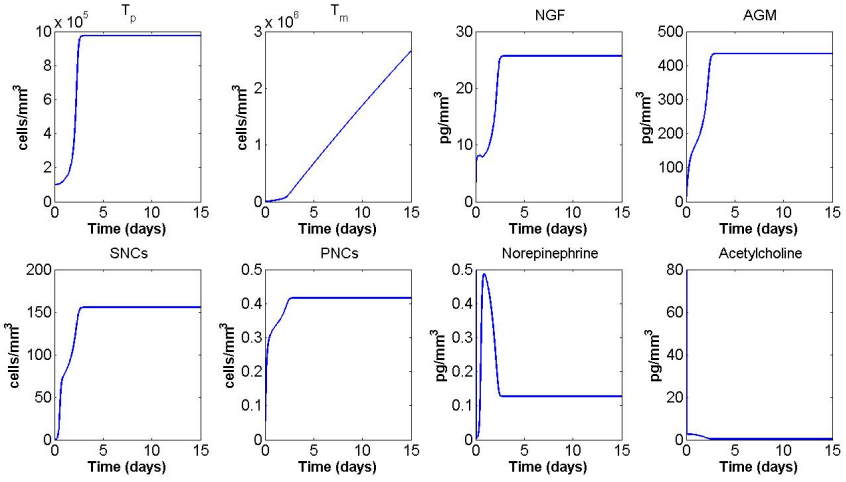

Figure 4.7: Time-course of the model variables over a period of 15 days for $T_0^{10\%}$.

Overall, the output is in good *qualitative* agreement with the experimental observations associated with aggressive human prostate tumour as reported by Ayala

and collaborators [6]. Both sympathetic and parasympathetic nerves are, in the presence of tumour, significantly increased in the region around the prostate, and the number of tumour cells leaving the domain are constantly increasing, matching the metastases-formation report in Ayala's and Magnon's works [6, 160]. Concerning the primary tumour mass, our model predicts that after an initial increase it reaches a non-zero equilibrium; this is in agreement with the results of Magnon and co-workers [160], which reports an increase in tumour mass within the prostate. Also the fact that NGF and AGM levels stay high seems realistic: NGF levels are higher in inflammation and some studies report that semaphorin 7A and netrin-1 levels are significantly elevated in patients subject to chemotherapy and some kinds of cancers, respectively. Neurotransmitters reduce rapidly to a low non-zero level following the sudden implantation of tumour cells. On the other hand, our results are not in *quantitative* agreement with Magnon et al. [160]; in particular, the present model reaches an equilibrium approximately 5 days after tumour cells implantation, whilst in Magnon's report [160] it takes weeks to observe such significant changes. This may be due to the fact that the model does not take into account other elements of the prostate environment (such as lymphatic and blood vasculature) which compete with the nervous system for growth factors and space, thus potentially slowing down the dynamics. In particular, in order to incorporate blood and lymphatic vasculature role in neoneurogenesis, one could consider extra variables representing blood and lymphatic endothelial cells as well as tumour (lymph)angiogenic growth factors. Of particular interest is the relation between NGF and vascular endothelial growth factor in prostate cancer, as proposed by Nico et al. [185] and Botelho et al. [21]. Including the immune system also has the potential to slow down the tumour's growth; this could be modelled for instance by considering lymphocyte dynamics or macrophage plasticity [159]. The inclusion of such extra elements is not put into practice here; however, the considered variables are sufficient to confirm the experimental evidence of tumour-nerve bilateral interactions. Also, we did investigate how perturbations in the parameter values may affect the model output and how different initial conditions will determine cancer progression.

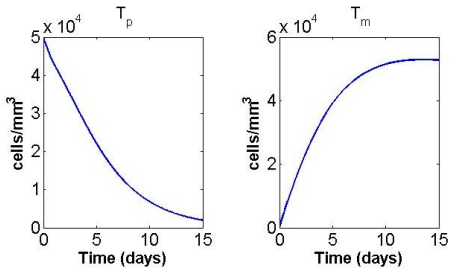

Figure 4.8: Primary and migrating tumour cells density time-course for initial condition $T_0^{5\%}$.

An interesting feature of the model is that a smaller initial condition for primary tumour cells, for instance $T_0^{5\%}$, gives rise to completely different dynamics. In this case the primary tumour goes to zero after a few days, while migrating tumour cells initially increase but then decrease to zero (Figure 4.8). This behaviour is in accordance with the hypothesis that a tumour cell colony has to be bigger than a certain threshold in order to proliferate [133]. Note that the migrating tumour cells could lead to tumour development in another site of the body where the conditions are more favourable. It is notable that the model is able to reflect this strong dependence of tumour progression on its initial conditions; this appears to be an important feature in modern cancer research inspired by ecological dynamics [133]. Our Allee threshold, lying between $T_0^{5\%}$ and $T_0^{10\%}$, appears to be unrealistically high but, to the authors' knowledge, no measurement of this parameter is available for comparison. In this model tumour cell survival and growth are affected only by nerves, while in reality blood vessels also contribute to tumour maintenance by providing oxygen and nutrients; this may (partially) account for the high threshold.

4.4.1 Parameter sensitivity analysis

To test the robustness of the model, we performed a parameter sensitivity analysis by observing the effect that a 10% increase/reduction of each parameter value has on tumour cell densities at day 15. The model appears to be very solid in the sense that final tumour cell densities are not greatly affected by perturbations in the parameter values. The only parameters that generate a change in the density of migrating tumour cells of 2% or more are reported in Figure 4.9. Of these, only

the tumour cell carrying capacity k_T has a similar effect on primary tumour cells.

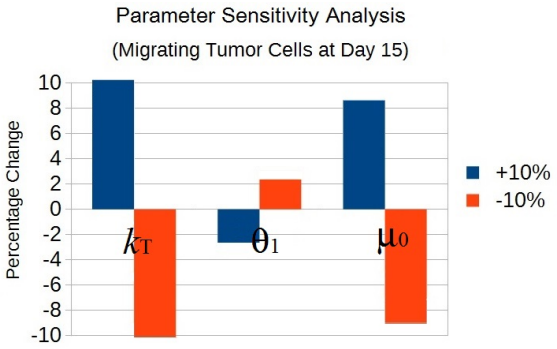

Figure 4.9: Parameter sensitivity analysis. The graph shows the effects on migrating tumour cells at day 15 after an increase (**blue**) or decrease (**orange**) of 10% in the parameters. Here only the parameters which induced a percentage change of 2% or more are shown; they are: the tumour cell carrying capacity k_T, the "basal" tumour cell Allee threshold θ_1, and the spontaneous tumour cell migration rate μ_0.

4.4.2 Stress and tumour progression

Many cancer patients exhibit stress and depression, which are known to have an effect on the immune system and consequently tumour growth [176, 263]. Additionally, they may have a direct effect as stress is associated with increased release of norepinephrine by the hypothalamus and sympathetic nerves [136]. Here we simulate a stress condition by increasing the norepinephrine release rate s_n by sympathetic nerves. Figure 4.10A shows the time course of primary and migrating tumour cells when s_n is multiplied by 10 for initial condition $T_0^{10\%}$. The plots show that when s_n is increased, the primary tumour cell density settles quickly to a higher equilibrium, while tumour cell migration is enhanced. This is in accordance with the experimental observation that stress is related to higher cancer metastasis and perhaps higher mortality [38, 175]. Again, our results agree qualitatively (but not quantitatively) with the experimental evidence.

Another interesting prediction of our model is that for some initial conditions, such as $T_0^{5\%}$, stress makes a crucial difference in tumour development. Here, if s_n is taken to be its baseline value, recall the primary tumour tends to zero (Figure 4.8); in stress conditions (simulated by multiplying s_n by 10) the same initial condition leads to primary tumour growth and a constant increase of migrating tumour cells

(Figure 4.10B). This observation suggests that a stressful environment can affect tumour development and therapeutic efficacy, in accordance with many findings in the biological literature [69, 263]. More experimental data are needed to precisely quantify this effect, however this already supports the potential for treatments targeting the sympathetic nervous system, as discussed by Cole & Sood [45].

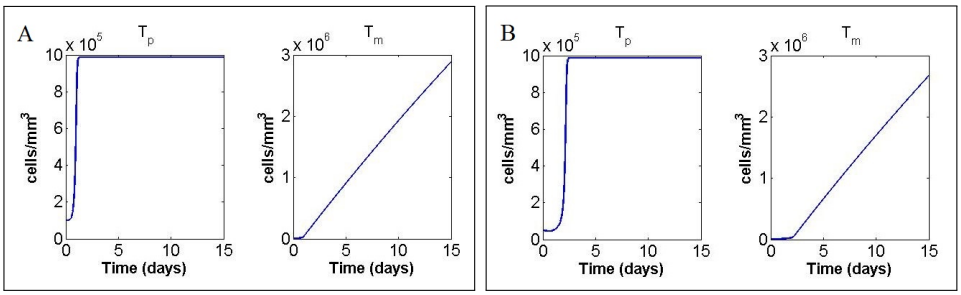

Figure 4.10: Primary and migrating tumour cells in stress conditions (simulated by multiplying s_n by 10) for initial conditions (A) $T_0^{10\%}$ and (B) $T_0^{5\%}$ respectively.

4.4.3 Blocking tumour acetylcholine receptors

Regarding parasympathetic neural activity, Magnon and collaborators [160] report that impairing the cholinergic (acetylcholine) receptors on tumour cells does not significantly affect tumour growth in the orthotopic site, but markedly reduces tumour cell spreading and metastasis. To simulate this phenomenon, we set $\mu_2 = 0$; that is, we consider tumour cells to be non-responsive to acetylcholine. In this case, we see (simulation not shown) that the number of migrated tumour cells after 15 days is reduced by about 0.5% and a similar reduction is also observed in primary tumour cell density. Thus, the model corroborates the findings of Magnon et al. [160] that cholinergic receptors on tumour cells are potential clinical targets in view of limiting cancer metastasis; again, for a quantitative assessment of the potential effectiveness of this treatment one would need to include more variables in the model.

4.5 Discussion

This work is the first mathematical confirmation of the major role played by the autonomic nervous system in promoting tumour development and progression of

prostate cancer and highlights neoneurogenesis as a target for cancer drug development. In the present paper we develop a simple mathematical model for tumour neoneurogenesis and cancer progression based on recent experimental evidence; the results show that, regardless of the presence of angiogenesis and lymphangiogensis, tumour-induced neoneurogenesis represents a symbiotic factor for prostate tumour. This work further expands our understanding of the process by which stress can regulate cancer initiation and development: previous research predominantly emphasised the role of the immune system in mediating stress effects on tumour growth and metastasis, while our model predicts that stress can directly affect primary tumour growth through the release of neurotransmitters. In addition, the effect of parasympathetic nerves is also captured by the model through the acetylcholine-induced tumour migration.

The use of ecological concepts in cancer biology and modelling is a promising development in tumour research [206]. Here we included an Allee effect in primary tumour cell dynamics, as suggested by Korolev et al. [133]. However, we suggest that one could couple tumour cell dynamics and nerves by introducing a norepinephrine dependence of the Allee threshold.

This model, though quite simple, gives good insights into tumour neoneurogenesis and offers many possibilities for expansion and improvement. First of all, the introduction of a spatial variable and thus the use of PDEs would allow a more precise description of the processes occurring during tumour neoneurogenesis. In particular, a spatial approach may be able to explain why sympathetic nerves tend to accumulate in normal tissues and only penetrate tumour edges, while parasympathetic nerves infiltrate tumour tissues [160]. Also, a more accurate description of the spatial component could allow for a distinction between axon elongation and nerve cell proliferation [6].

The model could be further improved by considering different variables for different kinds of AGMs, which are known to have diverse effects on tumour cells [35]. In fact, circulating tumour cells are probably attracted to a specific organ by chemokines and AGMs; the fate of a new tumour cell cluster will depend on the

sensitivity of the tumour cells to the specific factors and AGMs produced in the new environment.

One could also take into account the blood and lymphatic vasculatures. Guidance cues for axons also have a function in (lymph)angiogenesis [31, 68]. Both angio-, lymphangio- and neoneuro-genesis promote metastasis formation, although in different ways; for instance, blood and lymphatic vessels offer pathways for tumour cells to disseminate, similar to perineural invasion [73].

Another factor that could be included in the model is the immune system, which functions as a bridge between the tumour and nervous system and is the main cause of the *indirect* connections between the two (in addition, NGF also seems to be involved in immune response and inflammation [278]).

Finally, the model would highly benefit from more consistent datasets in order to include more realistic parameters values. Obtaining consistent parameter values would allow both qualitative and quantitative predictions to be formed.

Chapter 5

Modelling *Drosophila*'s courtship behaviour

Abstract: *Courtship behavioural patterns of Drosophila melanogaster are considered a good model to investigate neurodegenerative diseases (such as Parkinson's) in humans. This chapter illustrates the biological and health-care related background to this topic, and then presents a possible modelling approach, which is still work in progress.*

This chapter reports my contribution to the outcomes from the *NC3Rs/POEMS Network Maths Study Group: Applying mathematics to 3Rs problems*, held on 8$^{\text{th}}$-12$^{\text{th}}$ September 2014 in Cambridge, in response to a problem entitled *Improving the utility of Drosophila melanogaster for neurodegenerative disease research by modelling courtship behaviour patterns*, presented by Birgit Brüggemeier and Dr. Christian Schusterreiter from University of Oxford.

Our group presented three possible models to approach the study of *Drosophila* courtship behaviour, one of a probabilistic nature and two deterministic ones. The main difficulty in treating this problem mathematically is the nature of the data, which are sequences of behavioural patterns. While the probabilistic approach involves a Markov process (whose states are reported in Figure 5.1), the deterministic models presented at the end of the workshop in Cambridge focus on physiological mechanisms based on neuronal excitation, following Margaret Bastock's hypothesis.

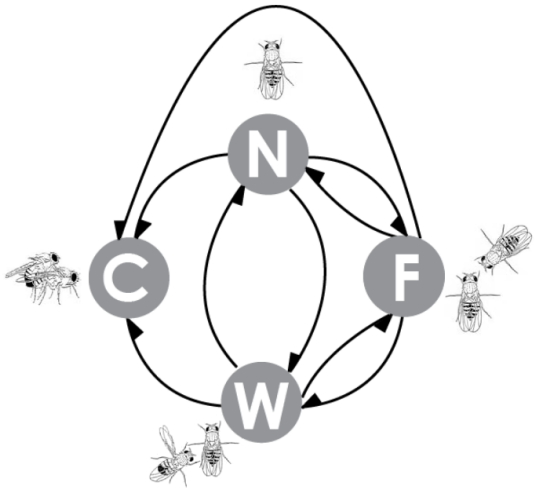

Figure 5.1: A schematic of the state space of the Markov process developed in the workshop. Each circle represents a displayed behaviour: N stands for *no courtship*, while F denotes *following*, W *wing extension* and C *copulation*. The arrows in the diagram indicate which behavioural switches are observed during courtship. Note that *copulation* terminates courtship display.

Bastock's theory states that switches between behaviours during courtship are due to hierarchical activity thresholds for successive courtship behaviours (for details, see [12]). The deterministic models have the advantage that they include a physiological mechanism: each behaviour is seen as the result of the neural activity, that triggers the behaviour when the activity or firing level of the related neurons is above a certain threshold. Although these kinds of models require parameter values which are difficult to obtain, parameter estimation might be possible through established statistical tools such as approximate Bayesian computation [145, 253].

In this Chapter I will present only one of the deterministic models developed during the workshop, which is the one I mostly contributed to design and implement. The model description is preceded by an introduction about the biology and interest of *Drosophila* courtship behaviour. The other model presented in Cambridge was an adaptation of the Fitzhugh-Nagumo equations [84, 181].

The model hereunder presented is still preliminary and some work still needs to be done for publication in terms of simulations and analysis, before it can be submitted.

5.1 Introduction

Figure 5.2: A male fruit fly. Credit: Jan Polabinski/iStockphoto.

The common fruit fly *Drosophila melanogaster* (Figure 5.2) was one of the first organisms used for genetic analysis. It was first proposed as a model organism by the American entomologist Charles W. Woodworth at the beginning of the 20$^{\text{th}}$ century and is nowadays one of the best-known eukaryotic organisms and one of the most used in biological research. There are many reasons for *Drosophila*'s popularity among biologists, in particular it is cheap to keep and breed in large quantities, its generation time is short (about 10 days), and its complete genome has been sequenced and published in 2000 [1]. Information from *Drosophila* is useful for understanding genetic processes in other eukaryotes, including humans: in particular, about three out of four known human disease genes have a recognizable match in the genome of the fruit fly [214]. For these reasons, *Drosophila melanogaster* has long been used as a genetic model for several human diseases, including neurodegenerative disorders (such as Parkinson's and Alzheimer's diseases) and those related to aging, diabetes, immunity and cancer [116].

Behavioural tests are crucial tools for screening new therapeutic agents for neurodegenerative disorders. Fruit fly courtship behaviour is a good model for research since as we will see in the following: it is modular, complex, partly innate and partly learnt from individual experience. In [231] the authors propose *Drosophila* courtship behaviour as a better behavioural assay for Parkinson's genetic model flies than other behavioural tests such as climbing ability. However, fruit fly courtship is not widely used in disease and drug studies (apart from a few exceptions), due to its complexity, despite its advantages over other fly behaviours. In this regard, mathematical modelling could potentially furnish a useful quantification and comparison method to extend the use of courtship behavioural tests in medical research.

5.1.1 Ethology of *Drosophila* courtship

Innate courtship of the male fruit fly *Drosophila melanogaster* consists of a series of behaviours (such as orientation towards the female, wing extension and copulation) which alternate in a complex pattern [18]. Figure 5.3 illustrates the observed behaviours displayed by the male fly during the courtship ritual.

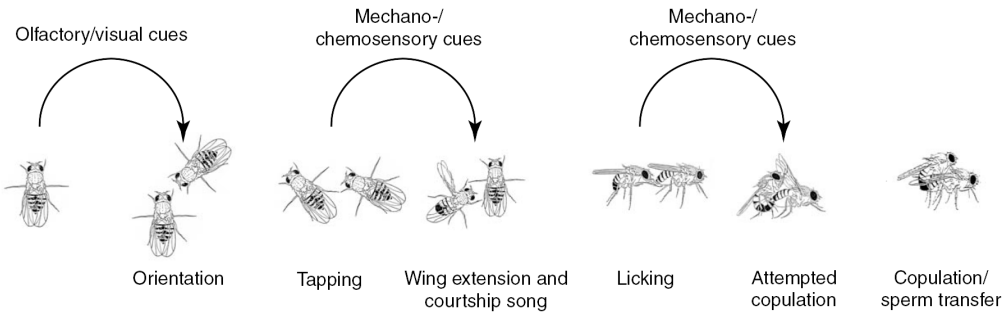

Figure 5.3: *Drosophila* courtship ritual as a series of successive behaviours, as presented in [18].

Although these behaviours are presented in an "ordered" fashion, transitions between different behaviours do not follow a fixed rule, since the male fly can switch from any one courtship behaviour to any other [13, 43, 165]. Figure 5.4 presents an ethogram of courtship behaviour taken from [43]: boxes denote different courtship behaviours, while arrows between boxes indicate the probability of a switch through the arrow's thickness.

In the 1950s, Margaret Bastock, a British zoologist and geneticist, advanced a hypothesis aiming to explain behavioural switches in innate fly courtship by considering excitatory thresholds and varying excitation in the male fly [12]. According to Bastock's theory, over the course of courtship male flies become increasingly sexually excited, and courtship behaviours are assumed to be hierarchical in the level of excitation they require to be displayed [4, 12, 195]. In addition, the female influences courtship choices of the male by sexually motivating him and thus increasing his excitation level [12].

Courtship is generated by one common neural network, with neuronal subsets sensitive to different excitatory frequencies [216]. The neural network determining courtship in the male fly consists of about 650 cells [216], and through the use of

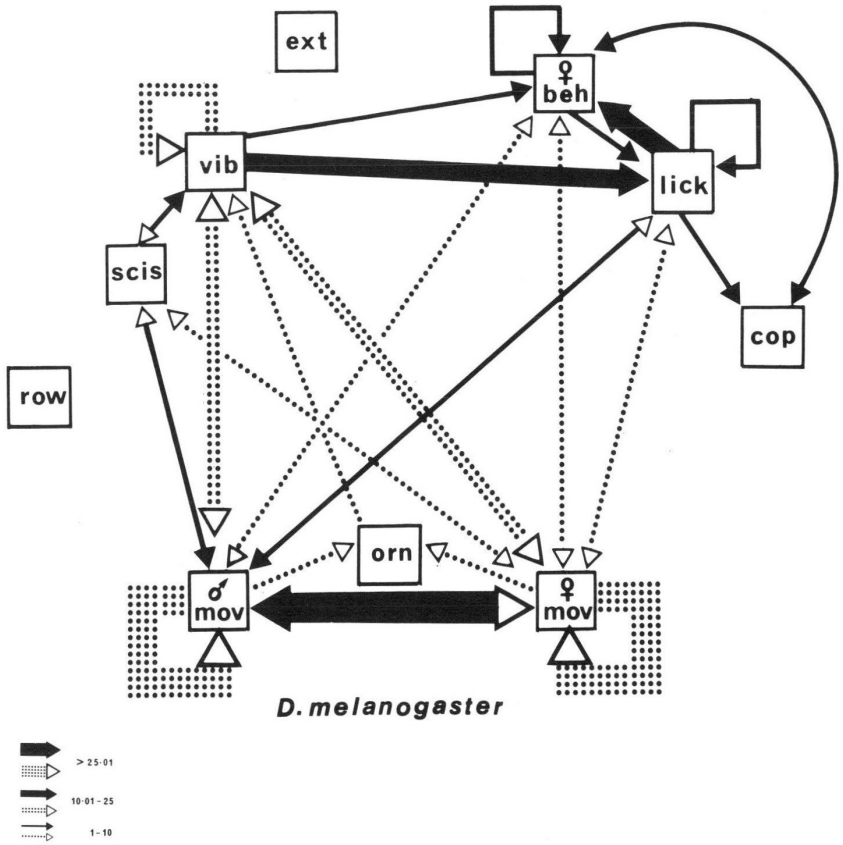

Figure 5.4: Ethogram of courtship behaviour for *Drosophila melanogaster* from [43, Figure 5]. The text in the boxes indicate the sub-behaviours of courtship: ♂ `mov` stands for male movement, ♀ `mov` stands for female movement, `orn` stands for male orienting towards the female, `scis` stands for wing scissoring, that is simultaneous extension of both wings, `row` stands for wing rowing, that is wing extension followed by immediate wing swing in, `vib` stands for wing vibration, ext stands for wing extension, `lick` stands for the male licking the female genitalia, ♀ `beh` stands for a class of behaviours shown by the female to express acceptance or rejection and `cop` stands for copulation. The thickness of arrows represents the frequency of transitions observed during courtship experiments, grouped in three classes: over 25 instances of a transition, 10 to 24 instances of a transition and transitions that occurred less than 10 times. Black arrows denote transitions significant at $P \leq 0.01$ in a stepwise search for identifying subsets of behaviours that significantly deviate from the assumption of quasi-random transitions. Accordingly, dotted arrows are not significant at $P \leq 0.01$.

genetic tools it is possible to narrow down even smaller neuronal subsets which are responsible for specific courtship behaviours [202]. These neuronal subsets can be tested both for their *necessity* in generating a given behaviour (through neuronal deactivation) and their *sufficiency* in generating a behaviour (by artificial neuronal excitation). Thus *Drosophila* allows for a systematic study of neural-driven behaviour.

5.1.2 A "courtship tracker"

A considerable amount of data is available concerning the behavioural patterns displayed by both healthy and Parkinson's-affected male fruit flies in response to different female subjects. An effective way to collect consistent behavioural data was developed by one of the members of our team, Dr. Christian Schusterreiter, during his PhD and this is summarised in [228]. It is a software tool which analyses videos of courting flies and discerns different behaviours, translating each of them into a specific colour and plotting it as a bar whose length is proportional to the time the behaviour has been displayed. A snapshot from the "courtship tracker" is shown in Figure 5.5. This tool provides a clear way to collect and present behavioural data which can then be compared with a model's output.

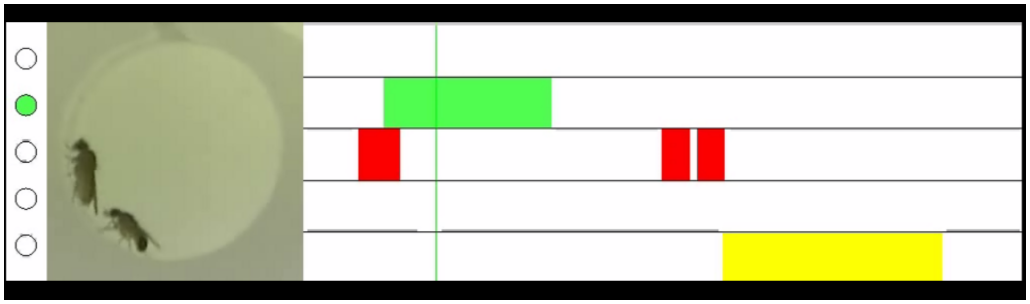

Figure 5.5: A snapshot from the software presented in [228]: the analysed video appears on the left, while the detected behaviours are printed as bars on the right; the thin green line represents the time point at which the video is captured. In this frame, **green** identifies following, **red** wing extension and **yellow** copulation.

5.1.3 Relevance for the 3Rs and human health

In the last century there has been increasing consideration for the ethical use of animals in research and testing. In particular, three guiding principles (known as "the Three Rs" or "3Rs") have been proposed in this regard since 1959 [221]:

1. *Replacement*, that is, the use of non-animal methods over animal methods when possible;

2. *Reduction*, which refers to methods that reduce the number of animals required to obtain scientific information;

3. *Refinement*, which invokes the development of methods that reduce pain, suffering, or distress and enhance animal welfare for the animals used.

In this context, promoting the modelling of fly courtship as an investigation method for neurodegenerative diseases meets many of these goals since both mathematical models and the use of invertebrates are regarded as main targets for replacement and reduction of animal experimentation.

However, the use of fly courtship as a standard behavioural tool for quantifying disease-related impairment is still problematic, given the complexity of courtship and the associated difficulty of defining normal courtship. Modelling can help with this problem by providing techniques and tools that define normal courtship on the basis of current theories of how *Drosophila* courtship patterns emerge. Currently courtship is mainly quantified with summary measures as the percentage of time spent courting (CI), which is easy to quantify. This allows large scale comparisons, but simplifying courtship to one index omits differences in behavioural patterns of healthy and non-healthy flies [12, 231]. The model presented in the following could be a starting point for studying behavioural patterns in a quantitative way and consequently could help to identify impairments that are otherwise overlooked in disease screens.

5.2 Mathematical Modelling

When modelling the courtship patterns of *Drosophila melanogaster*, it has been observed that certain neurons fire during the different stages of courtship. We decided to focus on a simple model of four neuron clusters, namely: Processing unit (P), which corresponds to no behaviour; Following cluster (F), which comprises several neuron types activated when following behaviour is displayed; Wing vibration cluster (W), more precisely defined as mesothoracic cluster; and finally Copulation cluster (C), located in the abdomen. As a simple starting point, we consider these four neuronal clusters as interconnected with differently-weighted excitatory and inhibitory connections between them. For simplicity, we assume that all neurons in a cluster fire at the same time, so that each cluster can be effectively regarded

as a single neuron. While a simplification, there are biological reasons to consider each cluster as one neuron. Each of the behaviours can be linked to a group of neurons which share a specific feature, for example an active gene sequence. When these neurons are activated *at the same time*, the behaviour is displayed. Hence we consider a single neuron from a cluster and assume all others share the same biological feature (active gene sequence).

In the following, a simple difference equation system is introduced to describe the interconnections among these neuronal clusters. This is still preliminary work; in particular, a precise way to quantitatively compare the model output with the observed behavioural data is to be defined. Once the model output fits the data, it will potentially have great value in identifying impaired neural connections in neurodegenerative cases.

5.2.1 Pasemann's model

In the 1990s, Pasemann proposed a simple model to describe interactions between neurons [199, 200]. Here the dynamics of neuronal interactions are described by discrete-time difference equations. To every "unit" (neuron) i corresponds one equation describing its *activation* a_i; this quantity is a real number (either positive or negative) which does not represent any specific physical parameter but is a measure of the neuronal activity. For each neuron i its total activation a_i is given by

$$a_i = \sum_j w_{ij} o_j + \theta_i,$$

where w_{ij} is the *weight* assigned to the connection between the units i and j ($i \neq j$), $\theta_i = \bar{\theta}_i + I_i$ (I_i total "external" input to unit i, $\bar{\theta}_i$ fixed bias) and o_j represents the *output* coming from unit j. The output function was taken to be

$$o_j = \sigma(a_j) = \frac{1}{1 + e^{-a_j}} \,. \tag{5.1}$$

All of these quantities are represented schematically in Figure 5.6.

Observe that transfer functions are here assumed to be sigmoid, that is bounded,

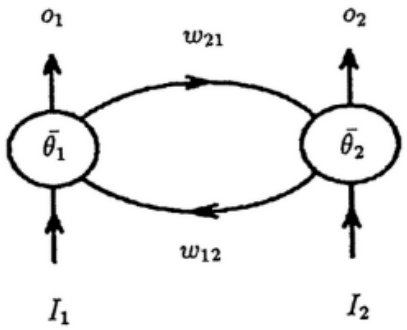

Figure 5.6: A schematic from Pasemann's paper [199, Figure 1] representing a 2-neuron network.

monotone increasing functions σ such that there exists a unique $x_M \in \mathbb{R}$ where $\sigma'(x_M)$ attains a local (and global) maximum. In fact, one can choose a constant $\alpha > 0$ to be this maximum, that is a positive number α such that

$$0 < \sigma'(x) \leq \alpha \quad \forall x \in \mathbb{R} \, . \tag{5.2}$$

In [199] the sigmoid (5.1) is chosen so that $\alpha = \sigma'(0) = 1/4$.

In [199] the author analyses the discrete dynamics of so-called *2-modules*, that is two-neuron networks of the form described in Figure 5.6, with $w_{11} = w_{22} = 0$ (no self-connections). The author also classifies different 2-modules depending on the sign of the product $A = w_{12} \cdot w_{21}$: if $A > 0$ the module is purely excitatory or inhibitory and is called an *even 2-module* (because the number of inhibitory connections in even); if $A < 0$ the module is inhibitory-excitatory and is called an *odd 2-module*. Modules with symmetric (respectively, anti-symmetric) weight matrix are special cases of even (respectively, odd) modules.

The equations for the 2-module dynamics at the equilibrium are

$$\begin{aligned} a_1^* &= \theta_1 + w_{12}\sigma(a_2^*) \, , \\ a_2^* &= \theta_2 + w_{21}\sigma(a_1^*) \, . \end{aligned}$$

From these one can see that the system can only have one or three steady states (this fact is related to the shape of the transfer functions, that being sigmoid can intersect only in either one or three points). In addition, by linearisation one finds

that the eigenvalues of the system at the equilibrium are given by

$$\lambda_{1,2} = \pm\sqrt{A \cdot \sigma'(a_1^*) \cdot \sigma'(a_2^*)}\ .$$

This tells us that, since $\sigma'(a_1^*) \cdot \sigma'(a_2^*)$ is strictly positive, the eigenvalues are real in the case of an even 2-module and imaginary for an odd 2-module. The distinction between even and odd 2-modules is also considered by studying the type of bifurcation occurring at $(a_1^*, a_2^*) = (0, 0)$. Note that unstable steady states are those of greater interest in the context of neuronal models.

Further on, the paper [199] provides results concerning the dynamics of even and odd 2-module systems for different values of the weights w_{12}, w_{21} (related via the constant α defined in (5.2)). It is worth stressing that the qualitative behaviour of the system does not depend on the particular choice of the sigmoid transfer function, but only on α.

Finally, in the discussion section of [199], the author points out how the continuous dynamics of a 2-module are very different from the discrete case presented above. In particular, it is proved that a time-continuous 2-module without self-connections cannot exhibit stable periodic behaviour.

Pasemann remarks how introducing self-connections to the units of a 2-module will generate much more complex behaviours.

5.2.2 A "Pasemann-like" model

In formulating our model we were inspired by the models presented in [199, 200], but contrary to Pasemann's assumptions we considered neural *clusters* instead of single neurons, assuming that neurons in the same cluster fire at the same time. Further, we did not take any bias into account and considered a random external input I_n (at each time point n). Another difference between Pasemann's work and ours is that here all the weights are taken to be positive and the distinction between *purely-excitatory* and *excitatory-inhibitory* connections is modelled through two types of

transfer functions:

$$\sigma_+(x) = \begin{cases} (1+\exp[m_1(-x+q)])^{-1} & \text{if } x > 0 \\ 0 & \text{if } x \leq 0 \end{cases}, \tag{5.3}$$

$$\sigma_\pm(x) = \begin{cases} (1+\exp[m_1(-x+q)])^{-1} & \text{if } x > 0 \\ 0 & \text{if } x = 0 \\ -(1+\exp[m_2(x+q)])^{-1} & \text{if } x < 0 \end{cases}, \tag{5.4}$$

whose graphs are plotted in Figure 5.7.

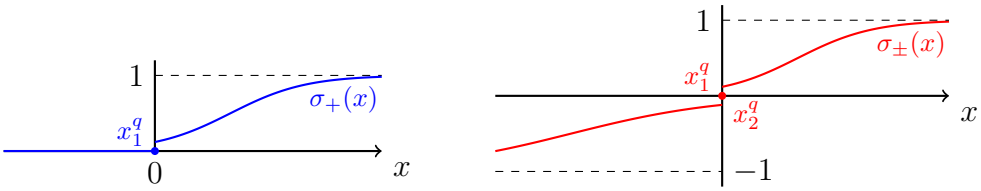

Figure 5.7: Plots of the functions σ_+ (left) and $\sigma_\pm$ (right).

Note that we considered more general sigmoid functions than in [199], with an input argument depending not only on x, but also on three parameters m_1, m_2 and q ($m_1, m_2 > 0$, $q \in \mathbb{R}$). Physically, the parameters m_1, m_2 represents the steepness of the "switch" between zero and excitation or inhibition. More precisely, m_1 determines the steepness of the switch between no-effect to excitation for both σ_+ and $\sigma_\pm$ while m_2 controls the same steepness in the case of a switch between no-effect and inhibition for $\sigma_\pm$. In the following, we will take $m_2 < m_1$ because it is known empirically that neural inhibition has less "immediate" effect on neural activity than excitation. The parameter q instead determines the position of the points x_1^q,x_2^q depicted in Figure 5.7 (that is, the lower bound for $|\sigma_+|$,$|\sigma_\pm|$ for $x \neq 0$). Although the results proven in [199] suggest that a more general shape for the transfer functions does not affect the qualitative behaviour of the system, our decision to introduce the three parameters m_1,m_2,q that control the exact shape of the sigmoid functions was in view of fitting to experimental data. It seems difficult to measure these parameters directly in an experimental setting, but as we will see in the following one could fit the model output to observed behavioural patterns.

Our model consists of the four units (neural clusters) described above, which

interact as described in Figure 5.8 through the transfer functions defined in (5.3) and (5.4).

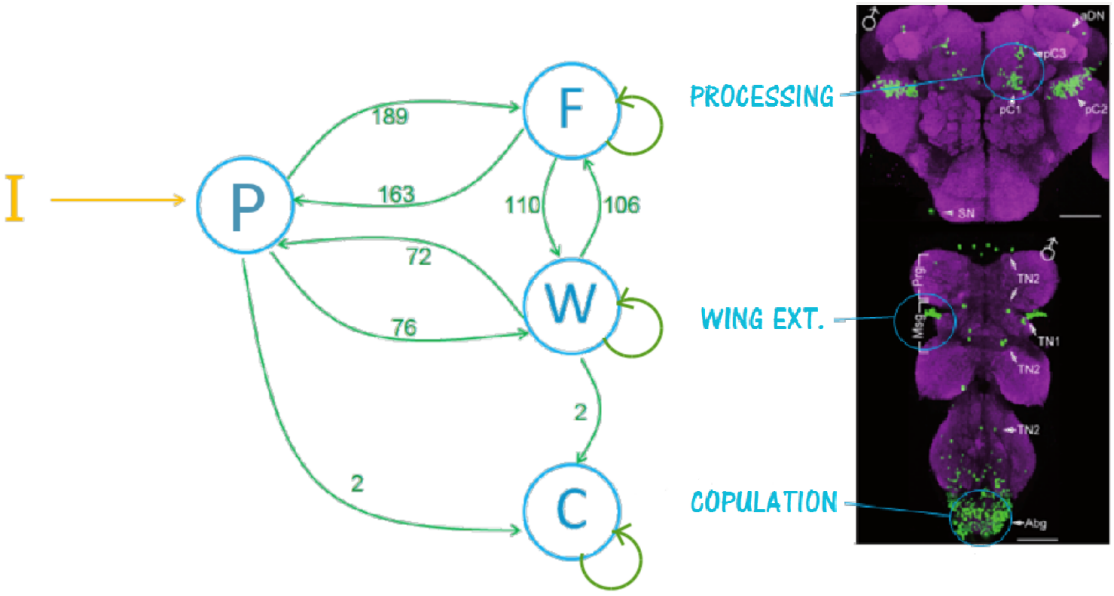

Figure 5.8: Schematic view of the model, compared with an image of neurons expressing the sex-determining gene *doublesex* (in green) in the *Drosophila* brain and ventral nerve cord (purple). The *doublesex* gene is necessary and sufficient for flies displaying male courtship behaviours [202]. The fly brain was prepared and imaged by Hania Pavlou, who was also a member of the workgroup. In the graph, the numbers on the edges are the number of times the corresponding behavioural switch has been observed in four experiments (their sum).

The numbers on the arrows shown in Figure 5.8 give the number of times (summed - *not* averaged - over four experiments) the corresponding behavioural transition is observed. The proportions between these values will be maintained across the values we will choose for the weights in our model. In this way, it is implicitly assumed that each behavioural switch is proportional to the weight of the corresponding connection. This assumption helps focus our parameter specification, given that there is no available data concerning these specific neural connections. Indeed, little is known about these connections. Thus, on the one hand it is difficult to realistically estimate parameters, but on the other the model therefore has potential to give a greater insight into the understanding of the system: estimating the relative importance of the connections between different neural clusters could help to identify impaired or lacking connections in the neurodegenerative case.

In writing the equations describing the activity of each cluster, the following assumptions are made:

- the external input I can be either positive or negative (depending on the female behaviour).
- the input I acts on the activation of the processing unit P in either an excitatory or inhibitory manner, thus modelled through the function $\sigma_{\pm}$;
- the activity of the cluster P can induce an increase in the activity of F and W through the purely excitatory output function σ_{+};
- P itself can be excited by the activity of the clusters F and W, via the function σ_{+};
- the activity of the copulation cluster C is only influenced by the processing unit P and the wing-extension cluster W.

These assumptions are motivated by the observed alternation of behaviours from none to following, from none to wing-extension and from following to wing-extension (while, for instance, no copulation after following is observed). In addition, the clusters F, W and C are supposed to have a self-excitatory mechanism (represented by the loops in Figure 5.8) suggested by the observation that neural activity in a cluster tends to maintain and increase itself (for example, even if the external stimuli suddenly end, an excited cluster will stay excited for a while – at least for the 4-minute duration of the standard experiment – although the level of excitation can vary). This approach will hopefully take into account a sort of "hierarchy" among the neural clusters: for example, it is observed that copulation is "stronger" than following and wing extension, so we hope to see a kind of ordered sequence in the behaviours emerging from this neural activity.

Applying the above reasoning gives rise to the following equations to describe the network:

$$P_{n+1} = w_I \sigma_{\pm}(I_n) + w_{FP}\, \sigma_{+}(F_n) + w_{WP}\, \sigma_{+}(W_n)\ , \tag{5.5}$$

$$F_{n+1} = w_{PF}\, \sigma_{\pm}(P_n) + w_{WF}\, \sigma_{+}(W_n) + \ell_F F_n\ , \tag{5.6}$$

$$W_{n+1} = w_{PW}\, \sigma_{\pm}(P_n) + w_{FW}\, \sigma_{+}(F_n) + \ell_W W_n\ , \tag{5.7}$$

$$C_{n+1} = w_{PC}\, \sigma_{\pm}(P_n) + w_{WC}\, \sigma_{+}(W_n) + \ell_C C_n\ . \tag{5.8}$$

In the above n is the (discrete) time and σ_+,$\sigma_\pm$ are defined in (5.3) and (5.4), respectively. Note that I_n here depends on the female response at time n and, in a first instance, we will take it to be random and uniformly distributed between $-1/2$ and $+1/2$. As a starting time point we will take the beginning of an experiment and consequently consider zero initial conditions for all the four clusters, reflecting the fact that the part of the male fruit fly's nervous system involved in courtship is not activated before he sees the female.

5.2.3 Simulations

A representative numerical simulation of the model (performed in MatLab) can be seen in Figure 5.9, where the neuronal activity of the different clusters is plotted over about 60 time steps. This particular number was chosen for the following reasoning: in a (video) experiment, the camera records about 25 frames per second and one experiment usually lasts around 4 minutes; one experiment should then correspond to approximately 6000 frames/timesteps, however plots over more than 100 timesteps are not clear to interpret, so we considered a time-rescaling of a factor of 100. This is justified by the fact that each behaviour displayed by a male fruit fly lasts several tens of frames anyway. More simulations (corresponding to different random inputs I) are plotted in Figure 5.11.

The simulation shows oscillatory increasing dynamics for P, F, W and a fairly steady increase in the activity of C, which is what we would expect during a normal courtship experiment in which the male is constantly exposed to the female's presence. Note that here we have considered a random input I coming from the female, I being uniformly distributed between -0.5 and 0.5; in this way, at every time n there is 50% chance that the male will get a negative input and 50% he will receive a positive one. We will explore different ranges of I in the following.

To convert these results into a behavioural output (which would then be comparable with real data), it is assumed that a certain behaviour is displayed by the fly when the activation of the corresponding neural unit is above a certain threshold. Figure 5.10 shows the "translation" of the dynamics shown in Figure 5.9 for a

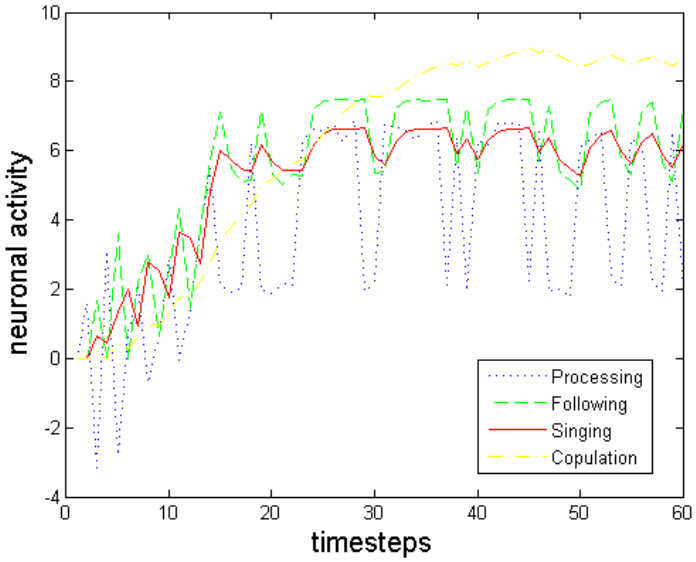

Figure 5.9: Simulation of neural activity of the four neural clusters. Here, the weights were taken to be random numbers normally distributed around the following values: 0.47 for w_{PF}, 0.41 for w_{FP}, 0.19 for w_{PW}, 0.18 for w_{WB}, 0.05 for w_{PC}, 0.28 for w_{FW}, 0.27 for w_{WF}, 0.05 for w_{WC} (w_{PC} and w_{WC} were multiplied by 10 since the "original" values seem too small to be realistic). The standard deviations were taken to be equal to 1/10 of these values, respectively. The other parameters considered are $m_1 = 1$, $m_2 = 0.5$ and $q = 2$ for the sigma-functions (5.3) and (5.4) and the loops $\ell_F = 0.1$, $\ell_W = 0.3$ and $\ell_C = 0.9$.

certain choice of thresholds. We assumed $\theta_C > \theta_W > \theta_F$ because it seems reasonable to require higher neural activity for behaviours generally associated with higher excitation. Again, more realisations of the same system are reported in Figure 5.12.

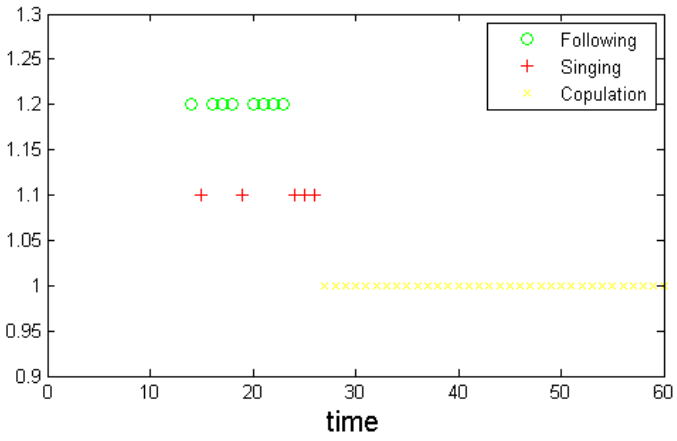

Figure 5.10: Behavioural pattern emerging from the previous simulation of neural activation. Here the thresholds are taken as follows: $\theta_F = 5$, $\theta_W = 6$ and $\theta_C = 7$.

The pattern shown in Figure 5.10 is encouraging because it shows an alternation between no behaviour, following and wing extension followed by copulation, which

is the same thing we observe in reality. Further study should include comparing the time each behaviour is displayed in relation to other behaviours, and then comparing this with experimental data (this could be an idea to design a "metric" to compare model outputs and data).

5.2.4 Rejective and receptive females

An idea for further exploring the model's potential to describe real fly behaviour could be to use different female/external inputs I and see how these affect the male behavioural display. For a non-receptive female we can consider a random input I uniformly distributed between -0.8 and 0.2 (that is, the female gives a negative cue 80% of the times). Four representative realisations of the model in this case are reported in Figure 5.13.

From these simulations, one sees that most of the time it takes longer before the male starts exhibiting any courtship-related behaviour, and that copulation does not always occur in the time of the experiment (about 4 minutes/6000 frames/60 time steps in the model). This reflects the fact that the male's excitement and propensity to proceed in the courtship ritual is strongly influenced by the female's behaviour. In a forced vicinity with the female (which is the case in the lab experiments) the male will eventually get excited anyway, but we could argue that in a natural/wild setting the female has time to flee and no copulation will occur.

Similarly, we can simulate a receptive female by taking the input to vary in the range $-0.2 \leq I \leq 0.8$ (that is, positive signals from the female in 80% of the cases). Again, four representative simulations are shown in Figure 5.14.

Here we observe that a positive input from the female accelerates the courtship process from the initial phase to copulation.

A more precise comparison between model outputs for the different choices of I can be done by calculating mean copulation time n_{cop} in the different cases (copulation time meaning the time at which copulation starts). We find that the mean copulation times over 10^4 simulations are respectively:

- $n_{cop} = 24$ for $-0.5 \leq I \leq 0.5$ (random female input);

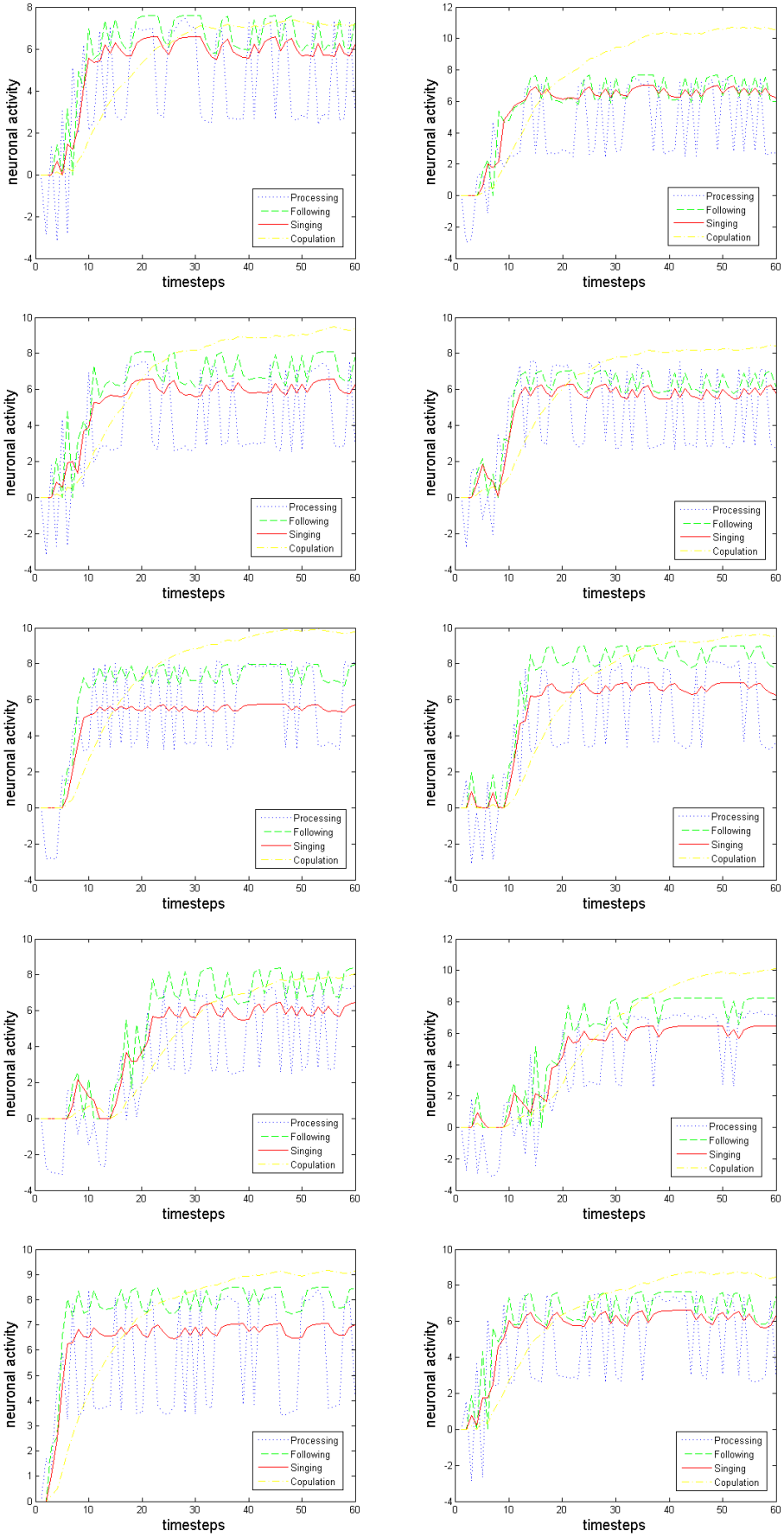

Figure 5.11: Simulations of neural activity of the four neural clusters for the same set of base parameters as Figure 5.9, but under different random inputs.

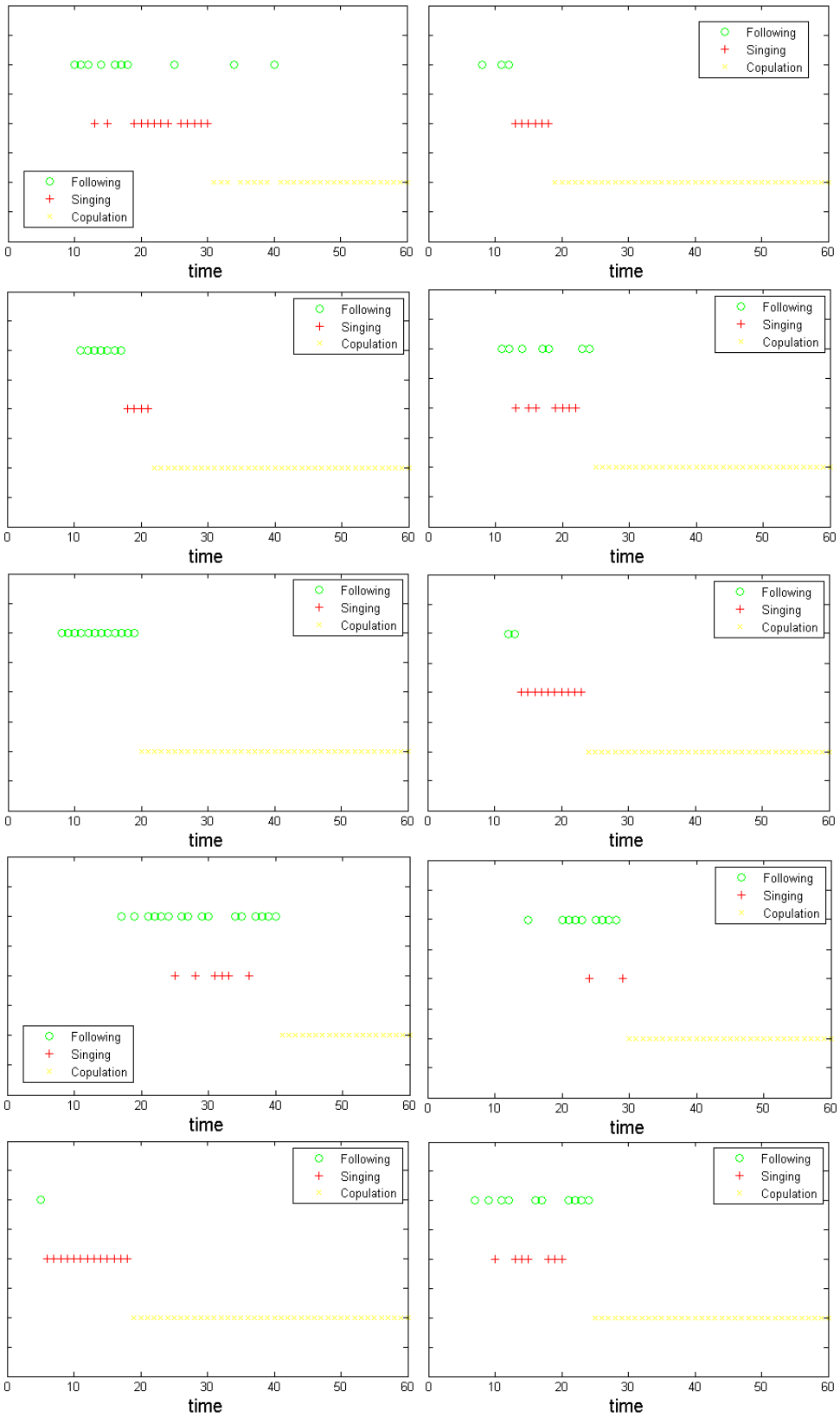

Figure 5.12: Plots of the behavioural patters corresponding to the solutions plotted in Figure 5.11.

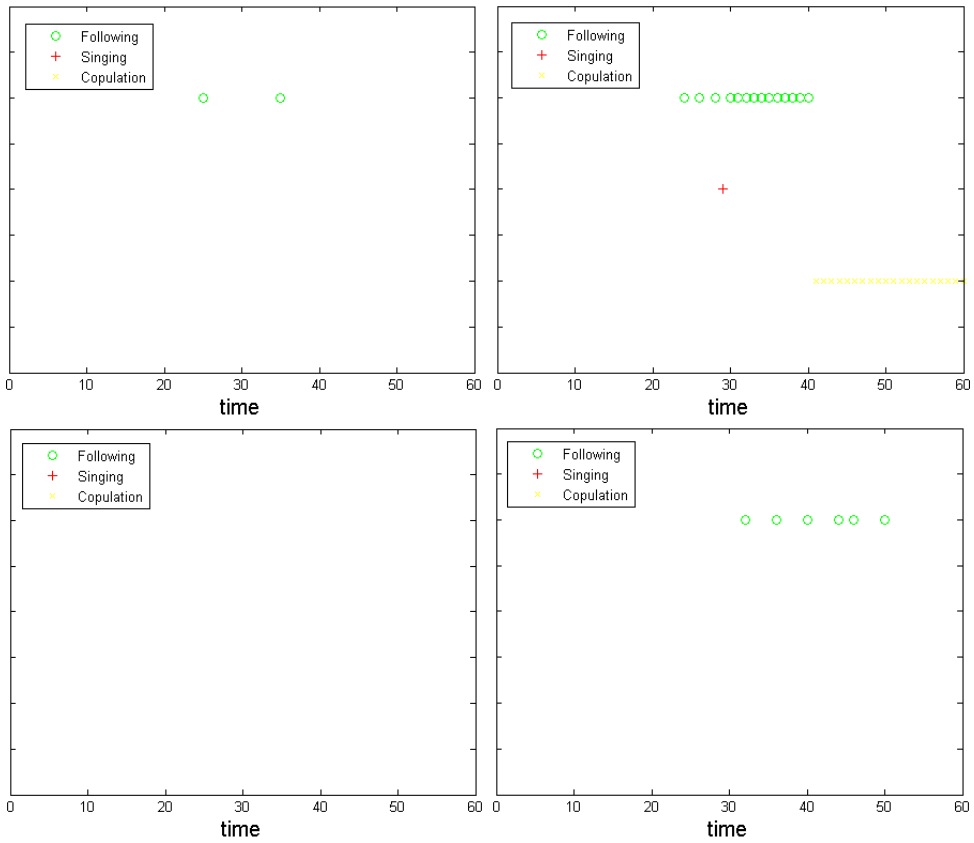

Figure 5.13: Plots of the behavioural patters in the case of a rejective female ($-0.8 \leq I \leq 0.2$). Same set of base parameters as Figure 5.10.

- $n_{cop} = 50$ for $-0.8 \leq I \leq 0.2$ (rejective female);
- $n_{cop} = 18$ for $-0.2 \leq I \leq 0.8$ (receptive female).

These numbers clearly show that the copulation time is affected by the female behaviour: the more receptive a female is, the earlier the male will mate with her.

While it is still too early to decide whether these outputs are "good" or not, these preliminary results suggest that this neural approach might be a good way to study the model. In fact, it produces an output which is comparable with the experimental data, and the general shape of the network is based on widely accepted biological knowledge.

5.3 Future work

The aspect of this model that would most benefit from improvement is the parameter estimation. The neural activation presently considered does not correspond to

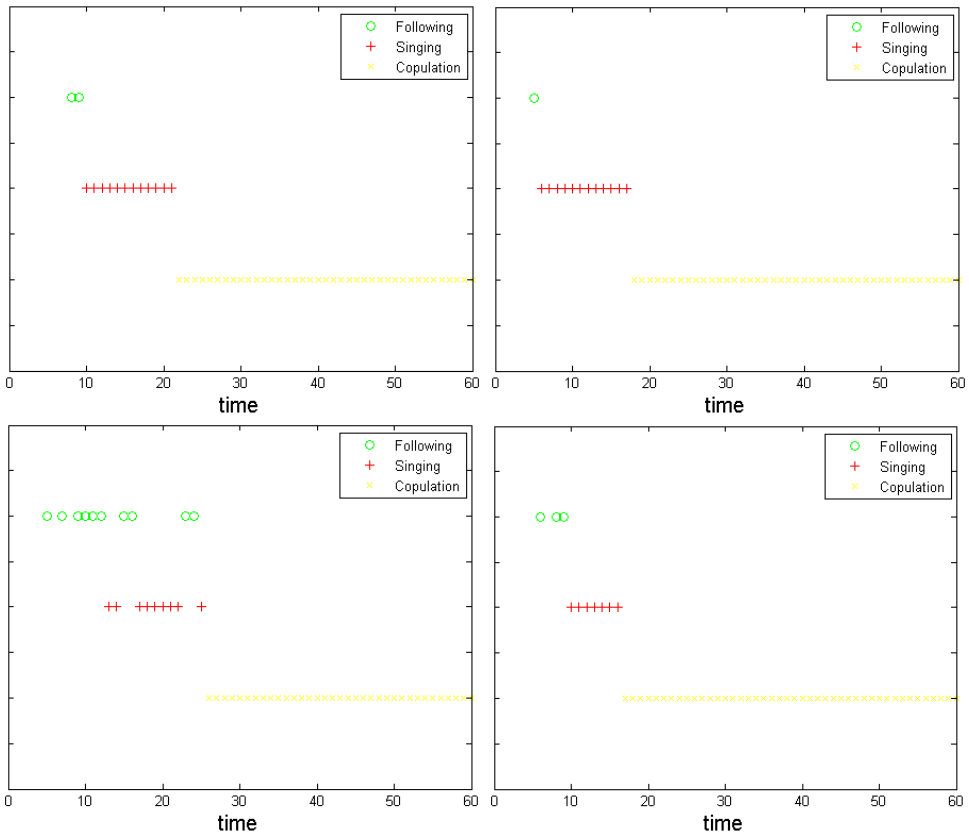

Figure 5.14: Plots of the behavioural patters in the case of a receptive female ($-0.2 \leq I \leq 0.8$). Same set of base parameters as Figure 5.10.

a precisely defined physical quantity, and it seems difficult to practically implement an experiment measuring the weights of connections between clusters. However, the data contained in the ethograms can be used to estimate the weights and the thresholds through an algorithm such as the one described in [145, 253], using quantities such as the CI (percentage of time spent courting) or the mean copulation time for comparison.

Also, one could follow Pasemann's steps and do a steady state analysis of the model, identifying the possible equilibria and their stability; for a deterministic female behaviour (that is, without a random input).

Then, once the model is thought to properly describe the biological dynamics in the case of a healthy fly, this system could be used to speculate about the most relevant connections between neuronal clusters. This would have a big impact in studying the underlying mechanisms of impaired neural activity as that observed in Parkinson's disease, identifying potential targets for therapy development.

Chapter 6

Conclusions

This thesis collects various projects related to modelling biomedical phenomena: they provide a broad slice of problems of interest to the mathematical biology community.

The main research topic has been modelling wound healing-related processes, and in this context two main works have been developed focussing on lymphangiogenesis.

6.1 Results

6.1.1 Wound healing lymphangiogenesis

In Chapter 2 an ODE model is presented which is able to capture the main elements describing lymphangiogenesis in both normal and diabetic tissues. The model's predictions reflect biological observations very well, not only in healthy subjects but also in the diabetic case. The model then offers deep insight into the complex phenomenon of wound healing lymphangiogenesis, identifying the key players in the process and thus the most promising targets for therapy. Several therapeutic approaches are suggested. Another valuable contribution of the work is the detailed parameter estimation reported in the Appendix: great care was put in determining realistic values for the parameters, which is a crucial feature of reliable models and hopefully the effort put in this parameter estimation will serve other models addressing wound healing-related processes.

In Chapter 3 we build upon the work conducted in the previous chapter and propose two PDE models to describe different hypotheses concerning lymphatic vasculature regeneration. Biologists do not agree on a single theory to describe lymphatic network restoration, and mathematical models could potentially give a great insight into the question. Our models account for a variety of scenarios and further biological data would be required to establish which hypothesis better describes the phenomenon under study. The resulting simulations give particularly interesting results about, for instance, the role of lymph/interstitial flow in chemotaxis and (lymph)angiogenesis; this is something very novel in modelling of capillary network formation.

6.1.2 Tumour neoneurogenesis and (direct) tumour-nerve interactions

Chapter 4 includes an ODE model that is a first attempt to mathematically investigate how tumours induce neoneurogenesis and how different nerve types affect tumour growth and metastasis by releasing substances such as neurotrasmitters. The model was mainly inspired by recent works presented in [6, 160], focussing predominantly on prostate cancer.

The model (a system of eight ODEs) gives good qualitative results; in particular, it confirms and explains the following experimental observations:

- nerve density is increased after tumour cell implantation;
- the initial condition for primary tumour cells determines whether the tumour mass develops and potentially creates metastases;
- factors such as nerve growth factor and axon guidance molecules are found at a higher levels around tumours.

We also used the model to explore how stress affects cancer progression. Simulating a stress condition via an increased norepinephrine secretion rate, we found that stress generally enhances tumour proliferation and metastasis. Even more noticeably, an initial condition for tumour cells that would normally evolve to a zero

steady state (that is, a tumour free scenario) can tend to a non-zero equilibrium in a stress situation. Finally, we simulated a possible metastasis-reducing treatment by blocking acetylcholine receptors on tumour cells, with positive results.

Although there is no quantitative match between available data and model output, the system confirms and explains biological and clinical observations.

6.1.3 *Drosophila* courtship behaviour

Chapter 5 constitutes a preliminary study of a possible way to model and quantify *Drosophila* courtship behaviour. The main idea is to link neural activity levels to displayed behaviours, and in our model such neuronal activity is initiated by an external input coming from the female. The model can produce output which is comparable to available behavioural data. Also, the model predicts an earlier copulation time for receptive females than for rejective females.

6.1.4 Remark – parameter estimation

Any parameter estimation is limited by, for example, the specific experimental method used or discrepancies between the system considered and that studied in a given reference. The results should therefore be viewed with care. Indeed, a common observation from all projects is the need for clear, suitable experimental datasets: more consistent parameter values would benefit any model with providing more realistic quantitative results.

6.2 Future work

6.2.1 Angio- and lymphangio-genesis in wound healing

Novel work could include a "parallel" system modelling both blood angiogenesis and lymphangiogenesis after wounding, in order to emphasise and compare the similarities and differences between these two systems.

Also, future work may include a simulation of the diabetic case in the PDE model and determine how different lymphangiogenesis hypotheses would affect treatment

delivery.

6.2.2 Tumour-nerve interactions

Further work should mainly aim to include more variables in the model to better describe the dynamics in the peritumoural environment. For instance, different kinds of AGMs (which are known to have diverse effects on tumour cells) could be included. One could also include the blood and lymphatic vasculatures, whose development seems to be guided by AGM. Finally, one could take into account the immune system, which is regulated by the nervous system and is known to affect tumour progression.

6.2.3 Ecological models for cancer

An emerging concept in cancer biology is the application of ecological concepts. In Chapter 4 we introduced a norepinephrine-dependent Allee threshold, but possibilities of application are many. For instance, the Allee threshold can be influenced by other cell populations, which can interact with tumour cells in many different ways potentially modelled by predation, cooperation or other ecological relationships.

In addition, a tumour is not a homogeneous mass: tumour cells are of different kinds which are believed to be selected by the environment and then potentially form metastasis; also, it seems that more than one genotype can persist in a tumour to allow an overall survival. Peritumoural environment is crucial in tumour cell selection and dissemination, and nerve-released factors may play a fundamental role in this.

6.2.4 Wound healing peripheral nerve regeneration

The knowledge built in Chapter 4 concerning the autonomic nervous system biology could be also usefully transferred to a wound healing setting: one characteristic of diabetes is nerve damage, which can affect several body functions including sensory feeling. Therefore, one could combine the results presented in Chapters 2, 3 and 4 to

mathematically address the problem of peripheral nerve function and regeneration in diabetic wound healing.

6.2.5 Nerve-mediated cell migration

A further area to build upon would be to develop models which investigate how nervous system activity affects (cancer) cell migration. Although the question is of major importance in biology and is well-addresses in this field, no mathematical model has yet been developed in this regard. Being such a new area to explore, modelling nerve-mediated cell migration would offer a variety of directions to follow. For instance, two promising approaches could be to develop:

- *macroscopic models to understand how a certain kind of primary tumour often induces metastases in a specific foreign region of the body.*

  There are reasons to believe that nerves play a key role in determining the fate of tumour cells. Their influence is both indirect (through, for example, perineural invasion; that is, through the spread of tumours along nerve fibres [73]) and direct (neurotransmitters have been found to have a migratory effect on cancer cells [137]). According to a modern version of the well-known "seed and soil" hypothesis, circulating tumour cells are attracted and settle in a specific region of the body because of favourable environmental conditions [80] and factors like chemokines or AGMs seem to provide such a setting [147].

- *intracellular models to investigate how neurotransmitters affect cell functions.*

  Several studies have shown that neurotransmitters influence the migratory activity of cancer cells, possibly through chemotaxis [64]. However, the effects of neurotransmitters on different cell types are various and often inconsistent [193]. It would therefore be useful to develop models describing this complex intracellular signalling to be able to predict what effect a certain neurotransmitter has on a specific tumour cell and why.

6.2.6 *Drosophila* courtship model

Further work will include an analysis of the system and the development of a numerical method to fit experimental data. Then one could apply the model to the Parkinson's case and identify potential targets for therapy.

Appendix A

Lymphangiogenesis ODE model – Appendix

A.1 ODE Parameter estimation

A.1.1 Equilibrium values and standard sizes

TGF-β equilibrium T^{eq}

The equilibrium value of active TGF-β is about 30 pg/mm^3 [283, Figure 2].

Macrophage equilibrium M^{eq}

The macrophage steady state can be estimated from [272, Figure 1], which plots typical macrophage density in the skin. This shows that there is an average of about 15 macrophages per 0.1mm^2 field. Assuming a visual depth of 80 μm, the macrophage density becomes 15 cells/(0.1mm^2 $\times$ 0.08mm) = 1875 cells/mm^3.

VEGF equilibrium V^{eq}

The VEGF equilibrium concentration is estimated to be 0.5 pg/mm^3 from [107, Figure 1] and [196, Figure 2].

Final LEC and Capillary density

In [223] we find that "it was not until *day 60*, when functional and continuous lymphatic capillaries appeared normal" and "at *day 60* the regenerated region had a complete lymphatic vasculature, the morphology of which appeared similar to

that of native vessels". Hence, if we assume that a capillary network that can be considered "final" appears at day 60, we will take C^{fin} (or C^{eq}) to be the number of LECs present at this time, and since in the normal case *all* the lymphatic endothelial cells will become part of the capillary network, we will further assume that $L^{eq} = 0$. In [223, Figure 2E] we see that at that time there are about 80 cells. This value corresponds to a 12 μm thin section. In addition, through [223, Figure 2D] we can calculate the observed wound area, which is about $5.6 \times 10^5\,\mu\text{m}^2$. In this way we get a volume of 0.0067 mm^3 with 80 cells, which corresponds to $C^{fin} = 1.2 \times 10^4$ cells/mm^3.

EC size and weight

[102] reports the cross-sectional area of an EC as $10\mu\text{m} \times 100\,\mu\text{m}$. In [258] the thickness of these cells is given as 0.5μm. Hence we can assume a cell volume of approximately $500\mu\text{m}^3 = 5 \times 10^{-7}$ mm^3. Moreover, if we assume the density of the cells to be 1 g/mL (the same as that of water), we have that a cell weighs about 5×10^{-10} g = 500 pg.

VEGF molecular weight

The molecular weight of VEGF is 40kDa = 66.4×10^{-9} pg/mol [219].

A.1.2 TGF-β equation

Enzyme-mediated activation rate a_p

For a_p, it seems reasonable to take the rate at which LAP binds to the receptors. Now, in [54] we find an estimate for the binding rate to be about 1.7×10^4 $\text{M}^{-1}\text{s}^{-1}$ [54, Tables I and IV]. Considering a protein weight of approximately 50 kDa (found in the same article) and converting the units we find: $a_p \approx 2 \times 10^{-5}$ $\text{mm}^3\text{pg}^{-1}\text{min}^{-1} = 2.9 \times 10^{-2}$ $\text{mm}^3\text{pg}^{-1}\text{day}^{-1}$.

Receptor-mediated activation rate a_M

[188] reports that ("activated") macrophages plated at 2×10^5 cells/well in a 24-well tissue culture dish (that is, about 10^2 cells/mm^3) activated approximately 8% of the total TGF-β secreted after 22 hours. This means that 1 cell/mm^3 activated about

0.087% of TGF-β per day. On the other hand, in [97] we find that macrophages cultured at 1×10^6 cells/dish in 100-mm plates (that is, about 10 cells/mm^3) activated 12.2% of total TGF-β1 after about 36 hours. So 1 cell/mm^3 activated approximately 0.8% of the TGF-β per day. Hence, for a_M we will take a value between 0.087 and 0.8, say the average 0.45.

TGF-β production rate r_1

In [124] it is reported that 10^6 macrophages produced about 30 pg of TGF-β after 24 hours. So one single macrophage produced 30×10^{-6} pg/day of TGF-β, and we can then take $r_1 = 3 \times 10^{-5}$ pg $\cdot$ cells^{-1} $\cdot$ day^{-1}.

TGF-β decay rate d_1

In [120] it is stated that "free TGF-β has a half life of about 2 min". We will therefore take the decay rate d_1 of active TGF-β to be $d_1 = \ln 2/(2 \text{ min}) = 0.35 \text{ min}^{-1} = 500 \text{ day}^{-1}$.

Constant amount of latent TGF-β T_L

At the equilibrium, the TGF-β equation becomes: $[0+a_M M^{eq}]\cdot[T_L+r_1 M^{eq}]-d_1 T^{eq} = 0$. Substituting the values of the parameters a_M, r_1, d_1 and of the equilibrium values T^{eq} and M^{eq} found before, we get an equation for T_L. Solving it, we find $T_L = 18.0916$ pg/mm^3. To compare this value with a "real" one, we consider [189]. Here, taking an average of 6 pg of TGF-β1 per mg of skin (from [189, Figure 3]) and assuming a skin density of 1 g/mL (as for water), we have a concentration of latent TGF-β of 6 pg/mm^3, which is of the same order as our previous estimate.

A.1.3 Macrophage equation

Fraction of monocytes migrating into the wound that differentiate into macrophages α

We follow [271] and take α to be equal to 0.5 in normal wound healing (reflecting the fact that in this case the number of inflammatory macrophages is the same of the repair ones), and $\alpha = 0.8$ in a diabetic wound (since there are more inflammatory than repair macrophages this time). However, it must be noted that [271] comments

that "there is currently no quantitative data on which the value of α for diabetic wounds can be based".

Migration of monocytes to the wound in response to TGF-β: shape of $h_1(T)$ and value of b_2

In [265] the authors study the migration of monocytes taken from healthy volunteers and observe that the motility of the cells depends on the dose of TGF-β to which they are exposed. Moreover, even if the response varied with individual donors, they see that "the optimal chemotactic concentration for TGF-β fell within the range 0.1-1.0 pg/mL". These findings are shown in Figure A.1, which shows the dataset reported in [265]. In light of these observations, it is reasonable to take the chemotactic function $h_1(T)$ to be

$$h_1(T) = \frac{b_1 T^m}{(b_2 + T^{2m})}$$

where we will take $m = 2$ from visual comparison with data.

To determine b_2 we look for the maximum of $h_1(T)$. This is located at the point T_{max} where $h_1'(T_{max}) = 0$, which is $T_{max} = \sqrt[2m]{b_2}$. [283] reports that the normal level of TGF-β in the skin is about 30 pg/mm^3, and that this amount increases up to 300 pg/mm^3 during wound healing. From this, and from the observation that macrophage levels also reach a peak soon after this TGF-β peak [186], we deduce that the maximum monocyte/macrophage migration occurs when the level of TGF-β in the skin is about 300 pg/mm^3. Thus we take $b_2 = 300^{2m}$; for $m = 2$ this gives $b_2 = 300^4 = 8.1 \times 10^9$ pg^4 (mm^{-3})^4. This seems to be in contrast with the data reported in [265, Figure 1]: here T_{max} is around 0.5 pg/mL $= 0.5 \times 10^{-3}$ pg/mm^3. However, this value does not seem realistic and should be considered carefully. In particular, we recall that chemotaxis occurs through *gradients* of a chemical, and considering this directed movement to depend only on the absolute concentration of the chemoattractant is a simplification. In fact, in the experiment described in [265] the diluted chemotactic stimuli were placed in the bottom wells of microchamber plates that were separated from the upper wells by a filter with 5.0 μm pores; then monocytes were put in the plates with human TGF-β diluted

at different concentrations. Chemotactic activity was defined as the mean number of monocytes that migrated through the pores. Therefore, we consider the value of T_{max} to be a "conventional" one and we keep the estimate for b_2 found above.

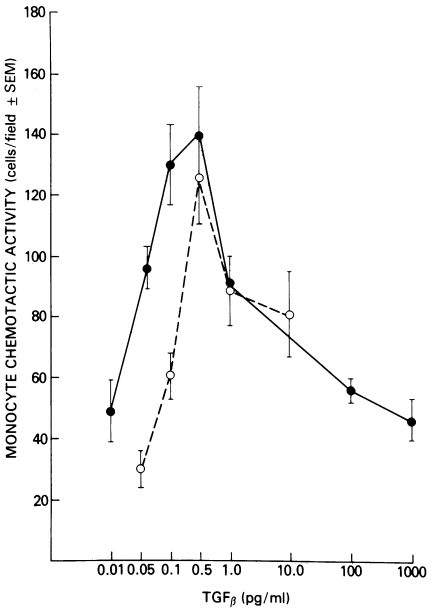

Figure A.1: Experimental data from [265, Figure 1] reporting a quantification of monocyte chemotaxis for different concentrations of TGF-β. Chemotactic activity is defined as the mean number of monocytes that migrated through the 5-μm pores in three standard fields for each of triplicate filters.

Percentage of monocytes/macrophages undergoing mitosis β

In [100, Figure 4] we see that only about 0.5% of monocytes *in vitro* show mitotic activity. Therefore we take $\beta = 0.005$.

Macrophage growth rate r_2 ***and carrying capacity*** k_1

To obtain estimates for these parameters, we first consider just the logistic part of the macrophage equation $dM/dt = r_2 M(1 - M/k_1)$, whose solution is

$$M(t) = \frac{k_1 M_0 e^{r_2 t}}{k_1 + M_0(e^{r_2 t} - 1)} \,. \tag{A.1}$$

In [289] murine macrophage-like cell growth is measured under different conditions. We then fit the data contained in [289, Figure 1] to the curve (A.1) using the MatLab function `nlinfit`. Moreover, [289] specifies that "6×10^6 cells were cultured in 100-mm tissue culture plates in 10 mL of the (above) medium". Then, taking $M_0 = 600$ cells/mm^3, we get the estimates $\widehat{r_2} = 1.22$, $\widehat{k_1} = 6 \times 10^5$, with 95%

confidence intervals $(0.82, 1.62)$ and $(4.40 \times 10^5, 7.61 \times 10^5)$ respectively (these are calculated using the MatLab function `nlparci`).

Macrophage constant removal rate d_2

[44] presents a mathematical model for keloid and hypertrophic scarring. Here we find that macrophages are known to exist in a wound for several days after the initial migration; so based on this we assume a decay rate for macrophage cells to be of the order of $d_2 \approx 0.2$ day^{-1}.

Macrophage capillary-dependent removal rate ρ

We assume that the term ρC becomes of the same order of d_2 when capillaries reach their "final" density, which we have estimated as 1.2×10^4. Since we estimate $d_2 = 0.2$, we take $\rho = 10^{-5}$.

Migration of monocytes to the wound in response to TGF-β: b_1

To find b_1 we notice that this parameter determines the maximum level of macrophages M during healing. To find this value, we refer to [186]. Here the authors investigate the role of TGF-β activation in wound repair, and assess several components of wound healing (including inflammatory cell infiltration) over a period of 28 days. [186] reports that at day 5 a maximum of about 70 macrophages/field (400x) are observed. Assuming a diameter field of view of 0.4 mm and a depth of field of 80 μm, 1 field corresponds to $(0.2)^2\pi$ mm$^2 \times 80 \times 10^{-3}$mm $\approx 10^{-2}$mm^3. Then 70 cells/field $\approx$ 7000 cells/mm^3. Numerical experimentation shows that reproduction of this result requires $b_1 \approx 8 \times 10^8$ cells mm pg^2/day.

Macrophage constant source s_M

At the steady state, the M-equation becomes

$$s_M + \alpha \frac{b_1 T^2}{b_2 + T^4} + \beta r_2 M \left(1 - \frac{M}{k_1}\right) - d_2 M - \rho C M = 0 \, .$$

Substituting the equilibrium values and the parameters found above, we get

$$s_M = 586 - b_1 \times 5.5 \times 10^{-8} \, .$$

Above, we chose $b_1 = 8 \times 10^8$ cells mm pg^2/day. Therefore $s_M = 542$ cells/day.

A.1.4 VEGF equation

VEGF production by macrophages r_3

From [130, Figure 1B] we have that human macrophages plated at 10^6 cells/ml = 10^3 cells/mm^3 produced 214 pg/ml = 214×10^{-3}pg/mm^3 of VEGF after 24 hours of culture. Then $r_3 \approx 8.9 \times 10^{-6}$pg $\cdot$ cells^{-1} $\cdot$ h^{-1} = 2.1×10^{-4} pg $\cdot$ cells^{-1} $\cdot$ day^{-1}. In fact, this value is a bit smaller than the one we use in the model, which we take to be $9 \times 2.1 \times 10^{-4} \approx 1.9 \times 10^{-3}$ pg/cell/day. This "adjustment" is done considering the data shown in [233, Figure 2], which reports that the VEGF peak (occurring at day 5) corresponds to a level of about 1000 pg/mL = 1 pg/mm^3. Since in our model we assume that the VEGF peak is due (mainly) to the macrophages, it seems reasonable to adjust the parameter r_3 to meet this observation.

Other estimates were obtained from [279, 285] and one "equivalent" parameter was found in the modelling paper [156]. Although the numerical values are different, they are all between 10^{-6} and 10^{-4} pg/cell/day. This variety is not surprising because different cell types produce VEGF at different rates (as clearly shown in [285]). Since in the context of wound healing lymphangiogenesis we are mainly concerned with macrophages, we focus more on the values for these cells [130, 279].

VEGF decay rate d_3

The half-life for VEGF$_{165}$ (the most common and biologically active VEGF protein) at room temperature is 90 minutes [131]. It follows that $d_3 = 11$ day^{-1}. To compare this value with those used in other modelling articles, we see that in [208] the VEGF decay rate is taken to be $\mu_v = 0.456$ h^{-1} = 10.9 day^{-1}, while in [286] the VEGF natural decay/neutralisation rate is $\mu_c = 0.65$ h^{-1} = 15.6 day^{-1}.

VEGF consumption/internalisation by ECs γ

In [155] the VEGF internalisation by a cell is described in the way schematised in Figure A.2. In that figure and the following text, V stands for VEGF, R for receptor and VR for the ligand-receptor complex.

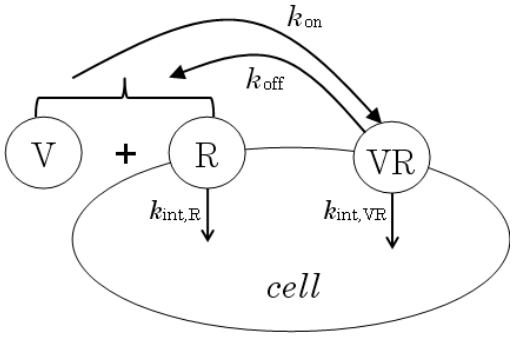

PARAMETER VALUES
$k_{\text{on},V,R1} = 3.8 \times 10^6 \text{M}^{-1}\text{s}^{-1}$
$k_{\text{on},V,R2} = 1.2 \times 10^6 \text{M}^{-1}\text{s}^{-1}$
$k_{\text{off},V,R1} = 95 \times 10^{-6}\text{s}^{-1}$
$k_{\text{off},V,R2} = 410 \times 10^{-6}\text{s}^{-1}$
$k_{\text{int},R1} = k_{\text{int},R2} = 1 \times 10^{-5}\text{s}^{-1}$
$k_{\text{int},VR1} = k_{\text{int},VR2} = 28 \times 10^{-5}\text{s}^{-1}$

Figure A.2: A schematic representation of the dynamics considered in [155]. V stands for VEGF, R for Receptor and VR for the ligand-receptor complex.

We will not distinguish between the two kinds of receptors $R1$ and $R2$, so we will just take the average of the above parameters. That is, we will take

$$\begin{aligned} k_{\text{on}} &= 2.5 \times 10^6 \text{M}^{-1}\text{s}^{-1}, & k_{\text{off}} &= 2.5 \times 10^{-4}\text{s}^{-1}, \\ k_{\text{int},R} &= 10^{-5}\text{s}^{-1}, & k_{\text{int},VR} &= 2.8 \times 10^{-4}\text{s}^{-1}. \end{aligned} \tag{A.2}$$

According to this reaction scheme, the corresponding equation for V (for a single cell) is

$$\frac{dV}{dt} = -k_{\text{on}} \cdot V \cdot R + k_{\text{off}} \cdot (VR) \ . \tag{A.3}$$

Here the dimensions of R are moles per unit volume. Similarly the equation for the ligand-receptor complex (VR) (per cell) is

$$\frac{d(VR)}{dt} = +k_{\text{on}} \cdot V \cdot R - k_{\text{off}} \cdot (VR) - k_{\text{int},VR} \cdot (VR) \ .$$

So, at equilibrium:

$$\begin{aligned} k_{\text{on}} \cdot V \cdot R - k_{\text{off}} \cdot (VR)_{eq} - k_{\text{int},VR} \cdot (VR)_{eq} = 0 \\ \Rightarrow \quad (VR)_{eq} = \frac{k_{\text{on}} \cdot R}{k_{\text{off}} + k_{\text{int},VR}} \cdot V \quad . \end{aligned} \tag{A.4}$$

To determine the value of R, we note that human endothelial cells (cultured *in vitro*) display 1,800 VEGFR1/cell and 5,800 VEGFR2/cell [111], giving a total of 7.6×10^3 receptors/cell. Assuming a cell volume of 500 μm^3 we take $R = 2.5 \times 10^{-14}$ mol/mm^3. Substituting this value for R and replacing the parameters with the values given in (A.2), the equation (A.4) gives $(VR)_{eq} \approx 118 \cdot V = \widehat{VR}_{eq} \cdot V$. Substituting this value

for (VR) in (A.3) we have

$$\frac{dV}{dt} = -\underbrace{\left(k_{\text{on}} \cdot R - k_{\text{off}} \cdot \widehat{VR}_{eq}\right)}_{=2.9\times10^3 \text{ day}^{-1}} \cdot V \cdot L$$

Then, again assuming a cell volume of $500\mu\text{m}^3$, we have that our parameter (per cell) is $\gamma = 5 \times 10^{-7}$ mm$^3 \times 2.9 \times 10^3$ day^{-1}cells$^{-1} = 1.4 \times 10^{-3}$ mm$^3 \cdot$day$^{-1} \cdot$cells^{-1}.

VEGF constant source s_V

At equilibrium, the V-equation becomes

$$s_V + r_3 M - d_3 V - \gamma V L = 0$$

Substituting the equilibrium values and the parameters gives $s_V = 1.9$ cells/day.

VEGF supply in [287]

In [287] control medium with or without growth factors was injected into wounded mice at a dose of 2 μg/wound/10 days. Since the experimental wounds are full-thickness with a 5-mm diameter, and assuming a skin thickness of 0.56 mm [103], this amount corresponds approximately to 1.8×10^4 pg/mm^3/day. Now, since the experiment is performed *in vivo*, it is reasonable to assume that the vast majority of the VEGF is washed away and dispersed by body fluids. In the absence of quantitative data, we assume that only 1% of the added VEGF is therapeutically active in the wound, giving a delivery of 1.8×10^2 pg/mm^3/day.

A.1.5 LECs equation

We consider first the parameter c_1, then k_2, and then the remaining parameters. For c_1 and k_2 we focus on the "logistic" part of the equation

$$\frac{dL}{dt} = c_1 L - \frac{L^2}{k_2} = c_1 L \left(1 - \frac{L}{c_1 k_2}\right) . \tag{A.5}$$

Recalling that the volume of an EC is approximately 500 μm^3, closely packed cells have a density of 1 cell/500μm^3 $= 2 \times 10^6$cells/mm^3. We assume the carrying

capacity to be 10% of this, so that $c_1 k_2 \approx 2 \times 10^5 \text{cells/mm}^3$. In the following, we will fit experimental data to the solution of (A.5), which is

$$L(t) = \frac{c_1 k_2 L_0 e^{c_1 t}}{c_1 k_2 + L_0 (e^{c_1 t} - 1)} \, . \tag{A.6}$$

"Normal" proliferation rate c_1

In [183] the different responses of lymphatic, venous and arterial endothelial cells to angiopoietins is studied; note that the cells were isolated and cultured from bovine mesenteric vessels. [183, Figure 4B] shows the evolution of LEC density in time. After converting these data (in particular, those corresponding to control, or 10% FBS) into cells/mm^3, we can fit the function (A.6) to them, obtaining the estimate $\widehat{c_1} = 0.42 \text{ day}^{-1}$ with 95% confidence interval $(0.15, 0.70)$. Again, we can compare this value with other estimates obtained from different biological sources, such as [178, 256, 275]; also, a similar parameter is estimated in [286]. Although the numerical values for c_1 found in these other references are all different, it is noticeable that they are all around 10^{-1}. This make us very confident in estimating this parameter.

Maximum density of cells (per unit time) k_2

In the previous section we found different possible values for c_1. Since $c_1 k_2 = 2 \times 10^5 \text{cells/mm}^3$, we can easily obtain k_2:

- From [183] we get $k_2 \approx 4.71 \times 10^5 \text{ cells} \cdot \text{day/mm}^3$ (this is the value used in our model);
- From [178] we get $k_2 \approx 4.77 \times 10^5 \text{ cells} \cdot \text{day/mm}^3$ for bovine cornea and $k_2 \approx 5.43 \times 10^5 \text{ cells} \cdot \text{day/mm}^3$ for bovine fetal heart;
- From [256] we get $k_2 \approx 3.13 \times 10^5 \text{ cells} \cdot \text{day/mm}^3$;
- From [275] we get $k_2 \approx 4.48 \times 10^5 \text{ cells} \cdot \text{day/mm}^3$ for 10% FBS and $k_2 \approx 18.52 \times 10^5 \text{ cells} \cdot \text{day/mm}^3$ for 2% FBS.

VEGF-dependence of LECs growth c_2, c_3

To estimate c_2 and c_3, we consider only the exponential VEGF-dependent part of

the LEC equation, that is

$$\frac{dL}{dt} = \left(c_1 + \frac{V}{c_2 + c_3 V} \right) \cdot L \, , \tag{A.7}$$

whose solution is

$$L(t) = L_0 \cdot \exp \left[\left(c_1 + \frac{V}{c_2 + c_3 V} \right) \cdot t \right] \, . \tag{A.8}$$

Recall that we already have an estimate for c_1. Also, notice that, if time is fixed, (A.8) can be seen as a function of V only.

[275, Figure 7A] shows the response of rat mesenteric LECs to VEGF-A and VEGF-C at low serum conditions (2% FBS). The cells were seeded at the density of 16,000 per well in 24-well plates. Then, VEGF_{165} and mature VEGF-C (2-100 ng/mL) were added 4 hours after seeding. Finally, cells were counted 72 hours later. This provides a set of data giving the cell densities for different concentrations of VEGF-A and C. These data refer to time $t = 72$ hours $= 3$ days, and our approach is to fit the function (A.8) as a function of V (with t fixed at 3 days) to the experimental data. Recalling that 1 ng/mL = 1 pg/mm^3, and considering a standard well of 1 mL = 10^3mm^3 (for a 24-well cell culture plate), we can convert these data into suitable units and use the MatLab function `nlinfit` to fit (A.8) to them. This gives $\widehat{c_2} = 42$ days and $\widehat{c_3} = 4.1$ pg/day/mm^3, with 95% confidence intervals $(-7.7, 92)$ and $(2.9, 5.3)$ respectively.

TGFβ-dependence of LECs growth c_4

We estimate c_4 using experimental data obtained in the absence of VEGF. Therefore we consider only the part of the LEC equation concerning TGF-β regulation of cell growth:

$$\frac{dL}{dt} = \left(\frac{c_1}{1 + c_4 T} \right) L \tag{A.9}$$

whose solution is

$$L(t) = L_0 \cdot \exp \left[\left(\frac{c_1}{1 + c_4 T} \right) \cdot t \right] \, . \tag{A.10}$$

In [178] the inhibitory action of TGF-β on bovine endothelial cells is studied. [178,

Figures 1(a) and 1(b)] demonstrate the growth in time of bovine cornea and fetal heart endothelial cells respectively, while [178, Figure 1(c)] shows the inhibition on cell growth by TGF-β. We can thus use these figures in different ways:

- In [178, Figures 1(a) and 1(b)] the amount of TGF-β is fixed, so we can consider (A.10) as a function of t only. Recalling that previously we found the value $c_1 = 0.42$ day^{-1} for [178, Figure 1(a)], and $c_1 = 0.37$ day^{-1} for [178, Figure 1(b)], we can fit the function (A.10) to the data corresponding to $T = 2$ ng/mL $= 2$ pg/mm^3 to find the parameter c_4. The MatLab functions `nlinfit` and `nlparci` give us the estimate $\widehat{c_4} = 0.16$ and its 95% confidence interval $(-0.25, 0.58)$ for cornea ECs, and $\widehat{c_4} = 0.22$ with 95% confidence $(-0.50, 0.95)$ for fetal heart ECs.

- Another strategy is to use the data contained in [178, Figure 1(c)], fixing the time ($t = 4$ days) and considering (A.10) as a function of T only. For bovine cornea ECs, in this case we have $\widehat{c_4} = 0.32$ with 95% confidence interval $(0.12, 0.51)$. Similarly the data for fetal heart ECs gives $\widehat{c_4} = 1.3$ with 95% confidence interval $(-0.66, 3.2)$.

Looking at the confidence interval for each of the estimates found above, we argue that the most "reliable" values for c_4 are the first three: $\widehat{c_4} = 0.16$, $\widehat{c_4} = 0.22$ and $\widehat{c_4} = 0.32$. Hence, in our model we chose to take the average of these numbers, that is $\widehat{c_4} = 0.24$ mm^3/pg.

To compare this number with a similar estimate found in another source, we consider [242, Figure 1], which also shows how cell growth is influenced by TGF-β. Here bovine retinal and aortic endothelial cells were plated at 25 cells/cm^2 and TGFβ-1 was added at different proliferation stages. Cell numbers were determined 5 days after the addition of different concentrations of TGFβ-1. Considering the data in [242, Figure 1B] and assuming a dish of 10mm height, we can fit the function (A.10) to the data with the MatLab function `nlinfit`, taking $L_0 \approx 10$ cells/mm^3 (estimated from [242, Figure 1A]) and consequently $c_1 = (1/t)\ln(L(t)/L_0) = 0.37$ day^{-1}, since $t = 5$ days. This gives the estimate $\widehat{c_4} = 6$ with 95% confidence interval $(-2.5, 14)$.

Threshold levels L^*,C^*

In [223] it is observed that in a wound space LECs begin to organise in a network-fashion after about 25 days. Hence, we take L^* to be the number of LECs present at day 25 during normal repair. In [223, Figure 2E] we see that at that time there are about 80 cells. This value corresponds to a section of width 12 μm. In addition, through [223, Figure 2D], we can calculate the observed wound area, which results to be $5.6 \times 10^5\,\mu\text{m}^2$. In this way we get a volume of 0.0067 mm^3 which contains 80 cells, which corresponds to 1.2×10^4 cells/mm^3. We take L^* to be 10^4 cells/mm^3.

For C^*, we assume that LECs stop coming into the wound when capillaries reach a level which is not far from the final one, that we have estimated to be $C^{fin} = 1.2 \times 10^4$ cells/mm^3. Therefore we take $C^* = 10^4$ cells/mm^3. Note that our estimate for L^* and C^{fin} are the same because in [223, Figure 2E] it happens that the cell numbers counted at day 25 and at day 60 are about the same.

A.2 Calculation of the steady states

For T we have immediately

$$T^{eq} = \frac{a_M}{d_1}(T_L + r_1 M^{eq})M^{eq}\,, \tag{A.11}$$

since the exponential tends to zero as $t \to \infty$. It follows that there is one T-steady state for every M-steady state.

For M the situation is more complicated. Writing down the equation (2.2) at the equilibrium and rearranging the terms one finds

$$-\beta\frac{r_2}{k_1}M^2 + (\beta r_2 - d_2 - \rho C)M + s_M + \alpha\frac{b_1 T^2}{b_2 + T^4} = 0\,. \tag{A.12}$$

Plugging in the expression for T found in (A.11), the equation (A.12) becomes a polynomial in M of degree 10. Plotting this polynomial for $M \in [0, 10^4]$ and $M \in [0, 10^7]$ gives the graphs shown in Figure A.3. The graphs are strongly indicative that there is only one stable steady state for (at least) $M < 10^7$ and this is around

2000. This finding is in agreement with the estimate $M^{eq} = 1875$ cells/mm^3 from the biological literature.

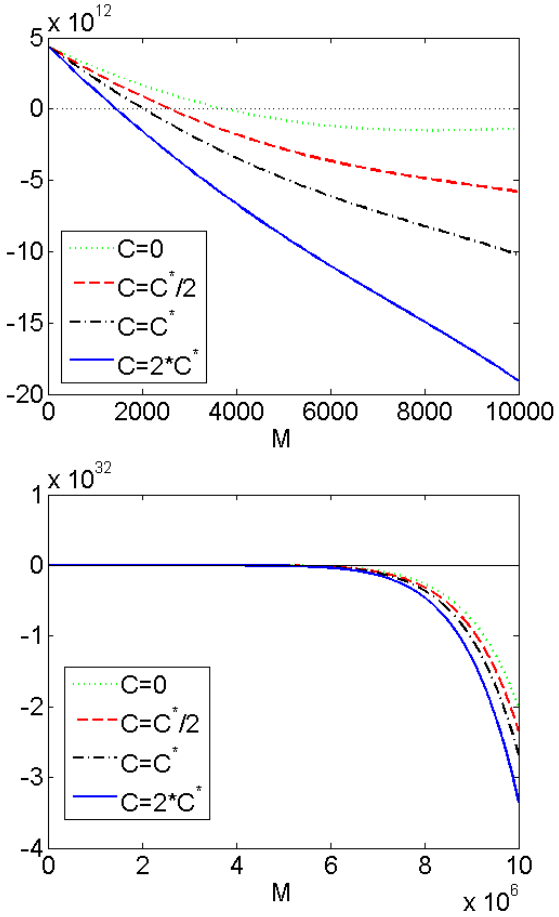

Figure A.3: Plots of the M-expresson at the equilibrium. The different lines refer to different representative values of C.

The equilibrium equation for V is

$$s_V + r_3 M - d_3 V - \gamma V L = 0 \quad \Rightarrow \quad V^{eq} = \frac{s_V + r_3 M^{eq}}{d_3 + \gamma L^{eq}} \,. \tag{A.13}$$

So there is one V-equilibrium for every M, L equilibrium.

At this point, it is more convenient to look at the capillary equation first, and afterwards consider the LEC one. There are two different cases to consider in the C-equation:

- if $L + C < L^*$, then $\sigma = 0$ and $dC/dt = 0$ always;
- if $L + C \geq L^*$, then $\sigma = 1$ and the equilibrium equation becomes

$$(\delta_1 + \delta_2 V)L = 0 \,,$$

whose only solution is $L = 0$ (since V cannot be negative).

Coming to the L-equation, it is necessary to consider a number of different cases, since there are two piecewise-defined functions involved:

CASE	CONDITIONS	FNs VALUE
I	$L + C \geq L^*$ and $C \leq C^*$	$\sigma(L, C) = 1$ and $f(C) = 1 - C/C^*$
II	$L + C \geq L^*$ and $C \geq C^*$	$\sigma(L, C) = 1$ and $f(C) = 0$
III	$L + C < L^*$ and $C \leq C^*$	$\sigma(L, C) = 0$ and $f(C) = 1 - C/C^*$
IV	$L + C < L^*$ and $C \geq C^*$	$\sigma(L, C) = 0$ and $f(C) = 0$

Note that case IV seems to be *not realistic*, since the estimates for the thresholds are $L^* \approx C^*$.

CASE I Since we must have $L = 0$ in order to have a steady state in the C-equation, the equilibrium L-equation reduces to

$$\left(s_L + \frac{b_3 V^2}{b_4 + V^4}\right)\left(1 - \frac{C}{C^*}\right) = 0 \,,$$

which implies

$$C^{eq} = C^* \,.$$

CASE II Again, we must have $L = 0$ for the equilibrium in the fifth equation. This time the steady state L-equation is automatically satisfied and therefore any value of C corresponds to a steady state.

CASE III In this case, rearranging the fourth equation for L one gets

$$\begin{aligned} -\frac{1}{k_2}L^2 + \left[\left(c_1 + \frac{V}{c_2 + c_3 V}\right)\left(\frac{1}{1 + c_4 T}\right) - \frac{M + C}{k_2}\right] L \\ + \left(s_L + \frac{b_3 V^2}{b_4 + V^4}\right)\left(1 - \frac{C}{C^*}\right) = 0 \end{aligned} \tag{A.14}$$

where V depends on L and this dependence is given by the expression (A.13). Notice that if $\gamma = 0$ then V does not depend on L. Hence, if we set $\gamma = 0$ the expression (A.14) becomes a simple quadratic equation for L. In order to study how the system changes as V depends on L, we gradually increase γ and see

how the roots change. The function (A.14) is therefore plotted numerically versus L and the resulting graphs are reported in Figure A.4. These show that increasing γ does not have a significant effect on the roots of (A.14): the function is always concave for $0 \leq L \leq 4 \times 10^5$ and intercepts the horizontal axis once. Thus for $C < C^*$ (which is the case we are studying) there is only one intersection for $L > 0$ at about $L = 2 \times 10^5$.

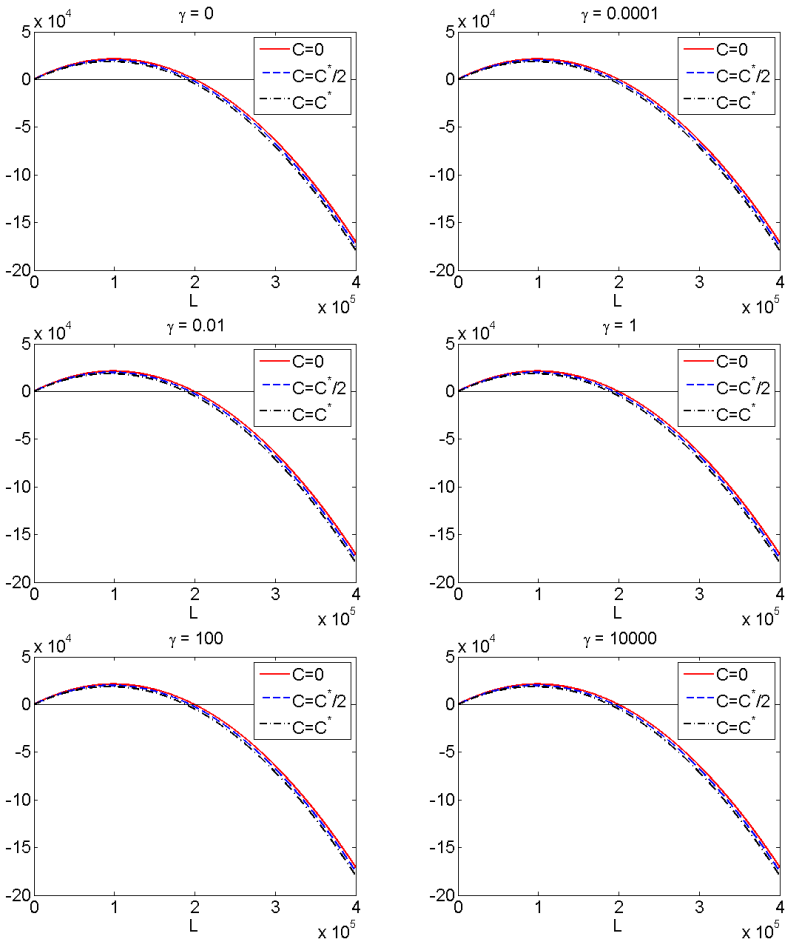

Figure A.4: Plots of the expression (A.14) as a function of L for different values of γ (more precisely, $\gamma = 0, 10^{-4}, 10^{-2}, 1, 10^2, 10^4$). In each picture the function is plotted for three different representative values of C, in particular 0, $C^*/2$ and C^*.

Appendix B

Lymphangiogenesis PDE model – Parameter estimation

B.1 Sizes, weights, equilibria and velocities

B.1.1 Domain size

We consider a full-thickness wound of 5-mm length, inspired by [287]. For the surrounding skin, we consider a (small) variable width ε (from 1 to 3 mm). Thus, we have a domain of length $\ell = 5\text{mm} + 2\varepsilon$.

B.1.2 Macrophage volume

A human alveolar macrophage has a volume $V_{M\Phi}$ of approximately $5000\mu\text{m}^3 = 5 \times 10^{-6}\text{mm}^3$ [134].

B.1.3 Molecular weights

We take TGF-β molecular weight to be approximately 25 kDa [22, 266, active/mature isoform] and VEGF one to be 38 kDa [122, 282, VEGF-165].

B.1.4 TGF-β equilibrium T^{eq}

The equilibrium value of active TGF-β is about 30 pg/mm^3 [283, Figure 2].

B.1.5 Macrophage equilibrium M^{eq}

The macrophage steady state can be estimated from [272, Figure 1], which plots typical macrophage density in the skin. This shows that there is an average of about 15 macrophages per 0.1mm^2 field. Assuming a visual depth of 80 μm, the macrophage density becomes 15 cells/(0.1mm^2 $\times$ 0.08mm) = 1875 cells/mm^3.

B.1.6 VEGF equilibrium V^{eq}

The VEGF equilibrium concentration is estimated to be 0.5 pg/mm^3 from [107, Figure 1] and [196, Figure 2].

B.1.7 Normal capillary density C^{eq}

In [223] we find that "it was not until *day 60*, when functional and continuous lymphatic capillaries appeared normal" and "at *day 60* the regenerated region had a complete lymphatic vasculature, the morphology of which appeared similar to that of native vessels". Hence, if we assume that a capillary network that can be considered "final" appears at day 60, we will take C^{eq} to be the number of LECs present at this time. In [223, Figure 2E] we see that at that time there are about 80 cells. This value corresponds to a 12 μm thin section. In addition, through [223, Figure 2D] we can calculate the observed wound area, which is about $5.6 \times 10^5\,\mu$m^2. In this way we get a volume of 0.0067 mm^3 with 80 cells, which corresponds to $C^{eq} = 1.2 \times 10^4$ cells/mm^3.

B.1.8 Maximum capillary density C_{max}

First of all, we want to convert 1 capillary section into a cell number. For this purpose, we consider EC cross-sectional dimensions reported in [102] as $10\,\mu$m $\times$ $100\,\mu$m. We then assume that LECs lie "longitudinally" along the capillaries, and therefore only the short dimension contributes to cover or "wrap" the circumference of the capillary. Considering a capillary diameter of 55 μm as in [82], we have that each lymphatic capillary section is made of approximately 20 LECs (taking into

account some overlapping).

Then, from [258] we know that EC thickness is approximately 0.5 μm. Thus a capillary section is a circle of about $55 + 2 \times 0.5\,\mu$m diameter, corresponding, as described above, to 20 cells.

If we imagine stacking 1 mm^3 with capillaries of this size, we see that we can pile on 1 mm/56 μm $\approx$ 18 layers of capillaries. Then, considering an EC length of 100 μm as in [102], we have that 1 mm^3 fits at most a number of capillaries equivalent to the following amount of ECs:

$$20 \text{ cells } \times 18 \times 18 \times \frac{1 \text{ mm}}{100\,\mu\text{m}} \approx 6.4 \times 10^4 \text{ cells } = C_{max} \, .$$

B.1.9 Lymph velocity

The abstract of [82] suggests that the high lymph flow value (0.51mm/s) is due to high pressure following die injection. This suggests that a lower value (9.7 microns/s) might be considered as typical, in agreement with [83]. In both papers the normal lymph velocity seems to be around 10 microns/sec.

We thus assume lymph velocity to be v_{lymph} = 10 micron/sec = 864 mm/day (from [82, 83]).

B.1.10 Interstitial flow velocity

First of all, we note that in [222] interstitial flow in the skin is calculated to be around 10 microns/sec. (Less important for the parameters, but related to our work is [104], where the synergy between interstitial flow and VEGF gradient is discussed.) Therefore, we will consider the interstitial flow to be also $v_{IF} = 10$ microns/sec = 864 mm/day (from [222]).

B.2 Re-calculation of s_M and k_1

s_M here is calculated in the same way as in [17], but using the equations presented here (in [17] it was 5.42×10^2).

For k_1, we point out that in Chapter 2 this parameter was appearing in the logistic part of the M-equation: $^{dM}/_{dt} = r_2 M - {}^{r_2}/_{k_1} \cdot M^2$. In the PDE systems we do not include such term because only a minor fraction of macrophages undergo mitosis [100]. However, death due to overcrowding is present in both models; comparing these terms, we see that our *new* k_1 corresponds to the "old" k_1/r_2.

B.3 Diffusion coefficients

B.3.1 VEGF diffusion coefficient D_V

In [174] the authors observe that "in general, the diffusion coefficient of protein molecules in liquid is of the order of $10^6\,\mu\text{m}^2/\text{h} = 24\,\text{mm}^2/\text{day}$. This intuitively means that a molecule moves 10 μm/sec. To generate a gradient over the order of 100 μm, the timescale of protein decay should be around 10 seconds. In this specific case the protein decay time is about 1-10 hours. Therefore, the observed diffusion coefficient is too large and we need some mechanism to slow down the diffusion."

In [174] VEGF diffusion coefficient is estimated in three different ways: by a theoretical model (0.24 mm^2/day), and by two different measuring techniques (24 mm^2/day). The authors then suggest a diffusion coefficient of the order of $10^6\,\mu\text{m}^2/\text{h} = 24$ mm^2/day. However, they also used the same technique to determine

the diffusion coefficient at the cell surface; this time the diffusion coefficient is estimated to be approximately $10^4\,\mu\text{m}^2/\text{h} = 0.24\,\text{mm}^2/\text{day}$. Keeping in mind all these considerations, for the model we take the intermediate value $D_V = 2.4\,\text{mm}^2/\text{day}$.

B.3.2 TGF-β diffusion coefficient D_T

In [140] the authors estimate a TGF-β diffusion coefficient of 0.36 mm^2/h = 8.64 mm^2/day from [25, 96]. In [179] the authors estimate a TGF-β diffusion coefficient of 2.54 mm^2/day using the Stokes-Einstein Formula.

Given these two mathematical-modelling references, we check their consistency with the estimate for D_V above. These calculations use the Stokes-Einstein equation, which assume spherical particles of radius r to have diffusion coefficient $D \sim 1/r$; since the molecular weight w of a particle proportional to its volume, we have that $D \sim 1/\sqrt[3]{w}$ and we get$D_T \approx 2.76$.

B.3.3 Macrophage random motility μ_M

In[78] we find "Population random motility was characterized by the random motility coefficient, μ, which was mathematically equivalent to a diffusion coefficient. μ varied little over a range of C5a [a protein] concentrations with a minimum of $0.86\times10^{-8}\text{cm}^2/\text{sec}$ in 1×10^{-7} M C5a to a maximum of $1.9\times10^{-8}\text{cm}^2/\text{sec}$ in 1×10^{-11} M C5a". We thus take the average value $\mu_M = 1.38\times10^{-8}\text{cm}^2/\text{s} \approx 0.12\ \text{mm}^2/\text{day}$.

B.4 Advection parameters λ_1 and λ_2

We will take λ_2^{chem} to be equal to v_{IF} calculated in B.1; thus $\lambda_2^{chem} = 864$ mm/day.

For λ_1^{chem} it is more complicated, but we would say that if C_{op} reaches the maximum possible value C_{max} calculated in B.1.8, then $\lambda_1^{chem}\cdot C_{op} = v_{lymph}$ calculated in B.1 (i.e. if the skin is "packed" with open capillaries, then the resulting flow will be the same as the usual lymph flow in the skin lymphatics). Hence $\lambda_1^{chem} = v_{lymph}/C_{max} = 0.0135\ \text{mm day}^{-1}\text{cell}^{-1}$.

For cells we assume smaller values due the higher friction that cells encounter in

the tissue. We will consider: $\lambda_1^{cell} = 1/10 \cdot \lambda_1^{chem}$ and $\lambda_2^{cell} = 1/10 \cdot \lambda_2^{chem}$.

B.5 Rate at which TGF-β is internalised by macrophages γ_1

At equilibrium, $C = C^{eq}$ and thus $p(C) = 0$. Therefore, the equation for T at equilibrium becomes

$$a_M M^{eq}(T_L + r_1 M^{eq}) - d_1 T^{eq} - \gamma_1 T^{eq} M^{eq} = 0 \,,$$

which leads to

$$\gamma_1 = \frac{a_M M^{eq}(T_L + r_1 M^{eq}) - d_1 T^{eq}}{T^{eq} M^{eq}} \approx 0.0042 \, \frac{\text{mm}^3}{\text{cells} \cdot \text{day}} \,.$$

B.6 Chemotaxis parameters

B.6.1 Macrophage chemotactic sensitivity towards TGF-β χ_1

In [143, Table 1] the chemotaxis coefficients of neutrophils for different gradients of interleukin-8 are listed (ranging from 0.6×10^{-7} to 12×10^{-7} $\text{mm}^2 \cdot \text{mL} \cdot \text{ng}^{-1} \cdot \text{s}^{-1}$). We take the intermediate value $\chi_1 = 5 \times 10^{-7} \text{mm}^2 \text{mL ng}^{-1} \text{s}^{-1} \approx 4 \times 10^{-2} \text{mm}^2 (\text{pg/mm}^3)^{-1} \text{day}^{-1}$. To compare this value with one from another source, we consider [255, Figure 8]: although the chemotaxis coefficient is shown to depend on the attractant concentration, taking the average value these give $\chi = 150 \text{ cm}^2 \text{sec}^{-1} \text{M}^{-1} \approx 5.18 \times 10^{-2} \text{mm}^2 (\text{pg/mm}^3)^{-1} \text{day}^{-1}$ (considering the TGF-β molecular weight found in B.1.3). This result is encouraging because it is of the same order of magnitude of the previous estimate.

B.6.2 LEC chemotactic sensitivity towards VEGF χ_2

In [10] a quantification is made of the effects of FGF2 and VEGF165 on HUVEC and HUAEC chemotaxis. In [10, Figure 6A] it is reported that the total distance migrated per HUVEC in response to a 50 ng/mL gradient of VEGFA165 was about 150 μm. Considering that the analysed area of the cell migration chamber was 800 μm long and that the experiment lasted 200 minutes, we can estimate the endothelial cell velocity to be $150/200 = 0.75$ μm/min $= 1.08$ mm/day and the VEGF gradient to be 50 ng/mL / 800 μm $= 62.50$ (pg/mm^3)/mm. Now, the flux $\mathcal{J}$ in our equation is given by $\mathcal{J} = \chi_2 L \frac{\partial V}{\partial x}$; however, $\mathcal{J}$ can also be seen as the product of the mass density and the velocity of the flowing mass [62]. Therefore, with L being our mass density, we have

$$\text{cell velocity} = \chi_2 \frac{\partial V}{\partial x}$$

and then we can use the previous calculations to estimate

$$\chi_2 = \frac{\text{cell velocity}}{\text{VEGF gradient}} = \frac{1.08\text{mm/day}}{62.50(\text{pg/mm}^3)/\text{mm}} = 0.0173 \, \frac{\text{mm}^2}{\text{day}} \frac{\text{mm}^3}{\text{pg}} \, .$$

In order to have realistic cell movement dynamics, χ_2 is taken to be 10 times bigger. This can be justified by the fact that the aforementioned data refer to HUVECs, and LECs might be faster than these cell types. A more suitable dataset for this parameter would be very useful to better inform this estimate, but it was not found by the authors. Also, chemical gradients created *in vitro* are usually different between those observed *in vivo* and they are known to highly affect cell velocity.

B.6.3 Density-dependence of the macrophage chemotactic sensitivity ω

Consider the cell density-dependent macrophage velocity (factor) $1/(1+\omega M)$. This velocity is maximal when M is close to zero and we assume that it is halved when M reaches its carrying capacity k_1^{old} (that is, the parameter k_1 in Chapter 2. We therefore take ω to be the inverse of the macrophage carrying capacity k_1^{old}.

B.7 Macrophage inflow ϕ_1

We expect ϕ_1 to be proportional to the lymph flow (estimated in B.1 as $v_{lymph} = 864$ mm day^{-1}) and macrophage presence in the lymph.

In the same source [82] used to estimate v_{lymph} it is reported that the mean capillary diameter is 55 μm. Thus about 2.05 mm^3 of lymph pass through a capillary bi-dimensional section in 1 day.

In [29] we find that a mouse leukocyte count in the blood is approximately 3 to 8×10^6 cells/mL, and that of these about 2×10^6 are macrophages coming from the lymph nodes; so we have a macrophage density of 2×10^3 cells/mm^3 in the lymph. Therefore, each day about 2.05 mm^3 $\times$ 2×10^3 cells/mm^3 $= 4.11 \times 10^3$ macrophages pass in one capillary. Converting capillaries into cell density as done in B.1.8, we have an influx equal to $\frac{4.11}{20} \times 10^3 \text{day}^{-1} = 0.205 \times 10^3 \text{day}^{-1}$. However, the macrophage density reported in [29] refers to blood; we assume that this quantity in lymph (especially during inflammation) will be about 10 times bigger. Therefore, we will take $\phi_1 = 2.05 \times 10^3 \text{day}^{-1}$.

Appendix C

Tumour-nerve interactions – Parameter estimation

C.1 Standard sizes and weights

Domain and normal prostate sizes

We take normal prostate size to be approximately 30mL $= 3 \times 10^4 \text{mm}^3 = V_{prost}$ [184]. Assuming a spherical shape, this implies a radius of about 20 mm.

For our model, we consider the prostate and its surroundings. Therefore we consider a slightly bigger sphere, with the same centre; say (for instance) of radius 25 mm. This leads to a domain volume $V_{dom} = 65.45 \times 10^3 \text{mm}^3$.

Tumour cell size

In Park et al. [198] the circulating tumour cells and the cultured tumour cells in prostate cancer patients are measured; the former are found to have an average diameter of 7.97 μm, while the latter of 13.38 μm. We then take a tumour cell diameter of $10\mu\text{m} = 10^{-2}\text{mm}$ and thus of approximate volume $V_{tum\,cell} = 5 \times 10^{-7}\text{mm}^3$ (assuming cells of spherical shape).

Neurite diameter and nerve cell size

Take neurite diameter to be about 1 μm (from Table 2.1 in Fiala & Harris [79]). Friede[88] reports that human Purkinje cell (a class of nerve cells) diameter is 27 μm. We then estimate the nerve cell volume to be approximately 10^{-5} mm^3.

NGF molecular weight

In Poduslo & Curran [210] and PhosphoSitePlus (`www.phosphosite.org`) NGF molecular weight is stated to be around 2.7×10^4 Da; in [7, 180] this is estimated to be between 10^4 and 10^5 Da. Therefore we will assume NGF molecular weight to be 10^4 Da $\approx 1.660 \times 10^{-8}$ pg.

AGM molecular weight

Molecular weight of Semaphorin 4D is 96,150 Da (see product at `www.abcam.com`). Netrin-1 molecular weight is 75 kDa = 1.245×10^{-7} pg [161].

Norepinephrine molecular weight

NE molecular weight = 169.17784 g/mol (from PubChem, `pubchem.ncbi.nlm.nih.gov`).

Acetylcholine molecular weight

Acetylcholine molecular weight = 146.20744 g/mol (from PubChem, `pubchem.ncbi.nlm.nih.go`

C.2 Initial and equilibrium values

Tumour cell initial value

As initial time $t = 0$, we take the moment at which the (primary) tumour cells occupy the (variable/adjustable) percentage p_0 of the prostate volume. Therefore, the initial tumour cell density is given by the expression

$$T_p(0) = \frac{p_0 \times V_{prost}}{V_{tum\,cell}} \times \frac{1}{V_{dom}} = p_0 \times 10^6$$

where V_{prost} denotes the prostate volume, $V_{tum\,cell}$ the volume of a tumour cell and V_{dom} the volume of the domain; their values are estimated hereunder in Section C.1. We also start "counting" the migrating tumour cells at $t = 0$; therefore we take $T_m(0) = 0$.

Sympathetic and parasympathetic nerve density

In Figure 7 from Magnon et al. [160] we find a quantification of sympathetic and parasympathetic (respectively) neural areas in normal human prostate tissues. From the graph, one can take a positive nerve area per field of about $1000\mu\text{m}^2$ for sympathetic and $100\mu\text{m}^2$ for parasympathetic fibres, field surface = 0.15mm^2. It follows that the percentage of the area occupied by nerve fibres is approximately 0.7% and 0.07 % for sympathetic and parasympathetic nerves respectively. Note that here a section is 5 μm thick. However, the staining here identify any kind of nerve fibres, and it is well known that axon size is extremely variable depending on the type (for instance, in Friede [88] it is recorded a nerve diameter of 27 μm, while Schuman et al. [227] report a nerve fibre layer thickness in the eye of about 100 μm). We will assume that the nerve fibres occupy the whole thickness of the sections; thus we conclude that sympathetic nerves account for 0.7% of the normal prostate tissue volume and parasympathetic ones for 0.07%.

To convert these values in an actual cells/mm^3 value, we recall that in C.1 we found a domain volume of 65,450 mm^3. Taking the above found percentages of volume occupied by neural fibres, we have 458.1500 mm^3 occupied by sympathetic nerves and 45.8150 mm^3 by parasympathetic ones. Approximating a nerve cell a sphere of 27 $\mu\text{m} = 27 \times 10^{-3}$ mm diameter [88], we have that 458.1500 mm^3 correspond to 16,969 cells and 45.8150 mm^3 to 1,697 cells. Therefore, the initial sympathetic nerve density will be $S^{eq} = 16,969/65,450 \approx 0.26$ cells/mm^3 and the initial parasympathetic nerve density $P^{eq} = 1,697/65,450 \approx 0.03$ cells/mm^3.

Norepinephrine level

Dodt et al.[59] measured plasma concentration of epinephrine and norepinephrine before, during and after sleep in volunteers. They found that, although the neurotransmitters levels did not change significantly from one sleep phase to another, they increased after standing up from the horizontal position. In a final experiment, the subjects were asked to stay horizontal for 30 minutes after waking up and then stand up for and additional 30 minutes. The norepinephrine levels registered in these settings are summarised here:

- REM and non-REM sleep: 615.4±67.8 PMol/L and 616.5±51.4 pmol/L respectively;
- after standing up: from 778.76±88.9 to 2202.7±247.55 pmol/L;
- after 30 minutes lying down plus 30 minutes standing: from 1075.2±48.9 to 3213.4±212.5 pmol/L.

So between pre- and post-sleep plasma norepinephrine levels change in a range going from 615.4 pmol/L $\approx$ 0.1 pg/mm^3 and 3213.4 pmol/L $\approx$ 0.5 pg/mm^3 (using the norepinephrine molecular weight found in C.1). Since this value is likely to be even higher in fully awake individuals (norepinephrine is associated with stress), we will consider the latter value $N_n^{eq} = 0.5$ pg/mm^3.

Acetylcholine level

- Wessler et al.[274] report that "non-neuronal acetylcholine is involved in the regulation of basic cell functions" and measured acetylcholine concentration in skin biopses from healthy volunteers. They found that "the superficial and underlying portion of skin biopsies contained 130 ± 30 and 550 ± 170 pmol/g acetylcholine, respectively".

  Since we are interested in the prostate region of the body, we will take the acetylcholine level in the "deeper" skin sample 550 pmol/g. Considering a tissue of the same density of water (1g=1mL) and the acetylcholine molecular

weight reported in C.1, we have that the acetylcholine equilibrium level is approximately $N_a^{eq} = 80$ pg/mm^3.

- Watanabe et al.[269] determined blood acetylcholine levels in healthy human subjects. They report that "The blood acetylcholine levels of healthy subjects varied over a wide range with a geometric mean of 0.49 mumole/liter, 90% of the levels falling into the range of 0.20 to 1.31 mumole/liter".

  Converting into our units we have $N_a^{eq} = 72$ pg/mm^3.

We will take $N_a^{eq} = 80$ pg/mm^3.

C.3 Primary tumour cells equation

Tumour constant growth rate r_{T_p}

Schmid and collaborators [225] report that prostate cancer has a very large doubling time. In particular: "Seventy-nine percent of all patients had a doubling time of more than 24 months. Twenty of 28 cancers thought to be clinically organ confined doubled at rates exceeding 48 months". We could then take $r_{T_p} = \ln 2/48\text{months} \approx 4.81 \times 10^{-4}\text{day}^{-1}$.

Tumour constant death/apoptotic rate d_T

Dachille et al. [49] calculate the apoptotic index (AI) of prostatic adenocarcinoma as

$$\text{AI } (\%) = 100 \times \text{apoptotic cells/total cells .}$$

The mean AI in 3,000 tumour nuclei was 1.27. We will therefore take $d_T = 1.27 \times 10^{-2}$.

To compare these *growth and death rates* with others, we see that in Stein et al. [241] it is stated that "The growth rate constants varied over a nearly 1,500-fold range, while the regression rate constants varied over a 50-fold range (Fig. 3A). Furthermore, the regression rate constants were consistently larger than the growth

rate constants, with median values of $10^{-1.7}\text{day}^{-1}$ versus $10^{-2.5}\text{day}^{-1}$, respectively." These observations correspond to $r_{T_p} \approx 10^{-2.5}\text{day}^{-1}$ and $d_T \approx 10^{-1.7}\text{day}^{-1}$. Now, while d_T is approximately the same computed above, r_{T_p} here is bigger; this difference is explained by the fact that prostate tumour is well-known for being particularly slow in growth.

NGF-enhanced tumour growth τ_1, τ_2

- Zhu et al. [288] report the dose-dependent effects of NGF on pancreatic cancer cell growth *in vitro* after 48 hours in Figure 4A. Here data are expressed as a percentage of increase or decrease of untreated controls. In particular, the data in Table C.1 are recorded.

NGF (ng/mL)	% increase of untreated controls
6.3	approx. 130
25	approx. 180
100	approx. 210

Table C.1: (Recall: 1 ng/mL = 1 pg/mm^3.) Time = 48 hours = 2 days.

We then consider the NGF-dependent growth part in the T_p-equation

$$\frac{dT_p}{dt} = \left(r_{T_p} + \frac{G}{\tau_1 + \tau_2 G} - d_T \right) \cdot T_p$$

that, assuming G constant, has solution

$$T(t) = T_0 \exp\left[\left(r_{T_p} + \frac{G}{\tau_1 + \tau_2 G} - d_T \right) \cdot t \right] \tag{C.1}$$

that for $G = 0$ reduces to

$$T(t) = T_0 \exp\left[\left(r_{T_p} - d_T \right) \cdot t \right] \ , \tag{C.2}$$

which will correspond to the control case.

Now, from the data in Table C.1 we see that if, for example, $G = 6.3$, then

$$\frac{T_{G=6.3}(t=2)}{T_{G=0}(t=2)} = \exp\left[\frac{G}{\tau_1 + \tau_2 G} \cdot t \right] = 1.3 \ .$$

Similarly

$$\frac{T_{G=25}(t=2)}{T_{G=0}(t=2)} = 1.8 \quad \text{and} \quad \frac{T_{G=100}(t=2)}{T_{G=0}(t=2)} = 2.1 \ .$$

We thus have a system of three equations in two unknowns τ_1, τ_2:

$$\begin{cases} \ln(1.3)\,[\tau_1 + 6.3 \cdot \tau_2] = 2 \cdot 6.3 \\ \ln(1.8)\,[\tau_1 + 25 \cdot \tau_2] = 2 \cdot 25 \\ \ln(2.1)\,[\tau_1 + 100 \cdot \tau_2] = 2 \cdot 100 \end{cases} \tag{C.3}$$

We can then consider the following function: $y = \tau_1 + \tau_2 x$; then the system (C.3) corresponds to the following data points:

$$(x_1 = 6.3, y_1 = 48.02) \quad , \quad (x_2 = 25, y_2 = 85.06) \quad , \quad (x_3 = 100, y_3 = 269.56) \ .$$

Fitting the values of the parameters τ_1 and τ_2 to these points with MatLab functions `nlinfit` gives the following estimates: $\tau_1 = 29.54$ and $\tau_2 = 2.39$, with 95% confidence intervals $(-30.2417, 89.3126)$ and $(1.3891, 3.3943)$, respectively, given by the function `nlparci`. Note that while the estimate for τ_2 seems quite accurate, the same can not be said for τ_1.

- We can do a similar reasoning taking the data from Sortino et al.[239], who investigated the effect of NGF in the androgen-dependent, prostate adenocarcinoma LNCaP cell line. The data reported by Sortino et al. are summarized in Table C.2.

(48 hours)	cells/well ($\times 10^3$)	
	+ serum	- serum
Control	153±11	110±2
NGF (25 ng/mL)	217±16	163±8

(7 days)	cells/well ($\times 10^3$)
Control	189±1.3
NGF (25 ng/mL)	385±4.6

Table C.2: Data from Table 1 (left) and Table 2 (right) from Sortino et al.[239]. Note that the second dataset was obtained in the presence of serum.

Following a similar reasoning as the one done above with the data from Zhu et al. [288], we find

$$\frac{T_{G=25}(t=2)}{T_{G=0}(t=2)} = \exp\left[\frac{G}{\tau_1 + \tau_2 G} \cdot t\right] = 1.42 \quad \Rightarrow \quad \ln(1.42)\,[\tau_1 + 25 \cdot \tau_2] = 2 \cdot 25$$

and

$$\frac{T_{G=25}(t=7)}{T_{G=0}(t=7)} = \exp\left[\frac{G}{\tau_1+\tau_2 G}\cdot t\right] = 2.04 \quad \Rightarrow \quad \ln(2.04)\left[\tau_1+25\cdot\tau_2\right] = 7\cdot 25$$

respectively from the two datasets reported in Table C.2 (note that 25 ng/mL = 25 pg/mm^3). Averaging, we obtain that $\tau_1 + 25\cdot\tau_2 \approx 194.02$. Substituting the previously found value of τ_2 ($\tau_2 = 2.39$), we get $\tau_1 = 134.27$.

We will therefore take $\tau_1 = 134.27$ and $\tau_2 = 2.39$.

Maximum tumour cell density k_T

The maximum tumour cell density is given by $1\text{mm}^3/V_{tum\,cell} = 2\times 10^6$; in fact, k_T corresponds to the maximum number of tumour cells that can fit in every mm^3. Now, because of the presence of the stroma and other cells not explicitly included in the model, we will take half of this value $k_T = 1\times 10^6$ cells/mm^3.

Shape of $\vartheta(N_n)$ and values of θ_1, θ_2

We want the function $\vartheta = \vartheta(N_n)$ to be such that $\vartheta(0) \neq 0$ (to reflect the presence of an Allee threshold in the absence of norepinephrine) and that ϑ is a decreasing function of N_n (in fact, our hypothesis is that norepinephrine lowers the Allee threshold, making the tumour more likely to proliferate). We thus consider $\vartheta(N_n) = \theta_1/(1+\theta_2 N_n)$, where θ_1 and θ_2 are two parameters to be determined.

For θ_2, we consider Figure 1 from the paper by Chiang and collaborators [37], where the time course of prostate tumour weight is shown in control mice and in mice treated with doxazosin, an α1-adrenergic-antagonist (α-blocker). In the plot, we observe that in the doxazosin-treated mice the tumour weight dropped down from about 5 g to zero, while in control mice a tumour of weight around 2 g kept growing. Assuming that the doxazosin treatment blocked all the adrenergic receptors on tumour cells (thus corresponding to the case $N_n = 0$), and that in the control experiment the norepinephrine was at its equilibrium value N_n^{eq}, we deduce that

- when $N_n = 0$ (i.e. norepinephrine does not make any effect on tumour growth), 5 g is *below* the Allee threshold;
- when $N = N_n^{eq}$, 2 g is *above* the Allee threshold.

Now, since it is difficult to translate these tumour weights in tumour cell densities (mouse prostate size and tumour cell size are probably different from human ones), we can only use the "relative" information contained above, that is

$$\left.\begin{array}{c} \theta_1 > 5 \text{ g} \\ \frac{\theta_1}{1+\theta_2 N_n^{eq}} < 2 \text{ g} \end{array}\right\} \Rightarrow 1 + \theta_2 N_n^{eq} > \frac{5}{2} \Rightarrow \theta_2 > 5 \times 10^{-3} \frac{\text{mm}^3}{\text{pg}} .$$

We can take for instance $\theta_2 = 1$ mm^3/pg.

As pointed out by Korolev et al. [133], no experiment has been done to measure the "basal" Allee threshold θ_1 for any kind of tumour. We will just assume that θ_1 is approximately the 1% of the carrying capacity k_T, i.e. $\theta_1 = 1 \times 10^4$.

AGM-induced tumour cell apoptosis δ

In Table 1 from Castro-Rivera and collaborators' work [33] we find a quantification of the effect of semaphorin 3B on two different kinds of cancer cells; these data are summarised in Table C.3.

Treatment	H1299 lung cancer cells	MDA-MB-231 breast cancer cells
Control-CM	11×10^4	16×10^4
SEMA3B-CM	6×10^4	5×10^4

Table C.3: Time = 5 days; $C_0 = 10^4$ cells/well (six-well plates)

We will then consider the following two equations for control tumour cells $T_{control}$ and for semaphorin-treated ones T_{SEMA}:

$$T_{control}(t) = T_0 \exp\left[\left(r_{T_p} - d_T\right) t\right] \quad \text{and} \quad T_{SEMA}(t) = T_0 \exp\left[\left(r_{T_p} - d_T - \delta A\right) t\right] ,$$

where A represents the concentration of axon guidance molecule (here, semaphorin). To estimate A we consider the statement "Semiquantitative assay showed an average of 1540 ng/mL SEMA3B in theCMafter transfection" in the *Materials and Methods*

section and the fact that the medium was diluted 1:2; in this way we approximate $A \approx 13.75$ pg/mm^3 (note that 1 ng/mL = 1 pg/mm^3). Equipped with all these values (recall: $t = 5$), we can use the data in Table C.3 as follows:

$$\text{for H1299 cells: } \frac{T_{SEMA}}{T_{control}} = \exp(-\delta A t) = \frac{6}{11} \quad , \quad \text{for MDA-MB-231 cells: } \frac{T_{SEMA}}{T_{control}} = \frac{5}{16}$$

and then calculate the corresponding δ values 0.0088 and 0.0169 respectively. Taking the average, we get $\delta \approx 1.29 \times 10^{-2}$.

No data for prostate tumour cells were found to inform the value of the parameter δ.

Spontaneous tumour cell migration μ_0

Pienta et al. [205] observed about 1,400 colonies of (rat) prostate tumour cells after 8 days (see Figure 4 in the same reference). Without knowing how big each colony is, we will assume that 1 colony corresponds to 1 cell. Therefore, taking an exponential decay $T_p(t) = T_p(0)\exp(-\mu_0 t)$ for the tumour cells and knowing that the initial cell density was $T_p(0) = 2 \times 4 \times 10^3$ cells/mL (stated also in the work by Pienta and co-workers [205]), we can calculate $\mu_0 = 0.22$ day^{-1}.

AGM-induced migration μ_1

In Figure 3 from Herman & Meadows' paper [106] the following % cell invasion are reported for semaphorin-treated PC-3 cells (androgen-independent prostate cell line):

$$\text{sema3A: } \sim 65\% \text{ of control} \quad , \quad \text{sema3C: } \sim 135\% \text{ of control}$$

after 20 hours incubation ($T_0 = 10^5$). The authors' comment is: "Overexpression of sema3A in PC-3 decreased the invasive characteristics of PC-3 cells by 33% compared to the untransfected cells. Sema3C, on the other hand, increased invasion by 33% compared to untransfected cells". To estimate the amount of semaphorin used in the experiment, we read: "The bacterial clones transfected with sema3A or sema3C were grown on agar plates and selected with 35 μg/mL of kanamycin". Therefore,

in our equation for tumour cell migration $T_m(t) = T_0 \exp[(\mu_0 + \mu_1 A)t]$ we will take $A = 35\,\mu\text{g/mL} = 35 \times 10^3\ \text{pg/mm}^3$. Finally, considering the 20-hours sema3C treatment, we have that

$$\frac{T_0 \exp\left[(\mu_0 + \mu_1 A)t\right]}{T_0 \exp\left(\mu_0 t\right)} = 1.33 \quad \Rightarrow \quad \mu_1 A t = \ln(1.33) \quad \Rightarrow \quad \mu_1 = 9.8{\times}10^{-6} \frac{\text{mm}^3}{\text{pg} \cdot \text{day}}\ .$$

Acetylcholine-induced migration μ_2

Figure 3A from Magnon et al.'s paper [160] reports an *ex vivo* quantification of tumour cell invasion of pelvic lymph nodes (which drain the prostate gland). Here data are reported both for control (saline-treated) and carbachol-treated mice, and in the second case the invading tumour cells are about the double than in the control. Notice that since carbachol is a non-selective cholinergic (muscarinic) receptor agonist, we can consider it as a substitute of acetylcholine. Then, denoting with c the carbachol amount, we can estimate from the equation $T_m(t) = T_0 \exp[(\mu_0 + \mu_2 N_a)t]$ and Figure 3A [160] that $\mu_2 c t = \ln(2)$ (since $T_0 \exp[(\mu_0 + \mu_2 c)t] \approx T_0 \exp(\mu_0 t)$). To estimate the value of c, we read in Magnon's paper [160]: "For experiments on the PNS, 15 days after tumour cell injection, animals received carbachol at 250 (day 0), 300 (day 1), 350 (day 2), 500 μg/kg per day (day 3) [every 12 hours, 8 divided doses]". First notice that the average of these amounts is 350 μ/kg over 5 weeks, which corresponds to 10 μg/kg/day. To convert the kilos in a volume, we take water density (1 g/mL); therefore we find the approximation $c = 10\ \text{pg/mm}^3\text{/day}$ and thus $\mu_2 = 2 \times 10^{-3}\ \text{mm}^3\text{pg}^{-1}\text{day}^{-1}$ ($t = 35$ days).

No more direct measurements of this kind of data were found by the authors.

C.4 NGF equation

NGF decay rate d_G

Tang and collaborators [248] state that "Nerve growth factor (NGF) mRNA is rapidly degraded in many non-neuronal cell types with a half-life of between 30 and 60 min". Hence, taking a half-life of 45 minutes, the resulting decay rate is

$d_G = 0.0154\ \text{min}^{-1} = 22.18\ \text{day}^{-1}$.

NGF production by tumour cells s_G

In Figure 1c from Dolle et al. [60] it is reported that after 24 hours, cultures of different lines of breast cancer cells expressed approximately 0.3 ng/(mg protein) of NGF. Considering a total protein amount of 300 pg per cell (as in HeLa cells (an immortalised cell type used in biological research, derived from cervical cancer cells taken from Henrietta Lacks), we have that 1 mg = 10^9 pg protein corresponds to approximately 3×10^6 cells. Now, we have to consider that in 24 hours the NGF also decayed; in fact the differential equation for G in this case is

$$\frac{dG}{dt} = s_G T - d_G G \quad \Rightarrow \quad G(t) = \left(G(0) - \frac{s_G}{d_G} T\right) \exp(-d_G t) + \frac{s_G}{d_G} T$$

where T denotes the number of tumour cells (and $G(0) = 0$ in our case). Thus, Dolle and co-workers [60] tell us that $G(t = 1\text{day}) = 0.3 \times 10^3\text{pg}$, $T = 3 \times 10^6\text{cells}$. Substituting these numbers in the equation (and taking the value of d_G estimated above), we determine $s_G = 2.22 \times 10^{-3}\ \text{pg} \cdot \text{cells}^{-1} \cdot \text{day}^{-1}$.

The authors did not find any suitable dataset with prostate cancer cells.

NGF internalisation rate by tumour cells γ_1

In Table 1 from Rakowicz-Szulczynska's paper [212] it is reported the internalisation of ^{125}I-NGF after 1 hour or 24 hours incubation of different breast carcinoma and melanoma cell lines with 10 ng/mL. For SKBr5 breast carcinoma cells, we find that 33,560 molecules/cell were internalised after 24 hours incubation. Considering a NGF molecular weight of 1.660×10^{-8} pg and knowing that the cells were seeded at density 2×10^7 cells/10 mL = 2×10^3 cells/mm^3, we can write down the equality

$$\gamma_1 \times \left(2 \times 10^3 \frac{\text{cells}}{\text{mm}^3}\right) \times \left(10 \frac{\text{pg}}{\text{mm}^3}\right) = 33.56 \times 10^3 \times 1.660 \times 10^{-8} \frac{\text{pg}}{\text{mm}^3} \times 2 \times 10^3\ \text{cells} \frac{1}{\text{day}}\ ,$$

which leads to $\gamma_1 = 5.57 \times 10^{-5}\ \text{mm}^3\text{cells}^{-1}\text{day}^{-1}$.

It was not possible to find data about NGF internalisation by prostate tumour

cells.

NGF internalisation rate by nerve cells γ_2

We can estimate the rate of NGF internalisation by cultured neurons using the data in Figure 1 by Claude et al. [41]. The plot reports the pg of ^{125}I-NGF binding to rat sympathetic neurons versus different amounts of free NGF. It is also stated that the neurons were incubated for 140 minutes with the NGF at a density of approximately 1,000 neurons/dish in 35-mm culture dishes.

Therefore, if we have a density of free NGF equal to G_0, the corresponding value on the y-axis of Figure 1 [41] corresponds to $G(t = 140\text{min}) = G_0 \exp(-\gamma_2 S t)$. Then, converting these data into our units (in particular, we considered $t = 140$ min $= 0.0972$ day and $S = 1000$ neurons/$35 - $mm dish $= 0.5$ cells/mm^3 from the data in Figure 1 [41], assuming a 35-mm dish of 2 mL), we can use the MatLab functions `nlinfit` and `nlparci` to get an estimate for γ_2 and its 95% confidence interval respectively. The plot of the fit is reported in Figure C.1 and the output gives an estimated γ_2 value of 0.048342 with 95% confidence interval $(0.0422, 0.0545)$.

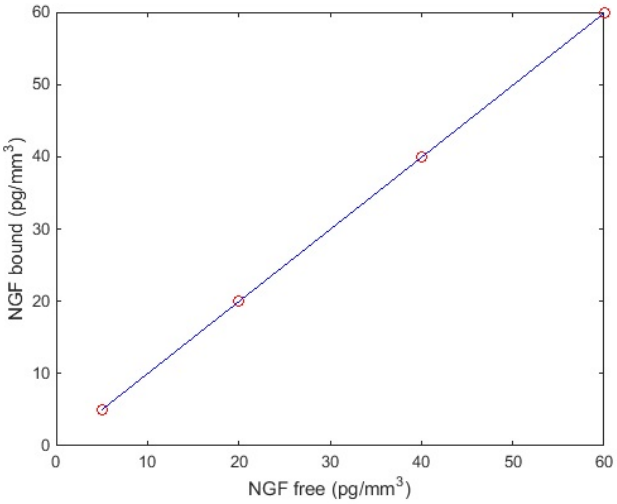

Figure C.1: Plotting the data from Claude et al. [41] (red circles) together with the function $G(t) = G_0 \exp(-\gamma_2 S t)$ (blue line) fitted to the data with the MatLab function `nlinfit`.

C.5 AGM equation

A large class of secreted or membrane bound axon guidance molecules are semaphorins and more specifically the so called class-3 semaphorins, that include seven family members. Class 3 semaphorins are the only secreted vertebrate semaphorins. In a recent work, Blanc et al. [19] highlighted that Semaphorin 3E is not only over-expressed in prostate cancer but also affects adhesion and motility of prostate cancer cells. They also demonstrated that all the prostate cancer cell lines that have been tested produce both the unprocessed (87kDa) and processed (61kDa) form of Sema3E. However the effect of tumour and stromal secreted semaphorins on tumour functionalities such as migration, apoptosis, growth and invasion is likely to depend on which co-receptors are expressed. Namely, sema3E act as a chemoattractant for neurons expressing NRP1 receptors, that have been found to have a high expression on prostate tumours.

AGM tumour secretion rate s_A

Kigel et al. [128] estimate the concentration of secreted sema3s in conditioned medium for specific (breast) tumour cell lines. As it can be deduced by Figure 2 from the same work [128] the relative concentrations of class-3 semaphorins secreted into the medium of tumour cell lines were 1000 and 500 sema3-expression per cell. Tumour cells were incubated for 48 hours = 2 days. Take an average of the aforementioned values, we deduce that the expression of sema3 per-cell per-day is 375. Taking the molecular weight of unprocessed sema3 to be 87kDa (as described at the beginning of this section C.5), we estimate that the secretion rate is: $s_A = 375 \times 87000 \times 1.66 \times 10^{-12}$pg cell^{-1}day^{-1}, thus $s_A \approx 5.42 \times 10^{-5}$pg cell^{-1}day^{-1}. However, Kigel and co-workers [128] highlight that the aforementioned expressed semaphorins did not affect the proliferation rate or the survival of the different semaphorin tumour producing cells. In this regard, we expect that during tumour driven neo-neurogenesis the expressed tumour secreted sema3E are 100 or 1000 higher then the estimated value, in other words we take $s_A = 5.42 \times 10^{-3}$pg cell^{-1}day^{-1}.

We did not find prostate cancer-specific data to inform this parameter.

AGM decay rate d_A

In the Supplementary Tables 1 and 2 provided by Sharova et al. [232] we find the mRNA half-life of different kinds of semaphorins. We take an average decay rate of $0.1\ \text{h}^{-1} = 2.4\ \text{day}^{-1}$.

Manitt et al. [161] write: "Currently, little is known about the half-life of netrin-1 protein in any context".

AGM internalisation by nerve cells γ_4

In Figure 4 by Keino-Masu and collaborators [123] it is studied the binding of netrin(VI•V)-Fc to DCC-expressing cells (spinal commissural axons). Here the counts per minute are reported for different concentrations of netrin. Assuming the every binding corresponds to 1 molecule, and taking the netrin molecular weight 1.245×10^{-7} pg, we can calculate the decrease of *free netrin*, that in our system is represented by the variable A and in this case is modelled by the equation $A(t) = A_0 \exp(-\gamma_4 S t)$. Then, having $S = 2.5 \times 10^5$ cells/24-well $= 71.43$ cells/mm^3 (24-well $\to$ 3.5 mL) and $t = 1$ minute $= 6.9444 \times 10^{-4}$ days, we can fit this as a function of A_0, as in Figure 4 [123]. The MatLab functions `nlinfit` and `nlparci` give the γ_4 estimate 1.4673×10^{-5} with 95% confidence interval $(0.0462 \times 10^{-4}, 0.2472 \times 10^{-4})$. The plot of this fitting is reported in Figure C.2.

C.6 SNC equation

Basal SNC growth rate r_S

In Table 1 presented by Dolle et al. [60] we find that 4.4% control sympathetic neurons cultured for 48 hours showed a neurite length of 29 mm. The initial cell density was 2×10^3 cells/well that, assuming a well volume of 100 mL, correspond to $S_0 = 2 \times 10^{-2}$ cells/mm^3; moreover, taking a neurite diameter of 1 μm, we have

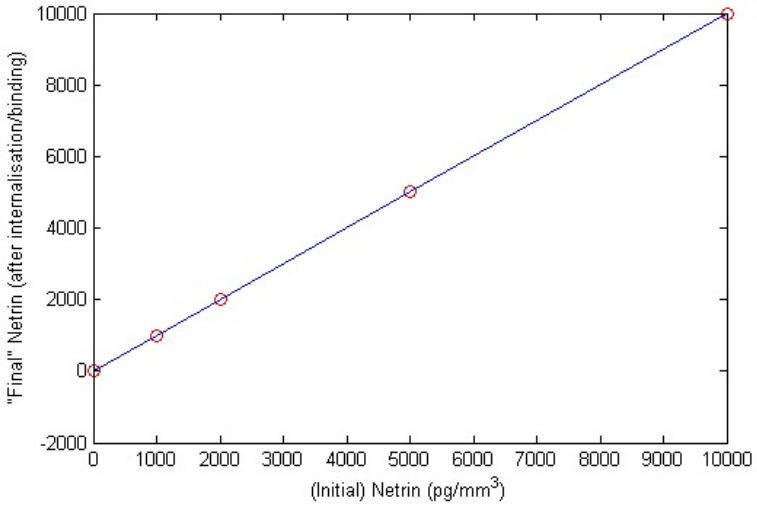

Figure C.2: Plotting the data from Keino-Masu et al. [123] (red circles) together with the function $A(A_0) = A_0 \exp(-\gamma_4 St)$ (blue line) fitted to the data with the MatLab function `nlinfit`.

that 29 mm neurite correspond o approximately 2.9 cells (recalling that we consider a nerve cell volume of about 10^{-5}mm^3).

From Dolle et al. [60]: "Cell culture plates (96-well) were prepared by incubating each well with 100 mL of 0.1mg/mL poly-L-lysin in sterile distilled water [...] Approximately 2×10^3 cells, prepared from embryonic day-12 chick paravertebral sympathetic ganglia, were added to each well in 100 mL of a 1:1 mixture of [...] medium".

Hence, we conclude that after 2 days of experiment there were

$$S(t=2) = S_0 + 0.044 \times S_0 \times 2.9 \text{ cells} \;\Rightarrow\; S(t=2) = 2.2552 \times 10^{-2} \text{cells/mm}^3 = S_0 \exp(2 \cdot r_S) \;,$$

from which we can calculate $r_S = 0.06$ day^{-1}.

SNC carrying capacity k_S

In absence of tumour, we know that the SNC equilibrium value is $S^{eq} = 0.26$ cells/mm^3 (see section C.2). We then take $k_S = S^{eq}$.

NGF-enhanced SNC growth σ_1, σ_2

In Table 1 by Ruit et al. [220] the effects of NGF treatment on superior cervical ganglion cell dendritic morphology are reported; they are summarised here in Table C.4.

Treatment	Animal size	Total dendritic length (μm)
Control	23.5 g	721
NGF	23.5 g	929

Table C.4: Mouse 2.5S NGF was administered daily to mice by subcutaneous injection in a dosage of 5 mg/kg. The animals were treated for 2 weeks.

Now, if we take a dendritic diameter of 1 μm and a nerve cell volume of 10^{-5} mm^3, we have that 1 μm dendrite corresponds to about 10^{-4} cells. Therefore, we can "convert" the previous dendritic lengths in cells (at least roughly). For the NGF treatment, we know that it was 5 mg/kg/day for 2 weeks. If a mouse was 23.5 g, we have that each animal received 117.50×10^6 pg/day. Being NGF injected subcutaneously, we assume that only 1% of the dosage actually contributed to the experiment (the rest being dispersed by body fluids). Additionally, we estimate a total mouse volume of 28.57×10^3 mm^3 (knowing that mice blood volume is about 2 mL and it constitutes 7-8% of their total volume [257]) and thus we have a daily NGF supply of 41.13 pg/mm^3/day. Now, to calculate the effective NGF present, we have to take into account its decay. We know that NGF decay rate is $d_G = 22.18$ day^{-1} (see C.4); if we define the constant supply $s = 41.13$ pg (mm^3)$^{-1}$day^{-1}, we have that the evolution equation for G in this setting is

$$\frac{dG}{dt} = s - d_G G \quad \Longrightarrow \quad G(t) = G_0 e^{d_G t} - \frac{s}{d_G} e^{-d_G t} + \frac{s}{d_G} \, .$$

Then, taking $G_0 = 0$, we have that at $t = 1$ day the amount of NGF is approximately 1.85 pg/mm^3. For the two-week experiment, we will then assume G to be $1.85 \times 14 = 25.96$ pg/mm^3. Then, back to the S-equation: we recall that the bit in which we are now interested is

$$\frac{dS}{dt} = \left(r_S + \frac{G}{\sigma_1 + \sigma_2 G} \right) S \quad \overset{G \text{ const}}{\Longrightarrow} \quad S(t) = S_0 \exp\left[\left(r_S + \frac{G}{\sigma_1 + \sigma_2 G} \right) t \right]$$

we have that at 2 weeks = 14 days

$$\frac{S_{NGF}}{S_{control}} = \exp\left(\frac{G}{\sigma_1 + \sigma_2 G} \times 14\right) = \frac{929}{721} = 1.29 \ .$$

From this equation (recall: $G = 25.96$) we derive $\sigma_1 = 25.96 \times (54.9791 - \sigma_2)$. Consequently, we have that it must be $\sigma_2 < 54.9791$ in order to have $\sigma_1 > 0$.

We can derive a second equation for σ_1 and σ_2 from the experimental results reported by Collins & Dawson [47]. In fact, Table 1 from the same work [47] lists the maximal effects on neurite lengths of various additions to the culture medium. In particular, the mean total neurite length per neuron after different treatments divided by the corresponding value of the untreated control is reported. For sympathetic neurons exposed for 2 hours to 1 ng/mL NGF, the relative length is 2.47; this observation allows us to write the following equality:

$$\exp\left(\frac{G}{\sigma_1 + \sigma_2 G} \times 0.0833\right) = 2.47 \quad \Longrightarrow \quad \sigma_2 = 57.1782 \ ,$$

the latter obtained after substituting the expression for σ_1 found previously (note that 2 hours = 0.0833 days). Notice that although σ_2 is bigger than 54.9791, the difference is small (less than one order of magnitude). This is probably due to the fact that the two references estimated σ_1, σ_2 in completely different experimental settings (for example, the experiment done by Ruit and co-workers [220] is *in vivo* while that reported by Collins & Dawson [47] is *in vitro*). Therefore it seems justified to take for instance $\sigma_2 = 50$ days and consequently $\sigma_1 \approx 129$ pg day $(\text{mm}^3)^{-1}$.

No human data were found to estimate these parameter values.

AGM-enhanced SNC growth σ_3, σ_4

In Figures 1A(*ii*) and 2A Kuzirian and collaborators [135] report the synapse density after 0.5, 1, 2 and 4 hours of Sema4D treatment as % of control. In particular, it is reported that after 0.5 hours = 0.0208 days = t_1 of 1nM-Sema4D-treatment GABAergic synapse formation in rodent hippocampus was about 130% of control, and after 1 hour = 0.0417 days = t_2 it was approximately 150% of control. Now,

recalling the "growth bit" of the S-equation

$$\frac{dS}{dt} = \left(r_S + \frac{A}{\sigma_3 + \sigma_4 A}\right) S \quad \overset{A\,\text{const}}{\Longrightarrow} \quad S(t) = S_0 \exp\left[\left(r_S + \frac{A}{\sigma_3 + \sigma_4 A}\right) t\right] ,$$

we have from the previous data points that

$$\exp\left(\frac{At_1}{\sigma_3 + \sigma_4 A}\right) = 1.3 \quad \text{and} \quad \exp\left(\frac{At_2}{\sigma_3 + \sigma_4 A}\right) = 1.5$$

(since the control corresponds to the $S(t)$ where $A = 0$). Note that taking molecular weight of 96,150 Da for A, we have that $A = 1$ nM $= 96.117$ pg/mm^3. Finally, considering the average of the two expressions above we can estimate

$$\sigma_3 + \sigma_4 A \approx \frac{1}{2}\left(\frac{At_1}{\ln(1.3)} + \frac{At_2}{\ln(1.5)}\right) \quad \Rightarrow \quad \sigma_3 \approx 8.75 - 96.12 \times \sigma_4 .$$

Note that we must choose $\sigma_4 < 0.0911$ in order to have $\sigma_3 > 0$. Taking for instance $\sigma_4 = 0.01$, we have consequently also $\sigma_3 = 7.79$.

No relevant data were found for human SNC.

C.7 PNC equation

Basal PNC growth rate r_P

In Table I Collins & Dawson [46] report that the mean total neurite length/neuron after 2¾ hours in conditioned medium was 408 μm, while in the unconditioned medium it was 118 μm (they study chicken embryo ciliary ganglia, which are parasympathetic ganglia located in the posterior orbit). Taking the latter as the initial value P_0, from the equation describing PNC dynamics in this context we have:

$$P(t = 2\tfrac{3}{4}\text{h} = 0.1146\text{day}) = P_0 \exp\left(r_P \times t\right)$$
$$\Rightarrow \quad 0.1146 \times r_P = \ln\left(\frac{408}{118}\right) \quad \Rightarrow \quad r_P = 10.83 \text{ day}^{-1} .$$

In the same reference we find another useful dataset in Table II [46]. Here it is stated that the mean elongation rate of 14 neurites (chosen to be at east 15 μm long) without any medium change was 22 μm/hour. Converting these lengths into cell numbers (using the calculations done in C.1) and keeping in mind that 1 hour = 0.0417 days, we calculate the growth rate "per cell" r_P as $^{22}/_{14\times15} \times {}^{1}/_{0.0417} = 2.51$ day^{-1}.

Another way to determine r_P could be to use the data in Table I [47]. Here the authors measure the maximal effect on ciliary (parasympathetic) and sympathetic neurite growth in various culture media after 2 hours. Considering the data regarding the "standard" conditioned medium, we have that the relative neurite length for ciliary neurons was 3.42, and for sympathetic neurons 1.81. Then, assuming an exponential growth for both cell cultures, we have that $P_0 \exp(r_P t)/S_0 \exp(r_S t) = 3.42/1.81$; furthermore, taking $P_0 = S_0$ and $t = 2\text{h} = 0.0833\text{day}$, we have that $r_P - r_S = 7.63$ day^{-1}. Now, recalling our previous estimate for r_S ($r_S = 0.06$, see C.6), we have $r_P = 7.70$ day^{-1}.

It is encouraging to see that all these three values are of the same order of magnitude. To choose an estimate for r_P, we take their average 7 day^{-1}.

The authors did not find data for human parasympathetic nerve growth.

PNC carrying capacity k_P

In absence of tumour, we know that the PNC equilibrium value is $P^{eq} = 0.026$ cells/mm^3 (see section C.2). We then take $k_P = P^{eq}$.

NGF-enhanced PNC growth π_1, π_2

Collins & Dawson [47] investigated the effect of NGF on promoting the chicken embryo parasympathetic ciliary ganglion outgrowth *in vitro*. Their calculations were used to calculate the mean total length of neurites per neuron. Their calculations were based on data from neurons that had at least one neurite greater then 15 μm in length ($\approx$ about the diameter of the neuronal soma). In this regard when they added NGF to dissociate ciliary ganglion neurons, resulted in a 2-fold increase

in neurite length over untreated, control cultures.They estimated the mean total neurite length per neuron for control cultures to be $79 \pm 19\mu$m. Parasympathetic ganglion neurons were exposed to a concentration of 10ng/mL $= \frac{10\times10^3}{10^3}\ \frac{\text{pg}}{\text{mm}^3}$ per h. Just two hours after addition of NGF the ratio $\frac{P_{NGF}}{P_{control}} \approx 2.08 \pm 0.12$.

Recalling the given P equation:

$$\frac{dP}{dt} = \left(r_P + \frac{G}{\pi_1 + \pi_2 G}\right) S \quad \overset{G\,\text{const}}{\Longrightarrow} \quad P(t) = P_0 \exp\left[\left(r_P + \frac{G}{\pi_1 + \pi_2 G}\right) t\right] ;$$

so after two hours we have

$$\frac{P_{NGF}}{P_{control}} = \exp\left(\frac{G}{\pi_1 + \pi_2 G} \times \frac{2}{24}\right) = 2.08 .$$

Taking into account that 2 hours $\approx \frac{2}{24}$day $= 0.083$day we deduce that

$$\frac{10}{\pi_1 + \pi_2 \times 10} \times 0.083 = \ln 2.08$$

and therefore $\pi_1 = 1.33 - 10 \times \pi_2$. Note that it must be $\pi_2 < 0.13$ in order to have $\pi_1 > 0$. We can take for example $\pi_2 = 0.1$ and thus $\pi_1 = 0.33$.

No data were found for human PNC.

C.8 Norepinephrine (noradrenaline) equation

Noradrenaline production by SNC s_n

Regarding the norepinephrine release rate, Esler et al. [76] estimated the apparent norepinephrine release rate at rest in humans to be $0.54 \pm 0.20\mu$g/(m^{2}min) $= 777.60\,\text{pg/mm}^2\times\text{day}$. Note that 90% of this release rate is due to the sympathetic nerves. To convert the mm^2 in cells, we assume once again a nerve cell radius $r = 13.5\mu\text{m} = 13.5 \times 10^{-3}$m (see C.1); the surface area is given by $4\pi r^2 = 4\pi(13.5 \times 10^{-3})^2 \approx 2.29 \times 10^{-3}\text{mm}^2$, thus we deduce that in 1 mm^2 there are $1/(2.29 \times 10^{-3}) = 436.7$ nerve cells. The noradrenaline secretion rate is then given

by $s_n = 0.9 \times {}^{777.60}/_{436.7} \approx 1.6$ pg cells^{-1}day^{-1}.

Noradrenaline decay rate d_n

Taubin et al. [249] report that the noradrenaline half-life is about 10 hours (although this value is different in different tissues). This leads to a decay rate $d_n = 1.66$ day^{-1}.

Noradrenaline uptake rate (by tumour cells) γ_5

In Figure 4A by Jaques et al. [113] we find one set of measurements of NE uptake by human pheochromocytoma cells. A pheochromocytoma is a neuroendocrine tumour of the medulla of the adrenal glands; it secretes high amounts of catecholamines, mostly norepinephrine, plus epinephrine to a lesser extent. Recalling the molecular weight of NE found in C.1 and assuming a culture volume of 1 mL (it is not better specified in the paper), we can convert the data points in Figure 4A [113] into our units and fit the function $N(t) = N_0 - N_0 \exp(-\gamma_5 T t)$ to them; note that T represents the tumour cells, and that the value of this function at each time t is measured as the initial substrate concentration minus the uptaken NE. Using the MatLab function `nlinfit` to fit the data we obtain an estimated γ_5 value of 0.0019926 wih 95% confidence interval $(0.0018, 0.0022)$. The plot of the fit is reported in Figure C.3.

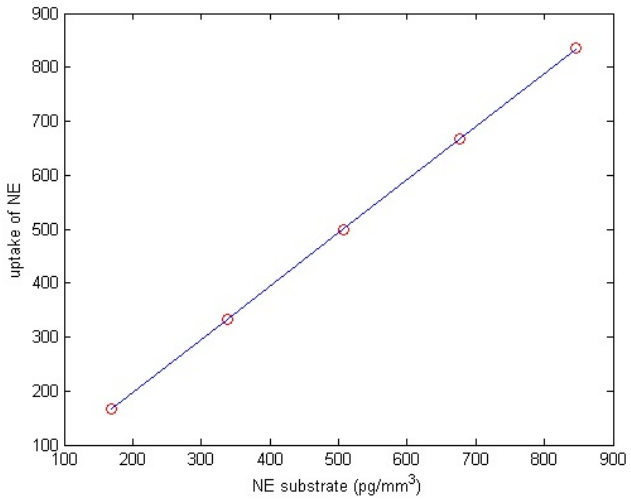

Figure C.3: Plotting the data from Jaques et al. [113] (red circles) together with the function $N(t) = N_0 - N_0 \exp(-\gamma_5 T t)$ (blue line) fitted to the data with the MatLab function `nlinfit`.

No data in this respect were found concerning prostate tumour cells.

Noradrenaline constant source c_n

We found in C.2 that in normal conditions (i.e. in the absence of a tumour) the level of noradrenaline is $N_n^{eq} = 0.5$ pg/mm^3. We can then calculate c_n from the equilibrium equation

$$c_n + s_n S^{eq} - d_n N_n^{eq} = 0 \quad \Rightarrow \quad c_n \approx 0.41 \, \frac{\text{pg}}{\text{mm}^3\text{day}} \, ,$$

where S^{eq} and P^{eq} were also found in C.2 and s_n,d_n were estimated above.

C.9 Acetylcholine equation

Acetylcholine release rate s_a

Paton et al. [201] use the output of acetylcholine from the plexus of the guinea-pig ileum longitudinal strip to study the mechanism of acetylcholine release. The resting output is reasonably constant for a given preparation for long periods; the mean value for eighty-four experiments was about 51 ng/g·min. The evoked output, however, usually changes as stimulation is prolonged, in a manner varying with the stimulation used. Assuming a nerve cell volume of 10^{-5} mm^3 (see C.1) and of density equal to water's one (1g/mL), we have that 1 g of parasympathetic nerves corresponds to approximately 10^8 cells. Therefore, we estimate the acetylcholine production rate as $s_a = 0.73\,\text{pg/cell day}$.

No better (human) dataset was found to inform this parameter value.

Acetylcholine decay rate d_a

Bechem et al. [14] studied the influence of the stimulus interval and the effect of Mn ions on facilitation of acetylcholine (ACh) release from parasympathetic nerve terminals in quiescent guinea-pig auricles (here the term *facilitation* denotes an increase in transmitter release during repetitive nerve excitation). Here we also find that when conditioning trains of stimuli were applied, a second much longer lasting component of facilitation was found ($t_{1/2} \approx 4$ s). Also, the decay to the control

level displays a half time of about 20 min and can also be accelerated by frequent stimulation of the parasympathetic nerve fibres. In this regard we can estimate $d_a = 49.91\text{day}^{-1}$ (taking 20 min).

No data were found regarding acetylcholine decay rate in human tissues.

Acetylcholine constant source c_a

In C.2 we estimated that in normal conditions (i.e. in the absence of a tumour) the acetylcholine level in the tissue is $N_a^{eq} = 80$ pg/mm^3. We can then calculate c_a from the equilibrium equation

$$c_a + s_a P^{eq} - d_a N_a^{eq} = 0 \quad \Rightarrow \quad c_a \approx 3.99 \times 10^3 \, \frac{\text{pg}}{\text{mm}^3\text{day}} \, ,$$

where S^{eq} and P^{eq} were also found in C.2 and s_a,d_a were estimated above.

Bibliography

[1] M. Adams, S. Celniker, R. Holt, et al. The genome sequence of drosophila melanogaster. *Science*, 287(5461):2185–95, 2000.

[2] R. H. Adams and K. Alitalo. Molecular regulation of angiogenesis and lymphangiogenesis. *Nat. Rev. Mol. Cell Biol.*, 8(6):464–478, 2007.

[3] F. Al-Mulla, S. J. Leibovich, I. M. Francis, and M. S. Bitar. Impaired TGF-β signaling and a defect in resolution of inflammation contribute to delayed wound healing in a female rat model of type 2 diabetes. *Mol. BioSyst.*, 7: 3006–3020, 2011.

[4] B. J. Arthur et al. Multi-channel acoustic recording and automated analysis of drosophila courtship songs. *BMC Biol.*, 11:1–11, 2013.

[5] J. Asai, H. Takenaka, S. Hirakawa, J. Sakabe, A. Hagura, S. Kishimoto, K. Maruyama, K. Kajiya, S. Kinoshita, Y. Tokura, and N. Katoh. Topical simvastatin accelerates wound healing in diabetes by enhancing angiogenesis and lymphangiogenesis. *Am. J. of Pathol.*, 181(6):2217–2224, 2012.

[6] G. E. Ayala, H. Dai, M. Powell, R. Li, Y. Ding, T. M. Wheeler, D. Shine, D. Kadmon, T. Thompson, B. J. Miles, M. M. Ittmann, and D. Rowley. Cancer-related axonogenesis and neurogenesis in prostate cancer. *Clin. Cancer Res.*, 14(23):7593–7603, 2008.

[7] M. E. Baker. Molecular weight and structure of 7 S nerve growth factor protein. *J. Biol. Chem.*, 250(5):1714–1717, 1975.

[8] F. Balkwill and A. Mantovani. Inflammation and cancer: back to Virchow? *The Lancet*, 357:539–545, 2001.

[9] A. M. Ballangrud, W. H. Yang, A. Dnistrian, N. M. Lampen, and G. Sgouros. Growth and characterization of LNCaP prostate cancer cell spheroids. *Clin. Cancer Res.*, 5:3171s–3176s, 1999.

[10] I. Barkefors, S. Le Jan, L. Jakobsson, E. Hejll, G. Carlson, H. Johansson, J. Jarvius, J. W. Park, N. Li Jeon, and J. Kreuger. Endothelial cell migration in stable gradients of vascular endothelial growth factor A and fibroblast growth factor 2: effects on chemotaxis and chemokinesis. *J. Biol. Chem.*, 283 (20):13905–13912, 2008.

[11] S. Barrientos, O. Stojadinovic, M. Golinko, H. Brem, and M. Tomic-Canic. Growth factors and cytokines in wound healing. *Wound Rep. Reg.*, 16:585–601, 2008.

[12] M. Bastock. A gene mutation which changes a behavior pattern. *Evolution*, 10:421–439, 1956.

[13] M. Bastock and A. Manning. The courtship of drosophila melanogaster. *Behaviour*, 8:85–111, 1955.

[14] M. Bechem, H. G. Glitsch, and L. Pott. Facilitation of acetylcholine release from cardiac parasympathetic nerve endings effect of stimulation pattern and mn ions. *Pflüg. Archiv Europ. J. Physiol.*, 391, 1981.

[15] A. V. Benest, S. J. Harper, S. Y. Herttuala, K. Alitalo, and D. O. Bates. VEGF-C induced angiogenesis preferentially occurs at a distance from lymphangiogenesis. *Cardiovasc. Res.*, 78(2):315–323, 2008.

[16] P. N. Bernatchez, S. Soker, and M. G. Sirois. Vascular endothelial growth factor effect on endothelial cell proliferation, migration, and platelet-activating factor synthesis is Flk-1-dependent. *J. Biol. Chem.*, 274(43):31047–31054, 1999.

[17] A. Bianchi, K. J. Painter, and J. A. Sherratt. A mathematical model for lymphangiogenesis in normal and diabetic wounds. *J. Theor. Biol.*, 383:61–86, 2015.

[18] J.-C. Billeter, E. J. Rideout, A. J. Dornan, and S. F. Goodwin. Control of male sexual behavior in drosophila by the sex determination pathway. *Curr. Biol.*, 16:766–776, 2006.

[19] V. Blanc, J. Nariculam, P. Munson, A. Freeman, H. Klocker, J. Masters, and M. Williamson. A role for class 3 semaphorins in prostate cancer. *Prostate*, 71(6):649–658, 2011.

[20] K. C. Boardman and M. A. Swartz. Interstitial flow as a guide for lymphangiogenesis. *Circ. Res.*, 92:801–808, 2003.

[21] F. Botelho, F. Pina, P. Silva, G. Figueiredo, F. Cruz, and N. Lunet. Vascular endothelial growth factor (VEGF) and prostate pathology. *International Braz. J. Urol.*, 36:430–438, 2010.

[22] R. Boulton, A. Woodman, D. Calnan, C. Selden, F. Tam, and H. Hodgson. Nonparenchymal cells from regenerating rat liver generate interleukin-1alpha and -1beta: a mechanism of negative regulation of hepatocyte proliferation. *Hepatology*, 26(1):49–58, 1997.

[23] A. Boyarsky. A stochastic model for wound healing. *Math. Modelling*, 7: 371–375, 1986.

[24] H. Brem and M. Tomic-Canic. Cellular and molecular basis of wound healing in diabetes. *J. Clin. Invest.*, 117(5):1219–1222, 2007.

[25] D. R. Brown. Dependence of neurones on astrocytes in a coculture system renders neurones sensitive to transforming growth factor β1-induced glutamate toxicity. *J. Neurochem.*, 72(3):943–953, 1999.

[26] F. Bruyere and A. Noel. Lymphangiogenesis: in vitro and in vivo models. *FASEB J.*, 24(1):8–21, 2010.

[27] H. M. Byrne, M. A. J. Chaplain, D. L. Evans, and I. Hopkinson. Mathematical modelling of angiogenesis in wound healing: Comparison of theory and experiment. *J. Theor. Med.*, 2(3):175–197, 2000.

[28] J. Calles-Escandon and M. Cipolla. Diabetes and endothelial dysfunction: a clinical perspective. *Endocr. Rev.*, 22(1):36–52, 2001.

[29] C. Cao, D. A. Lawrence, D. K. Strickland, and L. Zhang. A specific role of integrin Mac-1 in accelerated macrophage efflux to the lymphatics. *Blood*, 106 (9):3234–3241, 2005.

[30] L. Capparuccia and L. Tamagnone. Semaphorin signaling in cancer cells and in cells of the tumor microenvironment–two sides of a coin. *J. Cell. Sci.*, 122 (Pt 11):1723–1736, 2009.

[31] P. Carmeliet and M. Tessier-Lavigne. Common mechanisms of nerve and blood vessel wiring. *Nature*, 436:193–200, 2005.

[32] A. Castiglioni. *A History of Medicine*. Alfred A. Knopf, New York, 1947.

[33] E. Castro-Rivera, S. Ran, P. Thorpe, and J. D. Minna. Semaphorin 3B (SEMA3B) induces apoptosis in lung and breast cancer, whereas VEGF165 antagonizes this effect. *Proc. Natl. Acad. Sci. USA*, 101(31):11432–11437, 2004.

[34] M. A. J. Chaplain. Mathematical modelling of angiogenesis. *J. Neuro-Oncol.*, 50(1-2):37–51, 2000.

[35] A. Chédotal, G. Kerjan, and C. Moreau-Fauvarque. The brain within the tumor: new roles for axon guidance molecules in cancers. *Cell Death and Diff.*, 12:1044–1056, 2005.

[36] S. Cheifetz, H. Hernandez, M. Laiho, P. ten Dijke, K. K. Iwata, and J. Massague. Distinct transforming growth factor-beta (TGF-beta) receptor subsets as determinants of cellular responsiveness to three TGF-beta isoforms. *J. Biol. Chem.*, 265(33):20533–20538, 1990.

[37] C. F. Chiang, E. L. Son, and G. J. Wu. Oral treatment of the TRAMP mice with doxazosin suppresses prostate tumor growth and metastasis. *Prostate*, 64(4):408–418, 2005.

[38] Y. Chida, M. Hamer, J. Wardle, and A. Steptoe. Do stress-related psychosocial factors contribute to cancer incidence and survival? *Nat. Clin. Pract. Oncol.*, 5(8):466–475, 2008.

[39] C.-H. Cho, H.-K. Sung, K.-T. Kim, H. G. Cheon, G. T. Oh, H. J. Hong, O.-J. Yoo, and G. Y. Koh. COMP-angiopoietin-1 promotes wound healing through enhanced angiogenesis, lymphangiogenesis, and blood flow in a diabetic mouse model. *Proc. Natl. Acad. Sci. USA*, 103(13):4946–4951, 2006.

[40] I. Choi, S. Lee, and Y. K. Hong. The new era of the lymphatic system: no longer secondary to the blood vascular system. *Cold Spring Harb. Perspect. Med.*, 2(4):a006445, 2012.

[41] P. Claude, E. Hawrot, D. A. Dunis, and R. B. Campenot. Binding, internalization, and retrograde transport of 125I-nerve growth factor in cultured rat sympathetic neurons. *J. Neurosci.*, 2(4):431–442, 1982.

[42] N. W. Clavin, T. Avraham, J. Fernandez, S. V. Daluvoy, M. A. Soares, A. Chaudhry, and B. J. Mehrara. TGF-β1 is a negative regulator of lymphatic regeneration during wound repair. *Am. J. Physiol. Heart Circ. Physiol.*, 295 (5):H2113–2127, 2008.

[43] M. Cobb, B. Burnet, and K. Connolly. The structure of courtship in the drosophila melanogaster species sub-group. *Behaviour*, 97(1/2):182–212, 1986.

[44] C. A. Cobbold and J. A. Sherratt. Mathematical modelling of nitric oxide activity in wound healing can explain keloid and hypertrophic scarring. *J. Theor. Biol.*, 204:257–288, 2000.

[45] S. W. Cole and A. K. Sood. Molecular pathways: beta-adrenergic signaling in cancer. *Clin. Cancer Res.*, 18(5):1201–1206, 2012.

[46] F. Collins and A. Dawson. Conditioned medium increases the rate of neurite elongation: separation of this activity from the substratum-bound inducer of neurite outgrowth. *J. Neurosci.*, 2(8):1005–1010, 1982.

[47] F. Collins and A. Dawson. An effect of nerve growth factor on parasympathetic neurite outgrowth. *Proc. Natl. Acad. Sci. USA*, 80(7):2091–2094, 1983.

[48] F. Curcio and A. Ceriello. Decreased cultured endothelial cell proliferation in high glucose medium is reversed by antioxidants: new insights on the pathophysiological mechanisms of diabetic vascular complications. *In Vitro Cell. Dev. Biol.*, 28A(11-12):787–790, 1992.

[49] G. Dachille, T. Cai, G. M. Ludovico, G. Vestita, G. Pagliarulo, G. Nesi, S. Mazzoli, F. Meacci, N. Mondaini, B. Detti, and R. Bartoletti. Prognostic role of cell apoptotic rate in prostate cancer: outcome of a long-time follow-up study. *Oncol. Rep.*, 19(2):541–545, 2008.

[50] P. D. Dale, L. Olsen, P. K. Maini, and J. A. Sherratt. Travelling waves in wound healing. *Forma*, 10(3):205–222, 1995.

[51] P. D. Dale, J. A. Sherratt, and P. K. Maini. A mathematical model for collagen fibre formation during foetal and adult dermal wound healing. *Proc. R. Soc. Lond. B*, 263:653–660, 1996.

[52] J. C. Dallon, J. A. Sherratt, and P. K. Maini. Mathematical modelling of extracellular matrix dynamics using discrete cells: fiber orientation and tissue regeneration. *J. Theor. Biol.*, 199(4):449–471, 1999.

[53] I. A. Darby, T. Bisucci, T. D. Hewitson, and D. G. MacLellan. Apoptosis is increased in a model of diabetes-impaired wound healing in genetically diabetic mice. *Intl. J. Biochem. Cell Biol.*, 29(1):191–200, 1997.

[54] G. De Crescenzo, S. Grothe, J. Zwaagstra, M. Tsang, and M. D. O'Connor-McCourt. Real-time monitoring of the interactions of transforming growth factor-β (TGF-β) isoforms with latency-associated protein and the

ectodomains of the TGF-β type II and III receptors reveals different kinetic models and stoichiometries of binding. *J. Biol. Chem.*, 276(32):29632–29643, 2001.

[55] J. I. de la Torre and J. A. Chambers. Chronic wounds. *Medscape (http://emedicine.medscape.com/article/1298452-overview)*, 2013 (updated).

[56] R. Derynck and R. J. Akhurst. BMP-9 balances endothelial cell fate. *Proc. Natl. Acad. Sci.*, 110(47):18746–18747, 2013.

[57] B. Dickson. Molecular mechanisms of axon guidance. *Science*, 298:1959–1964, 2003.

[58] J. F. Dodson. Herophilus of alexandria. *Proc. R. Soc. Med.*, 18:19–32, 1924-5.

[59] C. Dodt, U. Breckling, I. Derad, H. L. Fehm, and J. Born. Plasma epinephrine and norepinephrine concentrations of healthy humans associated with nighttime sleep and morning arousal. *Hypertension*, 30:71–76, 1997.

[60] L. Dolle, I. El Yazidi-Belkoura, E. Adriaenssens, V. Nurcombe, and H. Hondermarck. Nerve growth factor overexpression and autocrine loop in breast cancer cells. *Oncogene*, 22(36):5592–5601, 2003.

[61] L. Dollé, M. Oliveira, E. Bruyneel, H. Hondermarck, and M. Bracke. Nerve growth factor mediates its pro-invasive effect in parallel with the release of a soluble E-cadherin fragment from breast cancer MCF-7/AZ cells. *J. Dairy Research*, 72:20–26, 2005.

[62] J. F. Douglas, J. M. Gasiorek, J. A. Swaffield, and L. B. Jack. *Fluid Mechanics*. Prentice Hall, 5th edition, 2005.

[63] C. Dowsett. Use of TIME to improve community nurses' wound care knowledge and practice. *Wounds UK*, 5(3):14–21, 2009.

[64] T. Drell IV, J. Joseph, K. Lang, B. Niggemann, K. Zaenker, and F. Entschladen. Effects of neurotransmitters on the chemokinesis and chemo-

taxis of MDA-MB-468 human breast carcinoma cells. *Breast Cancer Res. Treat.*, 80:63–70, 2003.

[65] P. Drew, J. Posnett, and L. Rusling. The cost of wound care for a local population in England. *Intl. Wound. J.*, 4(2):149–155, 2007.

[66] J. L. Dunster, H. M. Byrne, and J. R. King. The resolution of inflammation: a mathematical model of neutrophil and macrophage interactions. *Bull. Math. Biol.*, 76(8):1953–1980, 2014.

[67] L. Edelstein. The Propagation of Fungal Colonies: A Model for Tissue Growth. *J. Theor. Biol.*, 98:679–701, 1982.

[68] A. Eichmann, T. Makinen, and K. Alitalo. Neural guidance molecules reuglate vascular remodeling and vessel navigation. *Genes & Devel.*, 19:1013–1021, 2005.

[69] J. W. Eng, K. M. Kokolus, C. B. Reed, B. L. Hylander, W. W. Ma, and E. A. Repasky. A nervous tumor microenvironment: the impact of adrenergic stress on cancer cells, immunosuppression, and immunotherapeutic response. *Cancer Immunol. Immunother.*, 63(11):1115–1128, 2014.

[70] F. Entschladen, K. Lang, T. Drell, J. Joseph, and K. Zaenker. Neurotransmitters are regulators for the migration of tumor cells and leukocytes. *Cancer Immunol. Immunother.*, 51:467–482, 2002.

[71] F. Entschladen, T. L. Drell IV, K. Lang, J. Joseph, and K. S. Zaenker. Tumor-cell migration, invasion, and metastasis: navigation by neurotransmitters. *Lancet Oncol.*, 5:254–258, 2004.

[72] F. Entschladen, D. Palm, K. Lang, T. Drell IV, and K. Zaenker. Neoneurogenesis: Tumors may initiate their own innervation by the release of neurotrophic factors in analogy to lymphangiogenesis and neoangiogenesis. *Med. Hypoth.*, 67:33–35, 2006.

[73] F. Entschladen, D. Palm, K. Drell IV, TLand Lang, and K. Zaenker. Connecting a tumor to the environment. *Curr. Pharm. Des.*, 13(33):3440–3444, 2007.

[74] F. Entschladen, D. Palm, B. Niggemann, and K. Zaenker. The cancer's nervous tooth: Considering the neuronal crosstalk within tumors. *Sem. Canc. Biol.*, 18:171–175, 2008.

[75] A. Eslami, C. L. Gallant-Behm, D. A. Hart, C. Wiebe, D. Honardoust, H. Gardner, L. Hakkinen, and H. S. Larjava. Expression of integrin alphavbeta6 and TGF-beta in scarless vs scar-forming wound healing. *J. Histochem. Cytochem.*, 57(6):543–557, 2009.

[76] M. Esler, G. Jackman, A. Bobik, D. Kelleher, G. Jennings, P. Leonard, H. Skews, and P. Korner. Determination of norepinephrine apparent release rate and clearance in humans. *Life Sci.*, 25:1461–1470, 1979.

[77] G. P. Fadini, M. Albiero, L. Menegazzo, E. Boscaro, E. Pagnin, E. Iori, C. Cosma, A. Lapolla, V. Pengo, M. Stendardo, C. Agostini, P. G. Pelicci, M. Giorgio, and A. Avogaro. The redox enzyme p66Shc contributes to diabetes and ischemia-induced delay in cutaneous wound healing. *Diabetes*, 59 (9):2306–2314, 2010.

[78] B. E. Farrell, R. P. Daniele, and D. A. Lauffenburger. Quantitative relationships between single-cell and cell-population model parameters for chemosensory migration responses of alveolar macrophages to C5a. *Cell Motil. Cytoskeleton*, 16(4):279–293, 1990.

[79] J. C. Fiala and K. M. Harris. Dendrite structure. *Dendrites*, 1999.

[80] I. J. Fidler and S. Paget. The pathogenesis of cancer metastasis: the 'seed and soil' hypothesis revisited. *Nat. Rev. Cancer*, 3(6):453–458, 2003.

[81] K. W. Finnson, S. McLean, G. M. Di Guglielmo, and A. Philip. Dynamics of Transforming Growth Factor Beta Signaling in Wound Healing and Scarring. *Adv. Wound Care*, 2(5):195–214, 2013.

[82] M. Fischer, U. K. Franzeck, I. Herrig, U. Costanzo, S. Wen, M. Schiesser, U. Hoffmann, and A. Bollinger. Flow velocity of single lymphatic capillaries in human skin. *Am. J. Physiol.*, 270:H358–363, 1996.

[83] M. Fischer, U. Costanzo, U. Hoffmann, A. Bollinger, and U. K. Franzeck. Flow velocity of cutaneous lymphatic capillaries in patients with primary lymphedema. *Int. J. Microcirc. Clin. Exp.*, 17(3):143–149, 1997.

[84] R. Fitzhugh. Impulses and Physiological States in Theoretical Models of Nerve Membrane. *Biophys. J.*, 1(6):445–466, Jul 1961.

[85] J. A. Flegg, H. M. Byrne, M. B. Flegg, and D. L. S. McElwain. Wound healing angiogenesis: the clinical implications of a simple mathematical model. *J. Theor. Biol.*, 300:309–316, 2012.

[86] M. E. Fleury, K. C. Boardman, and M. A. Swartz. Autologous morphogen gradients by subtle interstitial flow and matrix interactions. *Biophys. J.*, 91: 113–121, 2006.

[87] S. Friberg and S. Mattson. On the growth rates of human malignant tumors: implications for medical decision making. *J. Surg. Oncol.*, 65(4):284–297, 1997.

[88] R. L. Friede. The relationship of body size, nerve cell size, axon length, and glial density in the cerebellum. *Proc. Natl. Acad. Sci. USA*, 49:187–193, 1963.

[89] A. Friedman and G. Lolas. Analysis of a mathematical model of tumor lymphangiogenesis. *Math. Models Meth. Appl. Sci.*, 15(1):95–107, 2005.

[90] A. Friedman and C. Xue. A mathematical model for chronic wounds. *Math. Biosci. Eng.*, 8(2):253–261, 2011.

[91] A. Gabriel, J. Mussman, L. Z. Rosenberg, and J. I. de la Torre. Wound Healing and Growth Factors. *Medscape (http://emedicine.medscape.com/article/1298196-overview)*, 2013 (updated).

[92] E. A. Gaffney, K. Pugh, P. K. Maini, and F. Arnold. Investigating a simple model of cutaneous wound healing angiogenesis. *J. Math. Biol.*, 45(4):337–374, 2002.

[93] P. Galie and R. L. Spilker. A two-dimensional computational model of lymph transport across primary lymphatic valves. *J. Biomech. Eng.*, 131(11):111004, 2009.

[94] L. Geris, A. Gerisch, and R. C. Schugart. Mathematical modeling in wound healing, bone regeneration and tissue engineering. *Acta Biotheor.*, 58(4):355–367, 2010.

[95] J. Goldman, J. M. Rutkowski, J. D. Shields, M. C. Pasquier, Y. Cui, H. G. Schmokel, S. Willey, D. J. Hicklin, B. Pytowski, and M. A. Swartz. Cooperative and redundant roles of VEGFR-2 and VEGFR-3 signaling in adult lymphangiogenesis. *FASEB J.*, 21(4):1003–1012, 2007.

[96] G. J. Goodhill. Diffusion in axon guidance. *Eur. J. Neurosci.*, 9(7):1414–1421, 1997.

[97] A. Gosiewska, C. Yi, O. Blanc-Brude, and J. C. Geesin. Characterization of a macrophage-based system for studying the activation of latent TGF-β. *Meth. Cell Sci.*, 21:47–56, 1999.

[98] D. J. Grainger, L. Wakefield, H. W. Bethell, R. W. Farndale, and J. C. Metcalfe. Release and activation of platelet latent TGF-beta in blood clots during dissolution with plasmin. *Nat. Med.*, 1(9):932–937, 1995.

[99] R. J. Greenspan and J. F. Ferveur. Courtship in Drosophila. *Annu. Rev. Genet.*, 34:205–232, 2000.

[100] B. Greenwood. The mitosis of sheep blood monocytes in tissue culture. *Quart. J. Exp. Physiol.*, 58:369–377, 1973.

[101] A. C. Guyton and J. E. Hall. *Textbook of medical physiology, Chapter 60.* 11th edition, 2006.

[102] T. L. Haas and B. R. Duling. Morphology favors an endothelial cell pathway for longitudinal conduction within arterioles. *Microvasc. Res.*, 53:113–120, 1997.

[103] L. S. Hansen, J. E. Coggle, J. Wells, and M. W. Charles. The influence of the hair cycle on the thickness of mouse skin. *Anat. Rec.*, 210(4):569–573, 1984.

[104] C. L. Helm, M. E. Fleury, A. H. Zisch, F. Boschetti, and M. A. Swartz. Synergy between interstitial flow and VEGF directs capillary morphogenesis in vitro through a gradient amplification mechanism. *Proc. Natl. Acad. Sci. USA*, 102 (44):15779–15784, 2005.

[105] C. Heppell, T. Roose, and G. Richardson. A model for interstitial drainage through a sliding lymphatic valve. *Bull. Math. Biol.*, 77:1101–1131, 2015.

[106] J. G. Herman and G. G. Meadows. Increased class 3 semaphorin expression modulates the invasive and adhesive properties of prostate cancer cells. *Int. J. Oncol.*, 30(5):1231–1238, 2007.

[107] E. Hormbrey, C. Han, A. Roberts, D. A. McGrouther, and A. L. Harris. The relationship of human wound vascular endothelial growth factor (VEGF) after breast cancer surgery to circulating vegf and angiogenesis. *Clin. Cancer Res.*, 9:4332–4339, 2003.

[108] R. Huggenberger and M. Detmar. The cutaneous vascular system in chronic skin inflammation. *J. Investig. Dermatol. Symp. Proc.*, 15(1):24–32, 2011.

[109] R. Huggenberger, S. S. Siddiqui, D. Brander, S. Ullmann, K. Zimmermann, M. Antsiferova, S. Werner, K. Alitalo, and M. Detmar. An important role of lymphatic vessel activation in limiting acute inflammation. *Blood*, 117(17): 4667–4678, 2011.

[110] M. Hyytiäinen, C. Penttinen, and J. Keski-Oja. Latent TGF-beta binding proteins: extracellular matrix association and roles in TGF-beta activation. *Crit. Rev. Clin. Lab. Sci.*, 41(3):233–264, 2004.

[111] P. I. Imoukhuede and A. S. Popel. Expression of VEGF receptors on endothelial cells in mouse skeletal muscle. *PLOS One*, 7(9):e44791, 2012.

[112] J. T. Isaacs. Cancer. Prostate cancer takes nerve. *Science*, 341(6142):134–135, 2013.

[113] S. Jaques, M. C. Tobes, and J. C. Sisson. Sodium dependency of uptake of norepinephrine and m-iodobenzylguanidine into cultured human pheochromocytoma cells: evidence for uptake-one. *Cancer Res.*, 47(15):3920–3928, 1987.

[114] E. Javierre, F. J. Vermolen, C. Vuik, and S. van der Zwaag. A mathematical analysis of physiological and morphological aspects of wound closure. *J. Math. Biol.*, 59(5):605–630, 2009.

[115] W. J. Jeffcoate and K. G. Harding. Diabetic foot ulcers. *Lancet*, 361(9368): 1545–1551, 2003.

[116] B. H. Jennings. Drosophila – a versatile model in biology & medicine. *Mater. Today*, 14(5):190–195, 2011.

[117] R. C. Ji. Characteristics of lymphatic endothelial cells in physiological and pathological conditions. *Histol. Histopathol.*, 20:155–175, 2005.

[118] L. Jussila and K. Alitalo. Vascular growth factors and lymphangiogenesis. *Physiol. Rev.*, 82(3):673–700, 2002.

[119] S. Kalghatgi, G. Friedman, A. Fridman, and A. M. Clyne. Endothelial cell proliferation is enhanced by low dose non-thermal plasma through fibroblast growth factor-2 release. *Ann. Biomed. Eng.*, 38(3):748–757, 2010.

[120] B. Kaminska, A. Wesolowska, and M. Danilkiewicz. TGF beta signalling and its role in tumor pathogenesis. *Acta Biochimica Polonica*, 52(2):329–337, 2005.

[121] R. P. Kataru, K. Jung, C. Jang, H. Yang, R. A. Schwendener, J. E. Baik, S. H. Han, K. Alitalo, and G. Y. Koh. Critical role of CD11b+ macrophages and VEGF in inflammatory lymphangiogenesis, antigen clearance, and inflammation resolution. *Blood*, 113(22):5650–5659, 2009.

[122] H. Kaur and L. Y. Yung. Probing high affinity sequences of DNA aptamer against VEGF165. *PLOS One*, 7(2):e31196, 2012.

[123] K. Keino-Masu, M. Masu, L. Hinck, E. D. Leonardo, S. S. Chan, J. G. Culotti, and M. Tessier-Lavigne. Deleted in Colorectal Cancer (DCC) encodes a netrin receptor. *Cell*, 87(2):175–185, 1996.

[124] N. Khalil, C. Whitman, L. Zuo, D. Danielpour, and A. Greenberg. Regulation of alveolar macrophage transforming growth factor-β secretion by corticosteroids in bleomycin-induced pulmonary inflammation in the rat. *J. Clin. Invest.*, 92:1812–1818, 1993.

[125] N. Khalil, S. Corne, C. Whitman, and H. Yacyshyn. Plasmin regulates the activation of cell-associated latent TGF-beta 1 secreted by rat alveolar macrophages after in vivo bleomycin injury. *Am. J. Respir. Cell Mol. Biol.*, 15(2): 252–259, Aug 1996.

[126] S. Khanna, S. Biswas, Y. Shang, E. Collard, A. Azad, C. Kauh, V. Bhasker, G. M. Gordillo, C. K. Sen, and S. Roy. Macrophage dysfunction impairs resolution of inflammation in the wounds of diabetic mice. *PLOS One*, 5(3): e9539, 2010.

[127] J. Kien and J. S. Altman. Modelling the generation of long-term neuronal activity underlying behaviour. *Progress in Neurobiology*, 45:361–372, 1995.

[128] B. Kigel, A. Varshavsky, O. Kessler, and G. Neufeld. Successful inhibition of tumor development by specific class-3 semaphorins is associated with expression of appropriate semaphorin receptors by tumor cells. *PLOS One*, 3(9): e3287, 2008.

[129] H. Kim, R. P. Kataru, and G. Y. Koh. Regulation and implications of inflammatory lymphangiogenesis. *Trends Immunol.*, 33(7):350–356, 2012.

[130] S. Kiriakidis, E. Andreakos, C. Monaco, B. Foxwell, M. Feldmann, and E. Paleolog. VEGF expression in human macrophages is NF-κB-dependent: studies

using adenoviruses expressing the endogenous NF-κB inhibitor IκBα and a kinase-defective form of the IκB kinase 2. *J. Cell Sci.*, 116(4):665–674, 2003.

[131] J. Kleinheinz, S. Jung, K. Wermker, C. Fischer, and U. Joos. Release kinetics of $VEGF_{165}$ from a collagen matrix and structural matrix changes in a circulation model. *Head Face Med.*, 6:6–17, 2010.

[132] G. K. Kolluru, S. C. Bir, and C. G. Kevil. Endothelial dysfunction and diabetes: effects on angiogenesis, vascular remodeling, and wound healing. *Intl. J. Vasc. Med.*, 2012:918267, 2012.

[133] K. S. Korolev, J. B. Xavier, and J. Gore. Turning ecology and evolution against cancer. *Nature Rev. Canc.*, 14(5):371–380, 2014.

[134] F. Krombach, S. Munzing, A. M. Allmeling, J. T. Gerlach, J. Behr, and M. Dorger. Cell size of alveolar macrophages: an interspecies comparison. *Environ. Health Perspect.*, pages 1261–1263, 1997.

[135] M. S. Kuzirian, A. R. Moore, E. K. Staudenmaier, R. H. Friedel, and S. Paradis. The class 4 semaphorin Sema4D promotes the rapid assembly of GABAergic synapses in rodent hippocampus. *J. Neurosci.*, 33(21):8961–8973, 2013.

[136] R. Kvetnansky, K. Pacak, K. Fukuhara, E. Viskupic, B. Hiremagalur, B. Nankova, D. S. Goldstein, E. L. Sabban, and I. J. Kopin. Sympathoadrenal system in stress. Interaction with the hypothalamic-pituitary-adrenocortical system. *Ann. N. Y. Acad. Sci.*, 771:131–158, 1995.

[137] K. Lang and P. Bastian. Neurotransmitter effects on tumor cells and leukocytes. *Prog. Exp. Tumor Res.*, 39:99–121, 2007.

[138] K. Lang, T. Drell IV, B. Niggemann, K. Zänker, and F. Entschladen. Neurotransmitters regulate the migration and cytotoxicity in natural killer cells. *Immunol. Letters*, 90:165–172, 2003.

[139] A. Langer and W. Rogowski. Systematic review of economic evaluations of human cell-derived wound care products for the treatment of venous leg and diabetic foot ulcers. *BMC Health Serv. Res.*, 9:115, 2009.

[140] S. Lee, H. J. Hwang, and Y. Kim. Modeling the role of TGF-β in regulation of the Th17 phenotype in the LPS-driven immune system. *Bull. Math. Biol.*, 76(5):1045–1080, 2014.

[141] O. Z. Lerman, R. D. Galiano, M. Armour, J. P. Levine, and G. C. Gurtner. Cellular dysfunction in the diabetic fibroblast: impairment in migration, vascular endothelial growth factor production, and response to hypoxia. *Am. J. Pathol.*, 162(1):303–312, 2003.

[142] A. Li, S. Dubey, M. L. Varney, B. J. Dave, and R. K. Singh. IL-8 directly enhanced endothelial cell survival, proliferation, and matrix metalloproteinases production and regulated angiogenesis. *J. Immunol.*, 170(6):3369–3376, 2003.

[143] N. Li Jeon, H. Baskaran, S. K. Dertinger, G. M. Whitesides, L. Van de Water, and M. Toner. Neutrophil chemotaxis in linear and complex gradients of interleukin-8 formed in a microfabricated device. *Nat. Biotechnol.*, 20(8):826–830, 2002.

[144] S. Liao, J. Liu, P. Lin, T. Shi, R. K. Jain, and L. Xu. TGF-β blockade controls ascites by preventing abnormalization of lymphatic vessels in orthotopic human ovarian carcinoma models. *Clin. Cancer Res.*, 17(6):1415–1424, 2011.

[145] J. Liepe, P. Kirk, T. Filippi, Sarah andToni, C. P. Barnes, and M. P. H. Stumpf. A framework for parameter estimation and model selection from experimental data in systems biology using approximate Bayesian computation. *Nat. Protoc.*, 9:439–456, 2014.

[146] R. M. Lindsay. Nerve growth factors (NGF, BDNF) enhance axonal regeneration but are not required for survival of adult sensory neurons. *J. Neurosci.*, 8(7):2394–2405, 1988.

[147] L. Liotta. An attractive force in metastasis. *Nature*, 410:24–25, 2001.

[148] M. Lohela, A. Saaristo, T. Veikkola, and K. Alitalo. Lymphangiogenic growth factors, receptors and therapies. *Thromb. Haemost.*, 90(2):167–184, 2003.

[149] M. Lohela, M. Bry, T. Tammela, and K. Alitalo. VEGFs and receptors involved in angiogenesis versus lymphangiogenesis. *Curr. Opin. Cell Biol.*, 21 (2):154–165, 2009.

[150] A. Louveau, I. Smirnov, T. J. Keyes, J. D. Eccles, S. J. Rouhani, J. D. Peske, N. C. Derecki, D. Castle, J. W. Mandell, K. S. Lee, T. H. Harris, and J. Kipnis. Structural and functional features of central nervous system lymphatic vessels. *Nature*, 523(7560):337–341, 2015.

[151] S. Lü, Y. Zhou, H. Que, and S. Liu. Peptidergic innervation of human esophageal and cardiac carcinoma. *World J. Gastroenterol.*, 9(3):399–403, 2003.

[152] D. Ludwig, D. G. Aronson, and H. F. Weinberger. Spatial Patterning of the Spruce Budworm. *J. Math. Biology*, 8:217–258, 1979.

[153] R. Luo, L. Tang, S. Zhong, Z. Yang, J. Wang, Y. Weng, Q. Tu, C. Jiang, and N. Huang. In vitro investigation of enhanced hemocompatibility and endothelial cell proliferation associated with quinone-rich polydopamine coating. *ACS Appl. Mater. Interf.*, 5(5):1704–1714, 2013.

[154] S. K. Lutgendorf, K. DeGeest, L. Dahmoush, D. Farley, F. Penedo, D. Bender, M. Goodheart, T. E. Buekers, L. Mendez, G. Krueger, L. Clevenger, D. M. Lubaroff, A. K. Sood, and S. W. Cole. Social isolation is associated with elevated tumor norepinephrine in ovarian carcinoma patients. *Brain Behav. Immun.*, 25(2):250–255, 2011.

[155] F. Mac Gabhann and A. S. Popel. Model of competitive binding of vascular endothelial growth factor and placental growth factor to VEGF receptors on endothelial cells. *Am. J. Physiol. Heart Circ. Physiol.*, 286:H153–H164, 2004.

[156] F. Mac Gabhann, J. W. Ji, and A. S. Popel. VEGF gradients, receptor activation, and sprout guidance in resting and exercising skeletal muscle. *J. Appl. Physiol.*, 102:722–734, 2007.

[157] A. J. Macdonald, K. P. Arkill, G. R. Tabor, N. G. McHale, and C. P. Winlove. Modeling flow in collecting lymphatic vessels: one-dimensional flow through a series of contractile elements. *Am. J. Physiol. Heart Circ. Physiol.*, 295(1): H305–313, 2008.

[158] M. J. Machado, M. G. Watson, A. H. Devlin, M. A. Chaplain, S. R. McDougall, and C. A. Mitchell. Dynamics of angiogenesis during wound healing: a coupled in vivo and in silico study. *Microcirculation*, 18(3):183–197, 2011.

[159] C. Magnon. Role of the autonomic nervous system in tumorigenesis and metastasis. *Molec. & Cell. Oncol.*, 2(2):e975643, 2015.

[160] C. Magnon, S. Hall, J. Lin, X. Xue, L. Gerber, S. Freedland, and P. Frenette. Autonomic nerve development contributes to prostate cancer progression. *Science*, 341:1236361, 2013.

[161] C. Manitt, M. A. Colicos, K. M. Thompson, E. Rousselle, A. C. Peterson, and T. E. Kennedy. Widespread expression of netrin-1 by neurons and oligodendrocytes in the adult mammalian spinal cord. *J. Neurosci.*, 21(11):3911–3922, 2001.

[162] H. Mannell, A. Hammitzsch, R. Mettler, U. Pohl, and F. Krotz. Suppression of DNA-PKcs enhances FGF-2 dependent human endothelial cell proliferation via negative regulation of Akt. *Cell. Signal.*, 22(1):88–96, 2010.

[163] A. Mantovani, A. Sica, S. Sozzani, P. Allavena, A. Vecchi, and M. Locati. The chemokine system in diverse forms of macrophage activation and polarization. *Trends Immunol.*, 25(12):677–686, 2004.

[164] K. N. Margaris and R. A. Black. Modelling the lymphatic system: challenges and opportunities. *J. R. Soc. Interf.*, 9(69):601–612, 2012.

[165] T. A. Markow and S. J. Hanson. Multivariate analysis of drosophila courtship. *Proc. Natl. Acad. Sci. USA*, 78:430–434, 1981.

[166] F. O. Martinez, S. Gordon, M. Locati, and A. Mantovani. Transcriptional profiling of the human monocyte-to-macrophage differentiation and polarization: new molecules and patterns of gene expression. *J. Immunol.*, 177(10): 7303–7311, 2006.

[167] K. Maruyama, J. Asai, M. Ii, T. Thorne, D. W. Losordo, and P. A. D'Amore. Decreased macrophage number and activation lead to reduced lymphatic vessel formation and contribute to impaired diabetic wound healing. *Am. J. Pathol.*, 70:1178–1191, 2007.

[168] T. Matsumoto and L. Claesson-Welsh. VEGF receptor signal transduction. *Science STKE*, 2001(112):re21, 2001.

[169] M. T. G. T. May. *Galen On the Usefulness of the Parts of the Body, Part II.* Cornell University Press, Ithaca, NY, 1968.

[170] P. Mehlen, C. Delloye-Bourgeois, and A. Chedotal. Novel roles for Slits and netrins: axon guidance cues as anticancer targets? *Nat. Rev. Cancer*, 11(3): 188–197, 2011.

[171] E. Mendoza and G. W. Schmid-Schönbein. A model for mechanics of primary lymphatic valves. *J. Biomech. Eng.*, 125:407–414, 2003.

[172] L. E. Miller, H. P. Justen, J. Scholmerich, and R. H. Straub. The loss of sympathetic nerve fibers in the synovial tissue of patients with rheumatoid arthritis is accompanied by increased norepinephrine release from synovial macrophages. *FASEB J.*, 14(13):2097–2107, 2000.

[173] R. Mirza and T. J. Koh. Dysregulation of monocyte/macrophage phenotype in wounds of diabetic mice. *Cytokine*, 56:256–264, 2011.

[174] T. Miura and R. Tanaka. *In vitro* vasculogenesis models revisited - mea-

surement of VEGF diffusion in matrigel. *Math. Model. Nat. Phenom.*, 4(4): 118–130, 2009.

[175] M. Moreno-Smith, S. K. Lutgendorf, and A. K. Sood. Impact of stress on cancer metastasis. *Future Oncol.*, 6(12):1863–1881, 2010.

[176] B. Mravec, Y. Gidron, and I. Hulin. Neurobiology of cancer: Interactions between nervous, endocrine and immune systems as a base for monitoring and modulating the tumorigenesis by the brain. *Sem. Canc. Biol.*, 18:150–163, 2008.

[177] A. C. Mullen, D. A. Orlando, J. J. Newman, J. Loven, R. M. Kumar, S. Bilodeau, J. Reddy, M. G. Guenther, R. P. DeKoter, and R. A. Young. Master transcription factors determine cell-type-specific responses to TGF-β signaling. *Cell*, 147(3):565–576, 2011.

[178] G. Müller, J. Behrens, U. Nussbaumer, P. Böhlen, and W. Birchmeier. Inhibitory action of transforming growth factor β on endothelial cells. *Proc. Natl. Acad. Sci. USA*, 84:5600–5604, 1987.

[179] K. E. Murphy, C. L. Hall, P. K. Maini, S. W. McCue, and D. L. S. McElwain. A fibrocontractive mechanochemical model of dermal wound closure incorporating realistic growth factor kinetics. *Bull. Math. Biol.*, 74(5):1143–1170, 2012.

[180] R. A. Murphy, J. D. Saide, M. H. Blanchard, and M. Young. Molecular properties of the nerve growth factor secreted in mouse saliva. *Proc. Natl. Acad. Sci. USA*, 74(7):2672–2676, 1977.

[181] J. Nagumo, S. Arimoto, and S. Yoshizawa. An active pulse transmission line simulating 1214-nerve axons. *Proc. IRL*, 50:2061–2070, 1970.

[182] S. Nakao, K. Maruyama, S. Zandi, M. I. Melhorn, M. Taher, K. Noda, E. Nusayr, T. Doetschman, and A. Hafezi-Moghadam. Lymphangiogenesis and angiogenesis: concurrence and/or dependence? Studies in inbred mouse strains. *FASEB J.*, 24(2):504–513, 2010.

[183] V. P. K. H. Nguyen, S. H. Chen, J. Trinh, H. Kim, B. L. Coomber, and D. J. Dumont. Differential response of lymphatic, venous and arterial endothelial cells to angiopoietin-1 and angiopoietin-2. *BMC Cell Biol.*, pages 8–10, 2007.

[184] J. C. Nickel. Benign prostatic hyperplasia: does prostate size matter? *Rev. Urol.*, pages S12–17, 2003.

[185] B. Nico, D. Mangieri, V. Benagiano, E. Crivellato, and D. Ribatti. Nerve growth factor as an angiogenic factor. *Microvasc. Res.*, 75(2):135–141, 2008.

[186] J. E. Nör, L. DiPietro, J. E. Murphy-Ullrich, R. O. Hynes, J. Lawler, and P. J. Polverini. Activation of latent TGF-β1 by thrombospondin-1 is a major component of wound repair. *Oral Biosci. Med.*, 2(2):153–161, 2005.

[187] C. Norrmen, T. Tammela, T. V. Petrova, and K. Alitalo. Biological basis of therapeutic lymphangiogenesis. *Circulation*, 123(12):1335–1351, 2011.

[188] I. Nunes, R. L. Shapiro, and D. B. Rifkin. Characterization of latent TGF-β activation by murine peritoneal macrophages. *J. Immunol.*, 155:1450–1459, 1995.

[189] M. Oi, T. Yamamoto, and K. Nishioka. Increased expression of TGF-β1 in the sclerotic skin in bleomycin-'susceptible' mouse strains. *J. Med. Dent. Sci.*, 51:7–17, 2004.

[190] M. Oka, C. Iwata, H. I. Suzuki, K. Kiyono, Y. Morishita, T. Watabe, A. Komuro, M. R. Kano, and K. Miyazono. Inhibition of endogenous TGF-beta signaling enhances lymphangiogenesis. *Blood*, 111(9):4571–4579, 2008.

[191] G. Oliver and M. Detmar. The rediscovery of the lymphatic system: old and new insights into the development and biological function of the lymphatic vasculature. *Genes Dev.*, 16(7):773–783, 2002.

[192] L. Olsen, P. Maini, and J. A. Sherratt. A mechanochemical model for normal and abnormal dermal wound repair. *Nonlinear Anal.*, 30(6):3333–3338, 1997.

[193] K. Ondicova and B. Mravec. Role of nervous system in cancer aetiopathogenesis. *Lancet Oncol.*, 11:596–601, 2010.

[194] D. Palm and F. Entschladen. Neoneurogenesis and the neuro-neoplastic synapse. *Prog. Exp. Tumor Res. Basel, Karger*, 39:91–98, 2007.

[195] Y. Pan, C. C. Robinett, and B. S. Baker. Turning males on: activation of male courtship behavior in drosophila melanogaster. *PLOS One*, 6:e21144, 2011.

[196] A. I. Papaioannou, E. Zakynthinos, K. Kostikas, T. Kiropoulos, A. Koutsokera, A. Ziogas, A. Koutroumpas, L. Sakkas, K. I. Gourgoulianis, and Z. D. Daniil. Serum VEGF levels are related to the presence of pulmonary arterial hypertension in systemic sclerosis. *BMC Pulm. Med.*, pages 9–18, 2009.

[197] N. J. Park, L. Allen, and V. R. Driver. Updating on understanding and managing chronic wound. *Dermatol. Ther.*, 26(3):236–256, 2013.

[198] S. Park, R. R. Ang, S. P. Duffy, J. Bazov, K. N. Chi, P. C. Black, and H. Ma. Morphological differences between circulating tumor cells from prostate cancer patients and cultured prostate cancer cells. *PLOS ONE*, 9(1):e85264, 2014.

[199] F. Pasemann. Discrete dynamics of two neuron networks. *Open Sys. & Inf. Dyn.*, 2(1):49–66, 1993.

[200] F. Pasemann. Neuromodules: A dynamical systems approach to brain modelling. In H. Herrman, D. Wolf, and E. Pöppel, editors, *Herrmann*, pages 331–347. Supercomputing in Brain Research - From Tomography to Neural Networks, 1995.

[201] W. D. Paton, E. S. Vizi, and M. A. Zar. The mechanism of acetylcholine release from parasympathetic nerves. *J. Physiol. (Lond.)*, 215(3):819–848, 1971.

[202] H. J. Pavlou. *Intersecting doublesex neurons underlying sexual behaviours in Drosophila melanogaster*. University of Oxford, UK, 2014.

[203] M. S. Pepper and G. Lolas. The lymphatic vascular system in lymphangiogenesis, invasion and metastasis: A mathematical approach. *Selected Topics*

in Cancer Modeling, Modeling and Simulation in Science, Engineering and Technology, pages 1–22, 2008.

[204] G. Pettet, M. A. Chaplain, D. L. McElwain, and H. M. Byrne. On the rôle of angiogenesis in wound healing. *Proc. Biol. Sci.*, 263(1376):1487–1493, 1996.

[205] K. J. Pienta, H. Naik, A. Akhtar, K. Yamazaki, T. S. Replogle, J. Lehr, T. L. Donat, L. Tait, V. Hogan, and A. Raz. Inhibition of spontaneous metastasis in a rat prostate cancer model by oral administration of modified citrus pectin. *J. Natl. Cancer Inst.*, 87(5):348–353, 1995.

[206] K. J. Pienta, N. McGregor, R. Axelrod, and D. E. Axelrod. Ecological therapy for cancer: defining tumors using an ecosystem paradigm suggests new opportunities for novel cancer treatments. *Transl. Oncol.*, 1(4):158–164, 2008.

[207] G. F. Pierce. Inflammation in nonhealing diabetic wounds: the space-time continuum does matter. *Am. J. Pathol.*, 159(2):399–403, 2001.

[208] M. J. Plank, B. D. Sleeman, and P. F. Jones. A mathematical model of tumor angiogenesis, regulated by vascular endothelial growth factor and the angiopoietins. *J. Theor. Biol.*, 229:435–454, 2004.

[209] S. Podgrabinska, P. Braun, P. Velasco, B. Kloos, M. S. Pepper, D. Jackson, and M. Skobe. Molecular characterization of lymphatic endothelial cells. *Proc. Natl. Acad. Sci. USA*, 99(25):16069–16074, 2002.

[210] J. F. Poduslo and G. L. Curran. Permeability at the blood-brain and blood-nerve barriers of the neurotrophic factors: NGF, CNTF, NT-3, BDNF. *Brain Res. Mol. Brain Res.*, 36(2):280–286, 1996.

[211] J. Posnett and P. J. Franks. The burden of chronic wounds in the UK. *Nurs. Times*, 104(3):44–45, 2008.

[212] E. M. Rakowicz-Szulczynska. Identification of the cell surface and nuclear receptors for NGF in a breast carcinoma cell line. *J. Cell. Physiol.*, 154(1): 64–70, 1993.

[213] N. P. Reddy and K. Patel. A mathematical model of flow through the terminal lymphatics. *Med. Eng. Phys.*, 17(2):134–140, 1995.

[214] L. T. Reiter, L. Potocki, S. Chien, M. Gribskov, and E. Bier. A systematic analysis of human disease-associated gene sequences in drosophila melanogaster. *Genome Res.*, 11(6), 2001.

[215] A. Ricci, S. Greco, S. Mariotta, L. Felici, E. Bronzetti, A. Cavazzana, G. Cardillo, F. Amenta, A. Bisetti, and G. Barbolini. Neurotrophins and neurotrophin receptors in human lung cancer. *Am. J. Respir. Cell Mol. Biol.*, 25:439–446, 2001.

[216] E. J. Rideout, A. J. Dornan, M. C. Neville, S. Eadie, and S. F. Goodwin. Control of sexual differentiation and behavior by the doublesex gene in drosophila melanogaster. *Nat. Neurosci.*, 13(4):458–466, 2010.

[217] M. P. Rodero and K. Khosrotehrani. Skin wound healing modulation by macrophages. *Intl. J. Clin. Exp. Pathol.*, 3(7):643–653, 2010.

[218] T. Roose and A. C. Fowler. Network development in biological gels: role in lymphatic vessel development. *Bull. Math. Biol.*, 70(6):1772–1789, 2008.

[219] R. Roskoski Jr. Vascular endothelial growth factor (VEGF) signaling in tumor progression. *Crit. Rev. Onc./Hem.*, 62:179–213, 2007.

[220] K. G. Ruit, P. A. Osborne, R. E. Schmidt, E. M. Johnson, and W. D. Snider. Nerve growth factor regulates sympathetic ganglion cell morphology and survival in the adult mouse. *J. Neurosci.*, 10(7):2412–2419, 1990.

[221] W. M. S. Russell and R. L. Burch. *The Principles of Humane Experimental Technique*. Methuen, London, 1959.

[222] J. M. Rutkowski and M. A. Swartz. A driving force for change: interstitial flow as a morphoregulator. *Trends Cell Biol.*, 17(1):44–50, 2007.

[223] J. M. Rutkowski, K. C. Boardman, and M. A. Swartz. Characterization of lymphangiogenesis in a model of adult skin regeneration. *Am. J. Physiol. Heart. Circ. Physiol.*, 291:H1402–H1410, 2006.

[224] A. Saaristo, T. Tammela, A. Farkkila, M. Karkkainen, E. Suominen, S. Yla-Herttuala, and K. Alitalo. Vascular endothelial growth factor-C accelerates diabetic wound healing. *Am. J. Pathol.*, 169:1080–1087, 2006.

[225] H. P. Schmid, J. E. McNeal, and T. A. Stamey. Observations on the doubling time of prostate cancer. The use of serial prostate-specific antigen in patients with untreated disease as a measure of increasing cancer volume. *Cancer*, 71 (6):2031–2040, 1993.

[226] R. C. Schugart, A. Friedman, R. Zhao, and C. K. Sen. Wound angiogenesis as a function of tissue oxygen tension: a mathematical model. *Proc. Natl. Acad. Sci. USA*, 105(7):2628–2633, 2008.

[227] J. S. Schuman, T. Pedut-Kloizman, E. Hertzmark, M. R. Hee, J. R. Wilkins, J. G. Coker, C. A. Puliafito, J. G. Fujimoto, and E. A. Swanson. Reproducibility of nerve fiber layer thickness measurements using optical coherence tomography. *Ophthalmol.*, 103(11):1889–1898, 1996.

[228] C. Schusterreiter and W. Grossmann. A two-fly tracker that solves occlusions by dynamic programming: computational analysis of Drosophila courtship behaviour. *EURASIP J. Im. Video Process.*, 64, 2013.

[229] M. Scianna, C. G. Bell, and L. Preziosi. A review of mathematical models for the formation of vascular networks. *J. Theor. Biol.*, 333:174–209, 2013.

[230] M. Shah, D. M. Foreman, and M. W. Ferguson. Neutralisation of TGF-beta 1 and TGF-beta 2 or exogenous addition of TGF-beta 3 to cutaneous rat wounds reduces scarring. *J. Cell. Sci.*, 108 (Pt 3):985–1002, 1995.

[231] R. Shaltiel-Karyo, D. Davidi, Y. Menuchin, M. Frenkel-Pinter, M. Marcus-Kalish, J. Ringo, E. Gazit, and D. Segal. A novel, sensitive assay for behavioral

defects in parkinson's disease model drosophila. *Parkinsons. Dis.*, 2012:1–6, 2012.

[232] L. V. Sharova, A. A. Sharov, T. Nedorezov, Y. Piao, N. Shaik, and M. S. Ko. Database for mRNA half-life of 19 977 genes obtained by DNA microarray analysis of pluripotent and differentiating mouse embryonic stem cells. *DNA Res.*, 16(1):45–58, 2009.

[233] A. Y. Sheikh, J. J. Gibson, M. D. Rollins, H. W. Hopf, Z. Hussain, and T. K. Hunt. Effect of hyperoxia on vascular endothelial growth factor levels in wound model. *Arch. Surg.*, 135:1293–1297, 2000.

[234] J. A. Sherratt and J. C. Dallon. Theoretical models of wound healing: past successes and future challenges. *C. R. Biol.*, 325(5):557–564, 2002.

[235] J. A. Sherratt and J. D. Murray. Models of epidermal wound healing. *Proc. R. Soc. Lond. B*, 241:29–36, 1990.

[236] M. Shi, J. Zhu, R. Wang, X. Chen, L. Mi, T. Walz, and T. A. Springer. Latent TGF-β structure and activation. *Nature*, 474:343–351, 2011.

[237] R. D. Sinclair and T. J. Ryan. Proteolytic enzymes in wound healing: the role of enzymatic debridement. *Australas. J. Dermatol.*, 35(1):35–41, 1994.

[238] A. J. Singer and R. A. Clark. Cutaneous wound healing. *N. Engl. J. Med.*, 341(10):738–746, 1999.

[239] M. A. Sortino, F. Condorelli, C. Vancheri, A. Chiarenza, R. Bernardini, U. Consoli, and P. L. Canonico. Mitogenic effect of nerve growth factor (NGF) in LNCaP prostate adenocarcinoma cells: role of the high- and low-affinity NGF receptors. *Mol. Endocrinol.*, 14(1):124–136, 2000.

[240] W. K. Stadelmann, A. G. Digenis, and G. R. Tobin. Physiology and healing dynamics of chronic cutaneous wounds. *Am. J. Surg.*, 176(2A Suppl):26S–38S, 1998.

[241] W. D. Stein, W. D. Figg, W. Dahut, A. D. Stein, M. B. Hoshen, D. Price, S. E. Bates, and T. Fojo. Tumor growth rates derived from data for patients in a clinical trial correlate strongly with patient survival: A novel strategy for evaluation of clinical trial data. *The Oncologist*, 13:1046–1054, 2008.

[242] A. B. Sutton, A. E. Canfield, S. L. Schor, M. E. Grant, and A. M. Schor. The response of endothelial cells to TGFβ-1 is dependent upon cell shape, proliferative state and the nature of the substratum. *J. Cell Sci.*, 99:777–787, 1991.

[243] M. A. Swartz. The physiology of the lymphatic system. *Adv. Drug Deliv. Rev.*, 50(1-2):3–20, 2001.

[244] R. S. Sweat, P. C. Stapor, and W. L. Murfee. Relationships between lymphangiogenesis and angiogenesis during inflammation in rat mesentery microvascular networks. *Lymphat. Res. Biol.*, 10(4):198–207, 2012.

[245] M. E. Swift, A. L. Burns, K. L. Gray, and L. A. DiPietro. Age-related alterations in the inflammatory response to dermal injury. *J. Invest. Dermatol.*, 117(5):1027–1035, 2001.

[246] K. Syrigos. *Prostate Cancer: Biology, Diagnosis and Management*. Oxford University Press, USA, 2001.

[247] T. Tammela and K. Alitalo. Lymphangiogenesis: Molecular mechanisms and future promise. *Cell*, 140:460–476, 2010.

[248] B. Tang, M. Wang, and B. Wise. Nerve growth factor mRNA stability is controlled by a cis-acting instability determinant in the 3'-untranslated region. *Brain Res. Mol. Brain Res.*, 46(1-2):118–126, 1997.

[249] H. L. Taubin, B. Djahanguiri, and L. Landsberg. Noradrenaline concentration and turnover in different regions of the gastrointestinal tract of the rat: an approach to the evaluation of sympathetic activity in the gut. *Gut*, 13(10): 790–795, 1972.

[250] A. W. Taylor. Review of the activation of TGF-β in immunity. *J. Leukocyte Biol.*, 85:29–33, 2009.

[251] P. H. Thaker and A. K. Sood. Neuroendocrine influences on cancer biology. *Semin. Cancer Biol.*, 18(3):164–170, 2008.

[252] K. Thiébault, L. Mazelin, L. Pays, F. Llambi, M. Joly, J. Scoazec, J. Saurin, G. Romeo, and P. Mehlen. The netrin-1 receptors UNC5H are putative tumor suppressors controlling cell death commitment. *Proc. Natl. Acad. Sci. USA*, 100(7):4173–4178, 2003.

[253] T. Toni, D. Welch, N. Strelkowa, A. Ipsen, and M. P. H. Stumpf. Approximate Bayesian computation scheme for parameter inference and model selection in dynamical systems. *J. R. Soc. Interface*, 6:187–202, 2009.

[254] R. T. Tranquillo and J. D. Murray. Continuum model of fibroblast-driven wound contraction: inflammation-mediation. *J. Theor. Biol.*, 158(2):135–172, 1992.

[255] R. T. Tranquillo, S. H. Zigmond, and D. A. Lauffenburger. Measurement of the chemotaxis coefficient for human neutrophils in the under-agarose migration assay. *Cell Motil. Cytoskeleton*, 11(1):1–15, 1988.

[256] S. Tsai, Y. Liu, . Li, T. Huang, and C. Lee. Sesamin inhibits vascular endothelial cell growth and angiogenic activity of lung adenocarcinoma cells. *J. Cancer Mol.*, 2(5):199–205, 2006.

[257] J. H. University. Animal care and use committee – the mouse. URL `http://web.jhu.edu/animalcare/procedures/mouse.html`.

[258] B. M. van den Berg, H. Vink, and J. A. E. Spaan. The endothelial glycocalyx protects against myocardial edema. *Circ. Res.*, 92:592–594, 2003.

[259] L. A. van Meeteren and P. ten Dijke. Regulation of endothelial cell plasticity by TGF-β. *Cell Tissue Res.*, 347(1):177–186, 2012.

[260] J. J. L. Velázquez. Point Dynamics in a Singular Limit of the Keller–Segel Model 1: Motion of the Concentration Regions. *SIAM J. Appl. Math.*, 64(4): 1198–1223, 2004.

[261] J. J. L. Velázquez. Point Dynamics in a Singular Limit of the Keller–Segel Model 2: Formation of the Concentration Regions. *SIAM J. Appl. Math.*, 64 (4):1224–1248, 2004.

[262] A. Villers, J. McNeal, E. Redwine, F. Freiha, and T. Stamey. The role of perineural space invasion in the local spread of prostatic adenocarcinoma. *J. Urol.*, 142(3):763–768, 1989.

[263] E. Vissoci Reiche, S. Odebrecht Vargas Nunes, and H. Kaminami Morimoto. Stress, depression, the immune system, and cancer. *The Lancet Oncol.*, 5: 617–625, 2004.

[264] H. von Staden. *Herophilus [and] The Art of Medicine in Early Alexandria.* Cambridge University Press, Cambridge, UK, 1989.

[265] S. M. Wahl, D. A. Hunt, L. M. Wakefield, N. McCartney-Francis, L. M. Wahl, A. B. Roberts, and M. B. Sporn. Transforming growth factor type β induces monocyte chemotaxis and growth factor production. *Proc. Natl. Acad. Sci. USA*, 84:5788–5792, 1987.

[266] L. M. Wakefield, D. M. Smith, K. C. Flanders, and M. B. Sporn. Latent transforming growth factor-beta from human platelets. A high molecular weight complex containing precursor sequences. *J. Biol. Chem.*, 263(16):7646–7654, 1988.

[267] K. H. Wang, K. Brose, D. Arnott, T. Kidd, C. S. Goodman, W. Henzel, and M. Tessier-Lavigne. Biochemical purification of a mammalian slit protein as a positive regulator of sensory axon elongation and branching. *Cell*, 96(6): 771–784, Mar 1999.

[268] T. Watabe, A. Nishihara, K. Mishima, J. Yamashita, K. Shimizu, K. Miyazawa, S. Nishikawa, and K. Miyazono. TGF-β receptor kinase inhibitor

enhances growth and integrity of embryonic stem cell-derived endothelial cells. *J. Cell Biol.*, 163(6):1303–1311, 2003.

[269] M. Watanabe, A. Kimura, K. Akasaka, and S. Hayashi. Determination of acetylcholine in human blood. *Biochem. Med. Metab. Biol.*, 36(3):355–362, 1986.

[270] K. Watari, S. Nakao, A. Fotovati, Y. Basaki, F. Hosoi, B. Bereczky, R. Higuchi, T. Miyamoto, M. Kuwano, and M. Ono. Role of macrophages in inflammatory lymphangiogenesis: Enhanced production of vascular endothelial growth factor C and D through NF-kappaB activation. *Biochem. Biophys. Res. Commun.*, 377(3):826–831, 2008.

[271] H. V. Waugh and J. A. Sherratt. Macrophage dynamics in diabetic wound healing. *Bull. Math. Biol.*, 68:197–207, 2006.

[272] K. Weber-Matthiesen and W. Sterry. Organization of the monocyte/-macrophage system of normal human skin. *J. Invest. Dermatol.*, 95:83–89, 1990.

[273] I. Wessler and C. J. Kirkpatrick. Acetylcholine beyond neurons: the non-neuronal cholinergic system in humans. *Br. J. Pharmacol.*, 154(8):1558–1571, 2008.

[274] I. Wessler, T. Reinheimer, H. Kilbinger, F. Bittinger, C. J. Kirkpatrick, J. Saloga, and J. Knop. Increased acetylcholine levels in skin biopsies of patients with atopic dermatitis. *Life Sci.*, 72(18-19):2169–2172, 2003.

[275] B. Whitehurst, C. Eversgerd, M. Flister, C. M. Bivens, B. Pickett, D. C. Zawieja, and S. Ran. Molecular profile and proliferative responses of rat lymphatic endothelial cells in culture. *Lymph. Res. Biol.*, 4(3):119–142, 2006.

[276] E. T. T. Withington. *Hippocrates On Joints*, volume 3. Harvard University Press, Cambridge, MA, 1984.

[277] M. H. Witte, M. J. Bernas, C. P. Martin, and C. L. Witte. Lymphangiogenesis and lymphangiodysplasia: from molecular to clinical lymphology. *Microsc. Res. Tech.*, 55:122–145, 2001.

[278] C. J. Woolf, B. Safieh-Garabedian, Q. P. Ma, P. Crilly, and J. Winter. Nerve growth factor contributes to the generation of inflammatory sensory hypersensitivity. *Neuroscience*, 62(2):327–331, 1994.

[279] M. Xiong, G. Elson, D. Legarda, and S. J. Leibovich. Production of vascular endothelial growth factor by murine macrophages. *Am. J. Pathol.*, 153(2): 587–598, 1998.

[280] F. Xu, C. Zhang, and D. T. Graves. Abnormal cell responses and role of TNF-α in impaired diabetic wound healing. *BioMed Res. Intl.*, 2013:1–9, 2013.

[281] S. Yamano, W. P. Kuo, and C. Sukotjo. Downregulated gene expression of TGF-βs in diabetic oral wound healing. *J. Cranio-Maxillo-Facial Surg.*, 41: e42–e48, 2013.

[282] J. P. Yang, H. J. Liu, S. M. Cheng, Z. L. Wang, X. Cheng, H. X. Yu, and X. F. Liu. Direct transport of VEGF from the nasal cavity to brain. *Neurosci. Lett.*, 449(2):108–111, Jan 2009.

[283] L. Yang, C. X. Qiu, A. Ludlow, M. W. J. Ferguson, and G. Brunner. Active transforming growth factor-β in wound repair – determination using a new assay. *Am. J. Pathol.*, 154(1):105–111, 1999.

[284] I. Zachary and G. Gliki. Signaling transduction mechanisms mediating biological actions of the vascular endothelial growth factor family. *Cardiovasc. Res.*, 49:568–581, 2001.

[285] Q. Zhang, C. J. Magovern, C. A. Mack, K. T. Budenbender, W. Ko, and T. K. Rosengart. Vascular endothelial growth factor is the major angiogenic factor in omentum: Mechanism of the omentum-mediated angiogenesis. *J. Surg. Res.*, 67:147–154, 1997.

[286] X. Zheng, G. Y. Koh, and T. Jackson. A continuous model of angiogenesis: initiation, extension, and maturation of new blood vessels modulated by vascular endothelial growth factor, angiopoietins, platelet-derived growth factor-B, and pericytes. *Discr. Cont. Dyn. Syst. Series B*, 18(4):1109–1154, 2013.

[287] Y. Zheng, M. Watanabe, T. Kuraishi, S. Hattori, C. Kai, and M. Shibuya. Chimeric VEGF-ENZ7/PlGF specifically binding to VEGFR-2 accelerates skin wound healing via enhancement of neovascularization. *Arterioscler. Thromb. Vasc. Biol.*, 27(3):503–511, Mar 2007.

[288] Z. W. Zhu, H. Friess, L. Wang, T. Bogardus, M. Korc, J. Kleeff, and M. W. Buchler. Nerve growth factor exerts differential effects on the growth of human pancreatic cancer cells. *Clin. Cancer Res.*, 7(1):105–112, 2001.

[289] J. C. Zhuang and G. N. Wogan. Growth and viability of macrophages continuously stimulated to produce nitric oxide. *Proc. Natl. Acad. Sci. USA*, 94: 11875–11880, 1997.